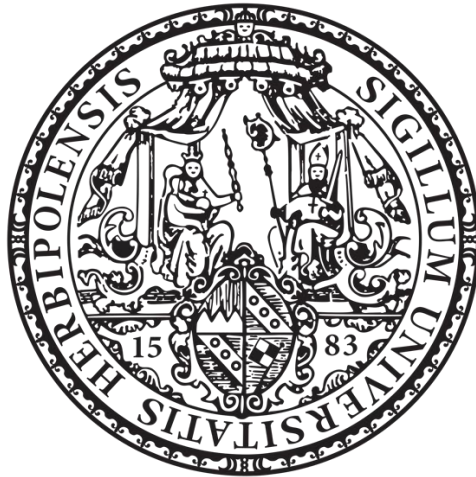


# Electrochromic systems based on metallopolymers and metal oxides: towards neutral tint and near-infrared transmission modulation



Kumulative Dissertation

zur Erlangung des naturwissenschaftlichen Doktorgrades der

Julius-Maximilians-Universität Würzburg

vorgelegt von

**Lukas Niklaus**

aus Hambach

Würzburg, 2021



Eingereicht bei der Fakultät für Chemie und Pharmazie am

24.09.2021

Gutachter der schriftlichen Arbeit

1. Gutachter: Prof. Dr. Gerhard Sextl

2. Gutachter: Prof. Dr. Anke Krüger

Prüfer des öffentlichen Promotionskolloquiums

1. Prüfer: Prof. Dr. Gerhard Sextl

2. Prüfer: Prof. Dr. Anke Krüger

3. Prüfer: Prof. Dr. Tobias Hertel

Datum des öffentlichen Promotionskolloquiums

24.01.2022

Doktorurkunde ausgehändigt am

---

The present work was carried out in the period from 17.06.2016 to 30.06.2020 at the Fraunhofer Institute for Silicate Research ISC in Würzburg under the supervision of Prof. Dr. Gerhard Sextl. The present cumulative dissertation is an abridged presentation of the research results. The detailed results are part of the following publications. The corresponding author is marked with \*. Reprints were made with permission from the respective publishers.

**Niklaus, L.**, Schott, M.\*, Mihelčič, M., Jerman, I., Posset, U., Sextl, G., Metallopolymers and non-stoichiometric nickel oxide: Towards neutral tint large-area electrochromic devices, *Sol. Energy Mater. Sol. Cells* 200 (2019), 9, 110002.

**Niklaus, L.**, Schott, M. \*, Posset, U., Giffin, G., Redox Electrolytes for Hybrid Type II Electrochromic Devices with Fe-MEPE or Ni<sub>1-x</sub>O as Electrode Materials, *ChemElectroChem* (2020), 7, 1-11.

**Niklaus, L.**, Schott, M. \*, Subel, J., Ulrich, S., Reichert, D., Posset, U., Giffin, G., Mixed metal oxides as optically-passive ion storage layers in electrochromic devices based on metallopolymers, *Sol. Energy Mater. Sol. Cells* 223 (2021), 110950.

**Niklaus, L.**, Schott, M. \*, Posset, U., Mihelčič, M., Jerman, I., Giffin, G., Charge balancing and optical contrast optimization in Fe-MEPE/Ni<sub>1-x</sub>O electrochromic devices containing a Li reference electrode, *Sol. Energy Mater. Sol. Cells* 227 (2021) 111080.

*You cannot get through a single day without  
having an impact on the world around you.*

*What you do makes a difference,  
and you have to decide  
what kind of difference you want to make.*

Dr. Jane Goodall

## Table of content

Table of content.....	i
List of figures .....	iii
List of tables.....	vi
List of abbreviations.....	viii
List of symbols/units .....	x
I. Introduction and Motivation .....	1
II. Theoretical part .....	4
1. Electrochromism.....	4
1.1. Electrochemical fundamentals.....	8
1.2. Electrochromic devices.....	11
1.3. Figures-of-merit .....	13
2. Electrochromic materials studied in this thesis.....	17
2.1. Metallopolymers.....	17
2.2. Metal oxides as counter electrodes .....	21
2.3. Redox mediators.....	28
III. Scope of the thesis .....	30
IV. Experimental part.....	31
1. Overview chemicals and substrates.....	31
2. Synthesis and film deposition .....	33
2.1. Iron-based metallopolymer .....	33
2.2. Non-stoichiometric nickel oxide .....	34
2.3. TiVO <sub>x</sub> and TMOs.....	35
3. Preparation and assembly of ECDs .....	36
4. Characterization methods.....	38
4.1. IR spectroscopy .....	38
4.2. UV-Vis and colorimetric measurements .....	38
4.3. Haze .....	38
4.4. Cross-cut test.....	38
4.5. Scanning electron microscopy and energy-dispersive X-ray spectroscopy .....	38
4.6. Electrochemical and <i>in situ</i> spectroelectrochemical measurements.....	38

## Table of content

4.7.	Transference number and T-dependent conductivity .....	40
4.8.	X-ray photoelectron spectroscopy .....	40
4.9.	Laser scanning microscope .....	40
V.	Results and discussion .....	41
1.	Substrate and electrolyte .....	41
2.	Fe-MEPE and Ni <sub>1-x</sub> O thin film electrodes and combinations thereof .....	43
2.1.	Detailed characterization of Fe-MEPE thin film electrodes .....	43
2.2.	Detailed characterization of Ni <sub>1-x</sub> O thin film electrodes .....	45
2.3.	ECDs containing Fe-MEPE and Ni <sub>1-x</sub> O .....	48
2.4.	Flexible ultra-thin glass Fe-MEPE/Ni <sub>1-x</sub> O ECDs .....	53
3.	ECDs based on Fe-MEPE and optically-passive mixed metal oxides .....	56
3.1.	Detailed characterization of TiVO <sub>x</sub> and TMO thin film electrodes .....	56
3.2.	ECDs containing Fe-MEPE and optically-passive mixed metal oxides .....	58
4.	Simplification of the cell architecture using redox mediators .....	61
VI.	Summary and Outlook .....	67
VII.	Zusammenfassung und Ausblick .....	69
	Selbstständigkeitserklärung .....	71
	Acknowledgment .....	72
	References .....	73
	Appendix .....	92
	Part I: Neutral tint with Fe-MEPE and Ni <sub>1-x</sub> O thin film electrodes .....	92
	Part II: Optically-passive mixed metal oxides .....	101
	Part III: Simplification of the cell architecture using redox mediators .....	102
	List of publications, posters, and conferences .....	105
	Contribution to the publications .....	107

## List of figures

Fig. 1: Solar radiation spectrum on earth according to ASTM G173. [14] .....	2
Fig. 2: (A) Exemplary CVs of Fe-MEPE on FTO glass with Li as RE and CE in 1 M LiClO <sub>4</sub> /PC and (B) corresponding $j$ vs. $v^{1/2}$ plot.....	8
Fig. 3: (A) Exemplary galvanostatic charging/discharging profiles of Fe-MEPE with Li as RE and CE in 1 M LiClO <sub>4</sub> /PC and (B) typical idealized Nyquist plot (imaginary ( $Z''$ ) vs. real part ( $Z'$ ) of the impedance) of the depicted equivalent electrical circuit model. The resistor and capacitor are indicated as R and C, respectively. Adapted from ref. [96] with permission from Springer.....	9
Fig. 4: Schematic structures of (A) type I, (B) type II, and (C) type III ECDs. Reproduced from ref. [103] with permission from Wiley.....	11
Fig. 5: ECD working principle. Reproduced from ref. [113] with permission of Elsevier. ....	12
Fig. 6: (A) Spectral intensity of the standard illuminant D65 and standardized spectral sensitivity of the human eye $V(\lambda)$ and (B) the representation of the $L^*a^*b^*$ color space and depiction of $\Delta E^*$ according to DIN 5033. [117] .....	14
Fig. 7: Change in optical density vs. charge density, with (I) and (II) representing commonly used approaches to calculate coloration efficiency. Reproduced from ref. [22] with permission from the Royal Society of Chemistry.....	15
Fig. 8: Definition of the response time of the decoloration/coloration process. Adapted from ref. [124] with permission from Elsevier.....	16
Fig. 9: Scheme of synthetic route and possibilities for synthetic variation (spacer unit, side chains on tpy units, the introduction of N atoms into tpy ring system) for the ligand (from L1 to L5). Adapted from ref. [81] with permission of the American Chemical Society. ....	18
Fig. 10: Molecular orbital (MO) scheme and ligand field splitting attributed to the absorption of MEPEs according to ref. [141]......	18
Fig. 11: (A) Defect-free crystal structure and (B) crystal facets of NiO. Adapted from ref. [177] with permission from Elsevier. ....	22
Fig. 12: CVs of the NiO thin film cycled in a 1 M LiClO <sub>4</sub> /PC electrolyte at different cycle numbers. Reproduced from ref. [165] with permission from the Royal Society of Chemistry. ....	24
Fig. 13: Structure of the ligand and the resulting Fe-MEPE. Reproduced from ref. [137] with permission from the American Chemical Society. ....	33
Fig. 14: Schematic representation of the dip-coating process from a 35 mmol·L <sup>-1</sup> Fe-MEPE solution in EtOH/MeOH/2-butoxyethanol. Adapted from ref. [228].....	33
Fig. 15: Schematic representation of the spin-coating process of the Ni <sub>1-x</sub> O dispersion. Adapted from ref. [229].....	34
Fig. 16: Simplified procedure for the preparation and assembly of three-electrode ECDs. ....	36
Fig. 17: Transmission spectra of the glass-based substrates. ....	41
Fig. 18: CVs of the FTO glass with Li as CE and RE in 1 M LiClO <sub>4</sub> /PC.....	42
Fig. 19: (A) EIS and chronoamperometric measurements used to calculate the Li transference number of 1 M LiClO <sub>4</sub> /PC electrolyte and (B) temperature-dependent conductivity measurements of LiClO <sub>4</sub> -	



## List of figures

containing liquid and gel electrolyte. The insets show the two set-ups for the corresponding measurement.....	42
Fig. 20: SEM images depicting (A) the layer thickness and (B) the surface structure of the Fe-MEPE thin films on FTO glass.....	43
Fig. 21: (A) Transmission spectra of Fe-MEPE (MLCT band at 584 nm) in 1 M LiClO <sub>4</sub> /PC with Pt as CE and Ag/AgCl as RE. (B) CV at 10 mV·s <sup>-1</sup> , and (C) charge density over 1,000 charging/discharging cycles (current density: 25 μA·cm <sup>-2</sup> ) of Fe-MEPE films on FTO glass in 1 M LiClO <sub>4</sub> /PC with Li as CE and RE. ....	44
Fig. 22: SEM images depicting (A) the layer thickness and (B) the surface structure of the Ni <sub>1-x</sub> O <sub>3</sub> thin film on FTO glass. ....	45
Fig. 23: (A) Spectroelectrochemical measurements of Ni <sub>1-x</sub> O with Pt as CE and Ag/AgCl as RE in 1 M LiClO <sub>4</sub> /PC, inset: photographic images of the bright (reduced) and colored (oxidized) state. (B) CVs at a scan rate of 10 mV·s <sup>-1</sup> with Li as CE/RE. (C) Charge retention over 1,000 charging/discharging cycles (current density: 25 μA·cm <sup>-2</sup> ) with Li as CE/RE and 1 M LiClO <sub>4</sub> /PC as electrolyte. (D) Visible light transmittance (τ <sub>v</sub> ) values for Ni <sub>1-x</sub> O electrodes deposited with 2 to 6 layers vs. the applied potential vs. Ag/AgCl in 1 M LiClO <sub>4</sub> /PC. ....	47
Fig. 24: Comparison of the spectroelectrochemical measurements of the two-electrode ECDs: (A) ECD1-1 (Fe-MEPE/Ni <sub>1-x</sub> O <sub>2</sub> ), (B) ECD1-2 (Fe-MEPE/Ni <sub>1-x</sub> O <sub>3</sub> ), (C) ECD1-3 (Fe-MEPE/Ni <sub>1-x</sub> O <sub>5</sub> ) and the three-electrode ECDs: (D) ECD1-1_RE (Fe-MEPE/Ni <sub>1-x</sub> O <sub>2</sub> ), (E) ECD1-2_RE (Fe-MEPE/Ni <sub>1-x</sub> O <sub>3</sub> ), and (F) ECD1-3_RE (Fe-MEPE/Ni <sub>1-x</sub> O <sub>5</sub> ). The insets show the photographic images of the colored and bright state. ....	49
Fig. 25: Cycle stability over 1,000 potentiostatic switching cycles monitored by transmittance change at 584 nm and the measured electrode potentials of the Fe-MEPE and Ni <sub>1-x</sub> O electrodes in (A,D) ECD1-1_RE, (B,E) ECD1-2_RE, and (C,F) ECD1-3_RE, respectively. ....	52
Fig. 26: SEM images depicting the layer thickness and the surface structure of the (A,B) Fe-MEPE and (C,D) Ni <sub>1-x</sub> O layer on ultra-thin ITO glass. ....	54
Fig. 27: (A) Spectroelectrochemical characterization and (B) change in transmittance at 584 nm over 1,000 potentiostatic cycles of ECD1-4. ....	55
Fig. 28: Transmission spectra of TiVO <sub>x</sub> and TMO thin films on FTO glass. The dotted line shows the spectrum of uncoated FTO glass as a reference. ....	56
Fig. 29: Spectroelectrochemical characterization of (A) ECD2-1 (Fe-MEPE/TiVO <sub>x</sub> ), (C) ECD2-2 (Fe-MEPE/TMO-1), and (E) ECD2-3 (Fe-MEPE/TMO-2). Photographic images of the ECDs in the dark (left) and bright (right) state before cycling are shown as insets. Cycling stability over 1,000 switching cycles of (B) ECD2-1, (D) ECD2-2 and (F) ECD2-3.....	59
Fig. 30: Chemical structures of the reduced (left) and oxidized (right) redox mediator species used in this work. (A) Potassium hexacyanoferrate(II)/(III) (KHCF(II)/(III)), (B) ferrocene/ferrocenium (Fc <sup>0/+</sup> ), and (C) tetramethylthiourea/tetramethylformaminium disulfide (TMTU/TMFDS <sup>2+</sup> ) accompanied by (D) the absorbance spectra of the redox electrolytes.....	61
Fig. 31: Spectroelectrochemical measurements of (A) ECD3-1 (reference cell), (B) ECD3-2 (0.001 M KHCF(III) in the 1 M LiClO <sub>4</sub> /H <sub>2</sub> O electrolyte), (C) ECD3-7 (0.1 M TMFDS <sup>2+</sup> in 1 M LiClO <sub>4</sub> /PC), and (D)	

## List of figures

ECD3-10 (0.1 M, molar ratio TMTU/TMFDS <sup>2+</sup> = 1:0.1) and the corresponding photographs indicating the color changes. ....	64
Fig. 32: Current density-time profiles of (A) ECD3-1 (reference cell), (B) ECD3-2 (0.001 M KHCF(III) in the 1 M LiClO <sub>4</sub> /H <sub>2</sub> O electrolyte), (C) ECD3-7 (0.1 M TMFDS <sup>2+</sup> in 1 M LiClO <sub>4</sub> /PC), and (D) ECD3-10 (0.1 M, molar ratio TMTU/TMFDS <sup>2+</sup> = 1:0.1).....	65

## List of tables

Tab. 1: Overview of commercially available EC windows for building applications described by their maximum size and modulation range.....	6
Tab. 2: Overview of optical properties of Fe(II)-, Ru(II), and Co(II)-based MEPEs depending on the ligand. Adapted from ref [81] with permission from the American Chemical Society. Images were taken from ref. [128] with permission of Wiley. ....	19
Tab. 3: Overview of EC properties of metal ion-based MEPEs. ....	20
Tab. 4: Overview of deposition method and EC properties of NiO described in the literature.....	23
Tab. 5: Overview of EC properties for ECDs with WO <sub>3</sub> as WE and NiO as CEs switching between blue (dark) and colorless (bright) states. ....	26
Tab. 6: Overview of EC properties for redox mediator-containing ECDs studied recently. ....	28
Tab. 7: List of chemicals and solvents used in this thesis.....	31
Tab. 8: List of TCO substrates used in this thesis.....	32
Tab. 9: Sputtering conditions and sample composition: gas flow q, pressure p, cathode power P, thickness t, and deposition rate r <sub>d</sub> . Target-substrate distance: 170 mm, target-size: 2''∅. ....	35
Tab. 10: Redox electrolytes with 1 M LiClO <sub>4</sub> in H <sub>2</sub> O or PC and gelling agent. Reproduced from ref. [103] with permission from Wiley.....	37
Tab. 11: Molar ratio of TMTU:TMFDS <sup>2+</sup> containing redox electrolytes with 1 M LiClO <sub>4</sub> /PC and gelling agent. Reproduced from ref. [103] with permission from Wiley. ....	37
Tab. 12: Color coordinates (L*a*b*), visible light transmittance (τ <sub>v</sub> ), sheet resistance, and haze of TCO-based substrates. ....	41
Tab. 13: Color coordinates (L*a*b*), transmittance (T) at 584 nm, visible light transmittance (τ <sub>v</sub> ), charge densities (q) after charging (2 V)/discharging (0 V), coulombic efficiency, and coloration efficiency (η) of the Fe-MEPE thin film electrodes.....	44
Tab. 14: Color coordinates (L*a*b*), transmittance (T) at 584 nm, visible light transmittance (τ <sub>v</sub> ), charge densities (q) after charging (2 V) and discharging (0 V), coulombic efficiency, and coloration efficiency (η) of the Ni <sub>1-x</sub> O thin film electrodes.....	47
Tab. 15: Color coordinates (L*a*b*), transmittance (T) at 584 nm, visible light transmittance (τ <sub>v</sub> ), charge densities (q) after charging (2 V) and discharging (0 V), coulombic efficiency, and coloration efficiency (η) of the Fe-MEPE/Ni <sub>1-x</sub> O ECDs.....	50
Tab. 16: Color coordinates (L*a*b*), transmittance (T) at 584 nm, visible light transmittance (τ <sub>v</sub> ), charge densities (q) after charging (2 V) and discharging (0 V), coulombic efficiency, and coloration efficiency (η) of the Fe-MEPE and Ni <sub>1-x</sub> O thin films on ultra-thin ITO glass. ....	54
Tab. 17: Color coordinates (L*a*b*), transmittance (T) at 584 nm, visible light transmittance (τ <sub>v</sub> ), charge densities (q) after charging (2 V) and discharging (0 V), coulombic efficiency, and coloration efficiency (η) of ECD1-4.....	54
Tab. 18: Color coordinates (L*a*b*), transmittance (T) and visible light transmittance (τ <sub>v</sub> ) values and charge densities (q) between the redox states, as well as Coulombic efficiency and coloration efficiency (η) of the thin film electrodes. ....	57

## List of tables

Tab. 19: Charge, density ratio (MEPE:ion storage layer), color coordinates ( $L^*a^*b^*$ ), transmittance (T) and visible light transmittance ( $\tau_v$ ) values, response times, charge densities (q) at 0 V (dark state) and 1.5 V or 2.5 V (bright state), respectively, as well as coloration efficiency ( $\eta$ ) of the ECDs. ....	58
Tab. 20: Concentration (c), color coordinates ( $L^*a^*b^*$ ), transmittance (T) at 584 nm, visible light transmittance ( $\tau_v$ ), charge densities (q) of the dark and bright states, and coloration efficiency ( $\eta$ ) of the Fe-MEPE-based ECDs with different redox mediators in the electrolyte (1 M LiClO <sub>4</sub> /PC). ....	62
Tab. 21: Color coordinates ( $L^*a^*b^*$ ), transmittance (T) at 584 nm, visible light transmittance ( $\tau_v$ ), charge densities (q) of the dark (-2 V) and bright (2 V) states, and coloration efficiency ( $\eta$ ) of the Ni <sub>1-x</sub> O-based ECDs with TMTU/TMFDS <sup>2+</sup> as redox mediator in the electrolyte (1 M LiClO <sub>4</sub> /PC). ....	62

## List of abbreviations

BMITFSI.....	1-Butyl-3-methylimidazolium bis(trifluoromethylsulfonyl)imide
CE.....	counter electrode
CIE.....	Commission Internationale de l'Éclairage
CO <sub>2</sub> .....	carbon dioxide
CR.....	contrast ratio
CV.....	cyclic voltammetry
CVD.....	chemical vapor deposition
DC.....	direct current
DEC.....	diethylcarbonate
DGU.....	double glazing unit
DSC.....	differential scanning calorimetry
DSSC.....	dye-sensitized solar cell
e <sup>-</sup> .....	electron
e <sup>+</sup> .....	hole
EC.....	electrochromic
ECD.....	electrochromic device
EDX.....	energy-dispersive X-ray spectroscopy
EIS.....	electrochemical impedance spectroscopy
EMITFSI.....	1-Ethyl-3-methylimidazolium bis(trifluoromethylsulfonyl)imide
EPMA.....	electron probe microanalysis
EtOH.....	ethanol
Fc <sup>0/+</sup> .....	ferrocene/ferrocenium
FcBF <sub>4</sub> .....	ferrocenium tetrafluoroborate
FcPF <sub>6</sub> .....	ferrocenium hexafluorophosphate
FTO.....	fluorine-doped tin oxide
IR.....	infrared
IRRAS.....	infrared reflection-absorption spectroscopy
ITO.....	tin-doped indium oxide
IVCT.....	intervalence charge transfer
KBr.....	potassium bromide
KCl.....	potassium chloride
KHCF.....	potassium hexacyanoferrate
LC.....	liquid crystal
LiClO <sub>4</sub> .....	lithium perchlorate
LMO.....	LiMn <sub>2</sub> O <sub>4</sub> , Lithium manganate
low-e.....	low emissivity
LSM.....	laser scanning microscopy
LTO.....	Li <sub>4</sub> Ti <sub>5</sub> O <sub>12</sub> , Lithium titanate
MeOH.....	methanol
MEPE.....	metallopolymer

## List of abbreviations

MLCT	metal-to-ligand charge transfer
MO	molecular orbital
NA	numerical aperture
NaClO <sub>4</sub>	sodium perchlorate
NaTFSI	sodium trifluoromethanesulfonimide
Nb <sub>2</sub> O <sub>5</sub> Mo	Mo-doped niobium oxide
Ni(OAc) <sub>2</sub>	nickel acetate
Ni(OH) <sub>2</sub>	nickel hydroxide
Ni <sub>1-x</sub> O	non-stoichiometric nickel oxide
NiCl <sub>2</sub>	nickel chloride
NiO	nickel oxide
NIR	near-infrared
NOBF <sub>4</sub>	nitrosonium tetrafluoroborate
OAc <sup>-</sup>	acetate
OD	optical density
OH <sup>-</sup>	hydroxide
OLED	organic light-emitting diode
PB	Prussian blue
PC	propylene carbonate
PDLC	polymer-dispersed liquid crystal
R2R	roll-to-roll
RE	reference electrode
SEM	scanning electron microscopy
SPD	suspended particle device
TBA <sup>+</sup>	tetrabutylammonium cation
TC	thermochromic
TCO	transparent conductive oxides
TGA	thermogravimetric analysis
TiVO <sub>x</sub>	titanium vanadium oxide
TMO	titanium manganese oxide
TMTU/TMFDS <sup>2+</sup>	tetramethylthiourea/tetramethylformaminium disulfide
tpy	(2,2':6',2''-terpyridine)
tpy-ph-tpy	4',4'''-(1,4-phenylene)bis(2,2':6',2''-terpyridine)
UV	ultraviolet
V <sub>2</sub> O <sub>5</sub>	vanadium pentoxide
Vis	visible
WE	working electrode
WO <sub>3</sub>	tungsten trioxide
XAFS	X-ray absorption fine structure
XPS	X-ray photoelectron spectroscopy
XRD	X-ray diffraction

**List of symbols/units**

$\Delta E^*$	color distance
A	electrode area / $\text{cm}^2$
$a^*$	from green (-128) to red (+127)
$b^*$	from blue (-128) to yellow (+127)
c	concentration / $\text{mol}\cdot\text{l}^{-1}$
D	diffusion coefficient / $\text{m}^2\cdot\text{s}^{-1}$
D65	solar radiation at a summer day in Northern and Central Europe
$D_\lambda$	relative spectral distribution of the standard illuminant D65
I	transmitted light
$I^0$	initial current / mA
$I_0$	incident light
$i_p$	current maximum / mA
$I^S$	steady-state current / mA
$j_p$	current density maximum / $\text{mA}\cdot\text{cm}^{-2}$
$L^*$	lightness from black (0) to white (100)
mA	milliampere
mC	millicoulomb
$n_e$	number of electrons transferred in the redox process
nm	nanometer, $10^{-9}$ m
q	charge density / $\text{mC}\cdot\text{cm}^{-2}$
$R^0$	initial resistance / $\Omega$
$R^S$	steady-state resistance / $\Omega$
S	Siemens
T	transmittance / nm
$T_+$	Li transference number
$T_b$	bright state transmittance / %
$T_c$	dark state transmittance / %
$t_s$	response time / s
TW	terawatt
v	scan rate / $\text{mV}\cdot\text{s}^{-1}$
$V(\lambda)$	spectral sensitivity of the human eye
Z	impedance / $\Omega$
$\eta$	coloration efficiency / $\text{cm}^2\cdot\text{C}^{-1}$
$\lambda$	wavelength / nm
$\lambda_{\text{max}}$	wavelength at local absorbance maximum / nm
$\tau(\lambda)$	spectral transmittance / %
$\tau_v$	visible light transmittance / %
$\omega$	frequency / $\text{s}^{-1}$

## I. Introduction and Motivation

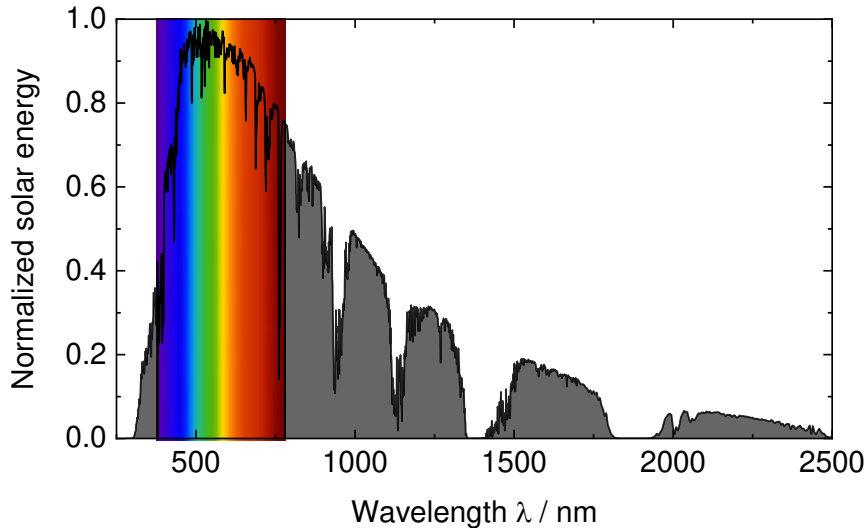
*"Climate change knows no borders. It will not stop before the Pacific Islands and the whole of the international community here has to shoulder a responsibility to bring about sustainable development."*

Dr. Angela Merkel

Around 1980, the German federal government decided to change its energy policy, which was further enforced in the Paris Agreement in December 2015. [1,2] The aim here was to reduce Germany's primary energy consumption by up to 50% until 2050 compared to 1990. [2,3] During the last decades and in the future, the growing population leads to increasing energy costs and global warming. The reason for global warming lies in the amount of greenhouse gases, e.g., carbon dioxide (CO<sub>2</sub>) mostly originated from burning coal, fossil oil, and gas, leading to rising sea levels and more extreme weather events such as hurricanes and droughts. [4–6] Nowadays, the climate crisis and worldwide public demonstrations, e.g., "Fridays for Future", force governments to further enhance their efforts to fight the increasing energy consumption and CO<sub>2</sub> emission. [7,8] In parallel with developing renewable energy sources, reducing and optimizing energy consumption has become ever more necessary and urgent. The building sector plays one crucial part here: It is responsible for 30-40% (approx. 1.4 TW) of the global use of primary energy and approx. 38% of greenhouse gasses in the US are produced in this sector. [9,10] A major trend in modern architecture is the use of large glass façades and roof elements to make time spent in these buildings more pleasant due to spacious rooms and their bright appearance.

The solar radiation spectrum of the sun shown in Fig. 1, consists of three parts: i) the ultraviolet (UV) part below 380 nm, ii) the visible (Vis) range from 380 nm to 780 nm, and iii) the near-infrared (NIR) region from 780 nm to 2500 nm, which contributes to solar heat. Large glass façades often allow huge energy flows to enter or exit a building, which means that energy-consuming cooling or heating is needed to create a comfortable indoor environment. Therefore, if the energy consumption in buildings can be reduced, substantial primary energy savings (on the order of 10%) will be achieved in many regions. [11,12] A solution to this challenge is to minimize the glazing size, but this negatively influences the visual comfort and use of daylighting. Therefore, the demand for dimmable glazing, which regulates light and energy transmittance, is increasing for reasons associated with comfort and rising energy costs, e.g., privacy, enhanced comfort, energy savings (up to 15%) [12], sunlight protection, and glare. Low-emissivity (low-e) coatings (i.e., thin metal layers absorb and dissipate heat, e.g., fluorinated tin dioxide) and heat mirrors (i.e., nanoscale coatings of metal between glass units reflect heat back to its source) are the two most widely used static window coatings to control the indoor temperature in cold and warm climate zones, respectively. [13] Solar heat can pass through low-e glass while indoor heat is stopped from escaping to the outside, and, thus, they are widely used in cold, high-latitude regions, e.g., Northern Europe. Solar control coatings are designed for warmer, low-latitude regions like Central Africa as they block most of the solar heat. [12]





**Fig. 1:** Solar radiation spectrum on earth according to ASTM G173. [14]

Smart (dimnable) windows based on thermochromic (TC) and electrochromic (EC) materials are more intelligent than the passive solar control coatings and the light and heat transmission can be varied by using an external electrical stimulus, *i.e.*, temperature and voltage/current, respectively. The EC windows increase comfort by adapting the amount of sunlight and lighting conditions to personal needs. The potential of actively dimmable windows to improve the energy efficiency in buildings and vehicles opens up the possibility of dynamically adapting the heat input from solar radiation to changing climate conditions. [15,16] According to a US simulation study, EC windows with a modulation in the VIS and NIR range can achieve up to 40% energy savings compared to classical windows (double glazing unit (DGU), without additional coatings). [17] According to Granqvist *et al.*, the annual peak cooling load can be reduced by 19-26% and the energy for lighting by 48-67% with EC windows. [15] Moreover, such electrochromic devices (ECDs) can be used in the automobile sector, especially for electric cars. They help decrease battery consumption due to a reduced need for heating, ventilation, and air conditioning. By this approach, the mileage of electric vehicles can be extended by approx. 5-10% as less energy is consumed. [18–20] This is an essential point for German policy as only CO<sub>2</sub>-neutral cars will be allowed to join the market in 2050. [1] In addition, passenger comfort is increased due to the possibility of modifying the amount of sunlight coming into the car.

Nevertheless, far-reaching market penetration of EC applications, *i.e.*, architectural or automotive glazing, has not been achieved despite the promising potential of the technology due to high production costs, *i.e.*, up to 1,000 €·m<sup>-2</sup> depending on the deposition method. [21] Thus, the availability of large-scale processing techniques, including roll-to-roll (R2R) coating, is key to integrating these components into economically attractive commercial devices. [22] To attain customer needs and industrial requirements, the color transition of commercially available EC windows has to be broadened towards neutral tint and independent modulation in the NIR region, *i.e.*, the so-called *g* value. It is a coefficient to measure the solar energy transmittance of windows from 0 (no solar energy transmittance) to 1 (total transmittance of solar radiation). While NIR light accounts for about half of the solar energy, it does not contribute to daylighting within a building. Hence, an optimized EC window affects a building's energy use and influences occupant comfort. [23] Therefore, new material combinations of suitable,

## Introduction and Motivation

complementary switching EC electrodes are necessary to achieve high transmittance modulation and colorless bright states. On one hand, suitable EC material candidates are metallopolymers (MEPEs), which offer an intense but narrow metal-to-ligand charge transfer (MLCT) band in the visible region and, on the other hand, broad-band absorbing metal oxides (*e.g.*, nickel oxide (NiO)) pave the way for neutral-colored EC cells in the dark state with an extended modulation into the NIR region of the electromagnetic spectrum.

## II. Theoretical part

### 1. Electrochromism

In general, chromogenic materials exhibit optical modulation (absorption, transmission, reflection) upon external stimuli, [16,24] such as temperature (thermochromism), [25,26] pH change (chemochromism), [27,28] photons (photochromism), [29,30] and mechanical stress (mechanochromism). [31,32] When an external voltage is used to obtain this effect, it is called electrochromism. EC materials are electrochemically oxidized or reduced by insertion/de-insertion of charge carriers into/from the electrodes. [33,34] Simultaneously, cations or anions are inserted in or extracted from the EC layer to provide charge compensation. Here, 'insertion' and 'de-insertion' are more general terms, while 'intercalation' and 'de-intercalation' are often used for reactions involving insertion/de-insertion of guest species with host materials that have a layer-type crystal structure. The obtained redox states exhibit different optical absorption characteristics while maintaining a high transparency in both states. If the absorption band is in the visible range, the EC layer shows a characteristic color. High transmissivity in the visible range is achieved, *e.g.*, by shifting the absorption band into the NIR range or by suppressing electronic transitions. [35] When a material can switch between more than two states, it is called polyelectrochromic. [36] Cathodically-coloring EC materials darken upon reduction, while anodically-coloring materials brighten up upon reduction. [34] For most applications, ECDs are studied in a simple two-electrode system (sandwich configuration). They can be thought of as a rechargeable electrochemical cell, in which the EC electrode is separated from a charge-balancing counter electrode (CE) by a solid, gel, or liquid electrolyte. [37]

Switchable transmittance in the visible range has been the subject of research for over 50 years. Besides tungsten trioxide ( $\text{WO}_3$ ), for which the EC effect was studied first in sulfuric acid and which is the most prominent member of EC metal oxides, a broad range of materials can be used, such as viologens, conducting polymers, and metallopolymers. [34,38] Comprehensive overviews of the current state-of-the-art concerning EC materials can be found in ref. [38–40]. Along with S.K. Deb, C.-G. Granqvist is an authority on metal oxide electrochromics, whereas the group of J. Reynolds has been especially influential in the field of conjugated conducting polymers, *e.g.*, thiophene-based EC polymers were studied to create the first set of soluble materials that exhibit the whole color palette. [41] Milliron *et al.* observed a so-called 'plasmonic electrochromism' during their research on colloidal transition metal oxides. [42–44] Here, the colloidal nano-crystals' plasmonic EC response controls NIR light transmission without affecting the visible light transmittance ( $\tau_v$ ). Therefore, amorphous transition metal oxides are recognized as leading candidates for EC smart windows that can dynamically modulate solar irradiation and glare to enhance energy efficiency and visual comfort in buildings.

To achieve far-reaching market penetration and integrate EC systems into everyday life (*i.e.*, architectural or automotive glazing, aircraft, marine, home appliances, and displays), neutral tinting and NIR modulation are two major hurdles to overcome. Smart windows modulate light transmission according to the user's comfort, in contrast to static systems, *e.g.*, low-e coatings. The active control of the light transmission saves cooling costs during summer, leading to reduced energy consumption in (non-)residual buildings. For the sake of completeness concerning commercially available solar control

systems, the suspended particle devices (SPD) and polymer-dispersed liquid crystal (PDLC) devices should be mentioned here. The working principle is based on particles dissolved in an electrolyte, in which they change their orientation depending on the applied field and thus influence the optical properties of the system. For SPDs, a thin film laminate of nanoparticles is suspended in a liquid and placed between two glass or plastic pieces or attached to one layer. When no voltage is applied, the suspended particles are randomly organized, thus blocking and absorbing light. When a voltage is applied, the suspended particles align and let light pass. Varying the voltage of the film varies the orientation of the suspended particles, thereby regulating the tint of the glazing and the amount of light transmitted. In addition, they are colored in the tension-free state. In PDLCs, liquid crystals (LC) are dissolved or dispersed into a liquid polymer followed by solidification or curing of the polymer. During the change of the polymer from a liquid to a solid, the liquid crystals become incompatible with the solid polymer and form droplets throughout the solid polymer increasing the haze of the device. Therefore, these devices switch from opaque to transparent. [45] One example here is the ICRIVISION® Solar system of Merck, in which a wide range of dye-doped LC mixtures is capable of achieving nearly every color and saturation level. [46] Unlike EC, electrical power is needed continuously to maintain their transparent state, while the colored state is rapidly obtained (in the order of 1–3 s) when the current is switched off. SPD can control their solar transmittance in a range of approximately 50%, similarly to EC, although with a lower selectiveness. While LC solar transmittance can vary in a smaller range (typically 15% – 20%), between 33% and 47% or between 20% and 37%, depending on the quantity of the dye introduced into the polymeric matrix. [47] Recently, more research efforts have been devoted to producing bi-stable PDLC technology. [48,49] Unlike traditional PDLC devices, bi-stable mode ones need not be placed in a sustained electric field to maintain their two optical states. Therefore, they can be used as an energy-saving light shutter for architectural and greenhouse windows for privacy and energy flow control. [50,51]

Electrochromism was first considered for use in information displays, and during the first half of the 1970s, several large companies invested heavily into research, such as IBM, Philips, and Canon. [52–54] However, electrochromism became less important in the 1970s due to the development of liquid crystals in displays. In 1984, EC windows were considered to be used in energy-efficient buildings by the U.S. Department of Energy. [55] In addition, Gentex Corp. started in 1987 to sell automatically dimming rear-view mirrors for glare elimination based on viologens and a thiazine dye or a phenylenediamine-species. Since that time, research on electrochromics has had a powerful boost, but it is still a niche application in the architectural and automotive sectors. Current studies on EC glazing have focused on energy efficiency, [17,56–61] lowering CO<sub>2</sub> emission, [62] and indoor comfort [63–65] in buildings. First-generation EC window products are on the market that exhibit a reversible transition from the clear to the dark state as listed in Tab. 1. The products from the companies EControl-Glas GmbH & Co. KG from Germany as well as from the US-based companies SageGlass (now owned by the French-based Saint-Gobain) and View Inc. are based on sputtered metal oxides as EC materials. Another advantage can be seen in the automotive sector. The energy reduction for air conditioning can lead to an extended range for electric cars combined with enhanced passenger comfort. A product from Saint-Gobain from France was only produced in small quantities for a Ferrari sunroof. [66–68]

**Tab. 1:** Overview of commercially available EC windows for building applications described by their maximum size and modulation range.

Manufacturer	Product	max. size / cm <sup>2</sup>	$\tau_v$ / %	g / %
SageGlass	Climaplus Classic	152 x 305	60-1	40-5
EControl-Glas GmbH & Co. KG	ec   smart glass   2	120 x 220	56-10	42-10
View Inc.	View Dynamic Glass	182 x 305	58-1	41-9
ChromoGenics AB	Dynamic 75 3G	155 x 440	61-33	40-14
	Dynamic 65 3G		56-14	36-6
Kinestral Technologies, Inc.	Halio	150 x 300	68-3	46-8
	Halio Black		59-0.1	39-8

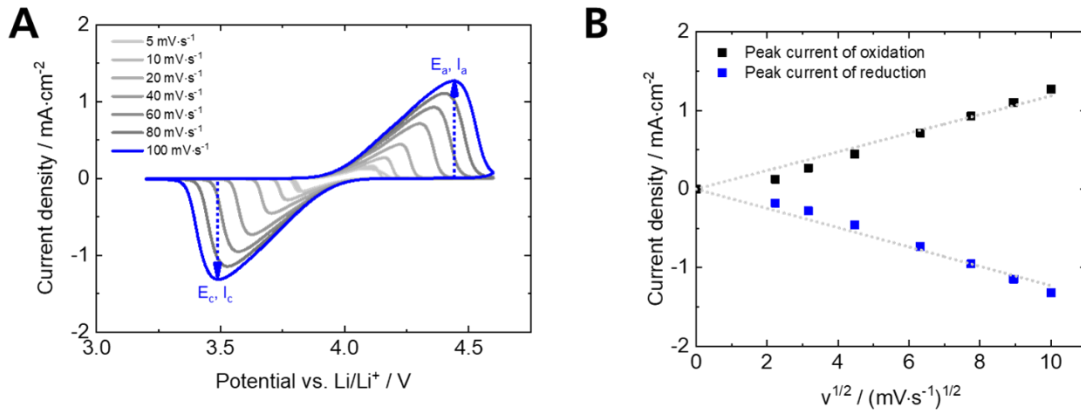
Up to now, only Kinestral showed technical maturity with a color-neutral layer combination of  $\text{WO}_3$  vs.  $\text{NiO}$ , while many more approaches with this combination are still under development. [66,68–70] While  $\text{WO}_3$  switches cathodically from colorless to blue,  $\text{NiO}$  enables an anodic color change from colorless to a gray hue. However,  $\text{NiO}$  is acid sensitive and difficult to manufacture; usually, there are color deviations in the brownish hue. [71–73] A gray color impression is also achieved by the cathodically-coloring Mo-doped niobium oxide ( $\text{Nb}_2\text{O}_5:\text{Mo}$ ), but the color transition is relatively slow (approx. 2 min, area: 7 cm<sup>2</sup>, applied cell voltage: -2.5 and 1.5 V). [74] A recently studied combination of cathodically-coloring  $\text{Li}_4\text{Ti}_5\text{O}_{12}$  (LTO) (colorless → deep blue) and anodically-coloring  $\text{LiMn}_2\text{O}_4$  (LMO) (pale green → orange-brown) is promising towards neutral tint in the dark state as the combined absorption of these intervalence charge transfer (IVCT) bands cover broad parts of the visible spectrum. [75]

Metallopolymeric compounds, on the other hand, can be synthesized using ditopic ligands, such as bis-(terpyridine)s (tpy), which react with metal cations such as  $\text{Fe}^{2+}$  or  $\text{Ru}^{2+}$  to form polycations, so-called metallopolymers. [76–78] They can be processed using standard wet-chemical methods such as dip or spin-coating. Due to their intense MLCT transitions-based absorption bands and their easy processability, MEPEs appear to be particularly suitable candidates for next-generation EC materials. However, there have been relatively few systematic studies on the relationship between structure and EC properties. [79–82] Only a few attempts to develop neutral gray switchable windows based on MEPE have been published so far. [83,84] Higuchi *et al.* studied a Co(II)-MEPE thin film, which showed a nearly transparent-to-black EC performance when immersed in alkaline aqueous solution (pH = 13, 0.1 M KCl) with a change in transmittance of 74.3% (81.9–7.6%) at 550 nm. This effect is due to the interaction between the d-orbital electron ( $e^-$ ) and hydroxide ions ( $\text{OH}^-$ ) affecting the d–d\* transition. A second approach is based on a spacer variation of the organic ligand in Fe-MEPEs, *i.e.*, two tpy units are connected without a phenyl spacer. By applying a potential of -2.5 V vs. Ag/AgCl in 1 M  $\text{LiClO}_4/\text{PC}$  as the electrolyte, the color of this Fe-MEPE film changes to a gray tint with a  $\tau_v$  value of 33% and an

intensive, distinct absorption peak in the NIR region with a maximum at 863 nm can be observed. This color change is due to the evident broadband absorption occurring throughout the Vis spectrum. It is not attributed to a MLCT transition but presumably due to a reduction of the bis-terpyridine ligand. [85–87] As the absorption of EC materials can be extended beyond the UV-Vis region into the infrared (IR) region, these EC materials are potentially useful in defense-related applications. [88] Therefore, EC materials that can be switched between other colors than blue hues are also known. Still, the realization of a neutral gray switchable window represents a technological challenge that has not yet been solved. [71–74,89] This is due to the fact that for neutral tinting, an ECD has to be capable of reversible (over thousands of switching cycles in ambient conditions), electrochemical switching between a dark and a bright state while exhibiting uniform, significant absorption, covering the Vis range in the dark state and either partial low-absorbance coverage or no absorption coverage in the bright state. [90]

## 1.1. Electrochemical fundamentals

In addition to the optical properties of EC materials, the electrochemical characterization is one of the most relevant measurements. [91,92] In the following part, a brief introduction to the theoretical background of these methods is given. [93] During cyclic voltammetric (CV) measurements, a triangular voltage is applied to the working electrode (WE), *i.e.*, the voltage is varied linearly with a defined scan rate  $\nu$  up to the reversal potential, and then returns to the output potential in a linearly descending manner. [93,94] The measured current consists of a Faradaic and a capacitive component. The Faradaic current is created by a heterogeneous charge transfer between the electrolyte and the electrode, whereas the capacitive current is generated by the formation of an electrical double layer at the phase boundary between the WE and the electrolyte. A typical CV of the redox process of a Fe-MEPE electrode can be seen in Fig. 2.



**Fig. 2:** (A) Exemplary CVs of Fe-MEPE on FTO glass with Li as RE and CE in 1 M LiClO<sub>4</sub>/PC and (B) corresponding  $j$  vs.  $\nu^{1/2}$  plot.

With this technique, the redox reactions at the electrodes and the reversibility of insertion/de-insertion reactions can be observed. For reversible redox reactions, the following points are valid: The difference of the anodic and cathodic peak potential ( $\Delta E_p = E_{p,a} - E_{p,c}$ ) is 59 mV divided by the number of electrons ( $n_e$ ) involved in the redox reaction. [93] Moreover, the potential peak does not change with the scan rate and the ratio of anodic and cathodic peak potential is 1. Here, the electrode reactions can be (semi-)quantitatively analyzed by means of the Randles-Sevcik equation at 25 °C:

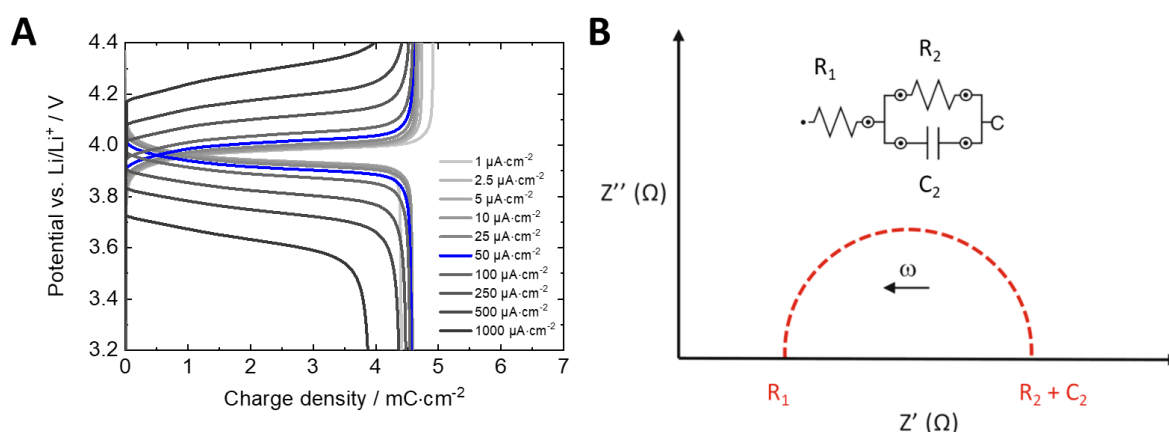
$$j_p = \frac{i_p}{A} = 2.69 \cdot 10^5 \cdot n_e^{3/2} \cdot D^{1/2} \cdot c \cdot \nu^{1/2} \quad (1)$$

where  $j_p$  and  $i_p$  is the current density [mA·cm<sup>-2</sup>] and current maximum [mA], respectively, A the electrode area [cm<sup>2</sup>], D the diffusion coefficient [m<sup>2</sup>·s<sup>-1</sup>], and c the concentration [mol·l<sup>-1</sup>]. The quantitative analysis is often challenging due to side reactions, *e.g.*, passivation and electrolyte decomposition. [94,95] These parasitic reactions lead to an inaccurate determination of the peak current as capacitive contributions cannot be neglected commonly.

Moreover, the charge density  $q$  [ $\text{mC}\cdot\text{cm}^{-2}$ ] of the electrode can be defined by the following equation:

$$q = \frac{1}{v} \int j \cdot dV \quad (2)$$

A second electrochemical method is the galvanostatic charging/discharging measurement as depicted in Fig. 3A. [93] Here, a constant current density is applied to insert/extract  $\text{Li}^+$  ions from the electrodes. As soon as the current is passed through the system, the electrochemical reaction begins and the concentration of the oxidized species in the vicinity of the electrode surface starts to decrease. The oxidized species diffuses from the bulk solution into the depleted layer and a concentration gradient grows out of the electrode surface into the solution. When the surface concentration of the oxidized species falls to zero, the electrode process can no longer be supported by the reduction of the oxidized species, which leads to an abrupt change in potential. With this method, the charge density of the layer is accessible. The steep drop in the potential of the discharge curve can be used to determine the maximum charge density. In the present case, the maximum charge density is determined during the charging (oxidation) and discharge process (reduction) at a potential of 4.4 V and 3.2 V vs.  $\text{Li}/\text{Li}^+$  at a current density of  $1 \mu\text{A}\cdot\text{cm}^{-2}$ . The largely symmetrical curve of the charging and discharging curves for all current densities indicates a reversible redox system, which can be evaluated by the coulombic efficiency, *i.e.*, defined as the ratio of discharge to charge density. This ratio is close to 1 and thus confirms the reversibility statement of the CV. [93]



**Fig. 3:** (A) Exemplary galvanostatic charging/discharging profiles of Fe-MEPE with Li as RE and CE in 1 M  $\text{LiClO}_4/\text{PC}$  and (B) typical idealized Nyquist plot (imaginary ( $Z''$ ) vs. real part ( $Z'$ ) of the impedance) of the depicted equivalent electrical circuit model. The resistor and capacitor are indicated as R and C, respectively. Adapted from ref. [96] with permission from Springer.

Finally, electrochemical impedance spectroscopy (EIS) is used to measure the impedance (analogous to the resistance in the ideal resistor that follows Ohm's law) of an electrochemical system, *e.g.* electrodes and electrolytes, over a wide range of frequencies. [96,97] Unlike galvanostatic and CV methods, where the electrode is usually driven rather far from the equilibrium conditions, the system is perturbed with a small alternating voltage or current signal in EIS. Subsequently, the current or voltage response from the system is measured. Here, the response to a sinusoidal potential will be a sinusoidal



## Theoretical part

current at the same frequency ( $\omega$ ) but shifted in phase. This situation can be represented in a Nyquist plot as depicted in Fig. 3B. It displays the imaginary ( $Z''$ ) and the real ( $Z'$ ) contribution to the complex impedance ( $Z = Z' + iZ''$ ). The experimental impedance data can be fitted with equivalent electrical circuit models (inset of Fig. 3B) that are able to represent the physical system and phenomena under investigation. [98] The impedance of the resistor is depicted as a point on the  $Z'$  axis, while an RC element leads to a half-circle. Following this procedure, the resistances and capacitances can be obtained.

An additional application of EIS is the determination of the Li transference number ( $T_+$ ), which describes the transport properties for ion-containing electrolytes [99,100] as well as the temperature-dependent conductivity. Both cations and anions are mobile in polymer electrolytes such as the studied proprietary gel electrolyte. Consequently, concentration gradients of the ion species are set up between anode and cathode upon potential application. This has an important influence on the electrical characteristics and performance of  $\text{Li}^+$ -containing electrolytes, as it provides information about the  $\text{Li}^+$  transport and thus about the efficiency of the electrochemical system. For low  $T_+$ , *e.g.*,  $\text{Li}^+$  is not replenished quickly enough during the discharge process and depletion of the electrolyte at the cathode can occur. [101]

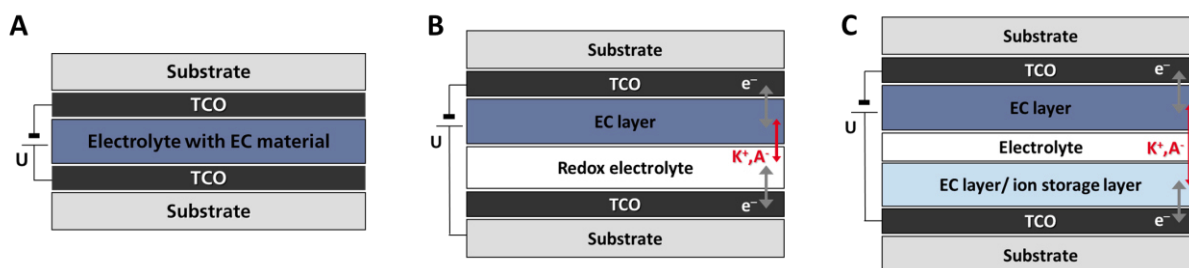
The transference number describes the transport properties of ion-containing electrolytes. It indicates the proportion of a particular particle in charge transport and is calculated with equation (3).

$$T_+ = \frac{I^S(\Delta V - I^0 R^0)}{I^0(\Delta V - I^S R^S)} \quad (3)$$

Here,  $R^0$  and  $R^S$  are the initial and steady-state resistance, respectively,  $I^0$  and  $I^S$  are the initial and steady-state current, respectively, and  $\Delta V$  is the constant applied voltage for the polarization of the cell. The transference number is between 0 and 1 (arbitrary unit). A transference number close to 1 implies that the ion-conducting performance in the electrolyte is mainly accomplished by the cation.

## 1.2. Electrochromic devices

There are three common types of ECDs as depicted in Fig. 4. All three types of ECDs consist of transparent conductive oxides (TCO), *e.g.*,  $\text{In}_2\text{O}_3$ ,  $\text{SnO}_2$ ,  $\text{ZnO}$ ,  $\text{In}_2\text{O}_3:\text{Sn}$  (ITO),  $\text{SnO}_2:\text{F}$  (FTO),  $\text{SnO}_2:\text{Sb}$ ,  $\text{ZnO}:\text{Al}$ , deposited as thin films on glass or plastic substrates. The TCOs must exhibit a low sheet resistance for fast response, while the ionic conductivity of the electrolyte should be optimized to allow a homogeneous coloration/decoloration of the EC layers. [102]

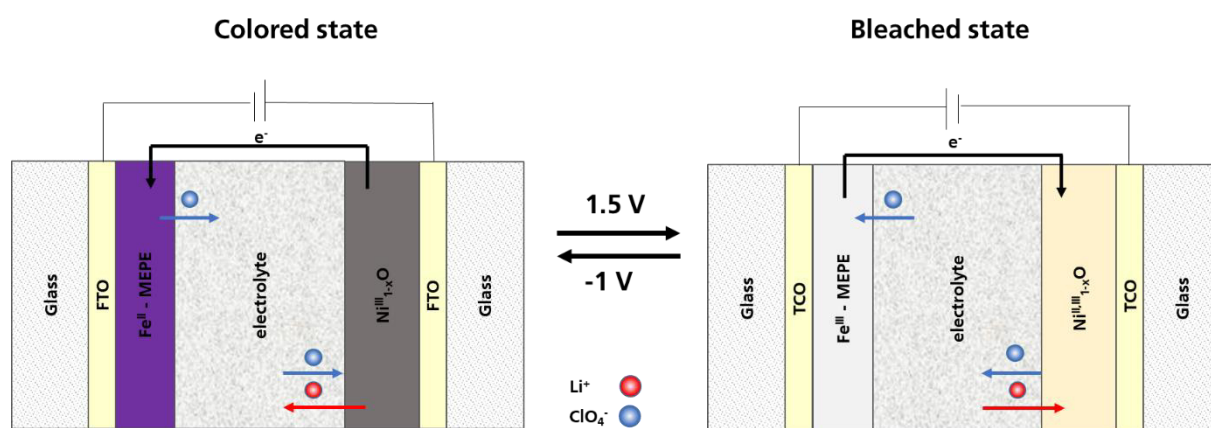


**Fig. 4:** Schematic structures of (A) type I, (B) type II, and (C) type III ECDs. Reproduced from ref. [103] with permission from Wiley.

Solution-phase ECDs (type I) contain dissolved EC species in the electrolyte (Fig. 4A). Commonly used EC materials are viologens, *e.g.*, methyl viologen, [104] and other organic dyes, *e.g.*, phenylenediamine. [105] Hybrid ECDs (type II) combine the principles of type I and III. Here, a redox mediator dissolved in the electrolyte counterbalances the redox reaction occurring during insertion/de-insertion of the cations (or anions) and electrons into/from the EC electrode, respectively (Fig. 4B). [88] The soluble EC material, *e.g.*, 1,1'-bis-cyanophenyl-4,4'-bipyridinium salts, benzyl-, and heptylviologens, may build a solid layer during coloration/decoloration. Compared to type I ECDs, a faster response can be obtained due to the EC materials attached to the substrate, *e.g.*, initially uncolored species may be dissolved, but the colored state is insoluble. [106] Moreover, only small molecules or metal-ligand complexes with high solubility in the electrolyte can be employed, which raises the question of reversibility and stability. The ECD types I and II are simple to assemble but require a constant current or voltage to maintain the redox states (no bi-stability). This results from the direct contact of the redox electrolyte with the EC layer that leads to a so-called 'loss current'. With a low loss current, this process is slow and may take several hours, [107] but a high loss current causes high energy consumption to keep the ECD in the dark or bright state. According to ref. [108], the loss current density should be ideally below  $10 \mu\text{A}\cdot\text{cm}^{-2}$ . This can be realized by either electronic barrier layers [108] or a catalytic  $\text{IrO}_x$  layer [109] between the redox electrolyte and the EC layer. EC materials and redox mediators with low redox potentials can be used to prevent degradation attributed to possible side reactions out of the stable electrochemical window of the electrolyte, *e.g.*, 1 M  $\text{LiClO}_4/\text{PC}$  is stable between 2 V and 4.5 V vs.  $\text{Li}/\text{Li}^+$ . [110] Moreover, low potentials involve lower energy consumption for switching to occur [111], which leads to more competitive ECDs from the industrial point of view. [112]

Thin film "battery-like" ECDs (type III) consist of one EC layer and a second complementary switching EC or highly transmissive (ideally) colorless ion storage layer (Fig. 4C). [34,88]. This device structure has the advantage of a certain bi-stability of the color states as both electrodes are separated by an ion-

conducting electrolyte (liquid, gel, or solid). The operating principle of ECDs with a cathodically- and anodically-coloring electrode (*e.g.*, Fe-MEPE and non-stoichiometric nickel oxide ( $\text{Ni}_{1-x}\text{O}$ )) is illustrated in Fig. 5. The transfer of electrons results in defined redox states having different optical absorption characteristics, while ions are inserted/de-inserted into/from the EC electrodes. A proper EC electrode should have a specific porosity for ion insertion/de-insertion and exhibit a substantial change in transmittance upon applying an external voltage. Both EC electrodes should offer a high transmittance in the visible range for their decolorized states with fast kinetics for the electrochemical reaction. In principle, CEs must have a sufficiently high charge density for the insertion/de-insertion of ions to balance the redox reactions at the WE. In addition, they should have sufficient chemical stability in the electrolytes used. There are two choices for the CE: they can be optically passive (ion storage layer), *i.e.*, their transmittance remains unchanged during the ion insertion/de-insertion process to avoid interference with the EC layer, or they switch complementary to the EC layer (WE). The combination of complementary coloring EC materials leads to an enhanced transmittance modulation, *i.e.*, ECDs can be comprised of a cathodically- and an anodically-coloring EC electrode so that both coatings color and decolor simultaneously. Additionally, for type III ECDs, a balanced and unbalanced configuration can be distinguished as the charging/discharging processes, as well as the charge balance, are of high importance.



**Fig. 5:** ECD working principle. Reproduced from ref. [113] with permission of Elsevier.

During the switching process, for which the necessary cell voltage is in the range of a few volts, both electrodes are mutually reduced and oxidized. These redox processes are accompanied by ion de-/insertion from/into the layer for maintaining the charge neutrality and charge balance between both electrodes. [102] The electrolyte separating the EC layers ideally combines high ionic conductivity (between  $10^{-3}$  and  $10^{-7}$   $\text{S}\cdot\text{cm}^{-1}$ ) to allow fast response and low electrical conductivity (lower than  $10^{-12}$   $\text{S}\cdot\text{cm}^{-1}$ ) to inhibit short circuits and enhance the bi-stability of the ECD. Bi-stable means that once the color change (by oxidation or reduction) has occurred, the state of the device remains even in the absence of applied voltage, *i.e.*, no energy is necessary to maintain the colored or colorless state. The necessary properties for the electrolyte can be reached by dissolving salts, *e.g.*,  $\text{LiClO}_4$ ,  $\text{LiTFSI}$ ,  $\text{LiFSI}$ , ionic liquids, as cation and anion source. [102] Gel and solid electrolytes, *e.g.*, polymer-ion-gel [114] or ion-conducting ceramics, are favored over liquid electrolytes. [115] The latter are prone to leakage, inflammation, and expansion with temperature leading to the damage of the device.

### 1.3. Figures-of-merit

Several metrics are used to characterize, evaluate, and compare the performance of EC materials and ECDs *via* standardized measurements, which are described in the following. The absorption/transmission of the EC layer as a function of the wavelength can be measured by UV-Vis-NIR spectroscopy and the visible light transmittance can be calculated therefrom. The relationship between transmitted light  $I$  and incident light  $I_0$  results from the Lambert-Beer law. The correlation between the optical density (OD) as a measure of the intensity of the absorption and the transmittance  $T$  is given according to equation (5).

$$-\log \frac{I}{I_0} = -\log T = OD \quad (4)$$

From the resulting transmission spectra, the visible light transmittance ( $\tau_v$ ) can be calculated according to DIN EN 410 as an important parameter to compare the bright and dark states of different EC materials and ECDs: [116]

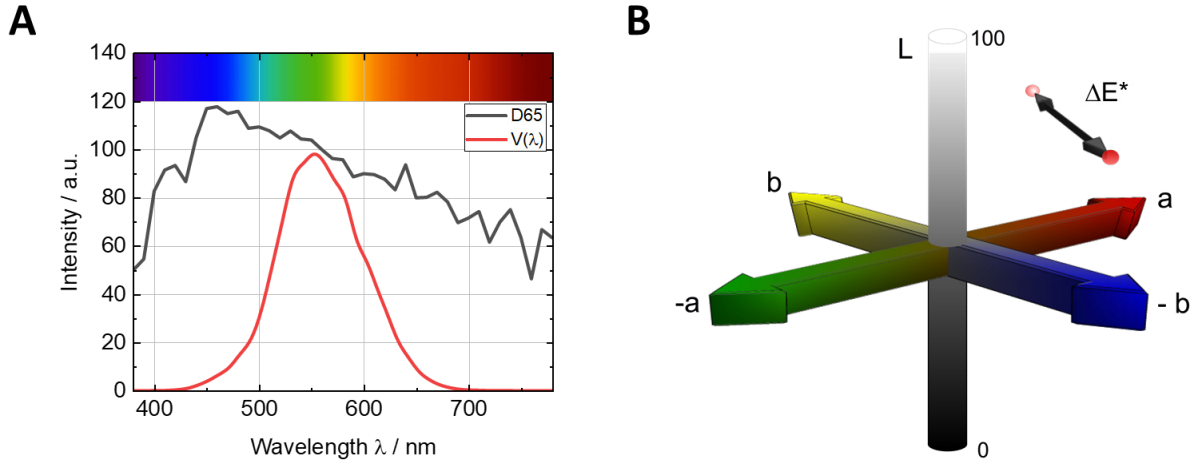
$$\tau_v = \frac{\sum_{380 \text{ nm}}^{780 \text{ nm}} D_\lambda \cdot \tau(\lambda) \cdot V(\lambda) \cdot \Delta\lambda}{\sum_{380 \text{ nm}}^{780 \text{ nm}} D_\lambda \cdot V(\lambda) \cdot \Delta\lambda} \quad (5)$$

Here,  $D_\lambda$  indicates the relative spectral distribution of the standard illuminant D65 (solar radiation at a summer day in Northern and Central Europe, 10° standard observer),  $\tau(\lambda)$  the spectral transmittance,  $V(\lambda)$  the spectral sensitivity of the human eye and the corresponding wavelength interval ( $\Delta\lambda$ ) as shown in Fig. 6A.

The color of an EC layer or ECD can be determined by colorimetric measurements according to the CIE-L\*a\*b\* system described in DIN 5033 (Fig. 6B). [117] The  $L^*$  value denotes the brightness and ranges from  $L^* = 0$  (black) to  $L^* = 100$  (white). The  $a^*$  value characterizes the red ( $a^* = 127$ ) to green ( $a^* = -128$ ) axis. Accordingly, the  $b^*$  value denotes the yellow ( $b^* = 127$ ) to blue ( $b^* = -128$ ) axis. [117] The (0,0) point in the  $a^*b^*$  coordinate system represents a neutral (achromatic) gray. [118]

A measure of the color homogeneity between two measurement points is the color distance  $\Delta E^*$ , which is defined according to equation (6). Here, a value between 0 and 1 indicates that the human eye can recognize no color difference.

$$\Delta E^* = \sqrt{(L_1^* - L_2^*)^2 + (a_1^* - a_2^*)^2 + (b_1^* - b_2^*)^2} \quad (6)$$



**Fig. 6:** (A) Spectral intensity of the standard illuminant D65 and standardized spectral sensitivity of the human eye  $V(\lambda)$  and (B) the representation of the  $L^*a^*b^*$  color space and depiction of  $\Delta E^*$  according to DIN 5033. [117]

The haze results from the material's surface structure, interactions with the surrounding medium and/or surface-related defects. Materials based on nanoparticles can form agglomerates during deposition, [119] on which the incident light is scattered, and thus, the layer becomes opaque. Its value is determined by measuring the diffuse light scattering and calculating the ratio of scattered light to transmitted light, according to DIN ISO 15082 and DIN ISO 3537. [120,121] Haze values below 2% indicate highly transparent layers.

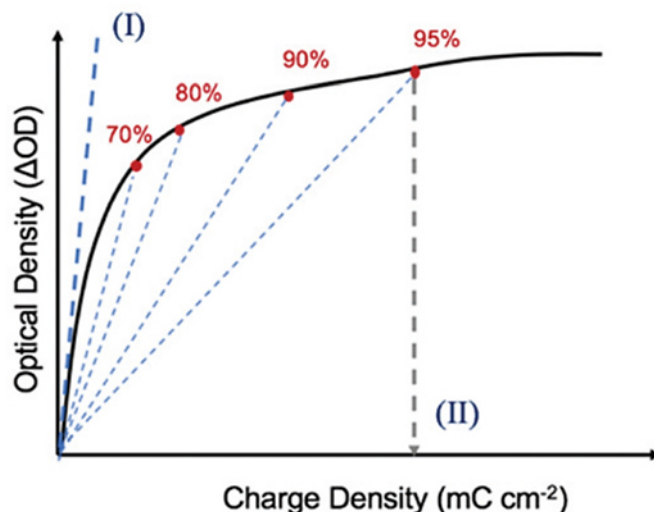
The contrast ratio (CR), defined as the ratio of the transmittance in the bright ( $T_b$ ) to the transmittance in the colored state ( $T_c$ ) at a specific wavelength (*e.g.*,  $\lambda_{max}$ ), is a further important parameter of EC elements. Apart from the measured wavelength, optical contrast depends on the thickness of the EC layer and its morphology [122] and processing conditions. [123] As the film thickness increases, the transmittance of both the colored and bright states usually decreases in a non-linear manner, and the maximum contrast is attained at an intermediate thickness.

$$CR = \frac{T_b}{T_c} \quad (7)$$

The logarithm of the CR corresponds to the change in the optical density ( $\Delta OD$ ). The ratio of  $\Delta OD$  to  $q$  is called the coloration efficiency ( $\eta$ ) with positive values for cathodically- and negative values for anodically-coloring EC materials: This parameter enables the direct comparison of different EC materials and ECDs.

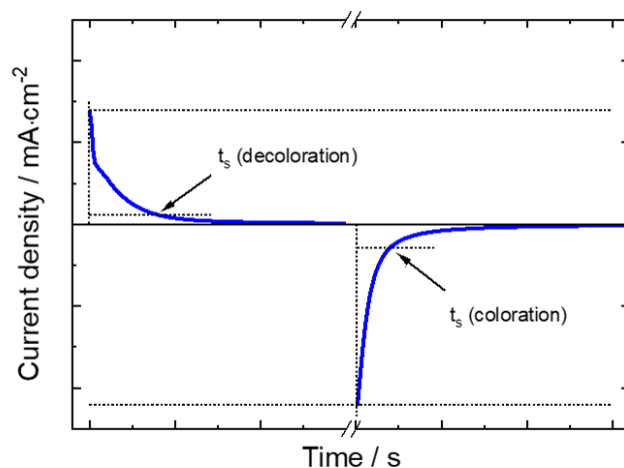
$$\eta = \frac{\log \frac{T_b}{T_c}}{q} = \frac{\Delta OD}{q} \quad [\text{cm}^2 \cdot \text{C}^{-1}] \quad (8)$$

Equation (8) suggests that a value for CE can be obtained by the slope of a plot of  $\Delta OD$  vs. charge density. However, for commonly studied EC materials, neither the optical density nor the charge density varies linearly with time when a constant potential (causing the oxidation or reduction of the material) is applied. Therefore,  $\Delta OD$  vs.  $q$  does not remain linear over the switching process and the reported  $\eta$  will depend on the selected percent change of transmittance used for the calculation, as shown in Fig. 7.



**Fig. 7:** Change in optical density vs. charge density, with (I) and (II) representing commonly used approaches to calculate coloration efficiency. Reproduced from ref. [22] with permission from the Royal Society of Chemistry.

The response time  $t_s$  is an important parameter for the application of an ECD. It indicates the time in which the current density is reduced to 10% of its initial value for decoloration and coloration as shown in Fig. 8. The value of  $t_s$  depends, among other things, on the ionic conductivity of the electrolyte, the resistance of the TCO substrate, the operating voltage/current, the layer thickness and structure, the ion diffusion at the electrolyte/EC layer interface, and the active area. [124,125] Response times for uniform coloration/decoulation are in the range of a few seconds (for automotive glazing, displays, and sunglasses) or several minutes (for architectural glazing). Enhancement of the switching speed without compromising the long-term stability and lifetime of the device constitutes a serious challenge for material scientists and manufacturers. [22]



**Fig. 8:** Definition of the response time of the decoloration/coloration process. Adapted from ref. [124] with permission from Elsevier.

The long-term cycling stability of EC materials can be evaluated by observing the loss of the optical contrast and charge density upon repetitive electrochemical cycling. Materials capable of maintaining over 95% of their maximum optical contrast during the application of boundary potentials in the form of square-wave pulses are deemed stable. They are expected to exhibit a cycle life of more than  $10^4$  cycles. [126] In addition to monitoring only the loss of the optical contrast, electrochemical measurements, *e.g.*, CVs, potentiostatic or galvanostatic steps before and after the cycling test should be provided together so that the condition of the overall thin film can be evaluated. [94] Here, the so-called Coulombic efficiency, defined as the ratio of discharge density to charge density of the EC/ion storage layer can be calculated to determine the cycling stability. Therefore, a stable operating voltage window can be defined as the potential range in which the EC material undergoes reversible electrochemical redox reactions in the absence of irreversible side reactions involving the other components of the ECDs. These components are the ion storage layer, electrolyte, and conductive substrates. Degradation of the TCO layer usually results in longer response times, while a loss of EC contrast is due to degradation of the EC layer. [127]

Finally, optical memory refers to maintaining the transmittance level once the supply voltage is dropped off. This open-circuit stability has a positive impact on the operation energy consumption of ECDs. The test of the optical memory of the device consists of bringing it to the fully colored or decolored state and then removing the driving voltage (OCP condition) while monitoring the transmittance. This bi-stability is highly dependent on the type of ECD, applied voltage/current, and side reactions occurring at the electrolyte/EC layer interface.

## 2. Electrochromic materials studied in this thesis

Before taking a look at material combinations for ECDs, firstly, different EC materials are reviewed. There are three main types of EC materials: organic, inorganic, and hybrid (organic-inorganic). Inorganic compounds usually have better long-term stability than organic EC materials, which outweighs side effects, such as the lower coloration efficiency. Organic compounds are more vulnerable to electrochemical and thermal stress as well as UV light exposure. Moreover, most EC polymers do not exhibit independent Vis and IR modulation, but rather an inversely dependent trend, *i.e.*, high transmittance in the Vis region but low transmittance in the NIR region. [35] Thus, there has been a growing interest in organic-inorganic hybrid materials in recent years. [128] These polymeric materials combine the properties of organic and inorganic EC materials. As the aim of this thesis is to fabricate and characterize ECDs with a wide modulation in the Vis region, insights into, firstly, cathodically-coloring EC materials, which are colored in their reduced states, and, secondly, anodically-coloring EC materials that are colored in their oxidized states, are given.

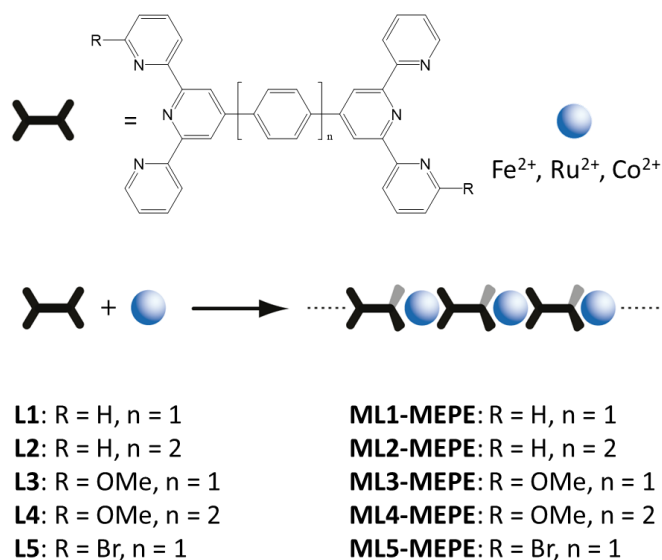
### 2.1. Metallopolymers

Metallopolymers combine the properties of organic chelate ligands, *e.g.*, bis-terpyridine and poly(ethylene oxide), and the electronic, optical, and electrochemical potential of metal ions by metal ion-induced self-assembly. Dependent on the interactions (coordinative number, binding strength, steric hindrance of the ligands, etc.) between the metal ions and the ligands, self-assembly leads to various supramolecular structures ranging from mononuclear compounds to nano-sized assemblies, soluble coordination polymers, gels, all the way to solid-state networks. [129,130] If the binding constants are sufficient, metal ion-induced self-assembly can lead to dynamic, polymeric assemblies in solution. [131] In the case of ditopic bis-terpyridine ligands, rigid rod-like metallopolymers are formed in solution with transition metal ions, such as  $\text{Fe}^{2+}$ ,  $\text{Ru}^{2+}$ , or  $\text{Co}^{2+}$  as depicted in Fig. 9. The coordination properties of the tridentate ligand 2,2':6',2''-terpyridine with metal salts were reported in 1992 by Constable *et al.* [132]. The resulting MEPEs are soluble in water, aqueous acetic acid, and polar solvents like EtOH or MeOH. Thin MEPE layers can be deposited *via* common wet-chemical methods, *e.g.*, spin/dip-coating or a layer-by-layer process. [133–135]

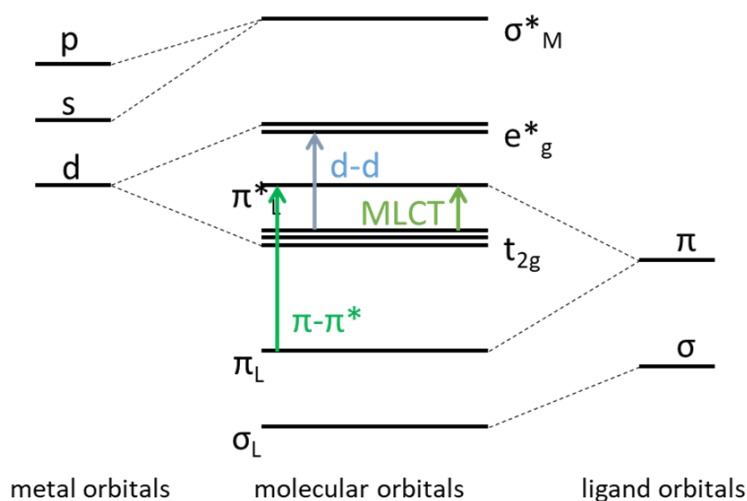
These thoroughly investigated EC metallopolymers have a strong optical absorption in the Vis range deriving from a MLCT transition as shown in Fig. 10. [134–136] Their optical properties can be modified easily by changing metal ions and/or ditopic ligands, making them very versatile EC materials. [81,128,136] In 2007 and 2008, Kurth *et al.* [81,128] reported the photophysical, electrochemical, and EC properties of MEPEs. Different types of MEPEs were assembled from various bis-terpyridine ligands (L1-L5) and investigated in detail (Fig. 9). [128,133,137–140] Tab. 2 summarizes the optical measurements for the solutions of Fe-, Co-, and Ni-MEPE, which show a deep blue, red, and yellow color, respectively. [81]



### Theoretical part




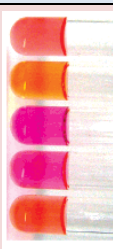

**Fig. 9:** Scheme of synthetic route and possibilities for synthetic variation (spacer unit, side chains on tpy units, the introduction of N atoms into tpy ring system) for the ligand (from L1 to L5). Adapted from ref. [81] with permission of the American Chemical Society.



**Fig. 10:** Molecular orbital (MO) scheme and ligand field splitting attributed to the absorption of MEPEs according to ref. [141].

Turning to the polymeric backbone of the MEPE structure: An extension of the spacer unit from one to two phenyl units leads to a hypsochromic shift of the MLCT band and to lower molar extinction coefficients as listed in Tab. 2. Electron-rich methoxy groups lead to a bathochromic shift of the MLCT band, while electron-deficient bromide substituents lead to a hypsochromic shift. In addition to the color, the modification of the ligands also influences the redox potential, as these ligands stabilize or destabilize the oxidized/reduced state. [81,142]

**Tab. 2:** Overview of optical properties of Fe(II)-, Ru(II), and Co(II)-based MEPEs depending on the ligand. Adapted from ref [81] with permission from the American Chemical Society. Images were taken from ref. [128] with permission of Wiley.

Metal ion	Ligand	Concentration / mM	Solvent	$\lambda_{\max}$ / nm	Molar extinction coefficient / $M^{-1}\cdot cm^{-1}$	Color
Fe(II)	L1	0.25	MeOH	586	18,500	
	L2			579	25,700	
	L3			585	14,300	
	L4			578	16,700	
	L5			612	7,700	
Ru(II)	L1	0.05	MeOH/H <sub>2</sub> O (v/v = 4:1)	513	40,960	
	L2			502	35,520	
	L3			536	25,420	
	L4			524	22,520	
	L5			507	32,460	
Co(II)	L1	0.5	MeOH	522	2,514	
	L2			521	2,300	
	L3			521	214	
	L4			519	457	
	L5			526	429	

These variations in the structure of the MEPEs lead to a wide variety of EC properties, which are summarized in Tab. 3. Moreover, polyelectrochromic behavior is accessible through the production of heterometallic MEPEs, *i.e.*, Fe-Ru, Fe-Cu, and Fe-Os-MEPE. [142–145] In recent studies, it has been reported that MEPEs display high CRs (demonstrated by  $T_{MLCT}$  values from < 5% (dark) to > 80% (bright), short response times (depending on the active area), high cycle stability (charge retention) over thousands of switching cycles, and high coloration efficiencies ( $\eta > 500 \text{ cm}^2\cdot\text{C}^{-1}$ ). [134,135] The redox reaction is limited to the metal ions. Hence, the bis-terpyridine ligands do not undergo electrochemical processes. EC layers made of MEPEs exhibit higher electrochemical stability compared to common EC polymers. [146] The thermal stability is also enhanced due to the metal-organic structure of the MEPEs. Nevertheless, irreversible thermochromic effects occur above a temperature of 100 °C due to reorganization processes in the layer leading to a loss of the EC properties. [147]

Regardless of the many color options, a color-neutral, gray coating for ECDs would be desirable. [16] Higuchi *et al.* have developed a first MEPE based on Co(II) that can be switched between black and transparent. [84] However, the switching behavior of this connection is strongly dependent on the pH value. The change in transmittance is maximum in a strongly alkaline environment (pH 13), but the response times are longer than in a neutral environment (pH 7). Thus, this system has not yet been

optimized and further research and development is required to implement a color-neutral MEPE or a MEPE that can be switched between a color-neutral and a colorless state. Recently, Higuchi *et al.* demonstrated the green to colorless [148] or black [149] switching process of a Cu-MEPE as well as a pink to green switching Os-MEPE. [150]

The Fe-MEPE used in this study consists of Fe<sup>2+</sup> ions, bis-terpyridine ligands, and acetate (OAc<sup>-</sup>) counter ions and exhibits a reversible EC effect due to the oxidation from Fe<sup>2+</sup> (blue-violet) to Fe<sup>3+</sup> (colorless). Up to now, device configurations comprising MEPE and metal oxides as EC layers are rarely studied in the literature. Schott *et al.* reported a combination of Fe-MEPE and a metal oxide CE, *i.e.*, vanadium pentoxide (V<sub>2</sub>O<sub>5</sub>) in flexible ECDs. *In operando* X-ray absorption fine structure (XAFS) measurements were performed to confirm the octahedral coordination geometry in the Fe-MEPE material showing no structural changes during the redox process. [135] The Fe-MEPE/V<sub>2</sub>O<sub>5</sub> ECDs exhibit a visible light transmittance ( $\tau_v$ ) change from 22% (colored, dark state) to 58% (uncolored, bright state). However, the bright state had a noticeable yellow tint due to the absorption up to 450 nm of the reduced V<sub>2</sub>O<sub>5</sub>.

**Tab. 3:** Overview of EC properties of metal ion-based MEPEs.

Metal ion	Ligand	Color red/ox	$\tau_v$ (red/ox) / %	$\lambda_{max}$ / nm	T (at $\lambda_{max}$ ) / %	Response time / s	Ref.
Fe(II)	L0	blue/colorless	26/83	614	3/81	7/2	[83]
	L1	violet/colorless	17/74	585	0.5/69	9/4	[83,134]
	L2	violet/yellow	11/71	584	0.3/75	6/3	[83]
	3D	violet/colorless	n.a.	579	54/82	0.6/0.4	[151]
Ru(II)	L1	red/yellow	n.a.	520	n.a.	1.4/2.3	[81]
Co(II)	L1	black/orange	n.a.	550	8/82	32/24	[84]
Cu(I)	P0	colorless/green	n.a.	721	n.a.	n.a.	[149]
Os(II)	3D	pink/green	n.a.	510	9/59	0.5/0.4	[150]
Fe(II), Ru(II)	L1	pink/green	n.a.	508/585	40/82	1.5/0.4	[152,153]
Fe(II), Cu(I)	L1	purple/colorless	n.a.	465/575	n.a.	5/4	[145]
Fe(II), Os(II)	L1	purple/yellow	n.a.	469/674 575	n.a.	0.9/0.7	[143,144]

## 2.2. Metal oxides as counter electrodes

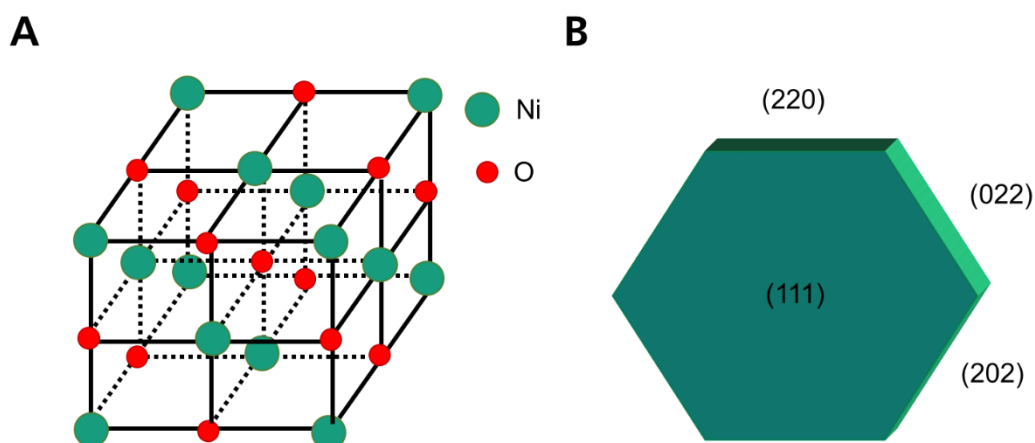
The EC effect of transition metal oxides has been known since the work of Deb [154,155] and the first reviews appeared in the early 1980s. [156] They can be divided into cathodically-coloring (oxides of W, Mo, V, Nb, and Ti) and anodically-coloring (oxides of Ir, Rh, Ni, and Co) EC materials. In addition, due to an IVCT, the Vis and the NIR region of the spectrum can be modulated simultaneously. The use of nanoparticles offers the possibility to change the optical properties in the NIR region independently, as described by Milliron *et al.* in several remarkable publications about plasmonic electrochromism. [23,42,157]

Electrochromic transition metal oxides exhibit a tunable color change in the Vis and IR region under external potentials arising from simultaneous  $e^-$  and cation insertion or de-insertion during switching. Most commonly reported EC transition metal oxide structures that are both electron and ion conductive are composed of highly distorted  $MO_6$  octahedra, [158,159] with M denoting the transition metal. The edge- or corner-shared octahedra form layered-like structures, leaving atomic openings for the intercalation of proton or alkali ion species. The EC properties of transition metal oxides can be affected by their size, [160] porosity, [161] and crystallinity, [162] therefore, the processing techniques and conditions need to be well-controlled to achieve reproducible performances.

When transition metal oxide thin films are used as CEs, they balance the charge consumed at the WE. A CE enables the ECD to operate in a smaller voltage range to achieve faster switching with high contrast and long-term stability. [163] The choice of an appropriate CE material mainly depends on its EC properties, which can be categorized as complementary switching and optically-passive CE materials. Complementary CE materials have coloration efficiencies comparable to that of the WE and exhibit a noticeable EC performance in the device. [164,165] In this configuration, the CE material is required to change the color from a dark state to a bright state (or *vice versa*) complimentary to the WE material. Optically-passive CE materials are either electrochromically inactive or exhibit low coloration efficiency in the Vis region. Owing to their low coloration efficiency, only minor changes in visible color are obtained during the switching process, making these materials useful for compensating the charges of the high coloration efficiency EC materials. For example, niobium oxide nanostructures exhibiting high structural stability during the  $Li^+$  insertion and de-insertion process and low coloration efficiency have been studied. [166,167] The optical purity of the ECDs can be further improved if the WE and CE are paired in an unbalanced configuration. [168]

### 2.2.1. Nickel oxide

NiO thin films are of special interest as electrode materials for EC applications because of the high ion storage capacities and broad transmittance modulation in the Vis and NIR. The crystal structure of NiO is based on the NaCl type that can be simplified to a network of NiO<sub>6</sub> octahedra analogously to other EC oxides (density of 6700 kg m<sup>-3</sup>) as depicted in Fig. 11. [34] A band structure with an unoccupied e<sub>g</sub><sup>\*</sup> band and partly occupied t<sub>2g</sub> band (valence band) can be derived from this according to the crystal field theory in the solid. The absorption is due to a p → d transition in one Ni atom or a d → d transition between two adjacent Ni atoms in the lattice. [169,170] Therefore, the color of the NiO is highly sensitive to the presence of higher valence states of nickel (Ni<sup>3+</sup>, Ni<sup>4+</sup>) due to cation vacancies and/or interstitial oxygen anions, even trace amounts. [71,165] These non-stoichiometric NiO are brownish. [171,172] Physical methods such as reactive dc magnetron sputtering or reactive electron beam evaporation techniques are preferred to prepare EC NiO thin films because they enable the controlled introduction of nickel vacancies. [70,171,173] Such NiO films are usually highly transparent and grayish-brown in their as-deposited state. There are several publications on the preparation of NiO and non-stoichiometric nickel oxide (Ni<sub>1-x</sub>O) used in this thesis. In previous publications for the synthesis of Ni<sub>1-x</sub>O by a sol-gel process, either sulfate or nitrate precursors were used. [72,174] Later on, other precursors like nickel chloride (NiCl<sub>2</sub>) and nickel acetate (Ni(OAc)<sub>2</sub>) have been used. [175] Layers prepared with sols of NiCl<sub>2</sub> in different solvents consist of nickel hydroxide (Ni(OH)<sub>2</sub>) together with NiO crystal structure after sintering at 300 °C for 1 h. In contrast, the pure NiO structure is formed at higher temperatures. The EC effect of the layers is enhanced with the sintering temperature up to 300 °C, at higher temperatures it decreases. [176] An overview of possible deposition methods and resulting EC properties are summarized in Tab. 4



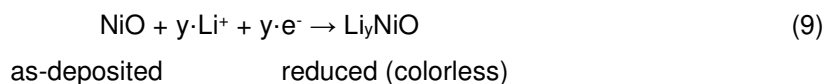
**Fig. 11:** (A) Defect-free crystal structure and (B) crystal facets of NiO. Adapted from ref. [177] with permission from Elsevier.

**Tab. 4:** Overview of deposition method and EC properties of NiO described in the literature.

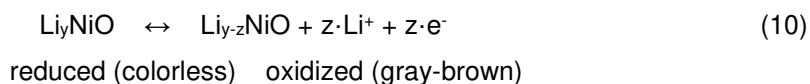
Deposition method	Annealing temperature / °C	$\lambda_{\max}$ / nm	$\Delta T$ (at $\lambda_{\max}$ ) / %	Response time / s	$\eta$ / cm <sup>2</sup> ·C <sup>-1</sup>	Ref.
Sputtering	---	633	57	n.a.	n.a.	[178]
	---	550	85	n.a.	n.a.	[179]
Electrodeposition	---	480	50	6/7	49	[180]
Inkjet	25		35	11/20	50	
	150		40	4/16	75	
	200	550	50	5/5	73	[181]
	250		45	6/3	30	
	300		10	2/2	20	
Chemical Bath	300	550	39	n.a.	n.a.	[164]
Spin-coating	300	600	41	1/4	69	[182]
	400	480	55	n.a.	71	[183]
Dip-coating	400	480	55	n.a.	72	[72]
	300	480	70	<5/<10	39	[71]
	150	480	72	<5/<7	39	[71]

In contrast to the well-known Bode scheme for the electrochromism of NiO in aqueous electrolytes involving different nickel hydroxide and oxyhydroxide structures, [184] the exact mechanism of the electrochromism of NiO is only partially elucidated when using Li<sup>+</sup>-based non-aqueous electrolytes. Here, the fact that the EC properties of NiO are highly dependent on the synthesis process and the resultant defect structure is one hurdle to overcome. [71,72,185] It is widely accepted that the EC performance of NiO is attributed to the insertion/de-insertion of electrons and cations, which strongly depend on the diffusion length of ions and the appropriate surface area. [186] Passerini *et al.* [187] first showed that NiO could undergo a reversal Li<sup>+</sup> insertion/de-insertion process accompanied by a relevant EC effect. Later, Li<sup>+</sup> insertion from aprotic electrolytes into the NiO layer has been divided into a two-stage electrochemical mechanism: [188] The initial non-reversible reduction step (1) is an activation step, which involves an irreversible uptake of Li<sup>+</sup> into the host structure of the NiO layer. This is followed by the reversible reaction (2) between colorless Li<sub>y</sub>NiO and colored Li<sub>y-z</sub>NiO, in which Ni<sup>2+</sup> and Ni<sup>3+</sup> are involved as active species. [165]

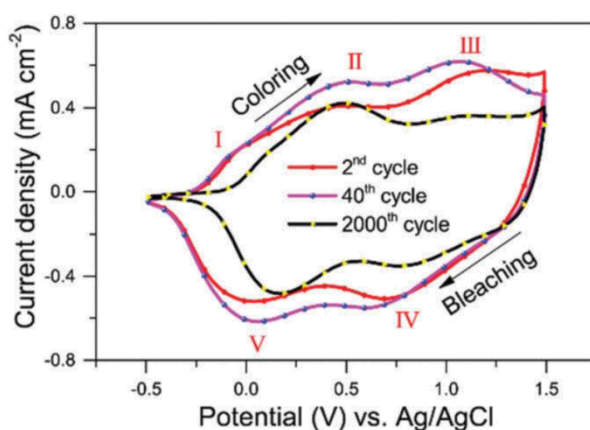
Initial decoloration:



Reversible EC reaction:



During the insertion,  $\text{Li}^+$  ions migrate into the NiO host lattice and occupy empty spaces. [71] CV measurements show that, unlike the mechanism described above, presumably, in addition to  $\text{Ni}^{2+}$  and  $\text{Ni}^{3+}$ ,  $\text{Ni}^{4+}$  ions are also involved in the redox process (Fig. 12). [165] Here, peak II indicates the redox process of  $\text{Ni}^{2+} \rightarrow \text{Ni}^{3+}$ , peak III is linked to the redox process  $\text{Ni}^{2+}/\text{Ni}^{3+} \rightarrow \text{Ni}^{4+}$ , while at peak IV ( $\text{Ni}^{4+} \rightarrow \text{Ni}^{3+}/\text{Ni}^{2+}$ ) and V ( $\text{Ni}^{3+} \rightarrow \text{Ni}^{2+}$ ) the reversible reaction occurs.



**Fig. 12:** CVs of the NiO thin film cycled in a 1 M  $\text{LiClO}_4/\text{PC}$  electrolyte at different cycle numbers. Reproduced from ref. [165] with permission from the Royal Society of Chemistry.

In parallel to the expected  $\text{Li}^+$  participation in the electrochromic effect, electrochemical characterization confirms the involvement of anions to counterbalance the  $\text{Ni}^{3+}/\text{Ni}^{2+}$  redox process. [73] This was further elucidated with *ex situ* infrared reflection-absorption spectroscopy (IRRAS) measurements in a  $\text{Li}^+$ -free electrolyte, where it was shown that anions, not  $\text{Li}^+$  ions, were inserted within a porous structure of NiO pigmented coatings. [185] Boschloo and Hagfeldt cycled NiO in 0.2 M  $\text{LiClO}_4$  and TBA<sup>+</sup> triflate dissolved in 3-methoxypropionitrile. The CVs were nearly identical, which can be attributed to the adsorption of TBA<sup>+</sup> cations replacing protons on the surface of the NiO grains. [189]. However, Uplane *et al.* pointed out in their studies of EC NiO films that their p-type conductivity explains the coloration and decoloration of the films without proton insertion/de-insertion reactions, knowing that other ions than protons are reversibly inserted. [190] Rougier and co-workers used Li-/NaTFSI-based electrolytes to compare their performance to electrolytes without small cations consisting of BMITFSI or EMITFSI to test the proposed mechanism. [191] The CVs of  $\text{Ni}_{1-x}\text{O}$  in those electrolytes showed a reversible behavior associated with a similar transmission change indicating that the presence of small cations is not required for EC

properties suggesting that surface phenomena may replace insertion processes. [192,193] Further insights into the EC mechanism were given in ref. [72]: The existence of holes ( $e^+$ ) and the p-type semiconductivity, providing  $e^+$  transport within the NiO grains, tends to indicate the presence of surface electrochemical reactions rather than  $Li^+$  ions insertion/de-insertion reactions, suggesting that thin films and pigment coatings behave similarly to NiO electrochemical capacitors, as reported by Srinivasan and Weidner. [194]

In most state-of-the-art ECDs, NiO thin films as an anodically-coloring electrode are combined with cathodically-coloring EC materials, such as  $WO_3$  (Tab. 5). [70,173] NiO electrodes can be used for neutral tinting applications due to their neutral color in the oxidized state and high transmittance (nearly colorless) in the reduced state. A prominent example in literature is an ECD comprising hydrated NiO and  $WO_3$  thin film electrodes that reach a neutral gray color in the dark state. [195] The visible light transmittance of an all-solid-state ECD [Glass/ITO/NiO/ $Ta_2O_5$ /  $WO_3$ /ITO/Glass] changes from 18% (dark) to 73% (bright) stable up to more than 100,000 cycles at 60 °C and offers the possibility of large-area EC applications. [196]

As glass-based EC devices have appeared on the market (around 1990), there still is an inevitable need for cost reduction by high-throughput manufacturing. One possibility for reducing the production costs of solar control products is their production [197] by means of high-throughput R2R [198] processes on flexible polymer films. Still, all known flexible polymer-based substrates do not withstand processing temperatures higher than 160 °C. This dismisses the possibility of depositing most inorganic electrochromics, which require post-deposition heat-treatment at elevated temperatures (> 300 °C). To overcome this hurdle,  $Ni_{1-x}O$  xerogel was obtained by heat treatment at 400 °C for 24 h. Subsequently, a  $NiO_xH_y$  containing binder and dispersant was added to enable the deposition of EC  $Ni_{1-x}O$  pigment coatings on transparent conductive substrates, such as FTO glass and PET-ITO. [71]  $NiO_xH_y$  had a dual function: it acted both as a dispersant and as the binder for the particles. A detailed overview of morphological properties is given in section 0 of the discussion and results part. The present type of non-stoichiometric nickel oxide exhibits a fast response. It can be decolorized or colored from the as-deposited state depending on the applied voltage because both cations ( $Li^+$ ) and anions ( $ClO_4^-$ ) from the electrolyte are involved in this charge exchange process. [34,71,193] The immediate EC response of  $Li^+$ -containing electrolytes was attributed to the films' porosity and the presence of nickel in two valences, *i.e.*,  $Ni^{2+}$  and  $Ni^{3+}$ . [199,200] Flexible ECDs with  $Ni_{1-x}O$  show a transmittance change  $\Delta T_{480\text{ nm}}$  of up to 34% when n- $TiO_2$  is used as cathodically-coloring material. A  $\Delta T_{634\text{ nm}}$  of 25% was achieved with PEDOT or  $WO_3$  as WEs. [183,185]



**Tab. 5:** Overview of EC properties for ECDs with WO<sub>3</sub> as WE and NiO as CEs switching between blue (dark) and colorless (bright) states.

Deposition method of electrodes	Electrolyte	Cell voltage / V	$\lambda_{\max}$ / nm	T (at $\lambda_{\max}$ ) / %	Response time / s	$\eta$ / cm <sup>2</sup> ·C <sup>-1</sup>	Ref.
Sputtering	LiClO <sub>4</sub> /PC/PMMA	-1.8	550	30	2	61	[178]
		1.8		80	5		
	0.3 M LiTFSI-BMITFSI/PMMA	-2	550	54	n.a.	53	[201]
Sputtering (WO <sub>3</sub> )	Li <sup>+</sup> -based solid hybrid polyelectrolyte	-2.5	550	20	10	87	[202]
Chemical Bath (NiO)		2.5		75	20		
Cathodic arc plasma	LiClO <sub>4</sub> /PC	-1.5	633	34	3	90	[203]
		0.8		76	5		
Chemical Bath	LiClO <sub>4</sub> /PC	-2.5	550	7	2	n.a.	[164]
		2.5		91	2		
Inkjet	LiClO <sub>4</sub> /PC/PMMA	-2.5	633	5	10	132	[181]
		2.5		80	13		
(amorphous) Photodeposition (crystalline)	LiClO <sub>4</sub> /PC/PMMA	-2.1	633	10	4	141	[204]
		2.1		70	6		
		-2.1	633	50	17	72	
		2.1		76	78		
Dip-coating	Li-triflate-based-polymer-membrane	-1.7	480	28	< 10	38	[71]
		1		75	< 10		
	1 M LiClO <sub>4</sub> /PC/PMMA	-1.5	600	35	1	131	[182]
		1.5		74	3		

### 2.2.2. Titanium-doped Vanadium and Manganese oxides

It has been shown that for a given pair of EC materials, the maximum contrast realized by one material may be higher than for any combination involving those two materials. [205] Therefore, a second coloring EC material may not be needed. An optically-passive ion storage layer as a CE may be the best solution to achieve high cycle stability as the CE is only partially oxidized/reduced, while the maximum possible contrast of the WE can be achieved. [168] The use of transparent, optically-passive ion storage layers has been explored in the past. [168,206] S. Hassab *et al.* used a cathodically-coloring thiophene derivative ( $2.2 \text{ mC}\cdot\text{cm}^{-2}$ ,  $\eta = 379 \text{ cm}^2\cdot\text{C}^{-1}$ ) as the WE and  $\text{WO}_3$  ( $24 \text{ mC}\cdot\text{cm}^{-2}$ ,  $\eta = 19 \text{ cm}^2\cdot\text{C}^{-1}$ ) as an optically-passive transparent CE. The difference in coloration efficiencies between these materials in combination with the high transparency of  $\text{WO}_3$  films, enabled a high optical contrast (57% at 566 nm), short response times (3 s), and low operating voltages (+0.8/-0.7 V) of this unbalanced configuration. The group of S. Ulrich prepared several mixed Ti-Nb oxide films for optically-passive electrodes with high transmittance values (>75%) in both the dark and bright states.

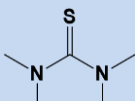
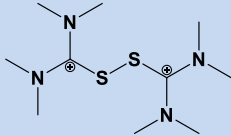
$\text{V}_2\text{O}_5$  exhibits a high charge density and ion storage capability. [135] It is an EC material showing color change at a low operating voltage and can be used as both cathodically- and anodically-coloring EC films. [207] The reversible intercalation of metal ions ( $\text{Na}^+$  or  $\text{Li}^+$ ) into the  $\text{V}_2\text{O}_5$  bilayer structure accompanied by a reduction of  $\text{V}^{5+}$  to  $\text{V}^{4+}$  is a common mechanism of EC behavior. [208] Therefore, it is already used in catalytic converters or lithium batteries, as its layered structure allows ions to be easily inserted. Such layers are produced by sol-gel processes, chemical vapor deposition processes (CVD), spray pyrolysis, or electrochemical methods. [209] It can change its color from yellow to a light gray/brown in the reduced state. Because of this yellow color in the bright (oxidized) state,  $\text{V}_2\text{O}_5$  is not an optimal material for use as an ion storage layer for architectural glass. [210] In addition, the charge density of  $\text{V}_2\text{O}_5$  decreases with an increasing number of cycles. [211] The addition of another transition metal can improve both the optical and electrochemical properties of  $\text{V}_2\text{O}_5$ . Ti-V oxides are particularly useful as ion storage materials combined with Fe-MEPE due to their high charge density and low coloration efficiency. [135] By doping V-oxides with Ti, the electrical conductivity, electrochemical stability, and reversibility are enhanced, the crystallization during cycling is prevented and the transmittance change during cycling is decreased. [212–214] Sajitha *et al.* have reported  $\text{MnO}_2$ -encrusted  $\text{V}_2\text{O}_5$  ( $\text{V}_2\text{O}_5/\text{MnO}_2$ ) on FTO substrates showing enhanced EC cycling stability compared with a bare  $\text{V}_2\text{O}_5$  FTO electrode. [215]

Mn oxides as EC materials have been thoroughly investigated in the literature. [75,216,217] The  $\text{Mn}^{4+}$  state of manganese oxides has an optical absorption due to their d-d transition in the visible range, giving rise to a brownish color. The electrochemical reduction to  $\text{Mn}^{3+}$  changes the color from brown to pale yellow.

## 2.3. Redox mediators

Instead of a second redox-active electrode, a redox mediator dissolved in the electrolyte can counterbalance the redox reaction occurring during the insertion/de-insertion of the cations (or anions) and electrons into/from the EC electrode, respectively. [88] Some promising combinations of redox mediators are summarized in Tab. 6. The reason for choosing potassium hexacyanoferrate(II)/(III) (KHCF(II)/(III)), ferrocene/ferrocenium ( $\text{Fc}^{0/+}$ ), and the organic tetramethylthiourea/tetramethylformaminium disulfide couple (TMTU/TMFDS<sup>2+</sup>) as redox mediators for this thesis is explained in the following.

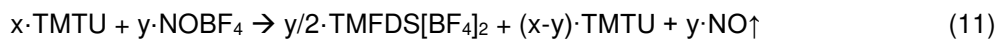
**Tab. 6:** Overview of EC properties for redox mediator-containing ECDs studied recently.

WE	Redox mediator	Cell voltage / V	L*	a*	b*	Ref.
TiO <sub>2</sub> - viologen	Iodide/triiodide (I <sup>-</sup> /I <sub>3</sub> <sup>-</sup> )	-1.5 0	40.7 59.5	-4.8 -10.0	-32.6 22.9	[218]
	I <sup>-</sup> /I <sub>3</sub> <sup>-</sup>	-0.7 0.6	33 75	-18 -0.5	37 85	[108,219,220]
WO <sub>3</sub>	2,2,6,6-tetramethyl-1- piperidinyloxy (TEMPO)/TEMPO <sup>+</sup>	-1.0 0.6	47 74	-0.3 14	25 57	[108]
	TMTU 	-0.8 0.6	44 87	-4 -3	-25 7	[108,109,219,221]
	/TMFDS <sup>2+</sup> 					
	KHCF(II)/KHCF(II)					[108]
Co(II)- MEPE	KHCF(II)/KHCF(II)	-1.5 0	74.2 98.1	4.0 0.3	-4.1 7.7	[222]
	$\text{Fc}^{0/+}$	-1.5 0	77.2 91.4	6.0 4.5	1.1 9.0	[222]

An overview of the various redox mediators suitable for ECDs has been published recently. [223] The most prominent candidate is iodide/triiodide (I<sup>-</sup>/I<sub>3</sub><sup>-</sup>), which is used in dye-sensitized solar cells (DSSCs). However, this redox mediator is not desirable for ECDs as its corrosiveness leads to poor stability and the absorption of visible light (brown-red colored) limits the use for EC applications. [220,224,225] Several redox mediators have been investigated for DSSCs [223] and showed promising initial results with common inorganic EC materials, such as (WO<sub>3</sub> and Prussian blue (PB)). [220,221].  $\text{Fc}^{0/+}$  has been used in viologen-based ECDs [226] and in combination with Co-MEPE [84,222]. The Co-MEPE based

## Theoretical part

ECD exhibits an optical change from a black-colored Co(II)-MEPE to a bright state with a yellow tint Co(III)-MEPE and good cycling stability. It was recently shown that KHCF(III) is not suitable for ECDs containing WO<sub>3</sub> due to the very low charge transfer resistance, which results in a high loss current and high power consumption. [108] TMTU/TMFDS<sup>2+</sup> is advantageous due to its non-corrosive nature, low cost, easy handling, and high transparency in both redox states. [224] The group of A. Georg demonstrated that an ECD consisting of a liquid electrolyte with TMTU/TMFDS<sup>2+</sup> and sol-gel-derived WO<sub>3</sub> thin film electrodes changes its visible light transmittance from 14% (dark) to 71% (bright). [108] Moreover, the TMTU/TMFDS<sup>2+</sup> redox mediator can be used in a solid electrolyte based on an organopolysiloxane matrix [221] to reduce long-term degradation. [108] A further advantage is that the ratio of TMTU:TMFDS<sup>2+</sup> can be simply adjusted using an oxidizing agent, such as nitrosonium tetrafluoroborate (NOBF<sub>4</sub>) [108,224,227] as described in equation (11):



### III. Scope of the thesis

This thesis aims to investigate electrochromic (EC) materials and cell configurations thereof, which hint towards neutral tinted EC devices (ECDs) with a distinct near-infrared (NIR) modulation. As the cathodically-coloring EC material, an iron-based metallopolymer (Fe-MEPE) is used due to its excellent EC properties, such as high coulombic efficiency, short response times, and high cycle stability. The properties and suitability as complementary-coloring counter electrode (CE) are investigated using the example of wet-chemical deposited, non-stoichiometric nickel oxide ( $\text{Ni}_{1-x}\text{O}$ ). Comparative experiments with Ti-containing doped vanadium or manganese oxides as optically-passive ion storage layers are carried out to show the benefits of the different metal oxides. Furthermore, a simplification of the device architecture (three-layer to two-layer set-up) using redox mediators is shown.

The working principle of glass-based Fe-MEPE/ $\text{Ni}_{1-x}\text{O}$  ECDs and the optimization of charge balancing and optical contrast with different charge density ratios of Fe-MEPE and  $\text{Ni}_{1-x}\text{O}$  is in the focus of section 0. These ECDs are studied (spectro-)electrochemically extensively to verify the influence of the charge density ratio of both electrodes on the overall cell voltage and EC performance. Therefore, a three-electrode setup comprising a Li reference electrode (RE) is to be used to evaluate the redox behavior of both electrodes during full cell operation in detail.

Fabricating and investigating Fe-MEPE as the working electrode (WE) and mixed metal oxides as CEs towards further development of color neutrality and stability is the motivation for the second part of this work. For this purpose, optically-passive electrode materials are tested, *e.g.*, sputtered mixed metal oxides such as titanium vanadium oxide ( $\text{TiVO}_x$ ) and titanium manganese oxide (TMO). In combination with Fe-MEPE, functional ECDs are assembled and their EC properties (*e.g.*, transmittance change, color values, coloration efficiency ( $\eta$ ), response time, cycle stability) are examined. The characteristic optical, electrochemical, and EC parameters are measured.

Finally, type II ECDs using Fe-MEPE or  $\text{Ni}_{1-x}\text{O}$  electrodes and gel electrolytes with redox mediators are studied. As potential candidates for the redox mediator  $\text{KHCF(II)/(III)}$ ,  $\text{Fc}^{0/+}$ , and  $\text{TMTU/TMFDS}^{2+}$  are to be tested.

The EC electrodes and the two- and three-electrode ECDs are characterized optically and electrochemically to determine the EC properties. UV-Vis spectroscopy, colorimetry, measurement of diffuse light scattering (haze), and scanning electron microscopy (SEM) are to be used as optical characterization methods. For electrochemical characterization, the cyclic voltammetry (CV), as well as measurements of the charging and discharging behavior, the coulombic efficiency, the memory effect, and the cycle stability are to be carried out. UV-Vis spectra, which are recorded *in situ* during the switching process, are intended to provide information about the EC properties of the materials, such as the transmittance (T) and optical density (OD) in the colored and bright state, the change in visible light transmittance ( $\tau_v$ ), or the coloration efficiency ( $\eta$ ).

## IV. Experimental part

### 1. Overview chemicals and substrates

All chemicals for the synthesis of the Fe-MEPEs, as well as for the preparation of Ni<sub>1-x</sub>O powder and pigment coatings were used without further purification (Tab. 7). The properties of the glass substrates with a transparent, conductive layer (ITO or FTO) are summarized in Tab. 8.

**Tab. 7:** List of chemicals and solvents used in this thesis.

Chemical	Supplier	Molecular formula	Molar mass / g·mol <sup>-1</sup>	Purity
acetic acid (CH <sub>3</sub> COOH)	Sigma	C <sub>2</sub> H <sub>4</sub> O <sub>2</sub>	60.05	≥ 99.7%
2-butoxyethanol	Schollbach GmbH	C <sub>6</sub> H <sub>14</sub> O <sub>2</sub>	118.17	
diethylcarbonate (DEC)	Sigma	C <sub>5</sub> H <sub>10</sub> O <sub>3</sub>	118.13	99%
ethanol (EtOH)	Sigma	C <sub>2</sub> H <sub>6</sub> O	46.07	
ferrocenium tetrafluoroborate (FcBF <sub>4</sub> )	Sigma	[Fe(C <sub>5</sub> H <sub>5</sub> ) <sub>2</sub> ]BF <sub>4</sub>	272.84	97%
ferrocenium hexafluorophosphate (FcPF <sub>6</sub> )	Sigma	[Fe(C <sub>5</sub> H <sub>5</sub> ) <sub>2</sub> ]PF <sub>6</sub>	331.00	97%
iron (powder)	Roth	Fe	55.85	≥99.5%
lithium	Sigma	Li	6.94	≥ 99.9%
lithium perchlorate (LiClO <sub>4</sub> )	Sigma	LiClO <sub>4</sub>	106.39	≥ 98%
Methanol (MeOH)	Sigma	CH <sub>4</sub> O	32.04	p.a. ≥ 99.8%
paraloid B72	Kremer Pigmente			
ligand L1	confidential supplier	C <sub>36</sub> H <sub>24</sub> N <sub>6</sub>	540.63	≥ 99%
potassium bromide (KBr)	Sigma	KBr	119.01	≥ 99%
potassium chloride (KCl)	Fluka Analytical	KCl	74.55	p.a.
propylene carbonate (PC)	Sigma	C <sub>4</sub> H <sub>6</sub> O <sub>3</sub>	102.09	battery grade
sodium perchlorate (NaClO <sub>4</sub> )	Sigma	NaClO <sub>4</sub>	122.44	≥ 98%
tetramethylthiourea (TMTU)	Sigma	(CH <sub>3</sub> ) <sub>2</sub> NCSN(CH <sub>3</sub> ) <sub>2</sub>	132.23	98%
zinc (powder)	Sigma	Zn	65.38	≥ 98%

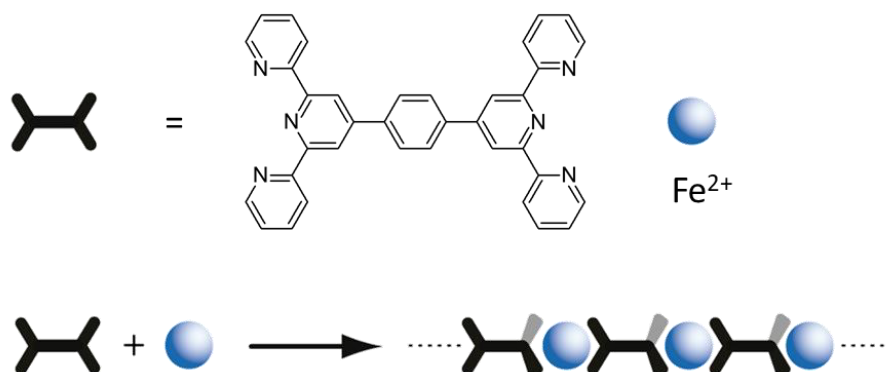
**Tab. 8:** List of TCO substrates used in this thesis.

<b>Substrate</b>	<b>Supplier</b>	<b>Thickness / mm</b>
<b>FTO glass</b>	Pilkington	4
<b>Ultra-thin ITO glass</b>	Fraunhofer FEP	0.1

## 2. Synthesis and film deposition

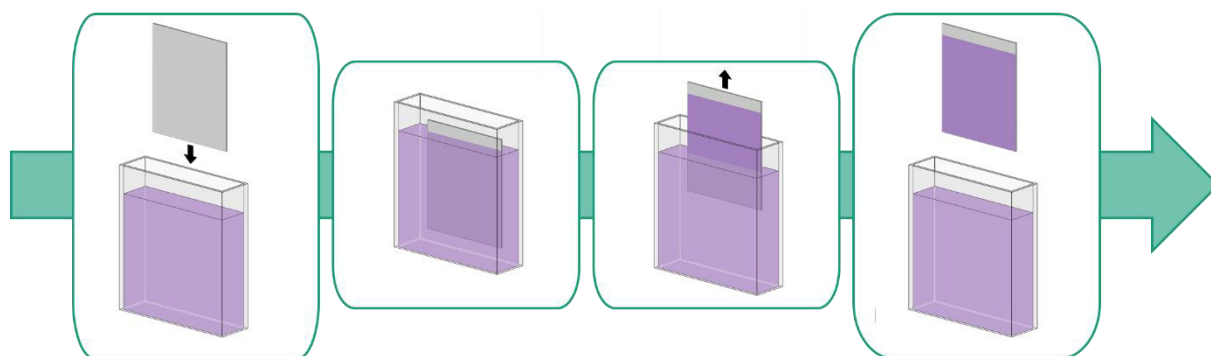
### 2.1. Iron-based metallopolymer

4',4''''-(1,4-phenylene)bis(2,2':6',2''-terpyridine) (tpy-ph-tpy) was synthesized according to the procedure given in ref. [132] and depicted in Fig. 13.



**Fig. 13:** Structure of the ligand and the resulting Fe-MEPE. Reproduced from ref. [137] with permission from the American Chemical Society.

The Fe-MEPE coating solution was prepared with a concentration of  $35 \text{ mmol}\cdot\text{L}^{-1}$  in EtOH/MeOH/2-butoxyethanol. The MEPE solution was stirred at room temperature for at least 24 h to obtain a homogenous coating solution. The FTO glass substrates were rinsed in EtOH and dried with compressed air prior to dip-coating. Before the dip-coating process, the substrates were covered with adhesive tape on the non-conductive side to avoid an unnecessary cleaning step. Homogeneous Fe-MEPE thin films were prepared utilizing a custom-made high-precision dip-coater and withdrawing speed of  $35 \text{ mm min}^{-1}$ , which is schematically depicted in Fig. 14. Finally, the Fe-MEPE films ( $\sim 330 \text{ nm}$ ) were annealed at  $60 \text{ }^\circ\text{C}$  for 24 h.

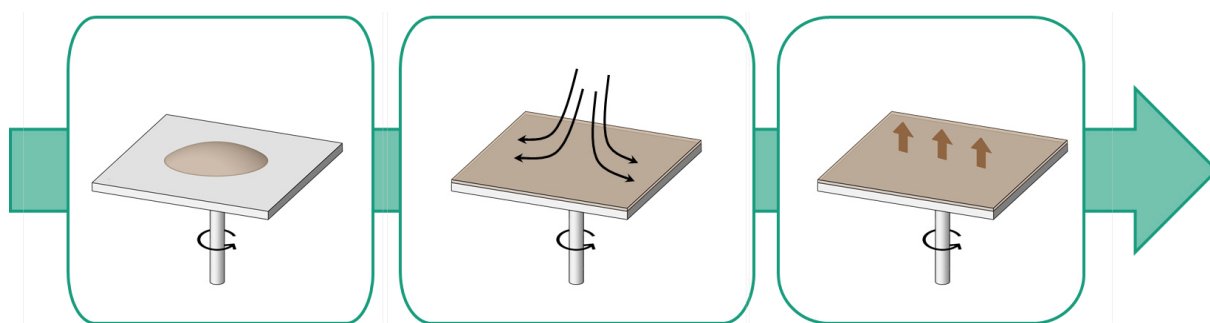


**Fig. 14:** Schematic representation of the dip-coating process from a  $35 \text{ mmol}\cdot\text{L}^{-1}$  Fe-MEPE solution in EtOH/MeOH/2-butoxyethanol. Adapted from ref. [228].



## 2.2. Non-stoichiometric nickel oxide

The  $\text{Ni}_{1-x}\text{O}$  electrodes were prepared by the *National Institute of Chemistry* (NIC) in Ljubljana (Slovenia) *via* spin-coating onto FTO glass as shown in Fig. 15. The  $\text{Ni}_{1-x}\text{O}$  dispersion was prepared *via* a two-step wet-chemical synthesis according to ref. [71] that yielded nickel oxide films with nickel vacancies and, therefore, higher  $\text{Ni}^{3+}$  content. [72,183] In brief, the  $\text{Ni}_{1-x}\text{O}$  pigment was synthesized *via* a sol-gel peroxo-route using an  $\text{H}_2\text{O}_2/\text{urea}$  mixture reacting with  $\text{Ni}(\text{OAc})_2$  powder. The obtained dried xerogel was thermally treated at  $400\text{ }^\circ\text{C}$  for 24 h to get the non-stoichiometric  $\text{Ni}_{1-x}\text{O}$  pigment ( $\text{Ni}^{2+}/\text{Ni}^{3+}$  ratio approx. 0.5). [72] Secondly,  $\text{NiO}_x\text{H}_y$  dispersant and binder were prepared by precipitation of nickel(II) sulfate with sodium hypochlorite. [174,183] The precipitate was then rinsed in distilled water to remove sulfate anions and dried at  $50\text{ }^\circ\text{C}$  overnight. The pigment dispersion consisted of 10 wt.% of  $\text{Ni}_{1-x}\text{O}$  pigment dispersed in distilled water in the presence of dispersant and was subsequently milled with zirconia beads. [72] The pigment dispersion's viscosity was adjusted for the spin-coating process ( $1.9\text{ mPa}\cdot\text{s}$  at a shear rate of  $500\text{ s}^{-1}$ ). Thin  $\text{Ni}_{1-x}\text{O}$  films were deposited on FTO glass with a rotation speed of 500 rpm for 5 s, followed by 1,000 rpm for 1 min. For an increase in film thickness, the two-step spin-coating cycle was repeated several times. In this study, samples with two to six  $\text{Ni}_{1-x}\text{O}$  thin layers were investigated and will be referred to as **Ni<sub>1-x</sub>O\_2** (thickness of 330 nm), **Ni<sub>1-x</sub>O\_3** (490 nm), **Ni<sub>1-x</sub>O\_4**, **Ni<sub>1-x</sub>O\_5** ( $1.25\text{ }\mu\text{m}$ ), and **Ni<sub>1-x</sub>O\_6**, respectively. The stoichiometry of the **Ni<sub>1-x</sub>O\_5** films was measured with XPS (see Fig. S4).



**Fig. 15:** Schematic representation of the spin-coating process of the  $\text{Ni}_{1-x}\text{O}$  dispersion. Adapted from ref. [229].

### 2.3. TiVO<sub>x</sub> and TMOs

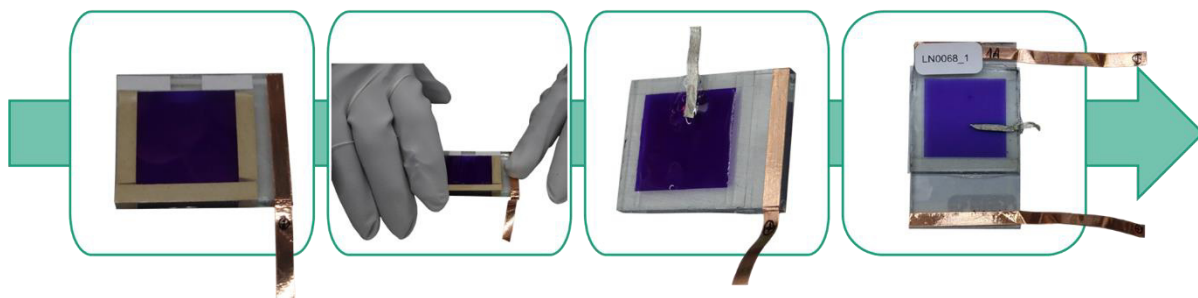
These samples were prepared by our partners according to the following physical deposition procedure. The sputter-deposited TiVO<sub>x</sub> electrodes were provided by EControl-Glas GmbH & Co. KG. TMO depositions on unheated substrates were carried out within a Systec ZVL 1000 *in-line* coater using a co-sputtering setup and reactive direct current (DC) sputtering processes. Two of the three cathodes were equipped with Ti and Mn targets. Thin films with a thickness of approx. 175 nm (Ti-rich) and 225 nm (Mn-rich) were prepared on rotating FTO glass substrates (10 x 10 cm<sup>2</sup>) and Si-wafers. The Ti- and Mn-rich compositions were obtained by varying the power ratios of the Ti and Mn cathodes (Tab. 9). For enhanced porosity, which promotes Li<sup>+</sup>-insertion, a high pressure of 2.8 Pa was applied. The Ti-rich and Mn-rich TMO electrodes are further referred to as **TMO-1** and **TMO-2**, respectively. The TMO films on silicon wafers were investigated by electron probe microanalysis (EPMA) using a CAMECA SX100 instrument ( $U_{\text{Beam}} = 10 \text{ keV}$ ,  $I_{\text{Beam}} = 100 \text{ nA}$ , five measurements for each sample, reference samples for stoichiometry calibration: TiMnO<sub>3</sub> and 10 wt% Ar implanted in Si). The evaluation was conducted with STRATAGEM software from SAMx using the thin film analysis scheme by Pouchou and Pichoir. [40,41] The resulting chemical composition is given in Tab. 9.

**Tab. 9:** Sputtering conditions and sample composition: gas flow  $q$ , pressure  $p$ , cathode power  $P$ , thickness  $t$ , and deposition rate  $r_d$ . Target-substrate distance: 170 mm, target-size: 2'' $\varnothing$ .

EC electrode	Sputtering conditions								Sample composition		
	$q(\text{Ar})$ / sccm	$q(\text{O}_2)$ / sccm	$p$ / Pa	$p(\text{O}_2)$ / mPa	$P(\text{Ti})$ / W	$P(\text{Mn})$ / W	$t$ / nm	$r_d$ / nm·min <sup>-1</sup>	Mn / at.%	Ti / at.%	O / at.%
TMO-1	400	15	2.76	53.2	168	36	182	1.40	8.2	25.1	66.5
TMO-2	400	15	2.75	54.4	75	91	223	1.35	33.7	2.9	63.0

### 3. Preparation and assembly of ECDs

Type III ECDs with the configuration glass/FTO/Fe-MEPE/gel electrolyte/metal oxide/FTO/glass, with an active (switchable) area of  $2 \times 2 \text{ cm}^2$  were manufactured in a glove box (inert atmosphere:  $\text{H}_2\text{O}$ ,  $\text{O}_2 < 5 \text{ ppm}$ ) by the following procedure (Fig. 16) and described in ref. [113]. After dip-coating, the active area of  $2 \times 2 \text{ cm}^2$  for the Fe-MEPE layer was prepared by removing surplus EC material with EtOH. This area was then surrounded by double-sided adhesive tape. A proprietary  $\text{LiClO}_4$ -containing gel electrolyte ( $\text{LiClO}_4/\text{PC}/\text{DEC}/\text{Paraloid}$ ) was prepared in an inert atmosphere and doctor blade coated onto the Fe-MEPE layer (wet film thickness: approx.  $90 \mu\text{m}$ ). The metal oxide-coated CE (ion storage layer) was then aligned and laminated on top. Adhesive Cu tape (6 mm) was used as bus bars. For the three-electrode ECDs (active area:  $3.5 \times 3.5 \text{ cm}^2$ ), a Li foil was embedded as RE into the cell. Thus, the individual electrode potentials (vs. RE) can be measured during device operation. The exact configuration of the ECDs is given in the corresponding chapter in the results and discussion part (see section V).



**Fig. 16:** Simplified procedure for the preparation and assembly of three-electrode ECDs.

Type II ECDs with the configuration glass/FTO/Fe-MEPE/redox electrolyte/FTO/glass were fabricated with an active area of  $4 \times 3.5 \text{ cm}^2$ , while the configuration glass/FTO/ $\text{Ni}_{1-x}\text{O}$ /electrolyte/FTO/glass ECDs had an active area of  $2 \times 2 \text{ cm}^2$ . The formulations of the redox electrolytes involving the non-corrosive, commercially available, and non-toxic redox pairs  $\text{KHCF(II)/(III)}$ ,  $\text{Fc}^{0/+}$ , and  $\text{TMTU}/\text{TMFDS}^{2+}$  are summarized in Tab. 10 and Tab. 11.

**Tab. 10:** Redox electrolytes with 1 M LiClO<sub>4</sub> in H<sub>2</sub>O or PC and gelling agent. Reproduced from ref. [103] with permission from Wiley.

ECD	Redox mediator	c (redox mediator) / mol·l <sup>-1</sup>	Solvent
ECD3-1	---	---	H <sub>2</sub> O
ECD3-2	K <sub>3</sub> [Fe(CN) <sub>6</sub> ]	0.001	H <sub>2</sub> O
ECD3-3	K <sub>3</sub> [Fe(CN) <sub>6</sub> ]	0.01	H <sub>2</sub> O
ECD3-4	K <sub>3</sub> [Fe(CN) <sub>6</sub> ]	0.1	H <sub>2</sub> O
ECD3-5	Fc-PF <sub>6</sub>	0.1	PC
ECD3-6	Fc-BF <sub>4</sub>	0.1	PC
ECD3-7	TMTU	0.1	PC

**Tab. 11:** Molar ratio of TMTU:TMFDS<sup>2+</sup> containing redox electrolytes with 1 M LiClO<sub>4</sub>/PC and gelling agent. Reproduced from ref. [103] with permission from Wiley.

ECD	Redox mediator	c (redox mediator) / mol·l <sup>-1</sup>	Molar ratio
ECD3-8	---	---	---
ECD3-9	TMTU/TMFDS <sup>2+</sup>	0.1	1:0
ECD3-10	TMTU/TMFDS <sup>2+</sup>	0.1	1:0.1
ECD3-11	TMTU/TMFDS <sup>2+</sup>	0.1	1:1

As KHCF(III) was only soluble in an aqueous Li<sup>+</sup>-containing electrolyte, the corresponding ECDs were fabricated in ambient conditions. The Fe-MEPE-based ECDs with 0 M, 0.001 M, 0.01 M, and 0.1 M KHCF(III) in 1 M LiClO<sub>4</sub>/H<sub>2</sub>O as redox electrolyte are referred to as **ECD3-1**, **ECD3-2**, **ECD3-3**, and **ECD3-4**, respectively. The devices containing Fe-MEPE and Fc-PF<sub>6</sub>, Fc-BF<sub>4</sub>, or TMTU were prepared in an inert atmosphere in a glove box (H<sub>2</sub>O, O<sub>2</sub> < 10 ppm) and are referred to as **ECD3-5**, **ECD3-6**, and **ECD3-7**, respectively. The combinations of Ni<sub>1-x</sub>O electrodes with different molar ratios of TMTU and TMFDS<sup>2+</sup> were also fabricated in a glove box. The ECD without a redox mediator (**ECD3-8**) was used as a reference. The ECDs with TMTU/TMFDS<sup>2+</sup> (molar ratios of 1:0, 1:0.1, 1:1) are **ECD3-9**, **ECD3-10**, and **ECD3-11**.

## 4. Characterization methods

### 4.1. IR spectroscopy

The IR spectra were recorded at a NICOLET 6700 FT-interferometer from Thermo SCIENTIFIC over a wavenumber region from 400 to 4000  $\text{cm}^{-1}$ . The measurements of the  $\text{Ni}_{1-x}\text{O}$  powder and layers were performed in transmission using a KBr pellet and the resolution was set to 4  $\text{cm}^{-1}$ . Coatings were measured with an ATR unit (Quest GS10800-X, Specac) with diamond versus air as reference.

### 4.2. UV-Vis and colorimetric measurements

UV-Vis spectra were recorded at room temperature with an Avantes AvaSpec-2048 standard fiber optic spectrometer combined with a balanced deuterium-halogen light source (DH-S-BAL, 200-1100 nm) utilizing optical fibers. The light ray went through the EC layer and then the TCO substrate. The spectra were recorded with air as a reference. The color values ( $L^*a^*b^*$ ) were calculated automatically in AvaSoft, while the  $\Delta E^*$  values were calculated as mean values for three or five different spots referenced to the center of the sample. The  $\tau_v$  value is calculated for the visible range according to DIN EN410.

### 4.3. Haze

The relative turbidity of the layers was recorded *via* diffuse light scattering according to DIN ISO 3537:2018-02 at a Hazegard® System XL-211. The coating was directed towards the light source and three to five measurements were performed for each sample to account for differences in the layer quality. The system was calibrated against air.

### 4.4. Cross-cut test

The adhesion of the EC layer on the substrate was measured with a cross-cut test and the result was classified according to DIN EN ISO 2409. [230] A lattice pattern containing six vertical and horizontal lines in a 1 mm distance was created on the test surface with a cutter and a stencil. Subsequently, adhesive tape was applied to cover the cut area and removed vigorously after 1 min.

### 4.5. Scanning electron microscopy and energy-dispersive X-ray spectroscopy

SEM and energy-dispersive X-ray spectroscopy (EDX) were used to analyze the topology (surface structure) and composition of the EC thin films on FTO glass, respectively. Here, the SEM images were recorded in the secondary electron and backscattered electron modes. Cross-sectional images of the coated glass substrates were recorded to determine the layer structure and thickness. The SEM measurements at the breaking edges were carried out using the Ultra 55 field emission SEM in a high vacuum from Carl Zeiss NTS GmbH. An InLens SE detector was used for image acquisition. The SEM images of the surfaces were taken on an Auriga® 60 device, from Carl Zeiss NTS GmbH.

#### 4.6. Electrochemical and *in situ* spectroelectrochemical measurements

The electrochemical properties of the EC electrodes were determined in 1 M LiClO<sub>4</sub>/PC as the electrolyte in a conventional three-electrode set-up utilizing standard electrochemical techniques such as CV, potentiostatic, and galvanostatic cycling. In brief, electrochemical characterization was carried out on the EC half-cells, with the EC electrodes serving as a WE with metallic lithium as the CE and RE. The entire measurement was performed under an argon atmosphere in a glove box (H<sub>2</sub>O, O<sub>2</sub> < 10 ppm). The copper tape was attached to the uncoated FTO surface of the EC electrodes (active area: 1 x 1 cm<sup>2</sup>) to maintain good electrical contact. Electrochemical characterization was performed by means of a Solartron Multistat 1470E potentiostat/galvanostat.

The Fe-MEPE samples were initially cycled at a scan rate of 5 to 100 mV·s<sup>-1</sup> between 2.4 V and 4.4 V vs. Li/Li<sup>+</sup>. Subsequently, the samples were galvanostatically charged up to 4.4 V and discharged to 3.2 V vs. Li/Li<sup>+</sup> with current densities from 1 to 1,000 μA·cm<sup>-2</sup>. This was followed by a galvanostatic cycling measurement over 1,000 switching cycles at 25 μA·cm<sup>-2</sup>. The mixed metal oxide electrodes were electrochemically characterized accordingly in the potential range from 2.0 to 4.0 V vs. Li/Li<sup>+</sup>.

Spectro-electrochemical measurements were performed *in situ* in a custom-made three-electrode measurement cell with platinum as counter and Ag/AgCl as RE and 1 M LiClO<sub>4</sub>/PC as the electrolyte. The copper tape was attached to the FTO surface to maintain good electrical contact. The background measurement was carried out with the electrolyte beforehand. The UV-Vis spectra and colorimetric values were acquired with an Avantes AvaSpec-2048 standard fiber optic spectrometer combined with a balanced deuterium–halogen light source. The corresponding photographic images of the EC materials and ECDs were modified in their color to fit the measured color coordinates as the camera does not take color-accurate photos.

The electrochemical characterization of the two- and three-electrode full cells was carried out in an inert atmosphere in the glove box. The ECDs were characterized by potentiostatic and CV measurements. The optimal operating voltages of the ECDs were adjusted by a stepwise increase of the cell voltage. The decoloration voltage is defined as the threshold voltage where the device was in the bright state and no further changes in the transmittance were observed at higher voltages. ECDs with a Li RE comprising different charge density ratios between the working and CE can be studied (spectro-)electrochemically to evaluate the redox behavior of both electrodes during full cell operation in detail and enhance the EC performance. The electrochemical characterization of the ECDs was performed with a Solartron Multistat 1470E potentiostat/galvanostat.

#### **4.7. Transference number and T-dependent conductivity**

The measurement of  $T_+$  was carried out in a symmetrical two-electrode cell (Li-Li) of conventional design according to a procedure described in ref. [99,100]. To determine the transference number, a constant potential (20 mV) is applied and the current is measured. Before and after this polarization, the electrode resistance is determined by means of an EIS measurement. The measurement of the T-dependent conductivity was carried out in a symmetrical two-electrode cell (steel-steel) and the electrode resistance at different temperatures is determined by means of an EIS measurement.

#### **4.8. X-ray photoelectron spectroscopy**

The chemical composition of the  $\text{Ni}_{1-x}\text{O}$  layers, specifically its surface, was analyzed by means of X-ray photoelectron spectroscopy (XPS). This method is based on the interaction of X-rays with the material, whereby an incident X-ray photon can remove a core electron when it hits the sample. By determining the kinetic energy of this photoelectron, the binding energy of the electrons in the material can be deduced. This is characteristic for each element, *i.e.*, the exact layer composition can be determined. However, hydrogen and helium are not able to be detected because the cross-section is too small. The measurements on the  $\text{Ni}_{1-x}\text{O}$  layers were carried out with an S-Probe spectrometer (SSI Surface Science Instruments). Monochromatic Al  $K_\alpha$  radiation at 10 kV served as the X-ray source. The measurement point size for overview recordings over the entire energy range was  $400 \times 1,000 \mu\text{m}^2$  and for recordings in smaller regions of the binding energies  $300 \times 300 \mu\text{m}^2$ . The data were obtained and evaluated with ESCA Hawk 7 and Hawk Data Analysis 7, respectively.

#### **4.9. Laser scanning microscope**

Laser scanning microscope (LSM) images were obtained with a Keyence VK-X200 microscope. The lateral and vertical resolution (beam width) is 219 nm and 3 nm, respectively. A magnification of 150 was used with a numerical aperture (NA) of 0.95 and a wavelength of 408 nm.

## V. Results and discussion

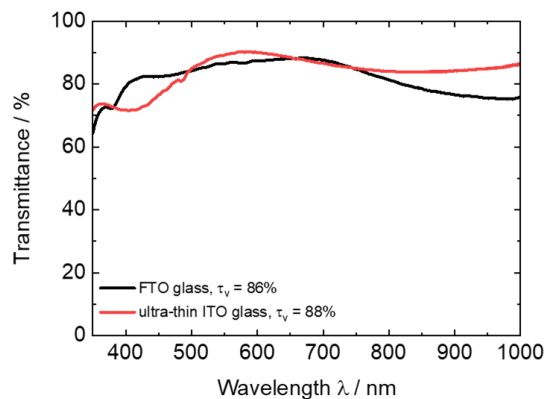
This part of the thesis is predominately made up of excerpts from published materials from internationally recognized peer-reviewed journals (cumulative Dissertation). For each chapter, the relevant publication/s is/are mentioned. Moreover, the publications are added to the appendix for further clarification. Prior to the in-depth characterization of the ECDs that pave the way towards neutral tint and NIR modulation, the compartments themselves have to be described and analyzed briefly.

### 1. Substrate and electrolyte

In this thesis, two different substrates were used and the optical data of the TCO substrates are summarized in Tab. 12. Due to the high thermal stability of glass, these substrates are interesting for the deposition of inorganic EC materials (*e.g.*, tungsten or nickel oxides) that are usually deposited by high-temperature sputtering processes. The most important parameters for the conductive substrates used for ECDs are a high level of transmittance in the visible range and the lowest possible sheet resistance to achieve high conductivity of the layers. The examined transparent conductive glasses show excellent optical properties. The absorption edge of ITO and FTO glass is below 350 nm, *i.e.*, UV light with shorter wavelengths is completely absorbed by the TCO-coated glass substrate. The  $\tau_v$  value is above 80% for both substrates (Fig. 17) and the haze values are below 1%, *i.e.*, the TCO layers show a high degree of transparency. Additionally, the low sheet resistance of approx. 14 and 23  $\Omega \cdot \text{sq}^{-1}$  for FTO glass and ultra-thin ITO glass, respectively, indicate a high conductivity that results in a low response time of the final ECDs. The results for the substrate are published in ref. [231].

**Tab. 12:** Color coordinates ( $L^*a^*b^*$ ), visible light transmittance ( $\tau_v$ ), sheet resistance, and haze of TCO-based substrates.

Substrate	$L^*$	$a^*$	$b^*$	$\tau_v$ / %	Sheet resistance / $\Omega \text{ sq}^{-1}$	Haze / %
FTO glass	94.3	0.2	2.6	86	14	0.6
ultra-thin ITO glass	94.9	-1.3	8.1	88	23	0.1

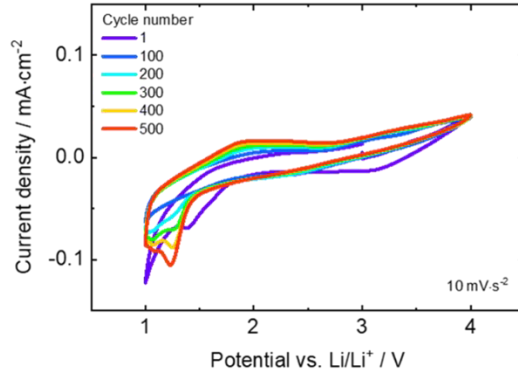


**Fig. 17:** Transmission spectra of the glass-based substrates.



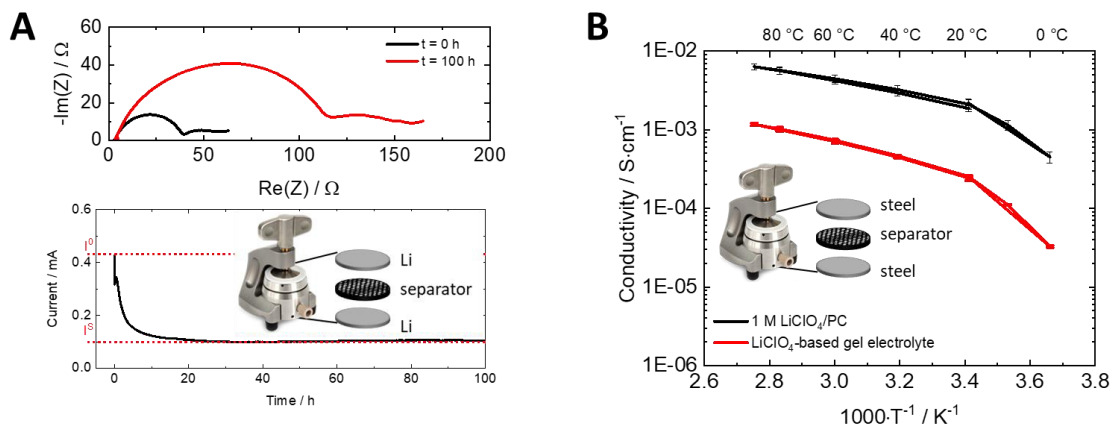
## Results and discussion

The CV curve in Fig. 18 shows that above 1.5 V vs. Li/Li<sup>+</sup> no side reactions or degradation occur, although double-layer capacitance can be detected. It should be noted that the current density (< 0.1 μA·cm<sup>-2</sup>) is significantly lower than that observed for the CEs (around 0.1 mA·cm<sup>-2</sup>).



**Fig. 18:** CVs of the FTO glass with Li as CE and RE in 1 M LiClO<sub>4</sub>/PC.

Next, the electrical properties of the electrolyte were measured. To determine the transference number of both electrolytes, a constant potential (20 mV) is applied and the current is measured. Before and after this polarization, the electrode resistance is determined by means of an EIS measurement (Fig. 19A). The  $T_+$  value at 25 °C for the LiClO<sub>4</sub>-containing liquid and gel electrolyte is 0.32 and 0.26, respectively. This value fits well with the ones given in ref. [232–235]. In a second experiment, the temperature-dependent conductivity was measured and determined at 25 °C to be  $2.2 \cdot 10^{-3}$  and  $2.8 \cdot 10^{-4}$  S·cm<sup>-1</sup> for the LiClO<sub>4</sub>-containing liquid and gel electrolyte (Fig. 19B). These values are in accordance with the ones for 1 M LiClO<sub>4</sub>/PC and other Li<sup>+</sup>-containing gel electrolytes. [236–238] Therefore, these values lie in the required high ionic conductivity range (between  $10^{-3}$  and  $10^{-7}$  S·cm<sup>-1</sup>) to allow fast response for ECDs.



**Fig. 19:** (A) EIS and chronoamperometric measurements used to calculate the Li transference number of 1 M LiClO<sub>4</sub>/PC electrolyte and (B) temperature-dependent conductivity measurements of LiClO<sub>4</sub>-containing liquid and gel electrolyte. The insets show the two set-ups for the corresponding measurement.

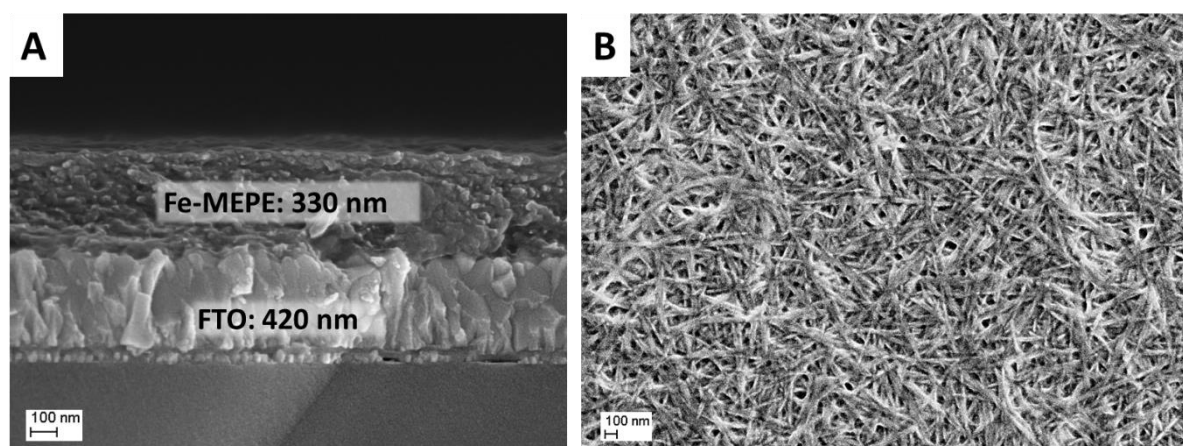
## 2. Fe-MEPE and Ni<sub>1-x</sub>O thin film electrodes and combinations thereof

In this chapter, the summary of results on cathodically-coloring Fe-MEPE and anodically-coloring Ni<sub>1-x</sub>O thin films are divided into four sections. Section 0 and 0 outline investigations of the morphology and electrochromism of both electrodes in a Li<sup>+</sup>-containing electrolyte, while the combination of Fe-MEPE electrodes with Ni<sub>1-x</sub>O electrodes of varying thickness, and hence charge densities, is discussed in section 0. Finally, section 0 presents a digression, in which the obtained results are transferred from thick FTO glass to flexible ultra-thin ITO glass.

### 2.1. Detailed characterization of Fe-MEPE thin film electrodes

The detailed characterization of the Fe-MEPE electrodes is published in ref. [103,113,239].

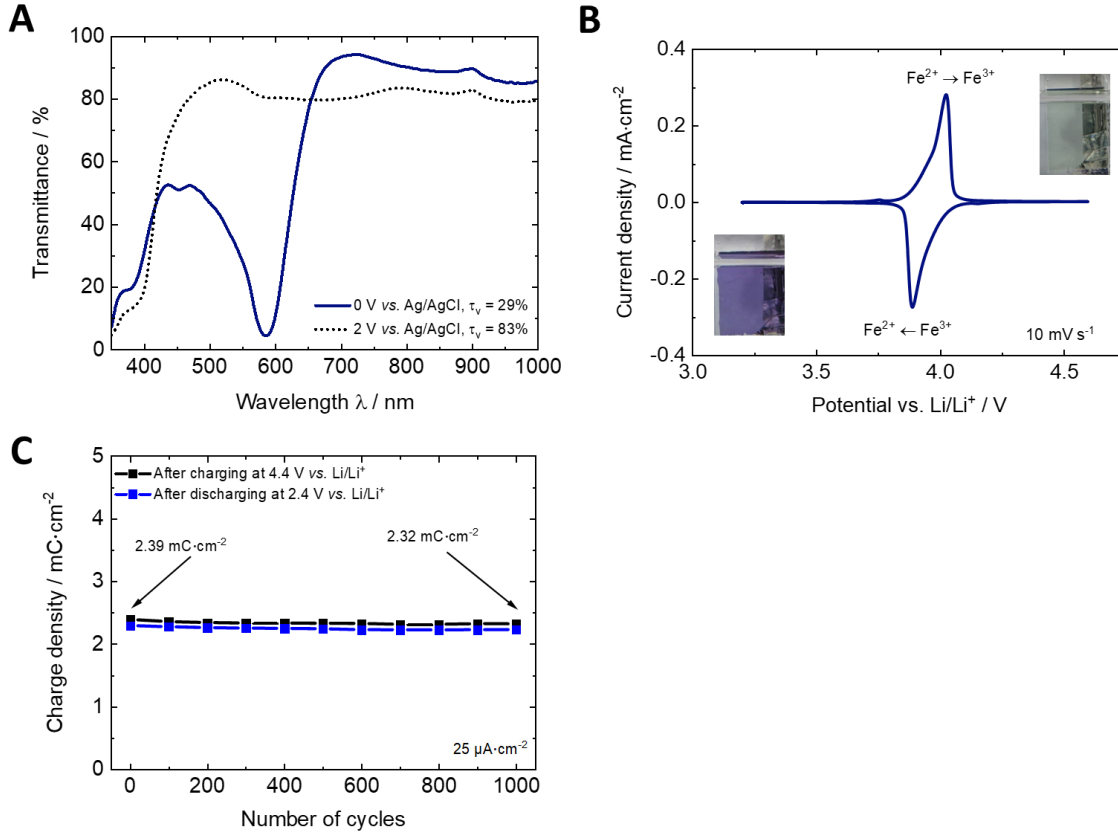
The adhesion of the EC layer on the substrate was measured with a cross-cut test and the result was classified according to DIN EN ISO 2409 as GT0, *i.e.*, very good adhesion. [230] The SEM images in Fig. 20 show that the FTO surface is well covered by the Fe-MEPE layer (~330 nm), showing a needle-like entangled structure. This homogeneous and defect-free surface is evident from the LSM images in Fig. S1. The optical characterization of the Fe-MEPE electrode is summarized in Fig. S2 and Tab. S1.



**Fig. 20:** SEM images depicting (A) the layer thickness and (B) the surface structure of the Fe-MEPE thin films on FTO glass.

The Fe-MEPE thin film electrodes were characterized *via* spectro-electrochemical measurements and electrochemical cycling as summarized in Fig. 21 and Tab. 13. The transmission spectra illustrate this effect in Fig. 21A, where the MLCT band at 584 nm completely disappears at an applied potential of 2 V vs. Ag/AgCl. The visible light transmittance changes from  $\tau_v = 29\%$  (dark) to 83% (bright). Fig. 21B shows the CV curves and transmission spectra obtained for Fe-MEPE on FTO glass. The peak potential for the oxidation of Fe<sup>2+</sup> to Fe<sup>3+</sup> occurs at 4.01 V vs. Li/Li<sup>+</sup>, whereas the reduction occurs at 3.90 V vs. Li/Li<sup>+</sup> at a scan rate of 10 mV s<sup>-1</sup>. A color change accompanies the oxidation of the Fe-MEPE film from blue-violet ( $L^* = 69.0$ ,  $a^* = 5.7$ ,  $b^* = -25.4$ ) to a virtually colorless state ( $L^* = 92.9$ ,  $a^* = -6.8$ ,  $b^* = 8.4$ ).

Furthermore, the Fe-MEPE electrodes were electrochemically charged (bright) and discharged (colored) with a current density of  $25 \mu\text{A}\cdot\text{cm}^{-2}$  in the same potential range (Fig. 21C). The charge density of  $2.39 \text{ mC}\cdot\text{cm}^{-2}$  (Coulomb efficiency of 98%) decreases about 3% over 1,000 continuous charging/discharging cycles, indicating very high cycle stability. Additionally, the coloration efficiency was determined to be  $524 \text{ cm}^2\cdot\text{mC}^{-1}$ .



**Fig. 21:** (A) Transmission spectra of Fe-MEPE (MLCT band at 584 nm) in 1 M  $\text{LiClO}_4/\text{PC}$  with Pt as CE and Ag/AgCl as RE. (B) CV at  $10 \text{ mV}\cdot\text{s}^{-1}$ , and (C) charge density over 1,000 charging/discharging cycles (current density:  $25 \mu\text{A}\cdot\text{cm}^{-2}$ ) of Fe-MEPE films on FTO glass in 1 M  $\text{LiClO}_4/\text{PC}$  with Li as CE and RE.

**Tab. 13:** Color coordinates ( $L^*a^*b^*$ ), transmittance (T) at 584 nm, visible light transmittance ( $\tau_v$ ), charge densities (q) after charging (2 V)/discharging (0 V), coulombic efficiency, and coloration efficiency ( $\eta$ ) of the Fe-MEPE thin film electrodes.

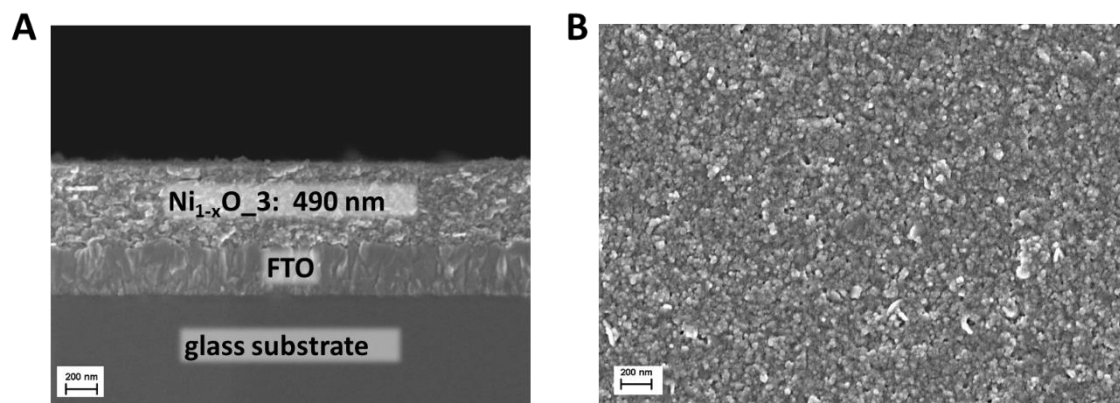
EC electrode	Potential vs. Ag/AgCl / V	$L^*$	$a^*$	$b^*$	T (at 584 nm) / %	$\tau_v$ / %	q / $\text{mC}\cdot\text{cm}^{-2}$	Coulombic efficiency / %	$\eta$ / $\text{cm}^2\cdot\text{C}^{-1}$
Fe-MEPE	0	69.0	5.7	-25.4	5	29	2.29	96	524
	2	92.9	-6.8	8.4	80	83	2.39		

## 2.2. Detailed characterization of Ni<sub>1-x</sub>O thin film electrodes

The detailed characterization of the Ni<sub>1-x</sub>O electrodes with different layer thicknesses (charge densities) is published in ref. [113,239].

Before turning to the optical and (spectro-)electrochemical characterization of the Ni<sub>1-x</sub>O thin films prepared by the *National Institute of Chemistry* in Ljubljana, Slovenia), a short digression to morphological and compositional insights of these thin films is given. In recent literature, the studied Ni<sub>1-x</sub>O electrodes were characterized *via* thermogravimetric analysis (TGA), differential scanning calorimetry (DSC), and IRRAS measurements, from which it can be deduced that due to the hydrated nature of the NiO<sub>x</sub>H<sub>y</sub> and the presence of loosely bonded OH groups, a medium temperature (~150 °C) was enough to link the individual Ni<sub>1-x</sub>O pigment particles together in the form of well cohesive Ni<sub>1-x</sub>O pigment coatings (Fig. S3A,B). [71,72,185] This offers the advantage that Ni<sub>1-x</sub>O coatings can not only be prepared on glass substrates but also flexible polymer-based substrates, *e.g.*, PET-ITO. The IR bands at 563-582 cm<sup>-1</sup> and 538-542 cm<sup>-1</sup> bands were assigned to grain and surface (intergranular) modes. Both bands remained in the spectra of the coatings heat treated up to 300 °C but diminished at 500 °C. This is in agreement with sintering leading to an increase in the grain size. X-ray diffraction (XRD) measurements revealed that Ni<sub>1-x</sub>O with a bunsenite structure formed after 24 h at 400 °C, which was inferred from the presence of (111), (200), and (220) diffraction peaks (Fig. S3C). [72,240] Finally, the stoichiometry (Ni<sup>2+</sup>/Ni<sup>3+</sup> ratio of approx. 0.5) of the deposited films was exemplary for **Ni<sub>1-x</sub>O\_5** measured with XPS as shown in Fig. S4. The binding energy of the peaks of the Ni<sup>2+</sup> and Ni<sup>3+</sup> states are in accordance with ref. [72], where a detailed XPS characterization is described.

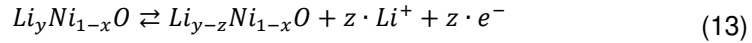
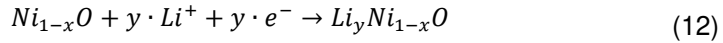
To get an overview of the properties of the Ni<sub>1-x</sub>O thin films, the following characterizations are shown for **Ni<sub>1-x</sub>O\_3** and the excellent results for thinner and thicker films are annotated. The SEM images in Fig. 22 and Fig. S5 show that the FTO surface is well covered by a porous nickel oxide deposited with a thickness of approx. 490 nm (**Ni<sub>1-x</sub>O\_3**) as derived from the cross-section image. The adhesion of the EC layer on the substrate was measured with a cross-cut test according to DIN EN ISO 2409 to be GT1, *i.e.*, good adhesion. [230]



**Fig. 22:** SEM images depicting (A) the layer thickness and (B) the surface structure of the **Ni<sub>1-x</sub>O\_3** thin film on FTO glass.

The transmission spectra of FTO glass coated with Ni<sub>1-x</sub>O in different layer thicknesses are shown in Fig. S6, while the optical characterization of the Ni<sub>1-x</sub>O electrodes is summarized in Tab. S1. The layers exhibit a broad absorption across the entire visible region of the spectrum. The thinner films have a higher  $\tau_v$  value, indicated by higher  $L^*$  values and sharper absorption edges. Films of higher thickness exhibit lower haze. Nevertheless, the haze was below 1% for all layer thicknesses, indicating excellent transparency (Fig. S7).

All five thin film electrode variations were characterized by spectroelectrochemical and electrochemical methods (CV and galvanostatic charging/discharging over 1,000 cycles). The result for **Ni<sub>1-x</sub>O\_3** is exemplary depicted in Fig. 23 and summarized in Tab. 14. As expected, for all films no pre-cycling was needed, *i.e.*, they could be immediately decolorized or colored from the as-deposited state in 1 M LiClO<sub>4</sub>/PC according to the following equations. [34,71,165,193,241,242]

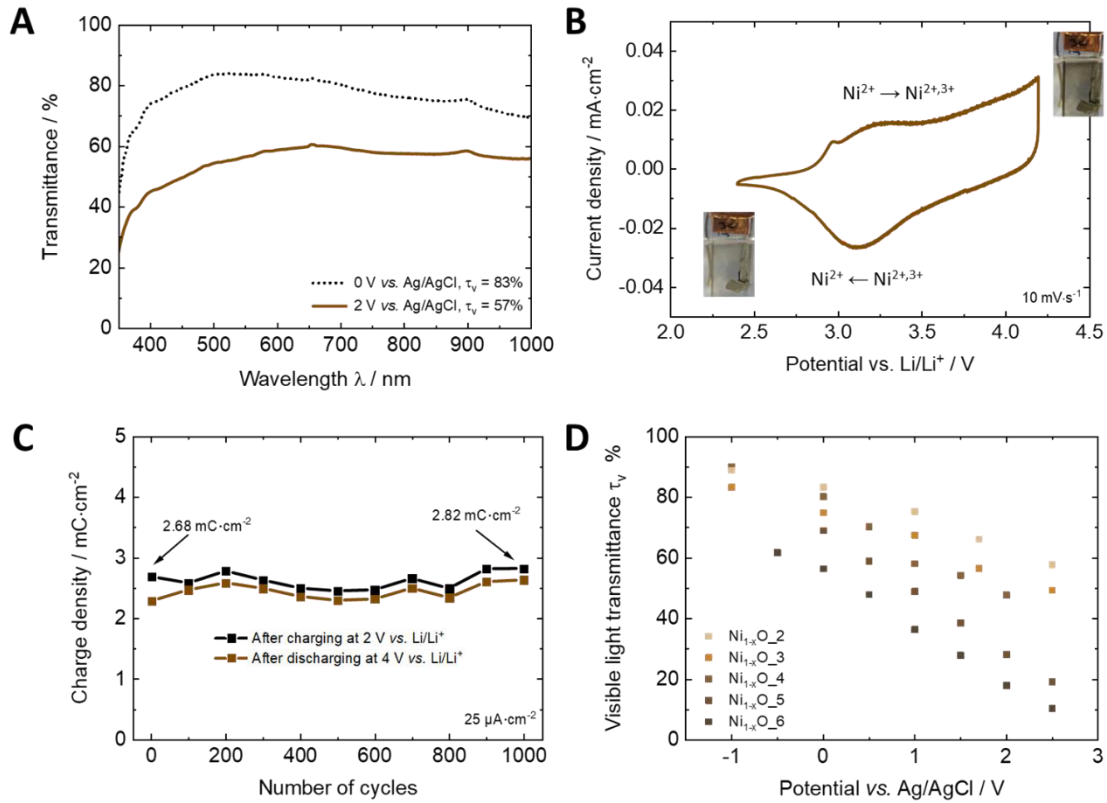


Equation (12) describes the initial decoloration, while equation (13) represents the reversible EC reaction. The immediate EC response on Li<sup>+</sup>-containing electrolytes was attributed to the films' porosity and the presence of nickel in two valences, *i.e.*, Ni<sup>2+</sup> and Ni<sup>3+</sup>. [199,200] The transmittance modulation of **Ni<sub>1-x</sub>O\_3** ( $\tau_v$  at 2 V) /  $\tau_v$  at 0 V [in %]) is 48/80 and decreases with increasing film thickness (Fig. 23D and Tab. 14). Moreover, the **Ni<sub>1-x</sub>O\_2** and **Ni<sub>1-x</sub>O\_3** electrodes exhibit a neutral tint in both states as the  $|a^*, b^*|$  values are below 5. An increase in the thickness leads to lower transmittance in the colored state and a more intense yellow hue in the bright state.

The CV curves in the potential range from 2.4 V to 4.2 V vs. Li/Li<sup>+</sup> were measured at a scan rate of 10 mV·s<sup>-1</sup> in Fig. 23B. The anodic peak centered around 3.1 V vs. Li/Li<sup>+</sup> is assigned to the oxidation of Ni<sup>2+</sup> to Ni<sup>3+</sup> and concurrent de-insertion of Li<sup>+</sup> ions. A reversible color change accompanies this process from colorless ( $L^* = 89.3$ ,  $a^* = -0.8$ ,  $b^* = 4.2$  for **Ni<sub>1-x</sub>O\_3**) to gray-brown with various intensities depending on the film thickness. The cathodic peak around 3.2 V vs. Li/Li<sup>+</sup> is due to the reduction of Ni<sup>3+</sup> to Ni<sup>2+</sup> and the simultaneous insertion of Li<sup>+</sup> ions from the electrolyte into the cationic vacancies in the Ni<sub>1-x</sub>O structure leading to a complete decoloration. [241,243]

Furthermore, the Ni<sub>1-x</sub>O electrodes were galvanostatically charged (colored) and discharged (decolored) at a current density of 25  $\mu\text{A}\cdot\text{cm}^{-2}$  in the same potential range as shown in Fig. 23C. The initial charge density of 2.68 mC·cm<sup>-2</sup> (coulombic efficiency of 95%) thereby decreased by about 5% over 1,000 galvanostatic charging/discharging cycles, indicating high cycle stability.

A further parameter for EC materials is the coloration efficiency, which is determined to be 60 cm<sup>2</sup>·C<sup>-1</sup> and decreases with increasing film thickness (Tab. 14). This decrease can be explained by the effect that different surface structures and topologies have on the EC properties of nickel oxide. I. Sorar *et al.* found that surface effects dominate the electrochromism of Ni-oxide-based films (sputter and reactive gas deposition) and that the optical modulation decreases with film thickness. [244]



**Fig. 23:** (A) Spectroelectrochemical measurements of  $\text{Ni}_{1-x}\text{O}$  with Pt as CE and Ag/AgCl as RE in 1 M  $\text{LiClO}_4/\text{PC}$ , inset: photographic images of the bright (reduced) and colored (oxidized) state. (B) CVs at a scan rate of  $10 \text{ mV}\cdot\text{s}^{-1}$  with Li as CE/RE. (C) Charge retention over 1,000 charging/discharging cycles (current density:  $25 \mu\text{A}\cdot\text{cm}^{-2}$ ) with Li as CE/RE and 1 M  $\text{LiClO}_4/\text{PC}$  as electrolyte. (D) Visible light transmittance ( $\tau_v$ ) values for  $\text{Ni}_{1-x}\text{O}$  electrodes deposited with 2 to 6 layers vs. the applied potential vs. Ag/AgCl in 1 M  $\text{LiClO}_4/\text{PC}$ .

**Tab. 14:** Color coordinates ( $L^*a^*b^*$ ), transmittance (T) at 584 nm, visible light transmittance ( $\tau_v$ ), charge densities (q) after charging (2 V) and discharging (0 V), coulombic efficiency, and coloration efficiency ( $\eta$ ) of the  $\text{Ni}_{1-x}\text{O}$  thin film electrodes.

EC electrodes	Potential vs. Ag/AgCl / V	$L^*$	$a^*$	$b^*$	T (at 584 nm) / %	$\tau_v$ / %	q / $\text{mC}\cdot\text{cm}^{-2}$	Coulombic efficiency / %	$\eta$ / $\text{cm}^2\cdot\text{C}^{-1}$
$\text{Ni}_{1-x}\text{O}_2$	0	92.9	0.1	4.4	90	89	1.27	96	96
	2	84.6	0.8	6.4	68	66	1.22		
$\text{Ni}_{1-x}\text{O}_3$	0	89.3	-0.8	4.2	84	83	2.68	95	60
	2	79.6	0.3	6.7	58	57	2.46		
$\text{Ni}_{1-x}\text{O}_4$	0	91.1	1.8	11.7	84	80	3.90	97	54
	2	74.3	5.0	15.7	52	48	3.78		
$\text{Ni}_{1-x}\text{O}_5$	0	86.1	1.6	13.6	73	69	7.51	95	50
	2	58.6	5.2	17.1	31	28	7.14		
$\text{Ni}_{1-x}\text{O}_6$	0	79.0	3.9	16.9	61	56	10.12	96	48
	2	48.1	7.8	20.3	21	18	9.68		

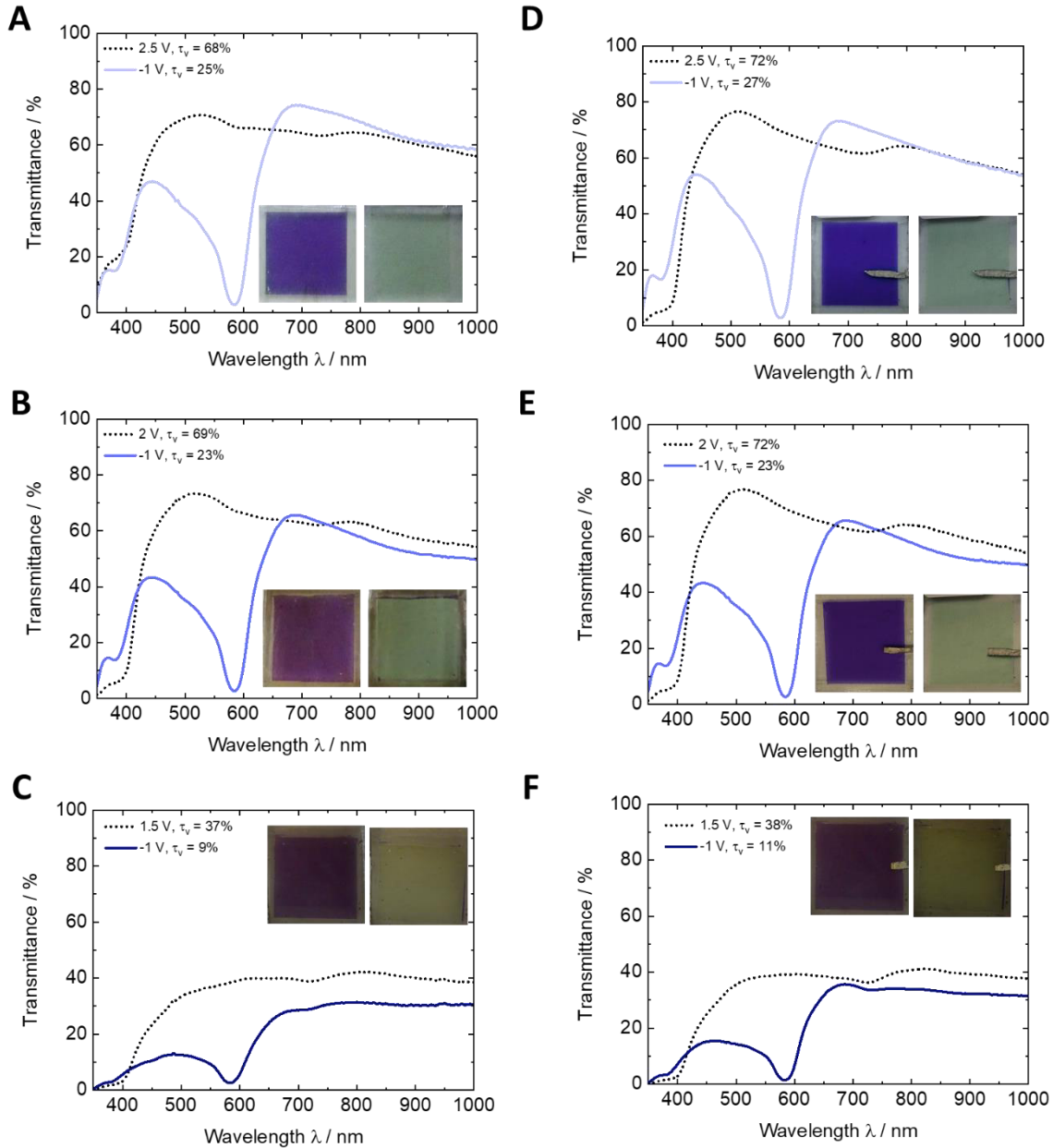
### 2.3. ECDs containing Fe-MEPE and Ni<sub>1-x</sub>O

In this part, results published in ref. [113,239] are summarized. Relying on the detailed characterization of the EC electrodes above, the EC properties (color, response time, and change in transmittance) of several ECDs have been studied. A series of three ECDs with the configuration glass/FTO/Fe-MEPE/electrolyte/Ni<sub>1-x</sub>O/FTO/glass was investigated to test the compatibility and efficiency of the Fe-MEPE electrodes in combination with Ni<sub>1-x</sub>O electrodes. Here, the charge density of the Fe-MEPE electrodes was 2.39 mC·cm<sup>-2</sup> and the charge density of Ni<sub>1-x</sub>O was varied (1.27 for **Ni<sub>1-x</sub>O\_2**, 2.68 for **Ni<sub>1-x</sub>O\_3**, and 7.51 mC·cm<sup>-2</sup> for **Ni<sub>1-x</sub>O\_5**). The corresponding ECDs are referred to as **ECD1-1**, **ECD1-2**, and **ECD1-3**, respectively.

In order to achieve the optimum EC performance, one electrode has to be pre-treated before device assembly. Therefore, the open-circuit memory, *i.e.*, the optical transmittance as a function of time under OCP conditions, of electrochemically decolorized Fe-MEPE and colored Ni<sub>1-x</sub>O electrodes were measured (Fig. S8). As the memory of the latter electrode immersed in the Li<sup>+</sup>-containing liquid electrolyte surpasses that of the Fe-MEPE electrode by far, the Ni<sub>1-x</sub>O electrode was chosen for pre-treatment and a potential of 2 V vs. Ag/AgCl was applied for ~10 min before device fabrication to ensure that both electrodes were in their colored states prior to assembly.

From the detailed characterization of the single electrodes and the mechanism discussed in ref. [34,165,241], the redox processes in the presented ECD are as follows (schematic representation is depicted in Fig. 5). During decoloration, the Fe-MEPE WE is oxidized and the Ni<sub>1-x</sub>O CE is reduced. The charge is compensated by the insertion of ClO<sub>4</sub><sup>-</sup> into the Fe-MEPE and the insertion of Li<sup>+</sup> ions into the Ni<sub>1-x</sub>O layer. The coloration occurs *via* the reduction of the Fe-MEPE and oxidation of the Ni<sub>1-x</sub>O electrode. The redox reaction is accompanied by de-insertion of ClO<sub>4</sub><sup>-</sup> from the Fe-MEPE and de-insertion of Li<sup>+</sup> ions from Ni<sub>1-x</sub>O.

The EC properties of **ECD1-2** are exemplarily described in detail in the following section and the results for thinner (**ECD1-1**) and thicker (**ECD1-3**) Ni<sub>1-x</sub>O thin films as CEs are annotated. The relevant (spectro-) electrochemical data are summarized in Fig. 24 and Tab. 15. Fig. 24A,B,C show that the as-prepared EC device has a blue tint as the MLCT band of Fe-MEPE is apparent in the transmission spectrum.



**Fig. 24:** Comparison of the spectroelectrochemical measurements of the two-electrode ECDs: (A) **ECD1-1** (Fe-MEPE/Ni<sub>1-x</sub>O<sub>2</sub>), (B) **ECD1-2** (Fe-MEPE/Ni<sub>1-x</sub>O<sub>3</sub>), (C) **ECD1-3** (Fe-MEPE/Ni<sub>1-x</sub>O<sub>5</sub>) and the three-electrode ECDs: (D) **ECD1-1\_RE** (Fe-MEPE/Ni<sub>1-x</sub>O<sub>2</sub>), (E) **ECD1-2\_RE** (Fe-MEPE/Ni<sub>1-x</sub>O<sub>3</sub>), and (F) **ECD1-3\_RE** (Fe-MEPE/Ni<sub>1-x</sub>O<sub>5</sub>). The insets show the photographic images of the colored and bright state.

The complete decoloration of Fe-MEPE defines the endpoint of switching for the ECDs (2 V,  $L^* = 87.1$ ,  $a^* = -9.0$ ,  $b^* = 10.1$  for **ECD1-2**). In this case, the charge consumed at each electrode is equal to the Fe-MEPE electrode, which switches completely between its fully colored (reduced) and colorless (oxidized) state. When the voltage is set to -1 V, both the Fe-MEPE and the Ni<sub>1-x</sub>O are colored and an almost neutral tint with very low  $a^*$  and  $b^*$  values is reached. The visible light transmittance changes from  $\tau_v = 23\%$  (dark) to 69% (bright) compared to **ECD1-1** ( $\tau_v$ : 25%  $\rightarrow$  68%) and **ECD1-3** ( $\tau_v$ : 9%  $\rightarrow$  37%), For **ECD1-3**, the Ni<sub>1-x</sub>O<sub>5</sub> film has a lower transmittance due to the larger layer thickness (charge density) as is expected from the half-cell characterization. Notably, with thicker Ni<sub>1-x</sub>O electrodes the cell voltage can be reduced, minimizing possible film degradation resulting from over-



oxidation and enhancing the cyclability of the ECDs. According to ref. [245], the lowest device voltage to fully oxidize the WE is achieved when a high charge density CE is used.

All ECDs exhibit a high coloration efficiency at the absorption maximum of 584 nm with approx.  $500 \text{ cm}^2 \cdot \text{C}^{-1}$ , matching the  $\eta$  values obtained for the Fe-MEPE electrodes (Tab. S1). Based on this result, it can be assumed that the  $\text{Ni}_{1-x}\text{O}$  electrode barely changes its transmittance. The thinner CEs (**Ni<sub>1-x</sub>O\_2** and **Ni<sub>1-x</sub>O\_3**) have only a slight change in transmittance, while **Ni<sub>1-x</sub>O\_5** is only partially reduced/oxidized during the decoloration/coloration process of the ECD due to its high charge density.

**Tab. 15:** Color coordinates ( $L^*a^*b^*$ ), transmittance (T) at 584 nm, visible light transmittance ( $\tau_v$ ), charge densities (q) after charging (2 V) and discharging (0 V), coulombic efficiency, and coloration efficiency ( $\eta$ ) of the Fe-MEPE/ $\text{Ni}_{1-x}\text{O}$  ECDs.

ECD	Cell voltage / V	L*	a*	b*	T (at 584 nm) / %	$\tau_v$ / %	q / $\text{mC} \cdot \text{cm}^{-2}$	$\eta$ / $\text{cm}^2 \cdot \text{C}^{-1}$	Response time / s
ECD1-1 (Fe-MEPE/ $\text{Ni}_{1-x}\text{O}_2$ )	-1	54.8	7.5	-23.5	3	25	2.30	584	0.4
	2.5	86.2	-6.7	8.8	66	68	2.36		2.0
ECD1-2 (Fe-MEPE/ $\text{Ni}_{1-x}\text{O}_3$ )	-1	56.7	6.2	-23.4	3	23	2.36	572	0.8
	2	87.1	-9.0	10.1	67	69	2.45		1.8
ECD1-3 (Fe-MEPE/ $\text{Ni}_{1-x}\text{O}_5$ )	-1	37.0	1.0	-3.4	3	9	2.42	475	1.0
	1.5	66.7	-2.8	19.9	38	37	2.32		1.8
ECD1-1_RE (Fe-MEPE/ $\text{Ni}_{1-x}\text{O}_2$ )	-1	58.1	8.2	-24.5	3	27	2.36	580	0.4
	2.5	86.1	-6.4	8.4	70	72	2.39		2.0
ECD1-2_RE (Fe-MEPE/ $\text{Ni}_{1-x}\text{O}_3$ )	-1	60.3	6.6	-28.0	3	23	2.69	597	0.8
	2.0	88.0	-9.9	9.7	70	72	2.29		1.8
ECD1-3_RE (Fe-MEPE/ $\text{Ni}_{1-x}\text{O}_5$ )	-1	39.7	7.9	-9.0	1	11	2.44	657	1.0
	1.5	67.6	-5.1	18.9	39	38	2.42		1.8

To compare the response times of the three ECDs, the charge density of the Fe-MEPE film is held constant and Fe-MEPE is completely oxidized (decolored) in all cell configurations, *i.e.*, the charge consumed by all three ECDs is ideally the same when no side reactions or current losses occur. The decoloration process is slightly faster (1.8 s vs. 2.0 s) and the coloration process slower (0.4 s vs. 1.0 s) with an increasing charge density of the CE (Fig. S10B). The  $\text{Ni}_{1-x}\text{O}$  CE increases the response time for coloration (at -1 V), due to the inherently slower switching kinetics of  $\text{Ni}_{1-x}\text{O}$  compared to Fe-MEPE. [245]

ECDs with a Li RE comprising different charge density ratios between the WE and CE can be studied (spectro-)electrochemically to evaluate the redox behavior of both electrodes during full cell operation in detail and enhance the EC performance. From the optical and electrochemical data shown in Fig. 24 and Tab. 15, it can be assumed that the additional Li RE does not influence the switching behavior of the ECDs, making it a useful tool to evaluate the redox behavior of the single electrodes. The CV data (Fig. S9) obtained from the two- and three-electrode ECDs performed in the cell voltage range from -1 V to 1.5 V is comparable in terms of form and peak position, further indicating that the three-electrode

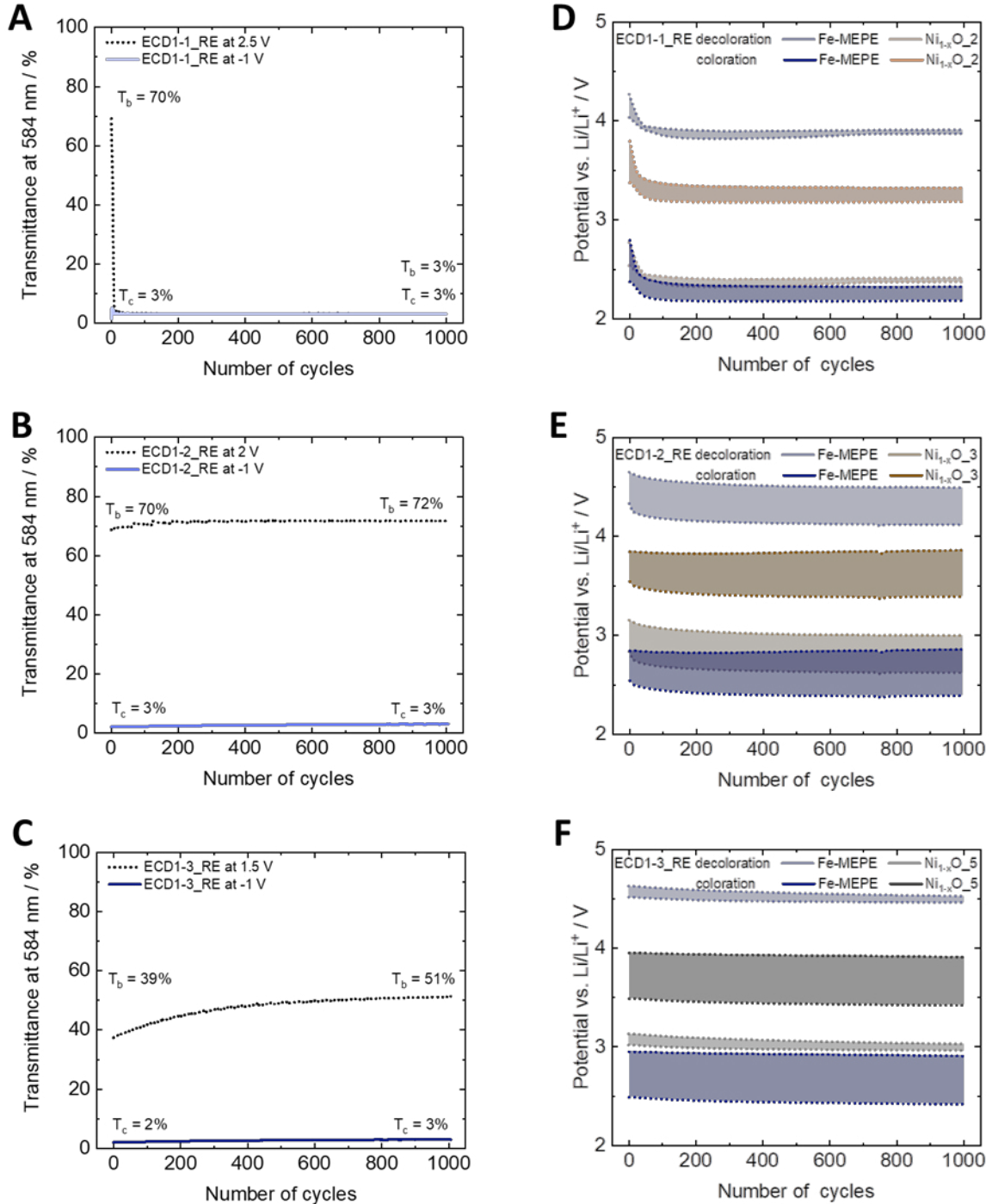
setup provides reliable results for the electrode potentials. Moreover, this method demonstrates that the upper cut-off cell voltage of 1.5 V is suitable for the complete decoloration of the overbalanced ECD (**ECD1-3\_RE**) but is insufficient to decolor the other two ECDs (**ECD1-1\_RE** and **ECD1-2\_RE**). This is further confirmed by the electrode potentials obtained with the three-electrode ECDs in Fig. S9. In this cell voltage window, both films can be reversibly switched (complete decoloration of Fe-MEPE) for the overbalanced (**ECD1-3\_RE**) and balanced (**ECD1-2\_RE**) configuration. In contrast, no oxidation nor reduction peaks for the Fe-MEPE and **Ni<sub>1-x</sub>O<sub>2</sub>** electrode, respectively, can be detected (both electrode potentials remain below 4.1 V vs. Li/Li<sup>+</sup>) with the underbalanced ECD (**ECD1-1\_RE**).

Long-term cycling stability is required for most commercial EC applications. Therefore, the cyclability of **ECD1-2\_RE** was measured over 1,000 cycles with lower and upper cut-off voltages of -1 V and 2 V. The potential at each electrode was measured to monitor the decoloration of the Fe-MEPE film electrochemically in addition to the spectroelectrochemical characterization in Fig. 25B,E. Here, the electrode potentials remain almost constant during the potentiostatic cycling (Fe-MEPE: 4.6 V - 4.2 V vs. Li/Li<sup>+</sup> and 2.8 V - 2.4 V vs. Li/Li<sup>+</sup>; **Ni<sub>1-x</sub>O<sub>3</sub>**: 3.1 V - 2.6 V vs. Li/Li<sup>+</sup> and 3.9 V - 3.4 V vs. Li/Li<sup>+</sup>, for decoloration and coloration, respectively). Finally, the high cycle stability of **ECD1-2\_RE** was further confirmed by a continuous switching behavior for more than 1,000 cycles between the fully colored (at 1 V) and the decolorated state (at 2 V) with a constant transmittance change from 3% to 70% (72% after 1,000 cycles), respectively (Fig. 25B) and the corresponding current-time profiles depicted in Fig. S11.

For **ECD1-1\_RE** (Fig. 25A), the evolution of the electrode potentials can explain the fast decrease of the bright state transmittance after less than 20 cycles ( $T_c$  at 2.5 V/ $T_b$  at -1 V [in %] from 70/3 to 3/3), *i.e.*, the MLCT band of Fe-MEPE is maintained even at applied voltages of 2.5 V. The irreversibility of the decoloration/coloration process for **ECD1-1** means that the FTO no longer supplies additional charge density (**Ni<sub>1-x</sub>O<sub>2</sub>** = 1.27 mC·cm<sup>-2</sup>) necessary to decolor the Fe-MEPE electrode after the first few cycles. [246] During the decoloration process at 2.5 V, the potential range of the cathodically-coloring Fe-MEPE electrode is above 4.2 V vs. Li/Li<sup>+</sup> in the first cycles. It drops below 4 V vs. Li/Li<sup>+</sup> as the ECD is switched to the bright state. As a consequence of this shift to lower potentials, the potential of the Fe-MEPE electrode no longer reaches its oxidation potential at around 4.0 V vs. Li/Li<sup>+</sup> and remains in its reduced (colored) state. This phenomenon has already been observed in previous studies. [168,247]

During the brightening of **ECD1-3\_RE** (Fig. 25D), the Fe-MEPE electrode potential is around 4.5 V vs. Li/Li<sup>+</sup>, which is above its oxidation potential, and the potential of the **Ni<sub>1-x</sub>O<sub>5</sub>** CE is between 2.9 V and 3.1 V vs. Li/Li<sup>+</sup>. This leads to a complete decoloration of the Fe-MEPE electrode and, hence, the ECD reaches its bright state. The potential of the Fe-MEPE and **Ni<sub>1-x</sub>O<sub>5</sub>** electrodes during coloration of the cell are approximately 2.5 V to 3.0 V vs. Li/Li<sup>+</sup> and 3.5 V and 4.0 V vs. Li/Li<sup>+</sup>, respectively. Despite the constant electrode potential during 1,000 switching cycles, a continuous brightening of the device ( $T_c$  at 1.5 V/ $T_b$  at -1 V [in %] from 39/2 to 51/3) is observed in Fig. 25B. This brightening is due to increasing amounts of Li<sup>+</sup> ions inserted into the Ni<sub>1-x</sub>O layer to balance the charge during the redox reactions and has already been described in ref. [248–250].

With this three-electrode set-up, degradation of the electrodes could be excluded during the potentiostatic cycling measurements as the potentials of the electrodes are close to but still above 2 V vs. Li/Li<sup>+</sup>. Below 2 V vs. Li/Li<sup>+</sup> side reactions occur at the FTO substrate according to Fig. 18. [127]



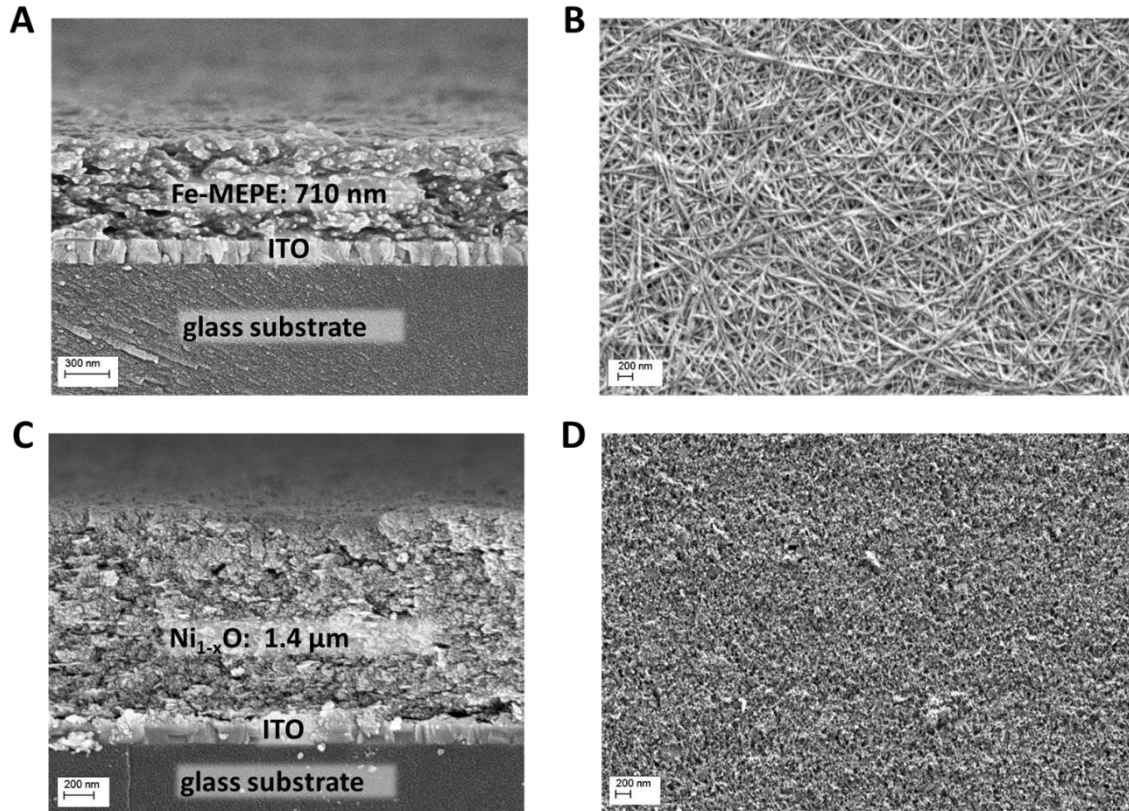
**Fig. 25:** Cycle stability over 1,000 potentiostatic switching cycles monitored by transmittance change at 584 nm and the measured electrode potentials of the Fe-MEPE and Ni<sub>1-x</sub>O electrodes in (A,D) **ECD1-1\_RE**, (B,E) **ECD1-2\_RE**, and (C,F) **ECD1-3\_RE**, respectively.

## 2.4. Flexible ultra-thin glass Fe-MEPE/Ni<sub>1-x</sub>O ECDs

The concept of the ultra-thin ITO glass is given in ref. [231] and demonstrated here with the combination of Fe-MEPE and Ni<sub>1-x</sub>O thin film electrodes. ECDs comprising Fe-MEPE and Ni<sub>1-x</sub>O as complementary switching electrode materials, a proprietary electrolyte, and ultra-thin ITO glass as transparent, conductive substrates with high optical quality were fabricated and investigated to demonstrate their EC properties. The promising properties of ultra-thin ITO glass as an alternative to polymer-based substrates ultra-thin glass gained attention in recent years for various applications such as organic light-emitting diodes (OLEDs), [251] electrowetting devices, [252] smart windows, [253,254] and solar cells. [255,256] Compared to commercially available ITO glass or PET-ITO-based transparent substrates, ultra-thin ITO glass provides good optical properties (Tab. 8 and Fig. 17), while possessing mechanical flexibility demonstrated by 1,600 bending cycles at 20.5 mm curvature. Fahland *et al.* presented a cost-effective R2R ITO deposition onto ultra-thin glass (100  $\mu\text{m}$ ) in specially developed coating equipment. [257] During the deposition, the substrate was heated and the optical properties of ITO were examined by resistivity, optical, and XRD measurements. Sung *et al.* demonstrated an anti-reflective coating with a conductive ITO layer on flexible glass (thickness: 100  $\mu\text{m}$ ) exhibiting excellent properties for the application in flexible and lightweight ECDs. [258]

The film thickness and surface morphology of the MEPE and Ni<sub>1-x</sub>O electrodes were characterized by SEM, as shown in Fig. 26. The cross-section images show the smooth Fe-MEPE and Ni<sub>1-x</sub>O layer with a film thickness of approx. 700 nm and 1.4  $\mu\text{m}$ , respectively, on the highly uniform ITO layer ( $\sim$  150 nm) with well-defined interfaces. Therefore, the adhesion of the EC thin films on ITO is very good. The top-view images of the Fe-MEPE and Ni<sub>1-x</sub>O surface are shown in Fig. 26.

The optical characterization of both thin films on ultra-thin ITO glass resembles those obtained with FTO glass substrates. Therefore, the results are briefly summarized in Tab. 16 and a detailed overview is given in Fig. S12 and Tab. S2. The same is valid for the spectroelectrochemical measurements of Fe-MEPE and Ni<sub>1-x</sub>O thin films on ultra-thin ITO glass shown in Fig. S13 and, therefore, the EC properties of the Fe-MEPE and Ni<sub>1-x</sub>O thin film electrodes and the Fe-MEPE/Ni<sub>1-x</sub>O ECD are summarized in Tab. 16.



**Fig. 26:** SEM images depicting the layer thickness and the surface structure of the (A,B) Fe-MEPE and (C,D) Ni<sub>1-x</sub>O layer on ultra-thin ITO glass.

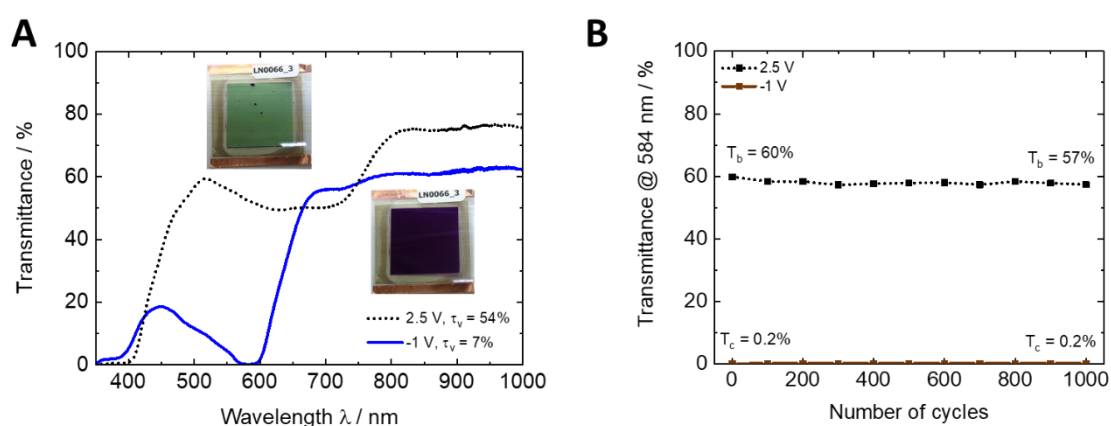
**Tab. 16:** Color coordinates ( $L^*a^*b^*$ ), transmittance (T) at 584 nm, visible light transmittance ( $\tau_v$ ), charge densities (q) after charging (2 V) and discharging (0 V), coulombic efficiency, and coloration efficiency ( $\eta$ ) of the Fe-MEPE and Ni<sub>1-x</sub>O thin films on ultra-thin ITO glass.

EC electrodes	Potential vs. Li/Li <sup>+</sup> / V	L*	a*	b*	$\tau_v$ / %	T (at 584 nm) / %	q / mC·cm <sup>-2</sup>	$\eta$ / cm <sup>2</sup> ·C <sup>-1</sup>
Fe-MEPE	3.2	41.7	18.8	-37.4	11	0.5	4.3	489
	4.4	83.9	-13.9	20.5	64	62	4.3	
Ni <sub>1-x</sub> O	4.2	74.3	5.0	15.7	38	42	3.9	69
	2.4	91.1	1.8	11.7	75	78	3.8	

**Tab. 17:** Color coordinates ( $L^*a^*b^*$ ), transmittance (T) at 584 nm, visible light transmittance ( $\tau_v$ ), charge densities (q) after charging (2 V) and discharging (0 V), coulombic efficiency, and coloration efficiency ( $\eta$ ) of ECD1-4.

ECD	Cell voltage / V	L*	a*	b*	$\tau_v$ / %	T (at 584 nm) / %	Response time / s
ECD1-4 (Fe-MEPE/Ni <sub>1-x</sub> O)	2.5	78.5	-14.0	21.3	54	60	5
	-1	35.6	19.4	-26.7	7	0.2	3

The use of ultra-thin ITO glass for ECDs is demonstrated with Fe-MEPE and Ni<sub>1-x</sub>O as EC materials for the WE and CE, respectively. They were characterized by standard spectroelectrochemical and electrochemical methods, as shown in Fig. 27. Here, **ECD1-4** switches between the dark/bright state at cell voltages of -1/2.5 V with a change of  $\tau_v$  from 7% (dark) to 54% (bright). In Tab. 17, the color coordinates ( $L^*a^*b^*$ ) and  $\tau_v$  values are summarized for the ECD consisting of Fe-MEPE and Ni<sub>1-x</sub>O ultra-thin electrodes. The response time (= time to reach 10% of initial current density) was determined according to the current density-time profile shown in Fig. S15. to 5 s and 3 s for decoloration/coloration, respectively. Fig. 27 demonstrates the stable cycling of the ultra-thin glass ECD for 1,000 switching cycles at room temperature. The transmittance change at 584 nm (maximum MLCT transition) remains constant between 0.2% (dark) and approx. 60% (bright). The ultra-thin ITO glass combines the flexibility of plastic substrates with the high optical quality and robustness of glass, such as high heat resistance that makes these substrates applicable to high-temperature deposition of other EC materials (*e.g.*, metal oxides). In addition, ultra-thin glass can be processed by continuous and large-scale R2R coating methods as an alternative to the commonly used PET-based ITO substrates. The MEPE/Ni<sub>1-x</sub>O cell configuration with a visible light transmittance change from 7% to 54% and good cycling stability (97% retention of transmittance change at 584 nm after 1,000 potentiostatic cycles) is auspicious for flexible, lightweight, and low-power ECDs in the future.



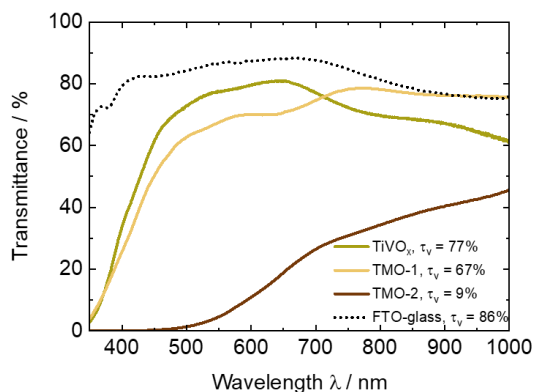
**Fig. 27:** (A) Spectroelectrochemical characterization and (B) change in transmittance at 584 nm over 1,000 potentiostatic cycles of **ECD1-4**.

### 3. ECDs based on Fe-MEPE and optically-passive mixed metal oxides

In this chapter, the results on bare mixed metal oxide thin films are divided into two sections. The basic EC investigation, including the electrochromism in LiClO<sub>4</sub>-based liquid and gel electrolytes of these Ti-containing electrodes, is shown in section 3.1. Subsequently, the combinations of Fe-MEPE with these optically-passive CEs are investigated in section 3.2. The results shown in this chapter were published in ref. [259].

#### 3.1. Detailed characterization of TiVO<sub>x</sub> and TMO thin film electrodes

The studied metal oxide electrodes do not feature distinct absorption peaks but broad d-d IVCT transitions. [34] The **TiVO<sub>x</sub>** (100 nm) layer has a light-yellow hue and is highly transmissive ( $\tau_v = 77\%$ , Fig. 28). The **TMO-1** (172 nm) and **TMO-2** (223 nm) layers exhibit a yellowish ( $L^* = 85.7$ ,  $a^* = -2.3$ ,  $b^* = 14.9$ ) and brown tint ( $L^* = 32.3$ ,  $a^* = 22.1$ ,  $b^* = 47.6$ ) with  $\tau_v$  values of 67% and 9%, respectively.



**Fig. 28:** Transmission spectra of TiVO<sub>x</sub> and TMO thin films on FTO glass. The dotted line shows the spectrum of uncoated FTO glass as a reference.

The (spectro-)electrochemical properties of the mixed metal oxide electrodes (**TiVO<sub>x</sub>**, **TMO-1**, and **TMO-2**) were investigated to explore their potential use as an ion storage layer with high charge density and low optical contrast are summarized in Tab. 18. The **TiVO<sub>x</sub>** electrode shows a weak color change upon reduction from light yellow to light gray, indicating a cathodically-coloring behavior (coloration upon reduction and Li<sup>+</sup> insertion) with a  $\tau_v$  change between 85% (at 0 V vs. Ag/AgCl) and 75% (at -2 V vs. Ag/AgCl). In contrast, **TMO-1** is anodically-coloring (coloration upon oxidation and Li<sup>+</sup> de-insertion) from light yellow to light gray with a small  $\tau_v$  change between 72% (at 0 V vs. Ag/AgCl) and 81% (at -2.5 V vs. Ag/AgCl). Moreover, **TMO-2** shows an anodic behavior with a color change from deep brown ( $\tau_v = 14\%$ ) at 0 V vs. Ag/AgCl to light brown ( $\tau_v = 42\%$ ) at -2.5 V vs. Ag/AgCl. As can be seen in Tab. 18, the **TiVO<sub>x</sub>** and **TMO-1** have similar color coordinates, with very high  $L^*$  values of over 85,  $|a^*| < 5$  and  $|b^*|$  values around 10, which potentially allows these materials to be implemented as virtually colorless CEs. In contrast, **TMO-2** has an unpleasant brown tint in the as-deposited film attributed to the higher amount of Mn in the crystal structure.

**Tab. 18:** Color coordinates ( $L^*a^*b^*$ ), transmittance (T) and visible light transmittance ( $\tau_v$ ) values and charge densities (q) between the redox states, as well as Coulombic efficiency and coloration efficiency ( $\eta$ ) of the thin film electrodes.

EC electrodes	Potential vs. Ag/AgCl / V	L*	a*	b*	T (at 584 nm) / %	$\tau_v$ / %	q / mC cm <sup>-2</sup>	Coulombic efficiency / %	$\eta$ (at 584 nm) / cm <sup>2</sup> ·C <sup>-1</sup>																																												
Fe-MEPE	0	61.3	-5.2	-22.7	5	29	2.43	97	496																																												
	2	88.6	-6.0	11.1	80	83				TiVO <sub>x</sub>	0	93.5	-4.5	12.6	86	85	26.76	98	2	-2	88.9	0.7	3.1	77	75	TMO-1	0	88.1	-2.3	10.0	74	72	10.49	87	-4	-2.5	92.3	-2.8	4.8	82	81	TMO-2	0	45.7	8.3	38.2	18	14	17.61	92	-24	-2.5	68.6
TiVO <sub>x</sub>	0	93.5	-4.5	12.6	86	85	26.76	98	2																																												
	-2	88.9	0.7	3.1	77	75				TMO-1	0	88.1	-2.3	10.0	74	72	10.49	87	-4	-2.5	92.3	-2.8	4.8	82	81	TMO-2	0	45.7	8.3	38.2	18	14	17.61	92	-24	-2.5	68.6	5.9	30.4	48	42												
TMO-1	0	88.1	-2.3	10.0	74	72	10.49	87	-4																																												
	-2.5	92.3	-2.8	4.8	82	81				TMO-2	0	45.7	8.3	38.2	18	14	17.61	92	-24	-2.5	68.6	5.9	30.4	48	42																												
TMO-2	0	45.7	8.3	38.2	18	14	17.61	92	-24																																												
	-2.5	68.6	5.9	30.4	48	42																																															

The electrochemical properties of the mixed metal oxide electrodes are investigated by CV measurements at 10 mV·s<sup>-1</sup> in a potential range from 2 V to 4 V vs. Li/Li<sup>+</sup>. Broad redox peaks indicate that as the voltage increases, the V<sup>5+</sup> is reduced to V<sup>4+</sup> for TiVO<sub>x</sub>, while Mn<sup>4+</sup> is reduced to Mn<sup>3+</sup> for the TMO electrodes. The broader peaks of the metal oxides, as compared to the Fe-MEPE, can be explained by slower processes, *e.g.*, redox reaction, ion de/insertion, and ad/desorption processes leading to longer response times. The cycle stability of the electrode materials is measured over 1,000 charging/discharging cycles at a current density of 50  $\mu$ A·cm<sup>-2</sup>. The charge density reaches approx. 27 mC·cm<sup>-2</sup>, 10 mC·cm<sup>-2</sup>, and 18 mC·cm<sup>-2</sup> with a high charge retention of 91%, 77%, and 75% for the **TiVO<sub>x</sub>**, **TMO-1**, and **TMO-2** electrodes, respectively. Additionally, TiVO<sub>x</sub> films are more stable than pure vanadium oxide films, which show a decrease in charge density after a few hundred cycles. [212] As the results obtained for the chosen ion storage materials indicate that only a small fraction of the charge density is necessary to completely decolor the Fe-MEPE (see charge density ratio shown on Tab. 19), it can be assumed that the contribution of these layers to the overall change in the transmittance of the ECDs will be even smaller. Moreover, the Coulombic efficiency is as high as 98%, 87%, and 92%, respectively. The  $\eta$  values for **TiVO<sub>x</sub>**, **TMO-1**, and **TMO-2** are 2 cm<sup>2</sup>·C<sup>-1</sup>, -4 cm<sup>2</sup>·C<sup>-1</sup>, and -24 cm<sup>2</sup>·C<sup>-1</sup> at 584 nm, respectively. Thus, Ti-doped vanadium and manganese oxides could be particularly useful as ion storage materials operating in conjunction with Fe-MEPE electrodes in ECDs due to their good ion storage capability.



### 3.2. ECDs containing Fe-MEPE and optically-passive mixed metal oxides

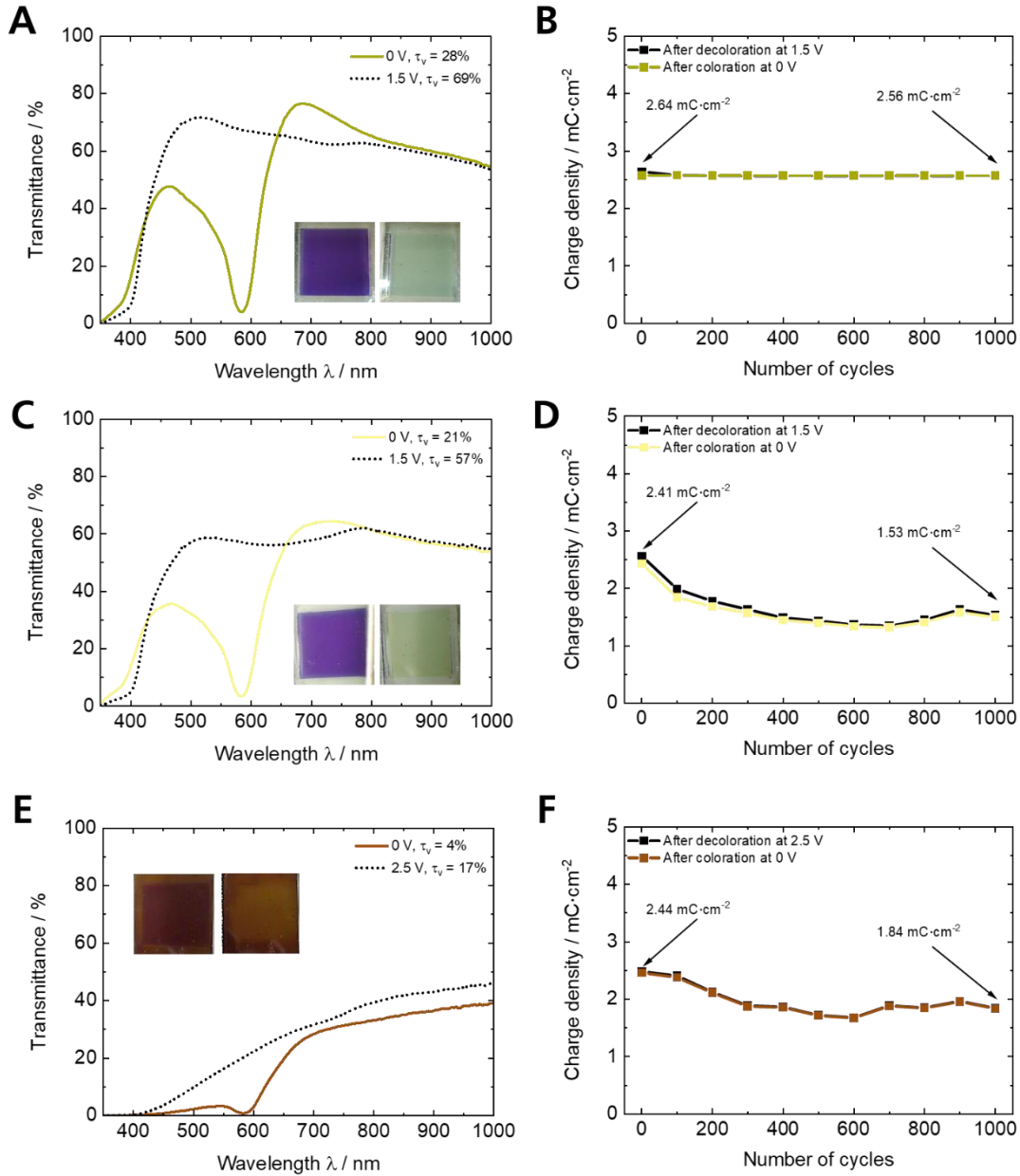
Using an ion storage layer with a substantially higher charge density with respect to the EC layer, only partial switching of the ion storage material is required to balance the charge generated at the WE corresponding to a complete switch of the EC material. Circumventing the requirement for complete switching of one active layer enables narrowing of the voltage window.

In the following section, the EC properties of **ECD2-1**, **ECD2-2**, and **ECD2-3** are described in detail. The relevant optical and electrochemical data are summarized in Tab. 19. The redox processes of the ECDs consisting of the Fe-MEPE and Ti-doped oxide electrodes occur as follows. During the decoloration (at 1.5 V for **ECD2-1** and **ECD2-2**, and 2.5 V for **ECD2-3**), the Fe-MEPE electrode is oxidized and the mixed metal oxide (counter) electrode is reduced. The charge balance is maintained by the insertion of  $\text{ClO}_4^-$  and  $\text{Li}^+$  ions in the MEPE and ion storage layer, respectively. The coloration (at 0 V) occurs *via* the reduction of the Fe-MEPE and oxidation of the mixed metal oxide electrodes. It is accompanied by the de-insertion of  $\text{ClO}_4^-$  and  $\text{Li}^+$  ions.

**Tab. 19:** Charge, density ratio (MEPE:ion storage layer), color coordinates ( $L^*a^*b^*$ ), transmittance (T) and visible light transmittance ( $\tau_v$ ) values, response times, charge densities (q) at 0 V (dark state) and 1.5 V or 2.5 V (bright state), respectively, as well as coloration efficiency ( $\eta$ ) of the ECDs.

ECD	Charge density ratio	Cell voltage / V	$L^*$	$a^*$	$b^*$	T (at 584 nm) / %	$\tau_v$ / %	Response time / s	q / $\text{mC}\cdot\text{cm}^{-2}$	$\eta$ (at 584 nm) / $\text{cm}^2\cdot\text{C}^{-1}$
ECD2-1 (Fe-MEPE/ $\text{TiVO}_x$ )	0.09	0	61.0	0.8	-18.4	4	28	15	2.57	476
		1.5	86.3	-8.9	13.3	67	69	3	2.61	
ECD2-2 (Fe-MEPE/ TMO-1)	0.23	0	54.2	2.1	-16.9	3	21	25	2.39	535
		1.5	80.3	-7.9	15.9	57	57	13	2.56	
ECD2-3 (Fe-MEPE/ TMO-2)	0.14	0	21.8	17.2	23.0	1	4	11	2.39	544
		2.5	47.4	8.0	39.8	20	17	9	2.44	

As shown in Fig. 29, the switching behavior of the three ECDs was investigated by means of *in situ* spectroelectrochemical measurements. The operating voltages of the ECDs were determined by increasing the cell voltage step-by-step. They were defined as the threshold voltages where the device showed no further changes in the transmittance at higher voltages. Fig. 29A illustrates the EC properties of **ECD2-1** (Fe-MEPE/ $\text{TiVO}_x$ ), which is blue-purple colored in the initial state. By applying a voltage of 1.5 V, the color of **ECD2-1** changes from blue-purple ( $\tau_v = 28\%$ ) to nearly colorless with a high bright state transmittance of  $\tau_v = 69\%$  in 3 s. In Fig. 29C, the transmission spectra in the dark and bright states of **ECD2-2** (Fe-MEPE/TMO-1) are depicted. The color changes in 13 s from blue-purple ( $\tau_v = 21\%$ ) to light yellow by applying a voltage of 1.5 V. By applying 2.5 V, **ECD2-3** (Fe-MEPE/TMO-2) switches from dark brown to brown in 9 s (Fig. S17). Unfortunately, the transmittance of **ECD2-3** changes from 4% to only 17% due to the deeply-colored **TMO-2** electrode.



**Fig. 29:** Spectroelectrochemical characterization of (A) **ECD2-1** (Fe-MEPE/TiVO<sub>x</sub>), (C) **ECD2-2** (Fe-MEPE/TMO-1), and (E) **ECD2-3** (Fe-MEPE/TMO-2). Photographic images of the ECDs in the dark (left) and bright (right) state before cycling are shown as insets. Cycling stability over 1,000 switching cycles of (B) **ECD2-1**, (D) **ECD2-2** and (F) **ECD2-3**.

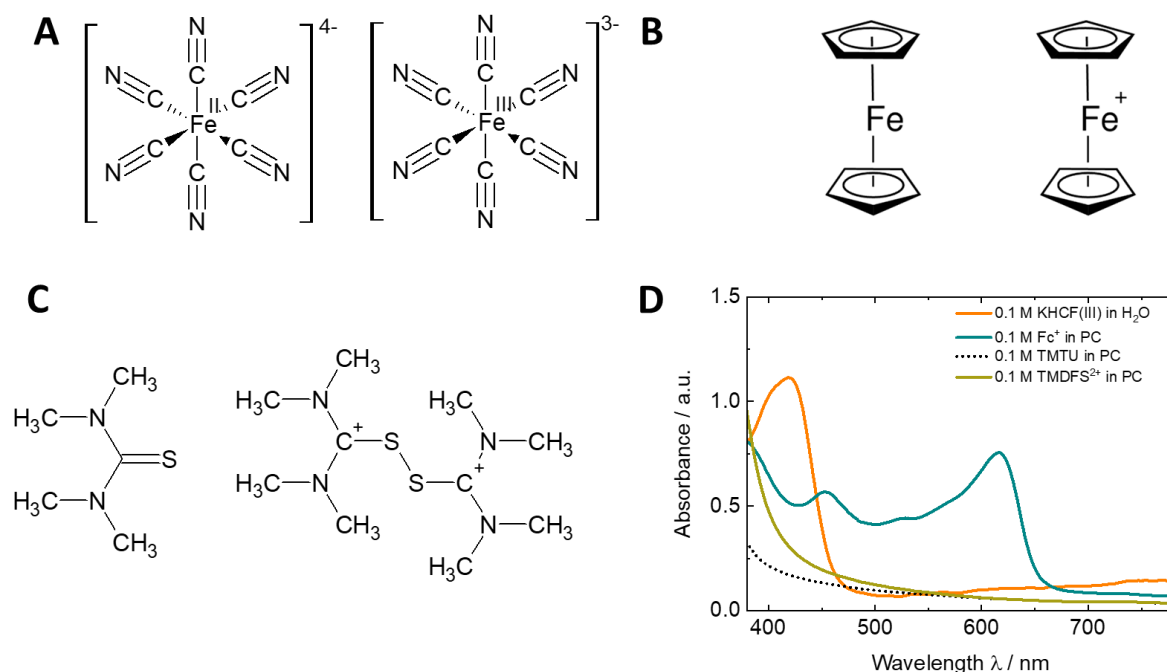
While discussing the characterization of the metal oxide films (see section 3.1), it was already mentioned that only a small fraction of the charge density is necessary to oxidize (discolor) the Fe-MEPE completely. This is demonstrated in Fig. S17, where the theoretical transmission spectra of the dark and bright states of the ECDs are calculated by considering both states of the single electrodes. Especially for **ECD2-3**, the optical effect of **TMO-2** is much smaller than can be expected from the spectroelectrochemical characterization. This is explained as the theoretical and experimental dark state match ( $\tau_v = 4\%$ ). Still, the theoretical bright state ( $\tau_v = 34\%$ ) is not achieved, which means that the **TMO-2** electrode is not fully reduced due to its high charge density of around 17.6  $\text{mC}\cdot\text{cm}^{-2}$ . Similar but less significant effects occur for **ECD2-1** and **ECD2-2**.

Finally, the cycling stability of the ECDs was measured over 1,000 switching cycles in an inert atmosphere. The results are illustrated in Fig. 29. **ECD2-1** shows a reversible color change from blue-purple to nearly colorless switching over 1,000 cycles between 0 V and 1.5 V without any signs of degradation. There is only a marginal decrease in the charge density for the decoloration from  $2.64 \text{ mC}\cdot\text{cm}^{-2}$  to  $2.56 \text{ mC}\cdot\text{cm}^{-2}$  (charge retention: approx. 9%). In contrast, the ECDs based on Fe-MEPE and TMO electrodes (**ECD2-2** and **ECD2-3**) show a decrease in charge density for the decoloration from  $2.56 \text{ mC}\cdot\text{cm}^{-2}$  to  $1.53 \text{ mC}\cdot\text{cm}^{-2}$  (60% charge retention) and  $2.44 \text{ mC}\cdot\text{cm}^{-2}$  to  $1.84 \text{ mC}\cdot\text{cm}^{-2}$  (75% charge retention), respectively. As the optical contrast is solely due to the Fe-MEPE electrode, the necessary charge density to completely brighten these ECDs matches that of the pristine Fe-MEPE electrode, and hence, the  $\eta$  value at 584 nm, *i.e.*,  $476 \text{ cm}^2\cdot\text{C}^{-1}$ ,  $535 \text{ cm}^2\cdot\text{C}^{-1}$ , and  $544 \text{ cm}^2\cdot\text{C}^{-1}$  for **ECD2-1**, **ECD2-2**, and **ECD2-3**, respectively match that of Fe-MEPE as well. This was expected as the ion storage electrodes were chosen with higher charge density and no significant color change. In addition, the charge retention of the ECDs matches that obtained for the pristine EC electrodes, *i.e.*, 91%, 77%, and 75% for **TiVO<sub>x</sub>**, **TMO-1**, and **TMO-2**, respectively. This study demonstrates the potential of binary mixed metal oxide materials like TiVO<sub>x</sub> and TMO for use as ion storage layers in MEPE-based ECDs. These ECDs show two distinct, individually addressable color states, with the color change pre-dominantly stemming from the Fe-MEPE, while the CEs are largely optically passive. Concerning future EC applications, *e.g.*, for architectural glazing, the aim is to increase the optical contrast and ensure the long-term stability of the ECDs, *e.g.*, by optimizing the charge balance of both electrodes in the device.

## 4. Simplification of the cell architecture using redox mediators

In this chapter, promising redox mediators are tested in type II ECDs with either Fe-MEPEs or Ni<sub>1-x</sub>O. Here, the EC characteristics of devices based on Fe-MEPE or Ni<sub>1-x</sub>O electrodes and a proprietary gel electrolyte containing various redox mediators are demonstrated. This approach simplifies the cell architecture by incorporating the charge balancing redox pair into the electrolyte instead of depositing a second redox-active layer as CE (four layers instead of five layers). Moreover, the combination of colorless redox mediators with Ni<sub>1-x</sub>O might lead to neutral tinting ECDs. The obtained results were published in ref. [103].

The structure and optical properties of the redox mediators are summarized in Fig. 30. KHCF(III) dissolved in H<sub>2</sub>O and ferrocenium in PC show orange and blue tints with distinct maxima at 419 nm and 616 nm, respectively (Fig. 30D). In contrast, TMTU does not exhibit any absorption in the visible region and the absorbance of TMFDS<sup>2+</sup> extends slightly into the UV range. It should be noted that the colors appear to be very intensive due to the long optical path through the cuvette (1 cm). However, the electrolyte thickness is reduced in the ECD to around 100 μm. Hence, the color impression is diminished. The redox potentials of KHCF(II)/(III), Fc<sup>0/+</sup>, and TMTU/TMFDS<sup>2+</sup> are 252 mV, [108] 201 mV, [260] and 450 mV vs. Ag/AgCl, [108] respectively.



**Fig. 30:** Chemical structures of the reduced (left) and oxidized (right) redox mediator species used in this work. (A) Potassium hexacyanoferrate(II)/(III) (KHCF(II)/(III)), (B) ferrocene/ferrocenium (Fc<sup>0/+</sup>), and (C) tetramethylthiourea/tetramethylformaminium disulfide (TMTU/TMFDS<sup>2+</sup>) accompanied by (D) the absorbance spectra of the redox electrolytes.

ECDs with combinations of cathodically-coloring Fe-MEPE or anodically-coloring Ni<sub>1-x</sub>O were prepared and characterized in detail and summarized in Tab. 20 and

Tab. 21. In the following, only the most promising ECDs towards neutral tinting and electrochemical stability are described.

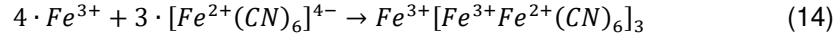
**Tab. 20:** Concentration (c), color coordinates ( $L^*a^*b^*$ ), transmittance (T) at 584 nm, visible light transmittance ( $\tau_v$ ), charge densities (q) of the dark and bright states, and coloration efficiency ( $\eta$ ) of the Fe-MEPE-based ECDs with different redox mediators in the electrolyte (1 M LiClO<sub>4</sub>/PC).

ECD	c (redox mediator) / mol·l <sup>-1</sup>	Voltage / V	L*	a*	b*	$\tau_v$ / %	T (at 584 nm) / %	$\eta$ (at 584 nm) / cm <sup>2</sup> ·C <sup>-1</sup>
ECD3-1 (ref)	0	0	54.5	-0.7	-25.8	25	4	533
		2	78.9	-7.9	5.2	75	75	
ECD3-2 (KHCF(III))	0.001	0	56.1	-1.4	-18.7	23	4	520
		1.5	87.3	-9.7	16.2	71	70	
ECD3-3 (KHCF(III))	0.01	0	53.1	16.0	-1.7	22	3	567
		1.5	85.5	15.8	34.1	68	68	
ECD3-4 (KHCF(III))	0.1	0	52.6	24.8	25.4	20	3	544
		1	81.7	21.1	59.9	60	60	
ECD3-5 (Fc-PF <sub>6</sub> )	0.1	0	48.6	6.5	-28.6	16	2	525
		0.8	70.7	11.8	0.4	42	36	
ECD3-6 (Fc-BF <sub>4</sub> )	0.1	0	49.4	9.0	-28.3	17	2	525
		0.8	72.6	11.6	1.6	44	36	
ECD3-7 (TMTU)	0.1	0	59.2	7.2	-29.1	25	3	572
		2	87.7	-9.2	11.6	72	70	

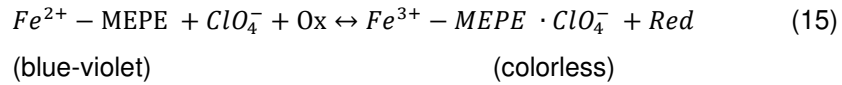
**Tab. 21:** Color coordinates ( $L^*a^*b^*$ ), transmittance (T) at 584 nm, visible light transmittance ( $\tau_v$ ), charge densities (q) of the dark (-2 V) and bright (2 V) states, and coloration efficiency ( $\eta$ ) of the Ni<sub>1-x</sub>O-based ECDs with TMTU/TMFDS<sup>2+</sup> as redox mediator in the electrolyte (1 M LiClO<sub>4</sub>/PC).

ECD	molar ratio TMTU:TMFDS <sup>2+</sup>	Voltage / V	L*	a*	b*	$\tau_v$ / %	T (at 584 nm) / %	q mC·cm <sup>-2</sup>	$\eta$ (at 584 nm) / cm <sup>2</sup> ·C <sup>-1</sup>
ECD3-8 (ref)	---	2	70.2	3.2	17.4	61	64	3.78	51
		-2	84.0	-0.3	15.0	37	41		
ECD3-9	1:0	2	66.6	4.7	18.2	65	68	3.04	59
		-2	81.9	1.3	16.0	42	45		
ECD3-10	1:0.1	2	67.1	3.9	17.2	70	73	4.04	85
		-2	86.6	-0.6	14.9	38	41		
ECD3-11	1:1	2	71.5	2.3	16.3	65	68	3.16	51
		-2	84.2	-1.7	13.0	44	47		

The reason for this selected view is on the one hand due to the high concentrations of KHCF(III), which led to the formation of PB (proven by IR in Fig. S20D according to equation (14)), and the deeply colored electrolytes using both Fc<sup>+</sup> derivatives.

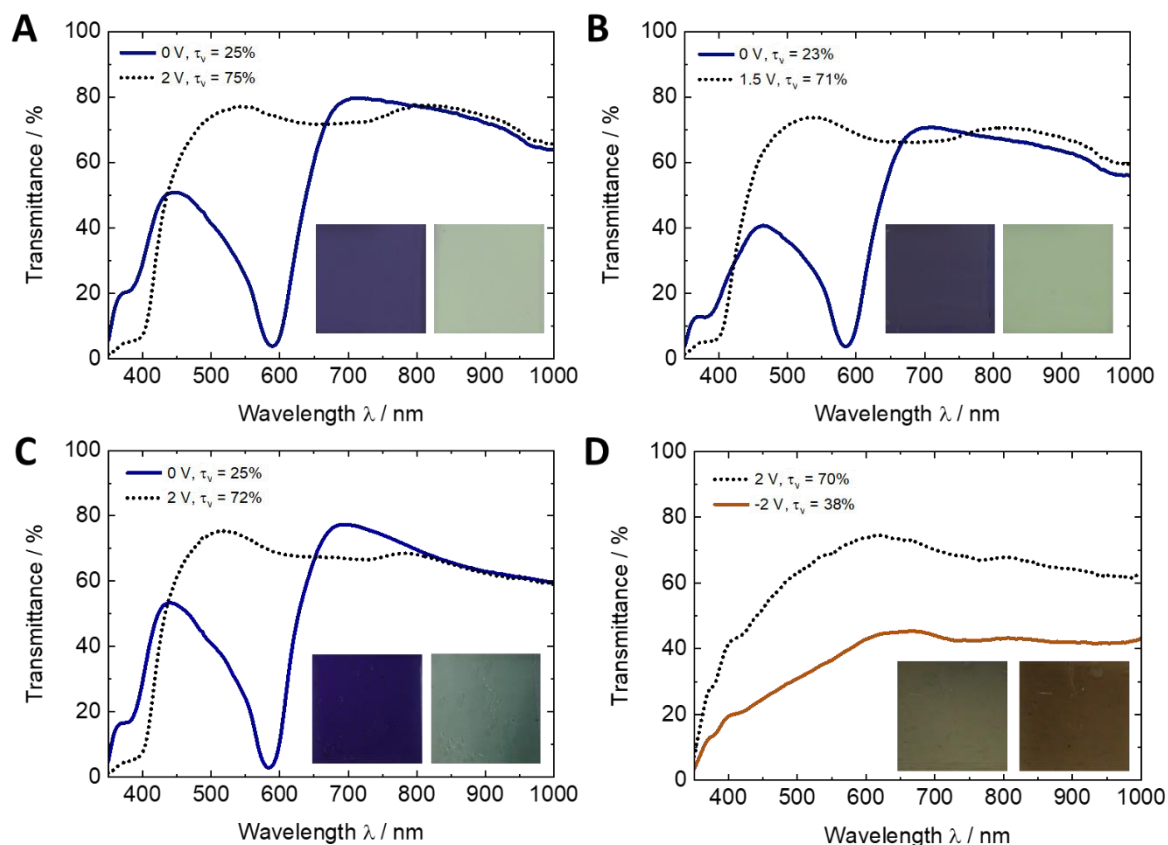


The general mechanism for the decoloration of Fe-MEPE-based ECDs containing a redox electrolyte is given in equation (15):



Where Ox is KHCF(III), Fc<sup>+</sup> or 1/2·TMFDS<sup>2+</sup>, while Red is KHCF(II), Fc<sup>0</sup>, or TMTU. During the decoloration process of the ECD, Fe-MEPE is oxidized at the WE, and ClO<sub>4</sub><sup>-</sup> ions are inserted into the MEPE layer. Simultaneously, the redox mediator is reduced at the CE to counterbalance the redox reaction during insertion/de-insertion of ClO<sub>4</sub><sup>-</sup> ions and electrons into/from the EC layer. The coloration of the ECD occurs by reversing the redox reaction. The necessary voltage of the device depends on the redox mediator because it defines the electrochemical potential at the CE.

The transmission spectra in Fig. 31A show that the as-prepared **ECD3-1** has a blue tint (L\* = 54.5, a\* = -0.7, b\* = -25.8) due to the apparent MLCT band of Fe-MEPE with a peak maximum at 584 nm. It was possible to decolor (oxidize) the Fe-MEPE electrode completely even without a redox mediator in the electrolyte as the FTO electrode itself can provide a certain ion storage capacity. [246] By applying a voltage of 2 V (for 5 min), the ECD switched to the colorless state (L\* = 78.9, a\* = -7.9, b\* = 5.2). The τ<sub>v</sub> changes from 25% (dark) to 75% (bright), consistent with the pristine Fe-MEPE electrode characterized in Tab. S1. However, the reversibility of the redox process was poor, *i.e.*, a completely darkened state of Fe-MEPE could not be obtained after one cycle even with a 30 min long potentiostatic step at 0 V. In the subsequent cycles, the contrast decreased further with a declining current density and drawing out response times for decoloration and coloration (Fig. 32A). This is probably due to either the low charge density of the FTO layer or an over-charging of the FTO electrode, leading to an irreversible reduction of SnO<sub>2</sub> to metallic Sn. [246] Upon addition of KHCF(III), the b\* values increases from -25.9 to -18.7 in the dark state and from 5.2 to 16.2 in the bright state (Fig. 31B).



**Fig. 31:** Spectroelectrochemical measurements of (A) **ECD3-1** (reference cell), (B) **ECD3-2** (0.001 M K<sub>2</sub>CrF<sub>6</sub>) in the 1 M LiClO<sub>4</sub>/H<sub>2</sub>O electrolyte), (C) **ECD3-7** (0.1 M TMTU/TMFDS<sup>2+</sup> in 1 M LiClO<sub>4</sub>/PC), and (D) **ECD3-10** (0.1 M, molar ratio TMTU/TMFDS<sup>2+</sup> = 1:0.1) and the corresponding photographs indicating the color changes.

A further redox mediator was tested in combination with Fe-MEPE, which was added in its oxidized state, *i.e.*, NOBF<sub>4</sub>-oxidized TMTU. The use of the redox mediator TMTU/TMFDS<sup>2+</sup> (0.1 M, molar ratio TMTU:TMFDS<sup>2+</sup> 1:10) in 1 M LiClO<sub>4</sub>/PC in combination with Fe-MEPE is a step towards a colorless bright state. Fig. 31C shows that **ECD3-7** has a blue tint ( $L^* = 59.2$ ,  $a^* = 7.2$ ,  $b^* = -29.1$ ) in the dark state and switches completely at 2 V ( $L^* = 87.7$ ,  $a^* = -9.2$ ,  $b^* = 11.6$ ). The visible light transmittance changes from  $\tau_v = 25\%$  (dark state) to 72% (bright state). When comparing the first five switching cycles, the peak current density decreases for **ECD3-7**. These results demonstrate that a better understanding of the reaction mechanism of the TMTU/TMFDS<sup>2+</sup> redox mediator couple is necessary for further improvement, particularly in terms of response time and cycling stability.

By changing the electrolyte from an aqueous (Fig. 32A,B) to a non-aqueous system (Fig. 32C,D), the loss current is significantly lowered from 600 to 70  $\mu\text{A}\cdot\text{cm}^{-2}$ . This can be explained by the diminishing of the hydration shell in size around the Li<sup>+</sup> ion as described in the ref. [261] and, therefore, a faster ion diffusion in the less polar solvent (PC).





The best EC performance in terms of change in  $\tau_v$  for the  $\text{Ni}_{1-x}\text{O}$  based ECD was obtained for **ECD3-10** (Fig. 31D). Here, the  $\tau_v$  value changes from 38% (dark) to 70% (bright) with a color change going from nearly colorless ( $L^* = 86.6$ ,  $a^* = -0.6$ ,  $b = 14.9$ ) to brown ( $L^* = 67.1$ ,  $a^* = 3.9$ ,  $b = 17.2$ ) as listed in

Tab. 21. The bright state of this ECD is comparable to the bright state of the pristine  $\text{Ni}_{1-x}\text{O}$  electrode ( $L^* = 86.1$ ,  $a^* = 1.6$ ,  $b^* = 13.6$ ), while the dark state still has a higher transmittance. This indicates that the  $\text{Ni}_{1-x}\text{O}$  electrode is only partially oxidized, according to the calculated charge density ( $q = 4.04 \text{ mC}\cdot\text{cm}^{-2}$ ) from the potentiostatic measurements in Fig. 32D. leading to a coloration efficiency of  $85 \text{ cm}^2\cdot\text{C}^{-1}$  at 584 nm. It seems that for the tested TMTU/TMDS<sup>2+</sup> ratios, 1:0.1 best fits the  $\text{Ni}^{2+}/\text{Ni}^{3+}$  ratio in the as-prepared  $\text{Ni}_{1-x}\text{O}$  electrode.

## VI. Summary and Outlook

While the field of electrochromic (EC) materials and devices (ECDs) continues to advance in terms of color palette and understanding the underlying mechanism, several scientific and technological challenges need to be addressed by optimizing the materials and understanding the electrochemical interplay of these materials in full cells. The main issue here is to further improve the EC profile for color neutrality and cycling stability in order to commercialize dimmable EC products. The transparent conductive substrates used in this work (FTO and ultra-thin ITO glass) have high visible light transmittance ( $\tau_v > 85\%$ ) and low sheet resistance ( $< 25 \Omega \cdot \text{sq}^{-1}$ ). In addition, the  $\text{Li}^+$ -containing gel electrolyte has sufficient ionic conductivity ( $2.8 \cdot 10^{-4} \text{ S} \cdot \text{cm}^{-1}$  at  $25 \text{ }^\circ\text{C}$ ), so the investigated ECDs could achieve a fast response (required ionic conductivity is between  $10^{-3}$  and  $10^{-7} \text{ S} \cdot \text{cm}^{-1}$ ).

This work shows that the combination of cathodically-coloring Fe-MEPE with anodically-coloring non-stoichiometric nickel oxide ( $\text{Ni}_{1-x}\text{O}$ ) electrodes (prepared by the *National Institute of Chemistry* in Ljubljana, Slovenia) can be used in neutral-coloring type III ECDs. The Fe-MEPE/ $\text{Ni}_{1-x}\text{O}$  ECD with the underbalanced CE (**ECD1-1**, 2: 1) and the balanced configuration (**ECD1-2**, 1: 1) are both nearly neutrally-colored (**ECD1-1**:  $a^* = -6.7$ ,  $b^* = 8.8$ ; ECD1-2:  $a^* = -9.0$ ,  $b^* = 10.1$ ) in the bright state with a  $\tau_v$  of almost 70%. Due to the overbalancing of the CE (**ECD1-3**, 1:3), a deviation ( $a^* = -2.8$ ,  $b^* = 19.9$ ) from the neutral coloration occurred here. The balanced as well as the overbalanced ECD configurations show high electrochemical cycling stability (over 1,000 potentiostatic switching cycles). In general, the overbalanced configuration offers the advantage of a smaller operating voltage range ( $-1 \text{ V} \leftrightarrow 2.5 \text{ V}$  to  $-1 \text{ V} \leftrightarrow 1.5 \text{ V}$ ), *i.e.*, avoiding possible electrochemical degradation of the EC materials, electrolyte, or conductive layers. By using a Li RE in the full cell, insights into the optimal matching of electrochemical and optical properties between the two electrodes are obtained to achieve more stable ECDs. Thereby, the redox potentials of both EC electrodes (Fe-MEPE and  $\text{Ni}_{1-x}\text{O}$ ) can be measured during operation. The incomplete decolorization of **ECD1-1** can be explained by the measured electrode potentials (below the required  $4 \text{ V vs. Li/Li}^+$ ), excluding side reactions and degradation at both electrodes. The results demonstrate the importance of using balanced and (slightly) overbalanced ECD configurations with complementary-coloring EC electrodes to achieve high cycling stability and fast switching at low operating voltages. Therefore, this three-electrode configuration provides an excellent method for *in situ* electrochemical characterization of the individual EC electrodes to better understand the redox processes during device operation and to further improve the optical contrast and cycle stability of ECDs.

The Fe-MEPE/ $\text{Ni}_{1-x}\text{O}$  combination was tested on flexible ultrathin ITO glass (**ECD1-4**). Here, by applying a low voltage of  $-1 \text{ V} \leftrightarrow 2.5 \text{ V}$ , the MEPE/ $\text{Ni}_{1-x}\text{O}$  ECDs can be reversibly switched from a colored ( $L^* = 35.6$ ,  $a^* = 19.4$ ,  $b^* = -26.7$ ) to a nearly colorless ( $L^* = 78.5$ ,  $a^* = -14.0$ ,  $b^* = 21.3$ ) state. This is accompanied by a change in  $\tau_v$  from 6% to 53%. The ECDs exhibit fast response and good cycling stability (5% loss of optical contrast over 100 switching cycles).

To further improve color neutrality and cycling stability, ECDs combining Fe-MEPE and mixed metal oxides as ion storage layers were investigated. Titanium manganese oxide (TMO, Fraunhofer IST) and titanium vanadium oxide ( $\text{TiVO}_x$ , EControl-Glas GmbH & Co. KG) electrodes are compared for use as optically-passive ion storage layers.  $\text{TiVO}_x$  with a maximum charge density of approx.  $27 \text{ mC} \cdot \text{cm}^{-2}$  and

## Summary and Outlook

a coloration efficiency of  $\eta = 2 \text{ cm}\cdot\text{C}^{-1}$  at 584 nm shows a color change from yellow to light gray at 2 V vs. Ag/AgCl, while the slightly anodically-coloring Ti-rich TMO ( $10.5 \text{ mC}\cdot\text{cm}^{-2}$ ,  $\eta_{584 \text{ nm}} = -4 \text{ cm}\cdot\text{C}^{-1}$ ) switches from light yellow to colorless at -2.5 V vs. Ag/AgCl. These materials show only a slight change in  $\tau_v$  value from 85% to 75% and from 72% to 81%, respectively, thus reaching the requirements for highly transmissive optical-passive ion storage layers. The ECDs with Fe-MEPE in combination with **TiVO<sub>x</sub>** (**ECD2-1**) and **TMO-1** (**ECD2-2**) are blue-purple in the dark state (0 V) and turn colorless by applying a voltage of 1.5 V, changing the  $\tau_v$  value from 28% to 69% and from 21% to 57% in 3 s and 13 s, respectively. The ECDs show fast responses and high cyclability over more than 100 cycles.

In the last section, the simplification of cell architecture by using redox mediators shows that different redox mediators (KHCF(III), Fc-PF<sub>6</sub>, Fc-BF<sub>4</sub>, and TMTU) can be used in type II ECDs (4 instead of 5 layers) consisting of Fe-MEPE or Ni<sub>1-x</sub>O thin film electrodes. The combination of KHCF(III) with Fe-MEPE has a low cycling stability due to the electrochemical formation of Prussian blue (PB). This side reaction is undesirable as it decreases the optical contrast. It can be avoided by using Fc<sup>+</sup> (**ECD3-5/6**) or TMTU-based (**ECD3-7**) redox mediators, which exhibit reversible redox behavior. A high  $\tau_v$  value of 72% is obtained for the use of TMTU. Low concentrations (<0.1 M) of redox mediators decrease the cell voltage for complete switching without affecting the optical properties of the ECDs. The redox couple TMTU/TMFDS<sup>2+</sup> (molar ratio of 1:0.1 in 1 M LiClO<sub>4</sub>/PC as electrolyte) works well in combination with Ni<sub>1-x</sub>O electrodes (**ECD3-10**), with a change in  $\tau_v$  value from 38% (colored at 2 V,  $L^* = 67.1$ ,  $a^* = 3.9$ ,  $b^* = 17.2$ ) to 70% at (decolored at -2 V,  $L^* = 86.6$ ,  $a^* = -0.6$ ,  $b^* = 17.2$ ). This result implies that incorporating redox mediators into the electrolyte is an effective means to simplify the cell assembly and color neutrality can be obtained with one optically active WE and a color-neutral redox mediator. Moreover, the combination of Ni<sub>1-x</sub>O and the colorless TMTU/TMFDS<sup>2+</sup> redox mediator is a potential candidate to obtain neutrally colored ECDs.

It is shown that the lab-sized FTO- and ultra-thin ITO-glass-based ECDs are very attractive for energy-efficient EC applications, *e.g.*, in architectural or automotive glazing, aircraft, ships, home appliances and displays. To monitor the EC performance and to prevent diverging electrode potentials during the switching process, the studied three-electrode configuration can help to extend the cycle stability as well as to improve the charge balancing of dimmable applications. The studied ECDs display a route towards neutral tint, *e.g.*, EC active Ni<sub>1-x</sub>O, optically-inactive mixed metal oxides, and colorless redox mediators. Nevertheless, color neutrality should be further improved to meet the requirements for industrial applications. For future work, a scale-up process from lab-sized (few cm<sup>2</sup>) to prototype (few m<sup>2</sup>) ECDs will be necessary.

## VII. Zusammenfassung und Ausblick

Während das Gebiet der elektrochromen (EC) Materialien in Bezug auf die Farbpalette und das Verständnis des zugrundeliegenden Mechanismus weiter erforscht wird, bleiben einige wissenschaftliche und technologische Herausforderungen bestehen, die sowohl durch Optimierung der EC Materialien als auch durch tiefergehendes Verständnis des elektrochemischen Zusammenspiels dieser Materialien in elektrochromen Elementen (ECD) angegangen werden müssen. Hier geht es vor allem darum, das EC-Profil in Bezug auf Farbneutralität und Stabilität weiter zu verbessern, um kostengünstige und energieeffiziente Produkte zu kommerzialisieren. Die in der Arbeit verwendeten Substrate (FTO-Glas und ultradünnes ITO-Glas) weisen einen hohen Transmissionsgrad ( $\tau_v > 85\%$ ) und einen geringen Oberflächenwiderstand ( $< 25 \Omega \cdot \text{sq}^{-1}$ ) auf. Zusätzlich hat der eingesetzte  $\text{Li}^+$ -haltige Elektrolyt ausreichend Ionenleitfähigkeit ( $2.8 \cdot 10^{-4} \text{ S} \cdot \text{cm}^{-1}$  bei  $25^\circ\text{C}$ ), so dass die untersuchten ECDs schnelle Schaltzeiten erreichen konnten (erforderliche Ionenleitfähigkeit:  $10^{-3}$  und  $10^{-7} \text{ S} \cdot \text{cm}^{-1}$ ).

Die Ergebnisse dieser Arbeit zeigen, dass die Kombination aus kathodisch färbenden Fe-MEPE-Elektroden mit anodisch färbenden  $\text{Ni}_{1-x}\text{O}$  Gegenelektroden (*National Institute of Chemistry*, Ljubljana, Slovenia) in neutralfärbenden Typ III ECDs verwendet werden kann. Sowohl die Fe-MEPE/ $\text{Ni}_{1-x}\text{O}$  ECD mit einer unterdimensionierten Gegenelektrode (**ECD1-1**, 2: 1) und die balancierte Konfiguration (**ECD1-2**, 1: 1) sind beide im entfärbten Zustand mit einem  $\tau_v$  von fast 70 % zudem fast neutral gefärbt (**ECD1-1**:  $a^* = -6,7$ ,  $b^* = 8,8$ ; **ECD1-2**:  $a^* = -9,0$ ,  $b^* = 10,1$ ). Durch die Überdimensionierung der Gegenelektrode (**ECD1-3**, 1:3) entstand hier eine Abweichung ( $a^* = -2,8$ ,  $b^* = 19,9$ ) von der geforderten Neutralfärbung. Die balancierte sowie die überdimensionierte ECD-Konfiguration zeigen eine hohe elektrochemische Zyklenstabilität (über 1.000 potentiostatische Schaltvorgänge). Im Allgemeinen bot die überdimensionierte Konfiguration den Vorteil eines kleineren Spannungsfensters ( $-1 \text{ V} \leftrightarrow 1,5 \text{ V}$  statt  $-1 \text{ V} \leftrightarrow 2,5 \text{ V}$ ), d.h. der Vermeidung einer möglichen Degradation der EC Materialien, des Elektrolyten oder der leitfähigen Schichten. Durch den Einsatz einer Li RE in der ECD wurden Erkenntnisse über die optimale Anpassung der elektrochemischen und optischen Eigenschaften zwischen beiden Elektroden erhalten. Hierdurch konnten die Redoxpotentiale beider EC Elektroden (Fe-MEPE und  $\text{Ni}_{1-x}\text{O}$ ) während des Schaltvorgangs gemessen werden. Das unvollständige Entfärben von **ECD1-1** kann durch die gemessenen Elektrodenpotentiale (unter den geforderten 4 V vs.  $\text{Li}/\text{Li}^+$ ) erklärt werden, wobei Nebenreaktionen und Degradation an beiden Elektroden ausgeschlossen sind. Die Ergebnisse zeigen, wie wichtig es ist, balancierte und (leicht) überdimensionierte Konfigurationen mit komplementär färbenden Elektroden für stabil schaltende ECDs mit niedriger Zellenspannung zu verwenden. Somit bietet die Drei-Elektroden-Konfiguration eine hervorragende Methode zur elektrochemischen *in situ* Charakterisierung der einzelnen EC-Elektroden, um die Redoxprozesse während des Schaltvorgangs besser zu verstehen und den optischen Kontrast und die Stabilität von ECDs weiter zu verbessern.

Die Fe-MEPE/ $\text{Ni}_{1-x}\text{O}$  Kombination wurde auf flexibles ultradünnes ITO-Glas übertragen (**ECD1-4**). Hier schaltet die MEPE/ $\text{Ni}_{1-x}\text{O}$ -ECD durch das Anlegen einer niedrigen Spannung von  $-1 \text{ V} \leftrightarrow 2,5 \text{ V}$  reversibel von einem gefärbten Zustand ( $L^* = 35,6$ ,  $a^* = 19,4$ ,  $b^* = -26,7$ ) in einen nahezu farblosen Zustand ( $L^* = 78,5$ ,  $a^* = -14,0$ ,  $b^* = 21,3$ ). Dies geht mit einer Änderung des  $\tau_v$ -Wertes von 6% auf 53% einher. Die ECD weist schnelle Schaltzeiten sowie eine gute Zyklenstabilität (5% Verlust des optischen Kontrasts über 100 Schaltzyklen) auf.

Um die Farbneutralität und Langzeitstabilität weiter zu verbessern, werden ECDs aus Fe-MEPE Arbeits- und mischmetalloxidische Ionenspeicherelektroden untersucht. Titan-Manganoxid (TMO)-Elektroden (vom Fraunhofer IST) wurden mit kommerziell erhältlichem Titan-Vanadiumoxid ( $\text{TiVO}_x$ , EControl-Glas GmbH & Co. KG) zur Verwendung als optisch passive Ionenspeicherschichten verglichen.  $\text{TiVO}_x$  mit einer maximalen Ladungsdichte von ca.  $27 \text{ mC}\cdot\text{cm}^{-2}$  und einer Färbefizienz von  $\eta_{584 \text{ nm}} = 2 \text{ cm}\cdot\text{C}^{-1}$  weist eine Farbänderung von gelb nach hellgrau bei  $2 \text{ V vs. Ag/AgCl}$ , während das anodisch färbende Ti-reichen TMO ( $10,5 \text{ mC}\cdot\text{cm}^{-2}$ ,  $\eta_{584 \text{ nm}} = -4 \text{ cm}\cdot\text{C}^{-1}$ ) bei  $-2,5 \text{ V vs. Ag/AgCl}$  von hellgelb nach farblos schaltete. Diese Materialien zeigen nur eine geringe Änderung des  $\tau_v$ -Wertes von 85 % auf 75 % bzw. von 72 % auf 81 %, wodurch die Anforderungen an hoch transmissive optisch-passive Ionenspeicherschichten erfüllt sind. Die ECDs mit Fe-MEPE in Kombination mit  $\text{TiVO}_x$  (**ECD2-1**) und **TMO-1 (ECD2-2)** sind im gefärbten Zustand (0 V) blau-lila gefärbt und werden durch Anlegen einer Zellspannung von 1,5 V farblos, wobei sich der  $\tau_v$ -Wert in 3 s bzw. 13 s von 28 % auf 69 % und von 21 % auf 57 % ändert. Die ECDs zeigen schnelle Reaktionen und eine gute Reversibilität (> 100 Zyklen).

Kapitel 4 befasste sich mit der Vereinfachung der Zellarchitektur durch Verwendung von Redoxmediatoren. Diese Arbeit zeigt, dass verschiedene Redoxmediatoren (KHCF (III), Fc-PF<sub>6</sub>, Fc-BF<sub>4</sub> und TMTU) in Typ II ECDs (4 statt 5 Schichten) verwendet werden können, die aus Fe-MEPE oder  $\text{Ni}_{1-x}\text{O}$  Elektroden bestehen. Die Kombination von KHCF(III) mit Fe-MEPE-Elektroden hat aufgrund der Bildung von Preußisch Blau (PB) eine geringe Zyklenstabilität. Diese Nebenreaktion ist unerwünscht, da sie den optischen Kontrast vermindert. Sie kann durch die Verwendung von Redoxmediatoren auf Fc<sup>+</sup>- (**ECD3-5/6**) oder TMTU-Basis (**ECD3-7**) vermieden werden, da diese ein reversibles Redoxverhalten aufweisen. Für den Einsatz von TMTU wurde ein hoher  $\tau_v$ -Wert von 72 % ( $L^* = 87,7$ ,  $a^* = -9,2$ ,  $b^* = 11,6$ ) erhalten. Niedrige Konzentrationen von Redoxmediatoren (< 0,1 M) verringern die Zellspannung, ohne die optischen Eigenschaften der ECDs zu beeinflussen. TMTU/TMFDS<sup>2+</sup> (Molverhältnis von 1:0,1 in 1 M LiClO<sub>4</sub>/PC als Elektrolyt) wurde erfolgreich als Redoxmediator in Kombination mit  $\text{Ni}_{1-x}\text{O}$ -Elektroden eingesetzt, wobei eine Änderung des  $\tau_v$ -Wertes von 38 % (gefärbt bei 2 V,  $L^* = 67,1$ ,  $a^* = 3,9$ ,  $b^* = 17,2$ ) auf 70 % bei (entfärbt bei -2 V,  $L^* = 86,6$ ,  $a^* = -0,6$ ,  $b^* = 17,2$ ) erzielt wurde. Dieses Ergebnis impliziert, dass der Einsatz von Redoxmediatoren in den Elektrolyten ein effektives Mittel zur Vereinfachung des Zellaufbaus sind und Farbneutralität mit einer optisch aktiven WE und einem farbneutralen Redoxmediator erreicht werden kann. Ein exzellentes Beispiel ist hierfür die Kombination von  $\text{Ni}_{1-x}\text{O}$  und des farblose TMTU/TMFDS<sup>2+</sup>-Redoxmediator.

Es wurde gezeigt, dass FTO- und ultradünnen ITO-Glas-basierte ECDs sehr attraktiv für energieeffiziente EC-Anwendungen sind, z. B. in Architektur- oder Automobilverglasungen, Flugzeugen, Schiffen, Haushaltsgeräten und Displays. Um die Änderung der Elektrodenpotentiale während des Schaltvorgangs zu überwachen, kann die Drei-Elektroden-Konfiguration helfen, die Zyklenstabilität zu verbessern. Die untersuchten ECDs zeigen einen Weg zur Farbneutralität auf, z.B. EC-aktives  $\text{Ni}_{1-x}\text{O}$ , optisch inaktive Mischmetalloxide und farblose Redoxmediatoren. Dennoch sollte die Farbneutralität weiter verbessert werden, um die Anforderungen für industrielle Anwendungen zu erfüllen und für zukünftige Arbeiten ist ein Scale-up-Prozess von Laborgröße (wenige  $\text{cm}^2$ ) zu Prototypen (wenige  $\text{m}^2$ ) ECDs notwendig.

## Selbstständigkeitserklärung

Hiermit erkläre ich, dass ich die vorliegende Arbeit selbstständig verfasst, keine anderen als die angegebenen Quellen und Hilfsmittel verwendet und die Arbeit keiner anderen Prüfungsbehörde zur Erlangung eines akademischen Grades vorgelegt habe.

Würzburg, 20. September 2021

.....

Lukas Niklaus

## Acknowledgment

Firstly, I would like to thank my doctoral supervisor, Prof. Dr. Gerhard Sextl, for the opportunity to carry out my Ph.D. at the Fraunhofer Institute for Silicate Research (ISC) in Würzburg.

Besides my doctoral supervisor, I would like to express my sincere gratitude to my advisors Dr. Uwe Posset and Dr. Marco Schott for the continuous support of my Ph.D. study and related research, for their patience, motivation, and immense knowledge. Their guidance helped me during the research and writing of this thesis. They provided me with the tools needed to choose the right direction and successfully complete my dissertation. In addition, my sincere gratitude to Dr. Guinevere Giffin, whose expertise was invaluable in formulating the research questions and methodology. Your insightful feedback pushed me to sharpen my thinking and brought my work to a higher level.

A sincere note of thanks to Christine Müller, Annalena Götz, and Vilija Anfimovaite for helping in carrying out cell assembly and electrochemical measurements. Furthermore, I would like to thank my Bachelor student Björn Ewald, who worked on optimizing Fe-MEPE and its combination with non-stoichiometric nickel oxide. I would like to thank Elena Fleder and Werner Stracke for the SEM measurements and Angelika Schmitt for performing the XPS measurements.

A big thanks to all colleagues of the Fraunhofer R&D Center for Electromobility Bavaria (FZEB), especially the OE323 and the Ph.D. students on electrochemistry. I thank Sven Macher for the stimulating discussions we have had in the last years.

The synthesis and the deposition of the  $\text{Ni}_{1-x}\text{O}$  films were carried out at the Department of Materials Chemistry at the National Institute of Chemistry (NIC) in Ljubljana, Slovenia. Moreover, my thanks go to Dr. Ivan Jerman and Dr. Mohor Mihelčič for their cooperation and support for the publications. The synthesis and deposition of the  $\text{TiVO}_x$  and TMO electrodes was carried out at EControl-Glas GmbH & Co. KG and the Fraunhofer IST, respectively. Here, I thank Dr. Daniel Reichert as well as Dr. Stephan Ulrich and Jonas Subel for their work and support. Furthermore, I would like to thank Dr. Manuela Junghähnel and Jasper Westphalen (Fraunhofer FEP) for providing the ultra-thin ITO glass samples.

I gratefully acknowledge the funding received towards my Ph.D. from FZEB (funded by the Bavarian Ministry of Economic Affairs and Media, Energy and Technology (StMWi)), Flex-G (funded by the German Federal Ministry for Economic Affairs and Energy (BMWi)), and ECWin2.0 (funded by the Federal Ministry of Education and Research (BMBF)).

Finally, my deep and sincere gratitude to my wife, parents, and siblings for their continuous and unparalleled love, help and support.

## References

- [1] United Nations, The Paris Agreement. <https://unfccc.int/process-and-meetings/the-paris-agreement/the-paris-agreement> (accessed 9 September 2020).
- [2] F. Krause, H. Bossel, K.-F. Müller-Reißmann, *Energie-Wende: Wachstum und Wohlstand ohne Erdöl und Uran; ein Alternativ-Bericht des Öko-Instituts/Freiburg*, S. Fischer u.a, Frankfurt a.M., 1980.
- [3] S. Giacobelli (Ed.), *Die Energiewende aus wirtschaftssoziologischer Sicht: Theoretische Konzepte und empirische Zugänge*, Springer, Wiesbaden, 2017.
- [4] T.F. Stocker, D. Qin, G.-K. Plattner, M. Tignor, S.K. Allen, J. Boschung, A. Nauels, Y. Xia, V. Bex, P.M. Midgley, IPCC, 2018: *Climate Change 2018: The Physical Science Basis. Contribution of Working Group I to the Fifth Assessment Report of the Intergovernmental Panel on Climate Change*, Cambridge, United Kingdom and New York, NY, USA, 2018.
- [5] H. Akbari, C. Cartalis, D. Kolokotsa, A. Muscio, A.L. Pisello, F. Rossi, M. Santamouris, A. Synnef, N.H. Wong, M. Zinzi, Local climate change and urban heat island mitigation techniques - the state of the art, *J. Civ. Eng. Manag.* 22 (2015) 1–16.  
<https://doi.org/10.3846/13923730.2015.1111934>.
- [6] Department of Economic and Social Affairs, Population Division, *World Population Prospects: The 2015 Revision, Methodology of the United Nations Population Estimates and Projections. Working Paper No. ESA/P/WP.242.*, 2015.
- [7] M.R. Raupach, Carbon cycle: Pinning down the land carbon sink, *Nat. Clim. Change* 1 (2011) 148. <https://doi.org/10.1038/nclimate1123>.
- [8] U.S. Department of Commerce, *Trends in Atmospheric Carbon Dioxide*, 2020.  
<https://www.esrl.noaa.gov/gmd/ccgg/trends/index.html>.
- [9] J. Fricke, W.L. Borst, *Essentials of Energy Technology: Sources, Transport, Storage, Conservation*, Wiley-VCH Verlag GmbH & Co. KGaA, Hoboken, 2013.
- [10] U.S. Energy Information Administration, *Annual Energy Outlook 2020: with projections to 2050, 2020*. <https://www.eia.gov/aeo>.
- [11] N. DeForest, A. Shehabi, G. Garcia, J. Greenblatt, E. Masanet, E.S. Lee, S. Selkowitz, D.J. Milliron, Regional performance targets for transparent near-infrared switching electrochromic window glazings, *Build. Environ.* 61 (2013) 160–168.  
<https://doi.org/10.1016/j.buildenv.2012.12.004>.
- [12] A. Cannavale, U. Ayr, F. Martellotta, Innovative electrochromic devices: Energy savings and visual comfort effects, *Energy Procedia* 148 (2018) 900–907.  
<https://doi.org/10.1016/j.egypro.2018.08.096>.
- [13] S.S. Kanu, R. Binions, Thin films for solar control applications, *Proc. R. Soc. A.* 466 (2010) 19–44. <https://doi.org/10.1098/rspa.2009.0259>.
- [14] ASTM G 173:2003: *Tables for Reference Solar Spectral Irradiances: Direct Normal and Hemispherical on 37 Tilted Surface*, ASTM International, West Conshohocken, PA.



## References

- [15] C.G. Granqvist, S. Green, G.A. Niklasson, N.R. Mlyuka, S. von Kræmer, P. Georén, Advances in chromogenic materials and devices, *Thin Solid Films* 518 (2010) 3046–3053. <https://doi.org/10.1016/j.tsf.2009.08.058>.
- [16] Y. Wang, E.L. Runnerstrom, D.J. Milliron, Switchable Materials for Smart Windows, *Annu. Rev. Chem. Biomol. Eng.* 7 (2016) 283–304. <https://doi.org/10.1146/annurev-chembioeng-080615-034647>.
- [17] N. DeForest, A. Shehabi, J. O'Donnell, G. Garcia, J. Greenblatt, E.S. Lee, S. Selkowitz, D.J. Milliron, United States energy and CO<sub>2</sub> savings potential from deployment of near-infrared electrochromic window glazings, *Build. Environ.* 89 (2015) 107–117. <https://doi.org/10.1016/j.buildenv.2015.02.021>.
- [18] N.I. Jaksic, C. Salahifar, A feasibility study of electrochromic windows in vehicles, *Sol. Energy Mater. Sol. Cells* 79 (2003) 409–423. [https://doi.org/10.1016/S0927-0248\(02\)00475-0](https://doi.org/10.1016/S0927-0248(02)00475-0).
- [19] G.J. Marshall, C.P. Mahony, M.J. Rhodes, S.R. Daniewicz, N. Tsolas, S.M. Thompson, Thermal Management of Vehicle Cabins, External Surfaces, and Onboard Electronics: An Overview, *Engineering* 5 (2019) 954–969. <https://doi.org/10.1016/j.eng.2019.02.009>.
- [20] F. Favoino, E. Raheli, D. Ramirez, F. Pilosio, S. Tavernese, M. Simonetti, M. Perino, M. Masoero, Impact of glass technology on future electrical individual transportation: the Pop.Up case study, *Glass Struct. Eng.* 5 (2020) 117–131. <https://doi.org/10.1007/s40940-019-00104-7>.
- [21] F. Gonzales, Smart Windows and Smart Glass 2014-2024: Technologies, Markets, Forecasts: Switchable, dynamic, magic glass; electrochromic glass; thermochromic glass; suspended particle device glass; liquid crystal glass; chromogenics; dynamic/smart/switchable glazing and self-dimming glass, 2014.
- [22] X. Li, K. Perera, J. He, A. Gumyusenge, J. Mei, Solution-processable electrochromic materials and devices: roadblocks and strategies towards large-scale applications, *J. Mater. Chem. C* 7 (2019) 12761–12789. <https://doi.org/10.1039/C9TC02861G>.
- [23] E.L. Runnerstrom, A. Llordés, S.D. Lounis, D.J. Milliron, Nanostructured electrochromic smart windows: traditional materials and NIR-selective plasmonic nanocrystals, *Chem. Commun.* 50 (2014) 10555–10572. <https://doi.org/10.1039/c4cc03109a>.
- [24] Y. Ke, J. Chen, G. Lin, S. Wang, Y. Zhou, J. Yin, P.S. Lee, Y. Long, Smart Windows: Electro-, Thermo-, Mechano-, Photochromics, and Beyond, *Adv. Energy Mater.* 9 (2019) 1902066. <https://doi.org/10.1002/aenm.201902066>.
- [25] Y. Cui, Y. Ke, C. Liu, Z. Chen, N. Wang, L. Zhang, Y. Zhou, S. Wang, Y. Gao, Y. Long, Thermochromic VO<sub>2</sub> for Energy-Efficient Smart Windows, *Joule* 2 (2018) 1707–1746. <https://doi.org/10.1016/j.joule.2018.06.018>.
- [26] L. Long, H. Ye, How to be smart and energy efficient: A general discussion on thermochromic windows, *Sci. Rep.* 4 (2014) 1–10. <https://doi.org/10.1038/srep06427>.
- [27] K. Sadeghi, J.-Y. Yoon, J. Seo, Chromogenic Polymers and Their Packaging Applications: A Review, *Polym. Rev.* 60 (2020) 442–492. <https://doi.org/10.1080/15583724.2019.1676775>.
- [28] A. Ritter, Smart materials in architecture, interior architecture and design, Birkhäuser, Basel, Boston, 2007.

## References

- [29] A.P. Periyasamy, M. Vikova, M. Vik, A review of photochromism in textiles and its measurement, *Text. Prog.* 49 (2017) 53–136. <https://doi.org/10.1080/00405167.2017.1305833>.
- [30] S. Wang, W. Fan, Z. Liu, A. Yu, X. Jiang, Advances on tungsten oxide based photochromic materials: strategies to improve their photochromic properties, *J. Mater. Chem. C* 6 (2018) 191–212. <https://doi.org/10.1039/C7TC04189F>.
- [31] D. Scheid, C. Lederle, S. Vowinkel, C.G. Schäfer, B. Stühn, M. Gallei, Redox- and mechano-chromic response of metallopolymer-based elastomeric colloidal crystal films, *J. Mater. Chem. C* 2 (2014) 2583–2590. <https://doi.org/10.1039/C3TC32525C>.
- [32] C. Calvino, L. Neumann, C. Weder, S. Schrettl, Approaches to polymeric mechanochromic materials, *J. Polym. Sci. A Polym. Chem.* 55 (2017) 640–652. <https://doi.org/10.1002/pola.28445>.
- [33] C. Cleveland, *Encyclopedia of energy*, Elsevier Academic Press, Amsterdam, Boston, 2004. <http://worldcatlibraries.org/wcpa/oclc/180851239>.
- [34] C.G. Granqvist, *Handbook of inorganic electrochromic materials*, Elsevier, Amsterdam, 1995.
- [35] S. Macher, M. Schott, M. Sassi, I. Facchinetti, R. Ruffo, G. Patriarca, L. Beverina, U. Posset, G.A. Giffin, P. Löbmann, New Roll-to-Roll Processable PEDOT-Based Polymer with Colorless Bleached State for Flexible Electrochromic Devices, *Adv. Funct. Mater.* 30 (2020) 1906254. <https://doi.org/10.1002/adfm.201906254>.
- [36] P.R. Somani, S. Radhakrishnan, Electrochromic materials and devices: present and future, *Mater. Chem. Phys.* 77 (2003) 117–133. [https://doi.org/10.1016/S0254-0584\(01\)00575-2](https://doi.org/10.1016/S0254-0584(01)00575-2).
- [37] R.J. Mortimer, Electrochromic materials, *Chem. Soc. Rev.* 26 (1997) 147. <https://doi.org/10.1039/cs9972600147>.
- [38] C.G. Granqvist, M.A. Arvizu, İ. Bayrak Pehlivan, H.-Y. Qu, R.-T. Wen, G.A. Niklasson, Electrochromic materials and devices for energy efficiency and human comfort in buildings: A critical review, *Electrochim. Acta* 259 (2018) 1170–1182. <https://doi.org/10.1016/j.electacta.2017.11.169>.
- [39] R. Baetens, B.P. Jelle, A. Gustavsen, Properties, requirements and possibilities of smart windows for dynamic daylight and solar energy control in buildings: A state-of-the-art review, *Sol. Energy Mater. Sol. Cells* 94 (2010) 87–105. <https://doi.org/10.1016/j.solmat.2009.08.021>.
- [40] B.P. Jelle, A. Hynd, A. Gustavsen, D. Arasteh, H. Goudey, R. Hart, Fenestration of today and tomorrow: A state-of-the-art review and future research opportunities, *Sol. Energy Mater. Sol. Cells* 96 (2012) 1–28. <https://doi.org/10.1016/j.solmat.2011.08.010>.
- [41] J.A. Kerszulis, K.E. Johnson, M. Kuepfert, D. Khoshabo, A.L. Dyer, J.R. Reynolds, Tuning the painter's palette: subtle steric effects on spectra and colour in conjugated electrochromic polymers, *J. Mater. Chem. C* 3 (2015) 3211–3218. <https://doi.org/10.1039/C4TC02685C>.
- [42] A. Lordés, G. Garcia, J. Gazquez, D.J. Milliron, Tunable near-infrared and visible-light transmittance in nanocrystal-in-glass composites, *Nature* (2013) 323. <https://doi.org/10.1038/nature12398>.
- [43] A. Lordés, Y. Wang, A. Fernandez-Martinez, P. Xiao, T. Lee, A. Poulain, O. Zandi, C.A. Saez Cabezas, G. Henkelman, D.J. Milliron, Linear topology in amorphous metal oxide electrochromic networks obtained via low-temperature solution processing, *Nat. Mater.* (2016) 1267. <https://doi.org/10.1038/nmat4734>.

## References

- [44] G. Garcia, R. Buonsanti, E.L. Runnerstrom, R.J. Mendelsberg, A. Llordes, A. Anders, T.J. Richardson, D.J. Milliron, Dynamically modulating the surface plasmon resonance of doped semiconductor nanocrystals, *Nano Lett.* 11 (2011) 4415–4420.  
<https://doi.org/10.1021/nl202597n>.
- [45] C.M. Lampert, Chromogenic smart materials, *Mater. Today* 7 (2004) 28–35.  
[https://doi.org/10.1016/S1369-7021\(04\)00123-3](https://doi.org/10.1016/S1369-7021(04)00123-3).
- [46] K. Werner, Innovative Glass and Polymer Components Impress at Display Week, *J. Soc. Inf. Disp.* 34 (2018) 32–35. <https://doi.org/10.1002/j.2637-496X.2018.tb01120.x>.
- [47] H. Khayyam, A.Z. Kouzani, E.J. Hu, S. Nahavandi, Coordinated energy management of vehicle air conditioning system, *Applied Thermal Engineering* 31 (2011) 750–764.  
<https://doi.org/10.1016/j.applthermaleng.2010.10.022>.
- [48] H. Wang, L. Wang, M. Chen, T. Li, H. Cao, D. Yang, Z. Yang, H. Yang, S. Zhu, Bistable polymer-dispersed cholesteric liquid crystal thin film enabled by a stepwise polymerization, *RSC Adv.* 5 (2015) 58959–58965. <https://doi.org/10.1039/C5RA08172F>.
- [49] E.A. Büyüktanir, N. Gheorghiu, J.L. West, M. Mitrokhin, B. Holter, A. Glushchenko, Field-induced polymer wall formation in a bistable smectic-A liquid crystal display, *Appl. Phys. Lett.* 89 (2006) 31101. <https://doi.org/10.1063/1.2221887>.
- [50] J. Ma, L. Shi, D.-K. Yang, Bistable Polymer Stabilized Cholesteric Texture Light Shutter, *Appl. Phys. Express* 3 21702. <https://doi.org/10.1143/APEX.3.021702>.
- [51] I. Dierking, Polymer Network–Stabilized Liquid Crystals, *Adv. Mater.* 12 (2000) 167–181.  
[https://doi.org/10.1002/\(SICI\)1521-4095\(200002\)12:3<167:AID-ADMA167>3.0.CO;2-I](https://doi.org/10.1002/(SICI)1521-4095(200002)12:3<167:AID-ADMA167>3.0.CO;2-I).
- [52] I. F. Chang, B. L. Gilbert, T. I. Sun, Electrochromic Systems for Display Applications, *J. Electrochem. Soc.* 122 (1975) 955. <https://doi.org/10.1149/1.2134377>.
- [53] I.F. Chang, *Electrochromic and Electrochemichromic Materials and Phenomena*, Springer, 1976.
- [54] Y. Hajimoto, T. Hara, Coloration in a WO<sub>3</sub> film, *Appl. Phys. Lett.* 28 (2008) 228.  
<https://doi.org/10.1063/1.88707>.
- [55] C.M. Lampert, Electrochromic materials and devices for energy efficient windows, *Sol. Energy Mater.* 11 (1984) 1–27. [https://doi.org/10.1016/0165-1633\(84\)90024-8](https://doi.org/10.1016/0165-1633(84)90024-8).
- [56] A. Azens, C. Granqvist, Electrochromic smart windows: energy efficiency and device aspects, *J. Solid State Electrochem.* 7 (2003) 64–68. <https://doi.org/10.1007/s10008-002-0313-4>.
- [57] E.S. Lee, D.L. DiBartolomeo, S.E. Selkowitz, Daylighting control performance of a thin-film ceramic electrochromic window: Field study results, *Energ. Buildings* 38 (2006) 30–44.  
<https://doi.org/10.1016/j.enbuild.2005.02.009>.
- [58] J.-M. Dussault, L. Gosselin, T. Galstian, Integration of smart windows into building design for reduction of yearly overall energy consumption and peak loads, *J. Sol. Energy* 86 (2012) 3405–3416. <https://doi.org/10.1016/j.solener.2012.07.016>.
- [59] M. Pittaluga, 17 - Electrochromic glazing and walls for reducing building cooling needs, in: L.F. Cabeza (Ed.), *Eco-efficient materials for mitigating building cooling needs - design, pro*, Elsevier Science & Technology, Oxford, 2015, pp. 473–497.

## References

- [60] N. DeForest, A. Shehabi, S. Selkowitz, D.J. Milliron, A comparative energy analysis of three electrochromic glazing technologies in commercial and residential buildings, *Appl. Energy* 192 (2017) 95–109. <https://doi.org/10.1016/j.apenergy.2017.02.007>.
- [61] P.F. Tavares, A.R. Gaspar, A.G. Martins, F. Frontini, 18 - The impact of electrochromic windows on the energy performance of buildings in Mediterranean climates: a case study, in: L.F. Cabeza (Ed.), *Eco-efficient materials for mitigating building cooling needs - design, pro*, Elsevier Science & Technology, Oxford, 2015, pp. 499–524.
- [62] C. Baldassarri, A. Shehabi, F. Asdrubali, E. Masanet, Energy and emissions analysis of next generation electrochromic devices, *Sol. Energy Mater. Sol. Cells* 156 (2016) 170–181. <https://doi.org/10.1016/j.solmat.2015.12.017>.
- [63] R.D. Clear, V. Inkarojrit, E.S. Lee, Subject responses to electrochromic windows, *Energ. Buildings* 38 (2006) 758–779. <https://doi.org/10.1016/j.enbuild.2006.03.011>.
- [64] M. Zinzi, Office worker preferences of electrochromic windows: a pilot study, *Build. Environ.* 41 (2006) 1262–1273. <https://doi.org/10.1016/j.buildenv.2005.05.010>.
- [65] A. Piccolo, F. Simone, Performance requirements for electrochromic smart window, *J. Build. Eng.* 3 (2015) 94–103. <https://doi.org/10.1016/j.jobe.2015.07.002>.
- [66] N. Sbar, M. Badding, R. Budziak, K. Cortez, L. Laby, L. Michalski, T. Ngo, S. Schulz, K. Urbanik, Progress toward durable, cost effective electrochromic window glazings, *Sol. Energy Mater. Sol. Cells* 56 (1999) 321–341. [https://doi.org/10.1016/S0927-0248\(98\)00141-X](https://doi.org/10.1016/S0927-0248(98)00141-X).
- [67] A. Kraft, M. Rottmann, Properties, performance and current status of the laminated electrochromic glass of Gesimat, *Sol. Energy Mater. Sol. Cells* 93 (2009) 2088–2092. <https://doi.org/10.1016/j.solmat.2009.05.010>.
- [68] F. Beteille, P. Boire, J.-C. Giron, Highly durable all-solid state electrochromic glazings, in: *Switchable Materials and Flat Panel Displays*, Denver, CO, SPIE, 1999, pp. 70–74.
- [69] H. Zheng, J.Z. Ou, M.S. Strano, R.B. Kaner, A. Mitchell, K. Kalantar-zadeh, Nanostructured Tungsten Oxide - Properties, Synthesis, and Applications, *Adv. Funct. Mater.* 21 (2011) 2175–2196. <https://doi.org/10.1002/adfm.201002477>.
- [70] G.A. Niklasson, C.G. Granqvist, Electrochromics for smart windows: thin films of tungsten oxide and nickel oxide, and devices based on these, *J. Mater. Chem.* 17 (2007) 127–156. <https://doi.org/10.1039/B612174H>.
- [71] F. Švegl, A.S. Vuk, M. Hajzeri, L. Slemenik Perše, B. Orel, Electrochromic properties of Ni(1-x)O and composite Ni(1-x)O-polyaniline thin films prepared by the peroxo soft chemistry route, *Sol. Energy Mater. Sol. Cells* 99 (2012) 14–25. <https://doi.org/10.1016/j.solmat.2011.11.043>.
- [72] M. Mihelčič, I. Jerman, F. Švegl, A.S. Vuk, L. Slemenik Perše, J. Kovač, B. Orel, U. Posset, Electrochromic Ni<sub>1-x</sub>O pigment coatings and plastic film-based Ni<sub>1-x</sub>O/TiO<sub>2</sub> device with transmissive light modulation, *Sol. Energy Mater. Sol. Cells* 107 (2012) 175–187. <https://doi.org/10.1016/j.solmat.2012.08.012>.
- [73] H. Moulki, C. Faure, M. Mihelčič, A. Šurca Vuk, F. Švegl, B. Orel, G. Campet, M. Alfredsson, A.V. Chadwick, D. Gianolio, A. Rougier, Electrochromic performances of nonstoichiometric NiO thin films, *Thin Solid Films* (2014) 63. <https://doi.org/10.1016/j.tsf.2013.10.154>.

## References

- [74] S. Heusing, D.-L. Sun, J. Otero-Anaya, M.A. Aegerter, Grey, brown and blue coloring sol–gel electrochromic devices, *Thin Solid Films* 502 (2006) 240–245.  
<https://doi.org/10.1016/j.tsf.2005.07.282>.
- [75] M. Röder, A.B. Beleke, U. Guntow, J. Buensow, A. Guerfi, U. Posset, H. Lorrmann, K. Zaghbi, G. SEXTL, Li<sub>4</sub>Ti<sub>5</sub>O<sub>12</sub> and LiMn<sub>2</sub>O<sub>4</sub> thin-film electrodes on transparent conducting oxides for all-solid-state and electrochromic applications, *J. Power Sources* 301 (2016) 35–40.  
<https://doi.org/10.1016/j.jpowsour.2015.09.063>.
- [76] U. Schubert, A. Winter, G.R. Newkome, Terpyridine-based materials: For catalytic, optoelectronic and life science applications, Wiley-VCH Verlag GmbH & Co. KGaA, Weinheim, 2011.
- [77] P.R. Andres, U.S. Schubert, New Functional Polymers and Materials Based on 2,2':6',2"-Terpyridine Metal Complexes, *Adv. Mater.* 16 (2004) 1043–1068.  
<https://doi.org/10.1002/adma.200306518>.
- [78] A. Wild, A. Winter, F. Schlütter, U.S. Schubert, Advances in the field of  $\pi$ -conjugated 2,2':6',2"-terpyridines, *Chem. Soc. Rev.* 40 (2011) 1459–1511. <https://doi.org/10.1039/c0cs00074d>.
- [79] S. Bernhard, J.I. Goldsmith, K. Takada, H.D. Abruña, Iron(II) and copper(I) coordination polymers: electrochromic materials with and without chiroptical properties, *Inorg. Chem.* 42 (2003) 4389–4393. <https://doi.org/10.1021/ic0207146>.
- [80] F.S. Han, M. Higuchi, D.G. Kurth, Diverse synthesis of novel Bisterpyridines via Suzuki-type cross-coupling, *Org. Lett.* 9 (2007) 559–562. <https://doi.org/10.1021/ol062788h>.
- [81] F.S. Han, M. Higuchi, D.G. Kurth, Metallo-supramolecular polyelectrolytes self-assembled from various pyridine ring-substituted bisterpyridines and metal ions: photophysical, electrochemical, and electrochromic properties, *J. Am. Chem. Soc.* 130 (2008) 2073–2081.  
<https://doi.org/10.1021/ja710380a>.
- [82] M. Higuchi, Y. Akasaka, T. Ikeda, A. Hayashi, D.G. Kurth, Electrochromic Solid-State Devices Using Organic-Metallic Hybrid Polymers, *J. Inorg. Organomet. Polym.* 19 (2009) 74–78.  
<https://doi.org/10.1007/s10904-008-9243-7>.
- [83] M. Schott, L. Niklaus, J. Clade, U. Posset, Electrochromic metallo-supramolecular polymers showing visible and near-infrared light transmittance modulation, *Sol. Energy Mater. Sol. Cells* 200 (2019) 110001. <https://doi.org/10.1016/j.solmat.2019.110001>.
- [84] C.-Y. Hsu, J. Zhang, T. Sato, S. Moriyama, M. Higuchi, Black-to-Transmissive Electrochromism with Visible-to-Near-Infrared Switching of a Co(II)-Based Metallo-Supramolecular Polymer for Smart Window and Digital Signage Applications, *ACS Appl. Mater. Interfaces* 7 (2015) 18266–18272. <https://doi.org/10.1021/acsami.5b02990>.
- [85] P.S. Braterman, J.I. Song, R.D. Peacock, Electronic absorption spectra of the iron(II) complexes of 2,2'-bipyridine, 2,2'-bipyrimidine, 1,10-phenanthroline, and 2,2':6',2"-terpyridine and their reduction products, *Inorg. Chem.* 31 (1992) 555–559. <https://doi.org/10.1021/ic00030a006>.
- [86] V.T. Coombe, G.A. Heath, A.J. MacKenzie, L.J. Yellowlees, Spectroelectrochemical studies on tris(bipyridyl)iridium complexes: ultraviolet, visible and near-infrared spectra of the series [Ir(bipyridyl)<sub>3</sub>]<sup>3+</sup>/<sub>2</sub>/<sub>+</sub>/<sub>+</sub>/<sub>0</sub>, *Inorg. Chem.* 23 (1984) 3423–3425.  
<https://doi.org/10.1021/ic00189a031>.

## References

- [87] H.-T. Zhang, P. Subramanian, O. Fussa-Rydel, J.C. Bebel, J.T. Hupp, Electrochromic devices based on thin metallopolymeric films, *Sol. Energy Mater. Sol. Cells* 315–325.
- [88] R.D. Rauh, Electrochromic windows: an overview, *Electrochim. Acta* 44 (1999) 3165–3176. [https://doi.org/10.1016/S0013-4686\(99\)00034-1](https://doi.org/10.1016/S0013-4686(99)00034-1).
- [89] M. Sassi, M.M. Salamone, R. Ruffo, C.M. Mari, G.A. Pagani, L. Beverina, Gray to colorless switching, crosslinked electrochromic polymers with outstanding stability and transmissivity from naphthalenediimide-functionalized EDOT, *Adv. Mater.* 24 (2012) 2004–2008. <https://doi.org/10.1002/adma.201200111>.
- [90] T. Jarosz, K. Gebka, A. Stolarczyk, W. Domagala, Transparent to Black Electrochromism-The "Holy Grail" of Organic Optoelectronics, *Polymers (Basel)* 11 (2019). <https://doi.org/10.3390/polym11020273>.
- [91] P. Monk, R. Mortimer, D. Rosseinsky, *Electrochemical background*, Cambridge University Press, 2009.
- [92] A. Kraft, Electrochromism: a fascinating branch of electrochemistry, *ChemTexts* 5 (2019) 1–18. <https://doi.org/10.1007/s40828-018-0076-x>.
- [93] A.J. Bard, L.R. Faulkner, *Electrochemical methods: Fundamentals and applications*, second. ed., Wiley, Hoboken, NJ, 2001.
- [94] N. Elgrishi, K.J. Rountree, B.D. McCarthy, E.S. Rountree, T.T. Eisenhart, J.L. Dempsey, A Practical Beginner's Guide to Cyclic Voltammetry, *J. Chem. Educ.* 95 (2018) 197–206. <https://doi.org/10.1021/acs.jchemed.7b00361>.
- [95] Y.B. Vogel, A. Molina, J. Gonzalez, S. Ciampi, Quantitative Analysis of Cyclic Voltammetry of Redox Monolayers Adsorbed on Semiconductors: Isolating Electrode Kinetics, Lateral Interactions, and Diode Currents, *Anal. Chem.* 91 (2019) 5929–5937. <https://doi.org/10.1021/acs.analchem.9b00336>.
- [96] E. Fontananova, Impedance Spectroscopy, Membrane Characterization by, in: E. Drioli, L. Giorno (Eds.), *Encyclopedia of Membranes*, Springer, Berlin, Heidelberg, s.l., 2016, pp. 1025–1027.
- [97] J.R. Macdonald, W.B. Johnson, Fundamentals of Impedance Spectroscopy, in: E. Barsoukov, J.R. Macdonald (Eds.), *Impedance spectroscopy: Theory, experiment, and applications*, Third edition, Wiley, Hoboken, NJ, 2018, pp. 1–20.
- [98] W. Zhang, U.E. Spichiger, An impedance study of Mg<sup>2+</sup>-selective membranes, *Electrochim. Acta* 45 (2000) 2259–2266. [https://doi.org/10.1016/S0013-4686\(00\)00323-6](https://doi.org/10.1016/S0013-4686(00)00323-6).
- [99] Electrochemical measurement of transference numbers in polymer electrolytes, *Polymer* 28 (1987) 2324–2328. [https://doi.org/10.1016/0032-3861\(87\)90394-6](https://doi.org/10.1016/0032-3861(87)90394-6).
- [100] P.G. Bruce, J. Evans, C.A. Vincent, Conductivity and transference number measurements on polymer electrolytes, *Solid State Ionics* 28-30 (1988) 918–922. [https://doi.org/10.1016/0167-2738\(88\)90304-9](https://doi.org/10.1016/0167-2738(88)90304-9).
- [101] S. Zugmann, Messung von Lithium-Ionen Überführungszahlen an Elektrolyten für Lithium-Ionen Batterien - Eine vergleichende Studie mit fünf verschiedenen Methoden, 2011.

## References

- [102] V.K. Thakur, G. Ding, J. Ma, P.S. Lee, X. Lu, Hybrid materials and polymer electrolytes for electrochromic device applications, *Adv. Mater.* 24 (2012) 4071–4096. <https://doi.org/10.1002/adma.201200213>.
- [103] L. Niklaus, M. Schott, U. Posset, G.A. Giffin, Redox Electrolytes for Hybrid Type II Electrochromic Devices with Fe-MEPE or Ni<sub>1-x</sub>O as Electrode Materials. *ChemElectroChem*, 7(15), 3274-3283 (2020). <https://doi.org/10.1002/CELC.202000583>.
- [104] Kanagaraj Madasamy, David Velayutham, Vembu Suryanarayanan, Murugavel Kathiresan, Kuo-Chuan Ho, Viologen-based electrochromic materials and devices, *J. Mater. Chem. C* 7 (2019) 4622–4637. <https://doi.org/10.1039/C9TC00416E>.
- [105] Huan-Shen Liu, Bo-Cheng Pan, De-Cheng Huang, Yu-Ruei Kung, Chyi-Ming Leu, Guey-Sheng Liou, Highly transparent to truly black electrochromic devices based on an ambipolar system of polyamides and viologen, *NPG Asia Mater.* 9 (2017) e388-e388. <https://doi.org/10.1038/am.2017.57>.
- [106] D.R. Rosseinsky, P.M.S. Monk, Anion Efficiencies in Electrochromic Bipyridilium Deposition, *J. Electrochem. Soc.* 147 (2000) 1595. <https://doi.org/10.1149/1.1393401>.
- [107] A. Hauch, A. Georg, U.O. Krašovec, B. Orel, Comparison of Photoelectrochromic Devices with Different Layer Configurations, *J. Electrochem. Soc.* 149 (2002) H159. <https://doi.org/10.1149/1.1496487>.
- [108] S. Bogati, A. Georg, C. Jerg, W. Graf, Tetramethylthiourea (TMTU) as an alternative redox mediator for electrochromic devices, *Sol. Energy Mater. Sol. Cells* 157 (2016) 454–461. <https://doi.org/10.1016/j.solmat.2016.07.023>.
- [109] S. Bogati, R. Basnet, A. Georg, Iridium oxide catalyst for hybrid electrochromic device based on tetramethylthiourea (TMTU) redox electrolyte, *Sol. Energy Mater. Sol. Cells* 189 (2019) 206–213. <https://doi.org/10.1016/j.solmat.2018.09.026>.
- [110] R. Marom, O. Haik, D. Aurbach, I.C. Halalay, Revisiting LiClO<sub>4</sub> as an Electrolyte for Rechargeable Lithium-Ion Batteries, *J. Electrochem. Soc.* 157 A972. <https://doi.org/10.1149/1.3447750>.
- [111] Q. Tang, H. Li, Y. Yue, Q. Zhang, H. Wang, Y. Li, P. Chen, 1-Ethyl-3-methylimidazolium tetrafluoroborate-doped high ionic conductivity gel electrolytes with reduced anodic reaction potentials for electrochromic devices, *Mater. Des.* 118 (2017) 279–285. <https://doi.org/10.1016/j.matdes.2017.01.033>.
- [112] H. Oh, D.G. Seo, T.Y. Yun, C.Y. Kim, H.C. Moon, Voltage-Tunable Multicolor, Sub-1.5 V, Flexible Electrochromic Devices Based on Ion Gels, *ACS Appl. Mater. Interfaces* 9 (2017) 7658–7665. <https://doi.org/10.1021/acsami.7b00624>.
- [113] L. Niklaus, M. Schott, M. Mihelcic, I. Jerman, U. Posset, G. Sestl, Metallopolymers and non-stoichiometric nickel oxide: Towards neutral tint large-area electrochromic devices, *Sol. Energy Mater. Sol. Cells* 200 (2019) 110002. <https://doi.org/10.1016/j.solmat.2019.110002>.
- [114] Wanyu Chen, Caizhi Zhu, Le Guo, MengYing Yan, Lili Wu, Bo Zhu, Chenjie Qi, Siyuan Liu, Heng Zhang, Yong Peng, A novel ionically crosslinked gel polymer electrolyte as an ion transport layer for high-performance electrochromic devices, *J. Mater. Chem. C* 7 (2019) 3744–3750. <https://doi.org/10.1039/C9TC00621D>.

## References

- [115] X. Wu, K. Pan, M. Jia, Y. Ren, H. He, L. Zhang, S. Zhang, Electrolyte for lithium protection: From liquid to solid, *Green Energy Environ.* 4 (2019) 360–374.  
<https://doi.org/10.1016/j.gee.2019.05.003>.
- [116] DIN EN 410:2011-04, Glas im Bauwesen - Bestimmung der lichttechnischen und strahlungsphysikalischen Kenngrößen von Verglasungen, Beuth Verlag GmbH, Berlin.
- [117] DIN 5033-1:2017-10, Farbmessung Teil 1: Grundbegriffe der Farbmessung, Beuth Verlag GmbH, Berlin.
- [118] R.G. McGuire, Reporting of Objective Color Measurements, *Hort. Sci.* 27 (1992) 1254–1255.  
<https://doi.org/10.21273/HORTSCI.27.12.1254>.
- [119] S. Pane, M. Caporusso, H. Hakemi, Haze and opacity control in polymer dispersed liquid crystal (PDLC) films with phase separation method, *Liq. Cryst.* 23 (1997) 861–867.  
<https://doi.org/10.1080/026782997207786>.
- [120] DIN ISO 3537:2018-02, Straßenfahrzeuge - Sicherheitsscheiben - Mechanische Prüfverfahren, Beuth Verlag GmbH, Berlin.
- [121] DIN ISO 15082:2018-02, Straßenfahrzeuge - Prüfverfahren für Sicherheitsscheiben aus hartem Kunststoff, Beuth Verlag GmbH, Berlin.
- [122] G. Cai, M. Cui, V. Kumar, P. Darmawan, J. Wang, X. Wang, A. Lee-Sie Eh, K. Qian, P.S. Lee, Ultra-large optical modulation of electrochromic porous WO<sub>3</sub> film and the local monitoring of redox activity, *Chem. Sci.* 7 (2016) 1373–1382. <https://doi.org/10.1039/c5sc03727a>.
- [123] J. Padilla, A.M. Österholm, A.L. Dyer, J.R. Reynolds, Process controlled performance for soluble electrochromic polymers, *Sol. Energy Mater. Sol. Cells* 140 (2015) 54–60.  
<https://doi.org/10.1016/j.solmat.2015.03.018>.
- [124] S. Hassab, D.E. Shen, A.M. Österholm, M. Da Rocha, G. Song, Y. Alesanco, A. Viñuales, A. Rougier, J.R. Reynolds, J. Padilla, A new standard method to calculate electrochromic switching time, *Sol. Energy Mater. Sol. Cells* 185 (2018) 54–60.  
<https://doi.org/10.1016/j.solmat.2018.04.031>.
- [125] Jacob Jensen, Markus Hösel, Inyoung Kim, Jong-Su Yu, Jeongdai Jo, Frederik C. Krebs, Fast Switching ITO Free Electrochromic Devices, *Adv. Funct. Mater.* 24 (2014) 1228–1233.  
<https://doi.org/10.1002/adfm.201302320>.
- [126] S.V. Vasilyeva, E. Unur, R.M. Walczak, E.P. Donoghue, A.G. Rinzler, J.R. Reynolds, Color purity in polymer electrochromic window devices on indium-tin oxide and single-walled carbon nanotube electrodes, *ACS Appl. Mater. Interfaces* 1 (2009) 2288–2297.  
<https://doi.org/10.1021/am900435j>.
- [127] S. Macher, M. Rumpel, M. Schott, U. Posset, G.A. Giffin, P. Löbmann, Avoiding Voltage-Induced Degradation in PET-ITO-Based Flexible Electrochromic Devices, *ACS Appl. Mater. Interfaces* 12 (2020) 36695–36705. <https://doi.org/10.1021/acsami.0c07860>.
- [128] F.S. Han, M. Higuchi, D.G. Kurth, Metallo-Supramolecular Polymers Based on Functionalized Bis-terpyridines as Novel Electrochromic Materials, *Adv. Mater.* 19 (2007) 3928–3931.  
<https://doi.org/10.1002/adma.200700931>.
- [129] J.-M. Lehn, Supramolecular polymer chemistry - scope and perspectives, *Polym. Int.* 51 (2002) 825–839. <https://doi.org/10.1002/pi.852>.



## References

- [130] A. Bétard, R.A. Fischer, Metal-organic framework thin films: from fundamentals to applications, *Chem. Rev.* 112 (2012) 1055–1083. <https://doi.org/10.1021/cr200167v>.
- [131] D.G. Kurth, M. Higuchi, Transition metal ions: weak links for strong polymers, *Soft Matter* 2 (2006) 915. <https://doi.org/10.1039/b607485e>.
- [132] E.C. Constable, A.M.W.C. Thompson, Multinucleating 2,2' 6',2"-terpyridine ligands as building blocks for the assembly of co-ordination polymers and oligomers, *J. Chem. Soc., Dalton Trans.* 114 (1992) 3467–3475. <https://doi.org/10.1039/DT9920003467>.
- [133] M. Schott, W. Szczerba, D.G. Kurth, Detailed study of layer-by-layer self-assembled and dip-coated electrochromic thin films based on metallo-supramolecular polymers, *Langmuir* 30 (2014) 10721–10727. <https://doi.org/10.1021/la501590a>.
- [134] M. Schott, H. Lorrmann, W. Szczerba, M. Beck, D.G. Kurth, State-of-the-art electrochromic materials based on metallo-supramolecular polymers, *Sol. Energy Mater. Sol. Cells* 126 (2014) 68–73. <https://doi.org/10.1016/j.solmat.2014.03.032>.
- [135] M. Schott, W. Szczerba, U. Posset, A.S. Vuk, M. Beck, H. Riesemeier, A.F. Thünemann, D.G. Kurth, In operando XAFS experiments on flexible electrochromic devices based on Fe(II)-metallo-supramolecular polyelectrolytes and vanadium oxide, *Sol. Energy Mater. Sol. Cells* 147 (2016) 61–67. <https://doi.org/10.1016/j.solmat.2015.10.015>.
- [136] S. Pai, M. Schott, L. Niklaus, U. Posset, D.G. Kurth, A study of the effect of pyridine linkers on the viscosity and electrochromic properties of metallo-supramolecular coordination polymers, *J. Mater. Chem. C* 6 (2018) 3310–3321. <https://doi.org/10.1039/C7TC04177B>.
- [137] M. Schott, M. Beck, F. Winkler, H. Lorrmann, D.G. Kurth, Fabricating Electrochromic Thin Films Based on Metallo-Polymers Using Layer-by-Layer Self-Assembly: An Attractive Laboratory Experiment, *J. Chem. Educ.* 92 (2015) 364–367. <https://doi.org/10.1021/ed5002174>.
- [138] E.C. Constable, M.D. Ward, Synthesis and Co-ordination Behaviour of 6',6"-BiS(2-pyridyl)-2,2' 4,4" 2"82'1'-quaterpyridine; 'Back-to-back' 2'2' 6',2"- Terpyridine, *J. Chem. Soc., Dalton Trans.* (1990).
- [139] G. Schwarz, I. HaBlauer, D.G. Kurth, From terpyridine-based assemblies to metallo-supramolecular polyelectrolytes (MEPEs), *Adv. Colloid Interface Sci.* 207 (2014) 107–120. <https://doi.org/10.1016/j.cis.2013.12.010>.
- [140] G. Schwarz, T.K. Sievers, Y. Bodenthin, I. Hasslauer, T. Geue, J. Koetz, D.G. Kurth, The structure of metallo-supramolecular polyelectrolytes in solution and on surfaces, *J. Mater. Chem.* 20 (2010) 4142. <https://doi.org/10.1039/b926783b>.
- [141] H. Basch, A. Viste, H.B. Gray, Molecular Orbital Theory for Octahedral and Tetrahedral Metal Complexes, *J. Chem. Phys.* 44 (1966) 10–19. <https://doi.org/10.1063/1.1726431>.
- [142] M. Higuchi, Stimuli-responsive metallo-supramolecular polymer films: design, synthesis and device fabrication, *J. Mater. Chem. C* 2 (2014) 9331–9341. <https://doi.org/10.1039/C4TC00689E>.
- [143] M.K. Bera, Y. Ninomiya, T. Yoshida, M. Higuchi, Precise Synthesis of Alternate Fe(II)/Os(II)-Based Bimetallic Metallo-Supramolecular Polymer, *Macromol. Rapid Commun.* 41 (2020) e1900384. <https://doi.org/10.1002/marc.201900384>.
- [144] M.K. Bera, Y. Ninomiya, M. Higuchi, Constructing Alternated Heterobimetallic Fe(II)/Os(II) Supramolecular Polymers with Diverse Solubility for Facile Fabrication of Voltage-Tunable

## References

- Multicolor Electrochromic Devices, *ACS Appl. Mater. Interfaces* 12 (2020) 14376–14385. <https://doi.org/10.1021/acsami.9b21966>.
- [145] M.D. Hossain, J. Zhang, R.K. Pandey, T. Sato, M. Higuchi, A Heterometallo-Supramolecular Polymer with Cu I and Fe II Ions Introduced Alternately, *Eur. J. Inorg. Chem.* 2014 (2014) 3763–3770. <https://doi.org/10.1002/ejic.201402468>.
- [146] M. Higuchi, Electrochromic Organic–Metallic Hybrid Polymers: Fundamentals and Device Applications, *Polym. J.* 41 (2009) 511. <https://doi.org/10.1295/polymj.PJ2009053>.
- [147] M. Schott, Neuartige Elektrodenmaterialien auf der Basis von Metallo-Polyelektrolyten und Hybridpolymeren für elektrochrome Fenster. PhD thesis, Würzburg, 2015.
- [148] Md. Delwar Hossain, Takashi Sato, Masayoshi Higuchi, A Green Copper-Based Metallo-Supramolecular Polymer: Synthesis, Structure, and Electrochromic Properties, *Chem Asian J.* 8 (2013) 76–79. <https://doi.org/10.1002/asia.201200668>.
- [149] M.D. Hossain, C. Chakraborty, U. Rana, S. Mondal, H.-J. Holdt, M. Higuchi, Green-to-Black Electrochromic Copper(I)-Based Metallo-Supramolecular Polymer with a Perpendicularly Twisted Structure, *ACS Appl. Polym. Mater.* (2020). <https://doi.org/10.1021/acsapm.0c00559>.
- [150] Manas Kumar Bera, Chanchal Chakraborty, Utpal Rana, Masayoshi Higuchi, Electrochromic Os(II)-Based Metallo-Supramolecular Polymers, *Macromol. Rapid Commun.* 39 (2018) 1800415. <https://doi.org/10.1002/marc.201800415>.
- [151] C.-W. Hu, T. Sato, J. Zhang, S. Moriyama, M. Higuchi, Three-dimensional Fe(II)-based metallo-supramolecular polymers with electrochromic properties of quick switching, large contrast, and high coloration efficiency, *ACS Appl. Mater. Interfaces* 6 (2014) 9118–9125. <https://doi.org/10.1021/am5010859>.
- [152] C.-W. Hu, T. Sato, J. Zhang, S. Moriyama, M. Higuchi, Multi-colour electrochromic properties of Fe/Ru-based bimetallo-supramolecular polymers, *J. Mater. Chem. C* 1 (2013) 3408–3413. <https://doi.org/10.1039/C3TC30440J>.
- [153] L.-Y. Hsiao, T.-H. Chang, H.-C. Lu, Y.-C. Wang, Y.-A. Lu, K.-C. Ho, M. Higuchi, A panchromatic electrochromic device composed of Ru(ii)/Fe(ii)-based heterometallo-supramolecular polymer, *J. Mater. Chem. C* 7 (2019) 7554–7562. <https://doi.org/10.1039/C9TC01452G>.
- [154] S.K. Deb, A Novel Electrophotographic System, *Appl. Opt.* 8 (1969) 192. <https://doi.org/10.1364/AO.8.S1.000192>.
- [155] S.K. Deb, Optical and photoelectric properties and colour centres in thin films of tungsten oxide, *Philos. Mag.* 27 (1973) 801–822. <https://doi.org/10.1080/14786437308227562>.
- [156] W.C. Dautremont-Smith, Transition metal oxide electrochromic materials and displays: a review: Part 1: oxides with cathodic coloration, *Displays* 3 (1982) 3–22. [https://doi.org/10.1016/0141-9382\(82\)90061-0](https://doi.org/10.1016/0141-9382(82)90061-0).
- [157] G. Garcia, R. Buonsanti, A. Llordes, E.L. Runnerstrom, A. Bergerud, D.J. Milliron, Near-Infrared Spectrally Selective Plasmonic Electrochromic Thin Films, *Adv. Opt. Mater.* 1 (2013) 215–220. <https://doi.org/10.1002/adom.201200051>.
- [158] C.G. Granqvist, Electrochromic materials: Microstructure, electronic bands, and optical properties, *Appl. Phys. A* 57 (1993) 3–12. <https://doi.org/10.1007/BF00331209>.

## References

- [159] B. Gerand, G. Nowogrocki, J. Guenet, M. Figlarz, Structural study of a new hexagonal form of tungsten trioxide, *J. Solid State Chem.* 29 (1979) 429–434. [https://doi.org/10.1016/0022-4596\(79\)90199-3](https://doi.org/10.1016/0022-4596(79)90199-3).
- [160] S. Cong, Y. Tian, Q. Li, Z. Zhao, F. Geng, Single-Crystalline Tungsten Oxide Quantum Dots for Fast Pseudocapacitor and Electrochromic Applications, *Adv. Mater.* 26 (2014) 4260–4267. <https://doi.org/10.1002/adma.201400447>.
- [161] W.J. Lee, Y.K. Fang, J.-J. Ho, W.T. Hsieh, S.F. Ting, D. Huang, F.C. Ho, Effects of surface porosity on tungsten trioxide(WO<sub>3</sub>) films' electrochromic performance, *J. Electron. Mater.* 29 (2000) 183–187. <https://doi.org/10.1007/s11664-000-0139-8>.
- [162] K. Miyake, H. Kaneko, M. Sano, N. Suedomi, Physical and electrochromic properties of the amorphous and crystalline tungsten oxide thick films prepared under reducing atmosphere, *J. Appl. Phys.* 55 (1998) 2747. <https://doi.org/10.1063/1.333280>.
- [163] D. Eric Shen, A.M. Österholm, J.R. Reynolds, Out of sight but not out of mind: the role of counter electrodes in polymer-based solid-state electrochromic devices, *J. Mater. Chem. C* 3 (2015) 9715–9725. <https://doi.org/10.1039/C5TC01964H>.
- [164] H. Huang, J. Tian, W.K. Zhang, Y.P. Gan, X.Y. Tao, X.-H. Xia, J.-P. Tu, Electrochromic properties of porous NiO thin film as a counter electrode for NiO/WO<sub>3</sub> complementary electrochromic window, *Electrochim. Acta* 56 (2011) 4281–4286. <https://doi.org/10.1016/j.electacta.2011.01.078>.
- [165] Q. Liu, Q. Chen, Q. Zhang, Y. Xiao, X. Zhong, G. Dong, M.-P. Delplancke-Ogletree, H. Terryn, K. Baert, F. Reniers, X. Diao, In situ electrochromic efficiency of a nickel oxide thin film: origin of electrochemical process and electrochromic degradation, *J. Mater. Chem. C* 6 (2018) 646–653. <https://doi.org/10.1039/C7TC04696K>.
- [166] L. Kong, C. Zhang, J. Wang, W. Qiao, L. Ling, D. Long, Free-Standing T-Nb<sub>2</sub>O<sub>5</sub>/Graphene Composite Papers with Ultrahigh Gravimetric/Volumetric Capacitance for Li-Ion Intercalation Pseudocapacitor, *ACS Nano* 9 (2015) 11200–11208. <https://doi.org/10.1021/acs.nano.5b04737>.
- [167] J. He, L. You, D.T. Tran, J. Mei, Low-Temperature Thermally Annealed Niobium Oxide Thin Films as a Minimally Color Changing Ion Storage Layer in Solution-Processed Polymer Electrochromic Devices, *ACS Appl. Mater. Interfaces* 11 (2019) 4169–4177. <https://doi.org/10.1021/acsami.8b16154>.
- [168] S. Hassab, J. Padilla, Using WO<sub>3</sub> as a transparent, optically-passive counter electrode in an unbalanced electrochromic configuration, *Electrochem. Commun.* 72 (2016) 87–90. <https://doi.org/10.1016/j.elecom.2016.09.001>.
- [169] R. Merlin, Electronic structure of NiO, *Phys. Rev. Lett.* 54 (1985) 2727. <https://doi.org/10.1103/PhysRevLett.54.2727>.
- [170] Williams, Kübler, Terakura, Williams, Kubler, and Terakura respond, *Phys. Rev. Lett.* 54 (1985) 2728. <https://doi.org/10.1103/PhysRevLett.54.2728>.
- [171] D.A. Wruck, M. Rubin, Structure and Electronic Properties of Electrochromic NiO Films, *J. Electrochem. Soc.* 140 (1993) 1097–1104.
- [172] S. Passerini, B. Scrosati, The Intercalation of Lithium in Nickel Oxide and Its Electrochromic Properties, *J. Electrochem. Soc.* 10 (1990) 3297–3300.

## References

- [173] A. Avendaño, A. Azens, G.A. Niklasson, C.G. Granqvist, Sputter deposited electrochromic films and devices based on these: Progress on nickel-oxide-based films, *Mater. Sci. Eng. B* 138 (2007) 112–117. <https://doi.org/10.1016/j.mseb.2005.07.029>.
- [174] C. Faure, C. Delmas, M. Fouassier, Characterization of a turbostratic  $\alpha$ -nickel hydroxide quantitatively obtained from an NiSO<sub>4</sub> solution, *J. Power Sources* 35 (1991) 279–290. [https://doi.org/10.1016/0378-7753\(91\)80112-B](https://doi.org/10.1016/0378-7753(91)80112-B).
- [175] W. Guo, K.N. Hui, K.S. Hui, High conductivity nickel oxide thin films by a facile sol–gel method, *Mater. Lett.* 92 (2013) 291–295. <https://doi.org/10.1016/j.matlet.2012.10.109>.
- [176] P. Sharma, Synthesis, characterization and electrochromic properties of NiO<sub>x</sub>H<sub>y</sub> thin film prepared by a sol–gel method, *Solid State Ionics* 113-115 (1998) 457–463. [https://doi.org/10.1016/S0167-2738\(98\)00310-5](https://doi.org/10.1016/S0167-2738(98)00310-5).
- [177] L. Lin, T. Liu, B. Miao, W. Zeng, Hydrothermal fabrication of uniform hexagonal NiO nanosheets: Structure, growth and response, *Mater. Lett.* 102-103 (2013) 43–46. <https://doi.org/10.1016/j.matlet.2013.03.103>.
- [178] Q. Liu, G. Dong, Y. Xiao, M.-P. Delplancke-Ogletree, F. Reniers, X. Diao, Electrolytes-relevant cyclic durability of nickel oxide thin films as an ion-storage layer in an all-solid-state complementary electrochromic device, *Sol. Energy Mater. Sol. Cells* 157 (2016) 844–852. <https://doi.org/10.1016/j.solmat.2016.07.022>.
- [179] S. Green, J. Backholm, P. Georén, C.G. Granqvist, G.A. Niklasson, Electrochromism in nickel oxide and tungsten oxide thin films: Ion intercalation from different electrolytes, *Sol. Energy Mater. Sol. Cells* 93 (2009) 2050–2055. <https://doi.org/10.1016/j.solmat.2009.05.009>.
- [180] M. P. Browne, Electrochromic Nickel Oxide Films for Smart Window Applications, *Int. J. Electrochem. Sci.* (2016) 6636–6647. <https://doi.org/10.20964/2016.08.38>.
- [181] G. Cai, P. Darmawan, M. Cui, J. Chen, X. Wang, A.L.-S. Eh, S. Magdassi, P.S. Lee, Inkjet-printed all solid-state electrochromic devices based on NiO/WO<sub>3</sub> nanoparticle complementary electrodes, *Nanoscale* 8 (2016) 348–357. <https://doi.org/10.1039/c5nr06995e>.
- [182] Z. Xie, Q. Liu, Q. Zhang, B. Lu, J. Zhai, X. Diao, Fast-switching quasi-solid state electrochromic full device based on mesoporous WO<sub>3</sub> and NiO thin films, *Sol. Energy Mater. Sol. Cells* 200 (2019) 110017. <https://doi.org/10.1016/j.solmat.2019.110017>.
- [183] M. Mihelčič, I. Jerman, B. Orel, Preparation of electrochromic Ni<sub>1-x</sub>O and TiO<sub>2</sub> coatings from pigment dispersions and their application in electrochromic foil based devices, *Prog. Org. Coat.* 76 (2013) 1752–1755. <https://doi.org/10.1016/j.porgcoat.2013.05.011>.
- [184] H. Bode, K. Dehmelt, J. Witte, Zur kenntnis der nickelhydroxidelektrode—I.Über das nickel (II)-hydroxidhydrat, *Electrochim. Acta* 11 (1966) 1079-IN1. [https://doi.org/10.1016/0013-4686\(66\)80045-2](https://doi.org/10.1016/0013-4686(66)80045-2).
- [185] M. Mihelčič, A.S. Vuk, I. Jerman, B. Orel, F. Švegl, H. Moulki, C. Faure, G. Campet, A. Rougier, Comparison of electrochromic properties of Ni<sub>1-x</sub>O in lithium and lithium-free aprotic electrolytes: From Ni<sub>1-x</sub>O pigment coatings to flexible electrochromic devices, *Sol. Energy Mater. Sol. Cells* 120 (2014) 116–130. <https://doi.org/10.1016/j.solmat.2013.08.025>.

## References

- [186] J. Zhang, X.L. Wang, X.H. Xia, C.D. Gu, J.P. Tu, Electrochromic behavior of WO<sub>3</sub> nanotree films prepared by hydrothermal oxidation, *Sol. Energy Mater. Sol. Cells* 95 (2011) 2107–2112. <https://doi.org/10.1016/j.solmat.2011.03.008>.
- [187] S. Passerini, An Electrochromic Window Based on Li<sub>x</sub>WO<sub>3</sub>(PEO)<sub>8</sub>LiClO<sub>4</sub>NiO, *J. Electrochem. Soc.* 136 (1989) 3394. <https://doi.org/10.1149/1.2096458>.
- [188] S. Passerini, The Intercalation of Lithium in Nickel Oxide and Its Electrochromic Properties, *J. Electrochem. Soc.* 137 (1990) 3297. <https://doi.org/10.1149/1.2086202>.
- [189] G. Boschloo, A. Hagfeldt, Spectroelectrochemistry of Nanostructured NiO. *The Journal of Physical Chemistry B*, 105(15), 3039–3044 (2001). <https://doi.org/10.1021/JP003499S>.
- [190] M.M. Uplane, S.H. Mujawar, A.I. Inamdar, P.S. Shinde, A.C. Sonavane, P.S. Patil, Structural, optical and electrochromic properties of nickel oxide thin films grown from electrodeposited nickel sulphide, *Appl. Surf. Sci.* 253 (2007) 9365–9371. <https://doi.org/10.1016/j.apsusc.2007.05.069>.
- [191] M. Da Rocha, B. Dunn, A. Rougier, Faradaic and/or capacitive: Which contribution for electrochromism in NiO thin films cycled in various electrolytes?, *Sol. Energy Mater. Sol. Cells* 201 (2019) 110114. <https://doi.org/10.1016/j.solmat.2019.110114>.
- [192] M. Da Rocha, A. Rougier, Electrochromic behavior of Ni<sub>1-x</sub>O thin films in various electrolytes, *ECS Trans.* 66 (2015) 1–8. <https://doi.org/10.1149/06631.0001ecst>.
- [193] R.-T. Wen, C.G. Granqvist, G.A. Niklasson, Anodic Electrochromism for Energy-Efficient Windows: Cation/Anion-Based Surface Processes and Effects of Crystal Facets in Nickel Oxide Thin Films, *Adv. Funct. Mater.* 25 (2015) 3359–3370. <https://doi.org/10.1002/adfm.201500676>.
- [194] V. Srinivasan, J.W. Weidner, An Electrochemical Route for Making Porous Nickel Oxide Electrochemical Capacitors, *J. Electrochem. Soc.* 144 L210. <https://doi.org/10.1149/1.1837859>.
- [195] A. Azens, E. Avendaño, J. Backholm, L. Berggren, G. Gustavsson, R. Karmhag, G.A. Niklasson, A. Roos, C.G. Granqvist, Flexible foils with electrochromic coatings: science, technology and applications, *Mater. Sci. Eng., B* 119 (2005) 214–223. <https://doi.org/10.1016/j.mseb.2004.12.085>.
- [196] J. Nagai, G.D. McMeeking, Y. Saitoh, Durability of electrochromic glazing, *Sol. Energy Mater. Sol. Cells* 56 (1999) 309–319. [https://doi.org/10.1016/S0927-0248\(98\)00140-8](https://doi.org/10.1016/S0927-0248(98)00140-8).
- [197] E.J. Widjaja, G. Delporte, F. Vandeveld, B. Vanterwyngen, Progress toward roll-to-roll processing of inorganic monolithic electrochromic devices on polymeric substrates, *Sol. Energy Mater. Sol. Cells* 92 (2008) 97–100. <https://doi.org/10.1016/j.solmat.2007.03.030>.
- [198] C. Brigouleix, P. Topart, E. Bruneton, F. Sabary, G. Nouhaut, G. Campet, Roll-to-roll pulsed dc magnetron sputtering deposition of WO<sub>3</sub> for electrochromic windows, *Electrochim. Acta* 46 (2001) 1931–1936. [https://doi.org/10.1016/S0013-4686\(01\)00362-0](https://doi.org/10.1016/S0013-4686(01)00362-0).
- [199] A. Azens, Electrochromic devices on polyester foil, *Solid State Ionics* 165 (2003) 1–5. <https://doi.org/10.1016/j.ssi.2003.08.009>.
- [200] A. Azens, L. Kullman, C.G. Granqvist, Ozone coloration of Ni and Cr oxide films, *Sol. Energy Mater. Sol. Cells* 76 (2003) 147–153. [https://doi.org/10.1016/S0927-0248\(02\)00213-1](https://doi.org/10.1016/S0927-0248(02)00213-1).
- [201] M. Da Rocha, A. Rougier, Electrochromism of non-stoichiometric NiO thin film: as single layer and in full device, *Appl. Phys. A* 122 (2016) 10555. <https://doi.org/10.1007/s00339-016-9923-z>.

## References

- [202] J. Zhang, J.P. Tu, X.H. Xia, Y. Qiao, Y. Lu, An all-solid-state electrochromic device based on NiO/WO<sub>3</sub> complementary structure and solid hybrid polyelectrolyte, *Sol. Energy Mater. Sol. Cells* 93 (2009) 1840–1845. <https://doi.org/10.1016/j.solmat.2009.06.025>.
- [203] P.-W. Chen, C.-T. Chang, T.-F. Ko, S.-C. Hsu, K.-D. Li, J.-Y. Wu, Fast response of complementary electrochromic device based on WO<sub>3</sub>/NiO electrodes, *Sci. Rep.* 10 (2020) 8430. <https://doi.org/10.1038/s41598-020-65191-x>.
- [204] W. Cheng, M. Moreno-Gonzalez, K. Hu, C. Krzyzskowski, D.J. Dvorak, D.M. Weekes, B. Tam, C.P. Berlinguette, Solution-Deposited Solid-State Electrochromic Windows, *iScience* 10 (2018) 80–86. <https://doi.org/10.1016/j.isci.2018.11.014>.
- [205] J. Padilla, T.F. Otero, Contrast limitations of dual electrochromic systems, *Electrochem. Commun.* 10 (2008) 1–6. <https://doi.org/10.1016/j.elecom.2007.10.004>.
- [206] S. Ulrich, C. Szyszko, S. Jung, M. Vergöhl, Electrochromic properties of mixed oxides based on titanium and niobium for smart window applications, *Surf. Coat. Technol.* 314 (2017) 41–44. <https://doi.org/10.1016/j.surfcoat.2016.11.078>.
- [207] R.S. de Oliveira, S.C. de Oliveira, O.C. Alves, F.S. Semaan, E.A. Ponzio, Electrochromic Behavior of Vanadium Oxide Nanostructures Synthesized by Melt Sonoquenching, *Rev. Virtual Quim.* 7 (2015). <https://doi.org/10.5935/1984-6835.20150109>.
- [208] I. Mjejri, M. Gaudon, A. Rougier, Mo addition for improved electrochromic properties of V<sub>2</sub>O<sub>5</sub> thick films, *Sol. Energy Mater. Sol. Cells* 198 (2019) 19–25. <https://doi.org/10.1016/j.solmat.2019.04.010>.
- [209] W. Kang, C. Yan, X. Wang, C.Y. Foo, A.W.M. Tan, K.J.Z. Chee, P.S. Lee, Green synthesis of nanobelt-membrane hybrid structured vanadium oxide with high electrochromic contrast, *J. Mater. Chem. C* 2 (2014) 4727–4732. <https://doi.org/10.1039/C4TC00158C>.
- [210] Stuart F. Cogan, Nguyet M. Nguyen, Stephen J. Perrotti, R. David Rauh, Optical properties of electrochromic vanadium pentoxide, *J. Appl. Phys.* 66 (1998) 1333. <https://doi.org/10.1063/1.344432>.
- [211] K. West, B. Zachau-Christiansen, T. Jacobsen, S. Skaarup, Lithium insertion into vanadium pentoxide bronzes, *Solid State Ionics* 76 (1995) 15–21. [https://doi.org/10.1016/0167-2738\(95\)94037-M](https://doi.org/10.1016/0167-2738(95)94037-M).
- [212] M. B. Sahana, C. Sudakar, C. Thapa, V. M. Naik, K. R. Padmanabhan, The effect of titanium on the lithium intercalation capacity of V<sub>2</sub>O<sub>5</sub> thin films, *Thin Solid Films* 517 (2009) 6642–6651. <https://doi.org/10.1016/j.tsf.2009.04.063>.
- [213] K. Lee, G. Cao, Enhancement of intercalation properties of V<sub>2</sub>O<sub>5</sub> film by TiO<sub>2</sub> addition, *J. Phys. Chem. B* 109 (2005) 11880–11885. <https://doi.org/10.1021/jp044651j>.
- [214] J.W. Lim, S.J. Yoo, S.H. Park, S.U. Yun, Y.-E. Sung, High electrochromic performance of co-sputtered vanadium–titanium oxide as a counter electrode, *Sol. Energy Mater. Sol. Cells* 93 (2009) 2069–2074. <https://doi.org/10.1016/j.solmat.2009.03.008>.
- [215] Surendren Sajitha, Unni Aparna, Biswapriya Deb, Ultra-Thin Manganese Dioxide-Encrusted Vanadium Pentoxide Nanowire Mats for Electrochromic Energy Storage Applications, *Adv. Mater. Interfaces* 6 (2019) 1901038. <https://doi.org/10.1002/admi.201901038>.

## References

- [216] C.G. Granqvist, Electrochromics for smart windows: Oxide-based thin films and devices, *Thin Solid Films* 564 (2014) 1–38. <https://doi.org/10.1016/j.tsf.2014.02.002>.
- [217] Nobuyuki Sakai, Yasuo Ebina, Kazunori Takada, Takayoshi Sasaki, Electrochromic Films Composed of MnO<sub>2</sub> Nanosheets with Controlled Optical Density and High Coloration Efficiency, *J. Electrochem. Soc.* 152 (2005) E384. <https://doi.org/10.1149/1.2104227>.
- [218] A. Danine, L. Mancieru, A. Fargues, A. Rougier, Eco-friendly redox mediator gelatin-electrolyte for simplified TiO<sub>2</sub>-viologen based electrochromic devices, *Electrochim. Acta* 258 (2017) 200–207. <https://doi.org/10.1016/j.electacta.2017.10.096>.
- [219] S. Bogati, A. Georg, W. Graf, Sputtered Si<sub>3</sub>N<sub>4</sub> and SiO<sub>2</sub> electron barrier layer between a redox electrolyte and the WO<sub>3</sub> film in electrochromic devices, *Sol. Energy Mater. Sol. Cells* 159 (2017) 395–404. <https://doi.org/10.1016/j.solmat.2016.08.023>.
- [220] A. Georg, A. Georg, Electrochromic device with a redox electrolyte, *Sol. Energy Mater. Sol. Cells* 93 (2009) 1329–1337. <https://doi.org/10.1016/j.solmat.2009.02.009>.
- [221] M. Hočevár, U. Opara Krašovec, Solid electrolyte containing a colorless redox couple for electrochromic device, *Sol. Energy Mater. Sol. Cells* 196 (2019) 9–15. <https://doi.org/10.1016/j.solmat.2019.03.027>.
- [222] M. Higuchi WO 2017/034036 A1.
- [223] Y. Saygili, M. Stojanovic, N. Flores-Díaz, S.M. Zakeeruddin, N. Vlachopoulos, M. Grätzel, A. Hagfeldt, Metal Coordination Complexes as Redox Mediators in Regenerative Dye-Sensitized Solar Cells. *Inorganics*, 7(3), 30 (2019). <https://doi.org/10.3390/INORGANICS7030030>.
- [224] D. Li, H. Li, Y. Luo, K. Li, Q. Meng, M. Armand, L. Chen, Non-Corrosive, Non-Absorbing Organic Redox Couple for Dye-Sensitized Solar Cells, *Adv. Funct. Mater.* 20 (2010) 3358–3365. <https://doi.org/10.1002/adfm.201000150>.
- [225] M. Grätzel, Solar energy conversion by dye-sensitized photovoltaic cells, *Inorg. Chem.* 44 (2005) 6841–6851. <https://doi.org/10.1021/ic0508371>.
- [226] H. Tahara, K. Uranaka, M. Hirano, T. Ikeda, T. Sagara, H. Murakami, Electrochromism of Ferrocene- and Viologen-Based Redox-Active Ionic Liquids Composite, *ACS Appl. Mater. Interfaces* 11 (2019) 1–6. <https://doi.org/10.1021/acsami.8b16410>.
- [227] Z. Zhang, P. Chen, T. N. Murakami, S. M. Zakeeruddin, M. Grätzel, The 2,2,6,6-Tetramethyl-1-piperidinyloxy Radical: An Efficient, Iodine-Free Redox Mediator for Dye-Sensitized Solar Cells, *Adv. Funct. Mater.* 18 (2008) 341–346. <https://doi.org/10.1002/adfm.200701041>.
- [228] M. Röder, Transparent thin film electrodes for lithium ion battery systems and electrochromic applications. PhD thesis, Würzburg, 2018.
- [229] S. Krishnamurthy, D.H.K. Reddy, G. Sankar, Y.-S. Yun, Facile room temperature deposition of gold nanoparticle-ionic liquid hybrid film on silica substrate, *Spectrochim. Acta Mol. Biomol. Spectrosc.* 170 (2017) 48–55. <https://doi.org/10.1016/j.saa.2016.07.004>.
- [230] DIN EN ISO 2409:2013-06, Beschichtungsstoffe - Gitterschnittprüfung, Beuth Verlag GmbH, Berlin.
- [231] M. Schott, L. Niklaus, B. Bozkaya, U. Posset, G.A. Giffin, Flexible electrochromic devices prepared on ultra-thin ITO glass, *Mater. Adv.* (2021) 4659. <https://doi.org/10.1039/D1MA00376C>.

## References

- [232] V. Mauro, A. D'Aprano, F. Croce, M. Salomon, Direct determination of transference numbers of LiClO<sub>4</sub> solutions in propylene carbonate and acetonitrile, *J. Power Sources* 141 (2005) 167–170. <https://doi.org/10.1016/j.jpowsour.2004.09.015>.
- [233] W. Pu, X. He, J. Lu, C. Jiang, C. Wan, Molar conductivity calculation of Li-ion battery electrolyte based on mode coupling theory, *J. Chem. Phys.* 123 (2005) 231105. <https://doi.org/10.1063/1.2149849>.
- [234] Y. Kato, S. Yokoyama, T. Yabe, H. Ikuta, Y. Uchimoto, M. Wakihara, Ionic conductivity and transport number of lithium ion in polymer electrolytes containing PEG–borate ester, *Electrochim. Acta* 50 (2004) 281–284. <https://doi.org/10.1016/j.electacta.2003.12.066>.
- [235] L.M. Mukherjee, D.P. Boden, R. Lindauer, Behavior of electrolytes in propylene carbonate. II. Further studies of conductance and viscosity properties. Evaluation of ion conductances, *J. Phys. Chem.* 74 (1970) 1942–1946. <https://doi.org/10.1021/j100704a020>.
- [236] L. Su, X. Liao, Z. Huang, A theoretical study on resistance of electrolytic solution: Measurement of electrolytic conductivity, *Results Phys.* 13 (2019) 102274. <https://doi.org/10.1016/j.rinp.2019.102274>.
- [237] Y. Suzuki, H. Maki, M. Matsui, M. Mizuhata, Conductivity of LiClO<sub>4</sub>/PC-DME Solution Impregnated in LiCoO<sub>2</sub> Powder, *Electrochemistry* 87 (2019) 294–296. <https://doi.org/10.5796/electrochemistry.19-00044>.
- [238] H.P. Chen, J.W. Fergus, B.Z. Jang, The Effect of Ethylene Carbonate and Salt Concentration on the Conductivity of Propylene Carbonate|Lithium Perchlorate Electrolytes, *J. Electrochem. Soc.* 147 399. <https://doi.org/10.1149/1.1393209>.
- [239] L. Niklaus, M. Schott, U. Posset, M. Mihelčič, I. Jerman, G.A. Giffin, Charge balancing and optical contrast optimization in Fe-MEPE/Ni<sub>1-x</sub>O electrochromic devices containing a Li reference electrode, *Sol. Energy Mater. Sol. Cells* (2021) 111080. <https://doi.org/10.1016/j.solmat.2021.111080>.
- [240] R. Cerc Korošec, M. Felicijan, B. Žener, M. Pompe, G. Dražić, J. Padežnik Gomilšek, B. Pihlar, P. Bukovec, The role of thermal analysis in optimization of electrochromic effect of nickel oxide thin films, prepared by the sol-gel method: Part III, *Thermochim. Acta* 655 (2017) 344–350. <https://doi.org/10.1016/j.tca.2017.07.010>.
- [241] W.-L. Jang, Y.-M. Lu, W.-S. Hwang, W.-C. Chen, Electrical properties of Li-doped NiO films, *J. Eur. Ceram. Soc.* 30 (2010) 503–508. <https://doi.org/10.1016/j.jeurceramsoc.2009.05.041>.
- [242] Xingfang Hu, Xiaofeng Chen, Michael G. Hutchins, Study on the electrochromic mechanism of rf diode sputtered nickel oxide films, *International Society for Optics and Photonics*, 1992, pp. 73–79.
- [243] M. Bonomo, A.G. Marrani, V. Novelli, M. Awais, D.P. Dowling, J.G. Vos, D. Dini, Surface properties of nanostructured NiO undergoing electrochemical oxidation in 3-methoxy-propionitrile, *Appl. Surf. Sci.* 403 (2017) 441–447. <https://doi.org/10.1016/j.apsusc.2017.01.202>.
- [244] I. Sorar, T.G. Welearegay, D. Primetzhofner, L. Österlund, C.G. Granqvist, G.A. Niklasson, Electrochromism in Ni Oxide Thin Films Made by Advanced Gas Deposition and Sputtering: A Comparative Study Demonstrating the Significance of Surface Effects, *J. Electrochem. Soc.* 167 116519. <https://doi.org/10.1149/1945-7111/aba5d9>.



## References

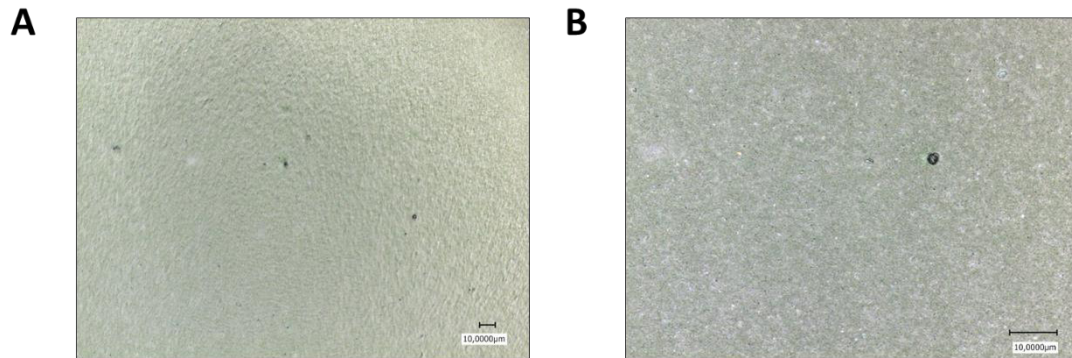
- [245] S. Hassab, D.E. Shen, A.M. Österholm, J.R. Reynolds, J. Padilla, Exploring unbalanced electrode configurations for electrochromic devices, *J. Mater. Chem. C* 6 (2018) 393–400. <https://doi.org/10.1039/C7TC04730D>.
- [246] D. Wang, L. Wei, P. Shi, Y. Chen, S. Yan, Y. Tian, J. Jiao, Electrochromic behavior of fluorine-doped tin oxide film via guided motion of Li ions, *J. Alloys Compd.* 771 (2019) 100–105. <https://doi.org/10.1016/j.jallcom.2018.08.268>.
- [247] J. Remmele, D.E. Shen, T. Mustonen, N. Fruehauf, High Performance and Long-Term Stability in Ambiently Fabricated Segmented Solid-State Polymer Electrochromic Displays, *ACS Appl. Mater. Interfaces* 7 (2015) 12001–12008. <https://doi.org/10.1021/acsami.5b02090>.
- [248] M.A. Arvizu, H.-Y. Qu, G.A. Niklasson, C.G. Granqvist, Electrochemical pretreatment of electrochromic WO<sub>3</sub> films gives greatly improved cycling durability, *Thin Solid Films* 653 (2018) 1–3. <https://doi.org/10.1016/j.tsf.2018.02.032>.
- [249] H.-Y. Qu, D. Primetzhofer, M.A. Arvizu, Z. Qiu, U. Cindemir, C.G. Granqvist, G.A. Niklasson, Electrochemical Rejuvenation of Anodically Coloring Electrochromic Nickel Oxide Thin Films, *ACS Appl. Mater. Interfaces* 9 (2017) 42420–42424. <https://doi.org/10.1021/acsami.7b13815>.
- [250] R.-T. Wen, C.G. Granqvist, G.A. Niklasson, Eliminating degradation and uncovering ion-trapping dynamics in electrochromic WO<sub>3</sub> thin films, *Nat. Mater.* 14 (2015) 996–1001. <https://doi.org/10.1038/nmat4368>.
- [251] M.D.J. Auch, O.K. Soo, G. Ewald, C. Soo-Jin, Ultrathin glass for flexible OLED application, *Thin Solid Films* 417 (2002) 47–50. [https://doi.org/10.1016/S0040-6090\(02\)00647-8](https://doi.org/10.1016/S0040-6090(02)00647-8).
- [252] Han You, Andrew J. Steckl, Lightweight electrowetting display on ultra-thin glass substrate, *J. Soc. Inf. Disp.* 21 (2013) 192–197. <https://doi.org/10.1002/jsid.169>.
- [253] C.G. Granqvist, G.A. Niklasson, Thermochromic Oxide-Based Thin Films and Nanoparticle Composites for Energy-Efficient Glazings, *Buildings* 7 (2017) 3. <https://doi.org/10.3390/buildings7010003>.
- [254] S. Loquai, B. Baloukas, O. Zabeida, J.E. Klemberg-Sapieha, L. Martinu, HiPIMS-deposited thermochromic VO<sub>2</sub> films on polymeric substrates, *Sol. Energy Mater. Sol. Cells* 155 (2016) 60–69. <https://doi.org/10.1016/j.solmat.2016.04.048>.
- [255] D. Kim, S.S. Shin, S.M. Lee, J.-S. Cho, J.H. Yun, H.S. Lee, J.H. Park, Flexible and Semi-Transparent Ultra-Thin CIGSe Solar Cells Prepared on Ultra-Thin Glass Substrate: A Key to Flexible Bifacial Photovoltaic Applications, *Adv. Funct. Mater.* 30 (2020) 2001775. <https://doi.org/10.1002/adfm.202001775>.
- [256] S. Castro-Hermosa, G. Lucarelli, M. Top, M. Fahland, J. Fahlteich, T.M. Brown, Perovskite Photovoltaics on Roll-To-Roll Coated Ultra-thin Glass as Flexible High-Efficiency Indoor Power Generators, *Cell Rep. Phys. Sci.* 1 (2020) 100045. <https://doi.org/10.1016/j.xcrp.2020.100045>.
- [257] M. Fahland, O. Zywitzki, T. Modes, K. Vondkar, T. Werner, C. Ottermann, M. Berendt, G. Pollack, Roll-to-roll sputtering of indium tin oxide layers onto ultrathin flexible glass, *Thin Solid Films* 669 (2019) 56–59. <https://doi.org/10.1016/j.tsf.2018.10.032>.
- [258] Y. Sung, R.E. Malay, X. Wen, C.N. Bezama, V.V. Soman, M.-H. Huang, S.M. Garner, M.D. Poliks, D. Klotzkin, Anti-reflective coating with a conductive indium tin oxide layer on flexible glass substrates, *Appl. Opt.* 57 (2018) 2202–2207. <https://doi.org/10.1364/AO.57.002202>.

## References

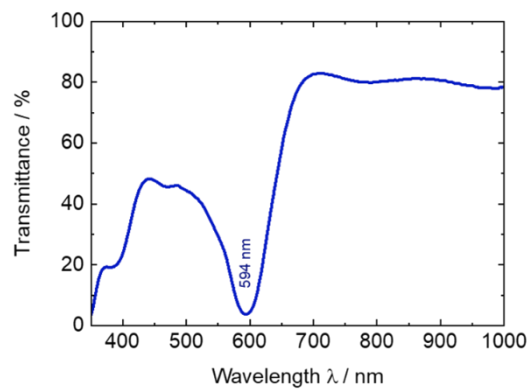
- [259]L. Niklaus, M. Schott, J. Subel, S. Ulrich, D. Reichert, U. Posset, G.A. Giffin, Mixed metal oxides as optically-passive ion storage layers in electrochromic devices based on metallopolymers, *Sol. Energy Mater. Sol. Cells* (2021) 110950. <https://doi.org/10.1016/j.solmat.2020.110950>.
- [260]R.R. Gagne, C.A. Koval, G.C. Lisensky, Ferrocene as an internal standard for electrochemical measurements. *Inorganic Chemistry*, 19(9), 2854-2855 (1980). <https://doi.org/10.1021/IC50211A080>.
- [261]K. Ueno, J. Murai, K. Ikeda, S. Tsuzuki, M. Tsuchiya, R. Tatara, T. Mandai, Y. Umebayashi, K. Dokko, M. Watanabe, Li + Solvation and Ionic Transport in Lithium Solvate Ionic Liquids Diluted by Molecular Solvents, *J. Phys. Chem. C* 120 (2016) 15792–15802. <https://doi.org/10.1021/acs.jpcc.5b11642>.

## Appendix

### Part I: Neutral tint with Fe-MEPE and Ni<sub>1-x</sub>O thin film electrodes



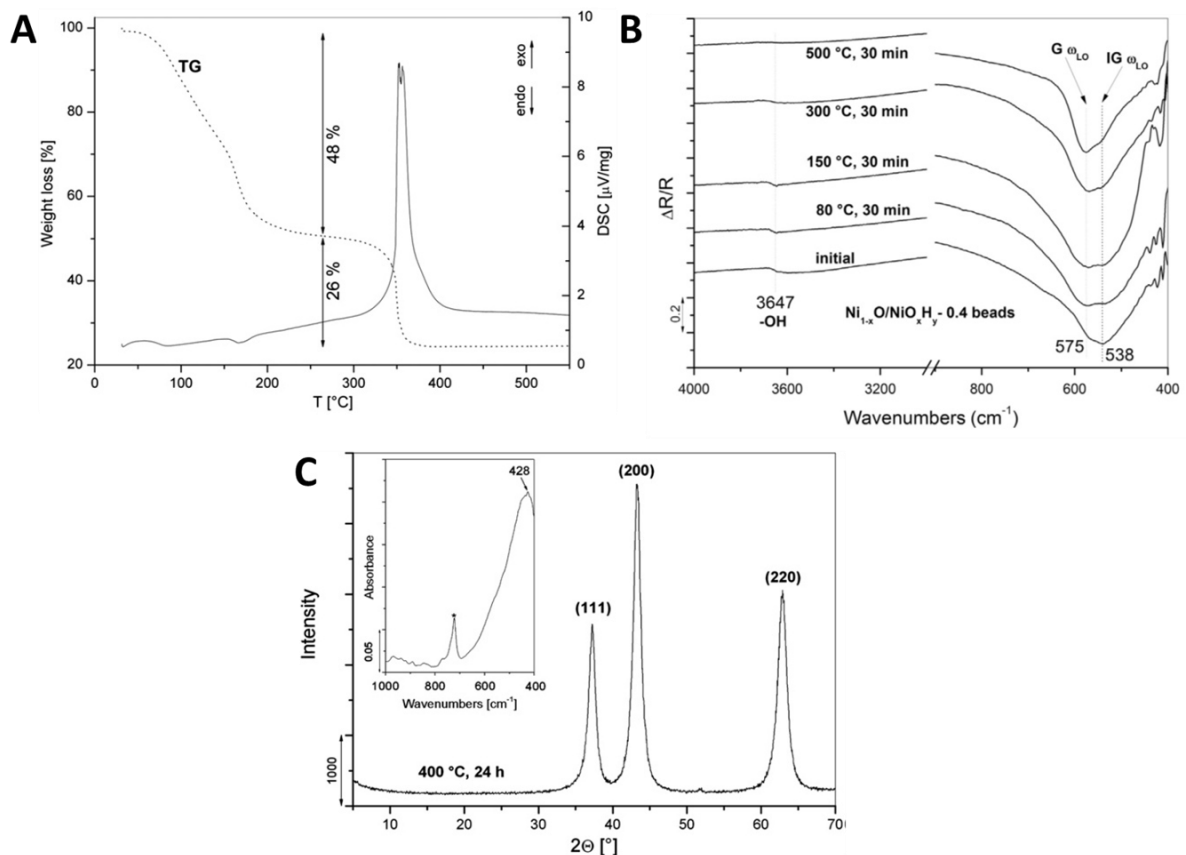
**Fig. S1:** LSM images depicting the surface of (A) the Fe-MEPE thin films and (B) Ni<sub>1-x</sub>O on FTO glass.

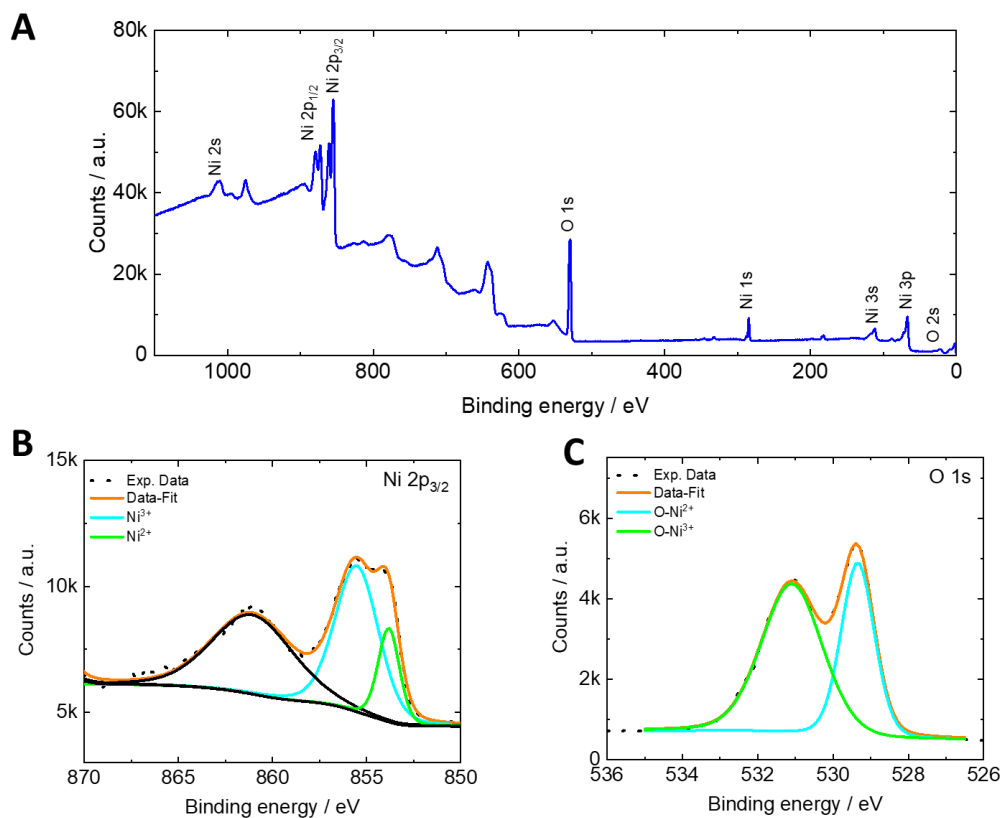


**Fig. S2:** Transmission spectra of Fe-MEPE (330 nm) on FTO glass.

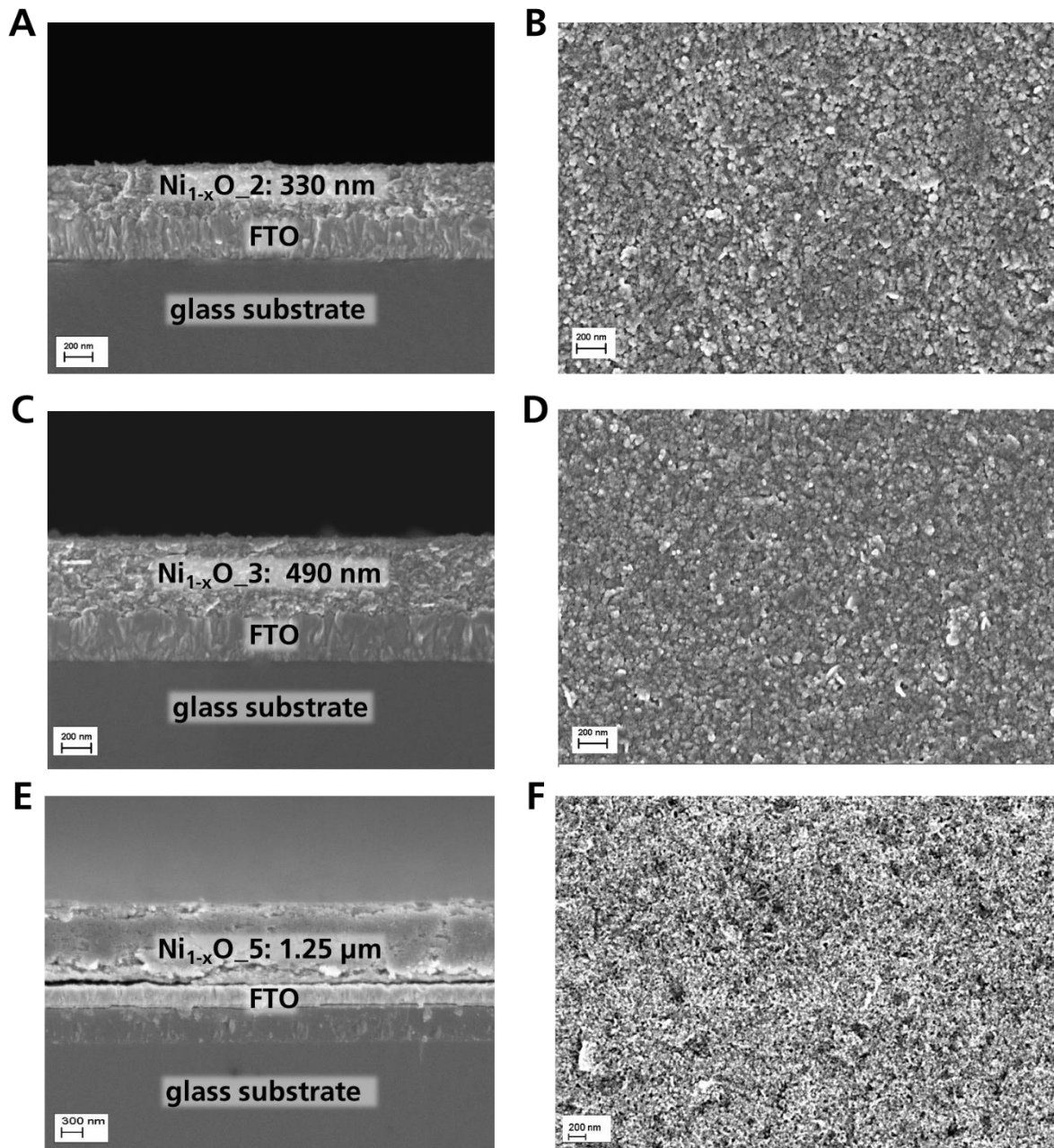
**Tab. S1:** Color ( $L^*a^*b^*$ ) coordinates, visible light transmittance ( $\tau_v$ ), and haze values of the Fe-MEPE and  $Ni_{1-x}O$  variants on FTO glass.

EC electrodes	$L^*$	$a^*$	$b^*$	T (at 584 nm) / %	$\tau_v$ / %	Haze / %
Fe-MEPE	60.3	13.1	22.4	4	27	1.0
$Ni_{1-x}O_2$	94.7	1.9	4.8	91	87	0.7
$Ni_{1-x}O_3$	91.4	0.7	6.4	82	80	0.6
$Ni_{1-x}O_4$	74.7	2.1	12.7	52	49	0.4
$Ni_{1-x}O_5$	70.0	2.7	14.8	47	43	0.4
$Ni_{1-x}O_6$	62.0	4.5	17.1	34	31	0.3

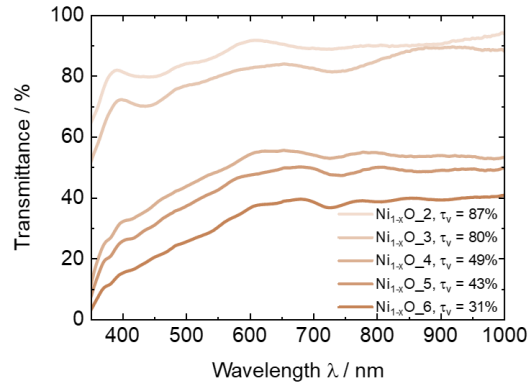
**Fig. S3:** (A) TGA and DSC curves for nickel oxide xerogel powder in air at a heating rate of  $10\text{ }^\circ\text{C}\cdot\text{min}^{-1}$ . Reproduced from ref. [71] with permission of Elsevier. (B) IR RA spectra of  $Ni_{1-x}O/NiO_xH_y$  pigment coatings prepared using milling beads of 0.4 mm and thermally treated at various temperatures. Reproduced from ref. [185] with permission of Elsevier. (C) XRD pattern and IR absorbance spectrum of NiO powder obtained after heat-treatment at  $400\text{ }^\circ\text{C}$  for 24h. Reproduced from ref. [72] with permission from Elsevier.



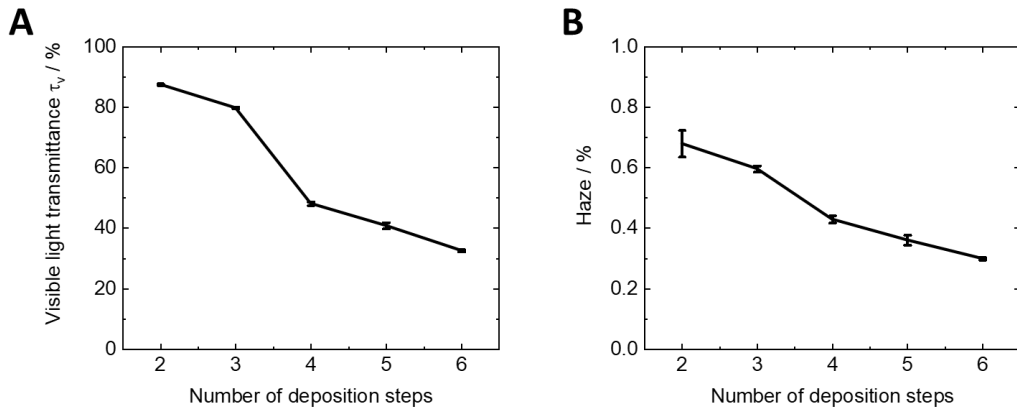
**Fig. S4:** XPS spectra of as-prepared  $\text{Ni}_{1-x}\text{O}_5$ : (A) overview spectra and zoomed in on the (B) Ni 2p<sub>3/2</sub> and (C) O 1s region.



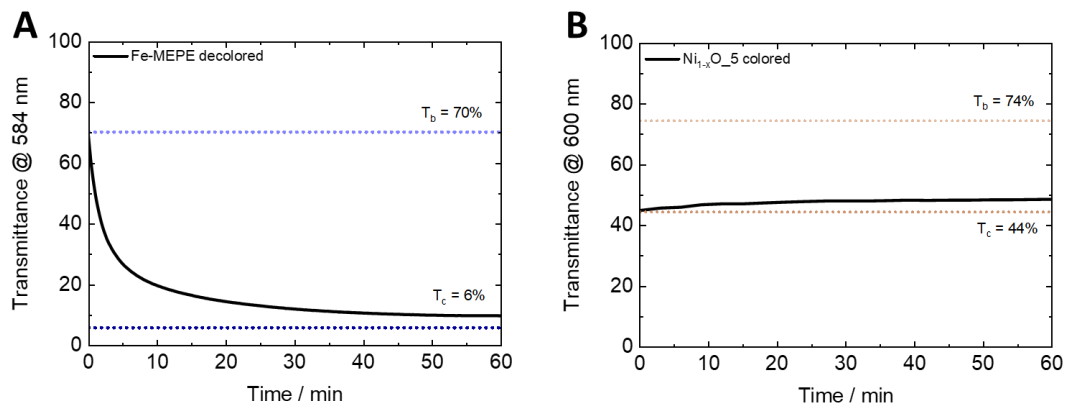
**Fig. S5:** SEM images depicting the layer thickness and the surface structure of the (A,B)  $\text{Ni}_{1-x}\text{O}_2$ , (C,D)  $\text{Ni}_{1-x}\text{O}_3$ , and (E,F)  $\text{Ni}_{1-x}\text{O}_5$  thin films on FTO glass. The delamination of  $\text{Ni}_{1-x}\text{O}_5$  is due to preparation issues.



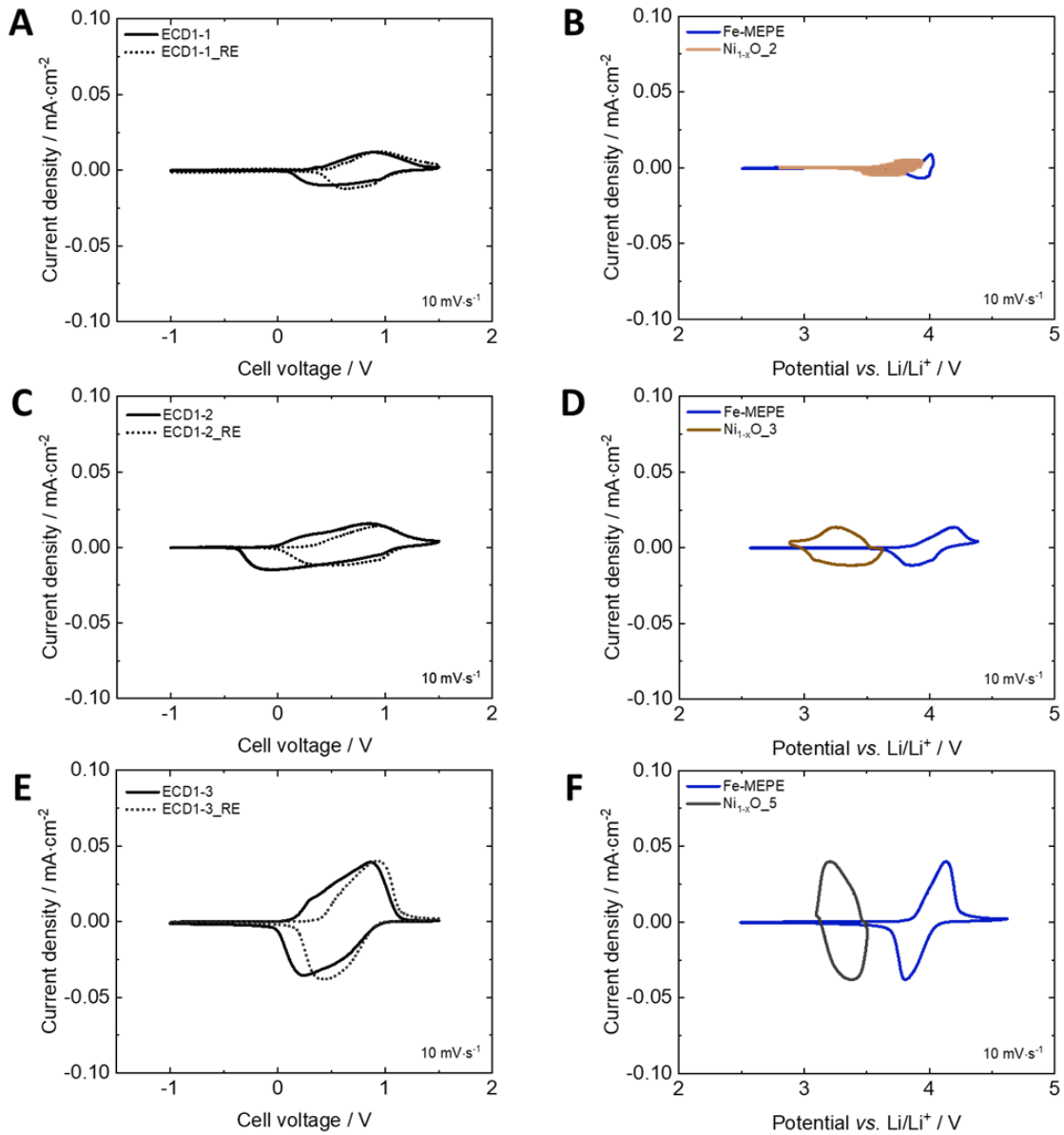
**Fig. S6:** Transmission spectra of Ni<sub>1-x</sub>O electrodes deposited with 2 to 6 layers.



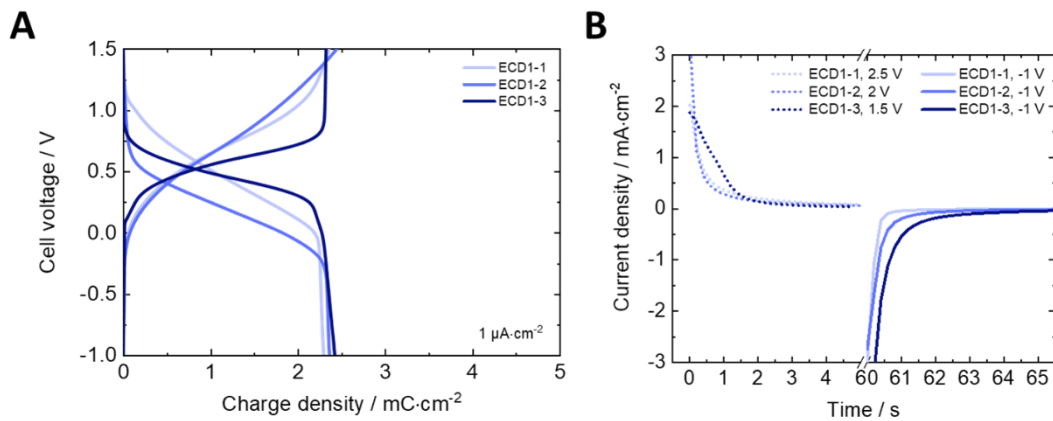
**Fig. S7:** Visible light transmittance (τ<sub>v</sub>) and haze values of Ni<sub>1-x</sub>O electrodes deposited with 2 to 6 layers vs. the number of deposition steps.



**Fig. S8:** Time-dependent transmittance change at 584 nm and 600 nm under OCP conditions for the (A) decolored Fe-MEPE and (B) colored Ni<sub>1-x</sub>O<sub>5</sub> electrodes, respectively. The dotted lines indicate the transmittance levels of the completely decolored (T<sub>b</sub>) and colored states (T<sub>c</sub>) of the electrodes.

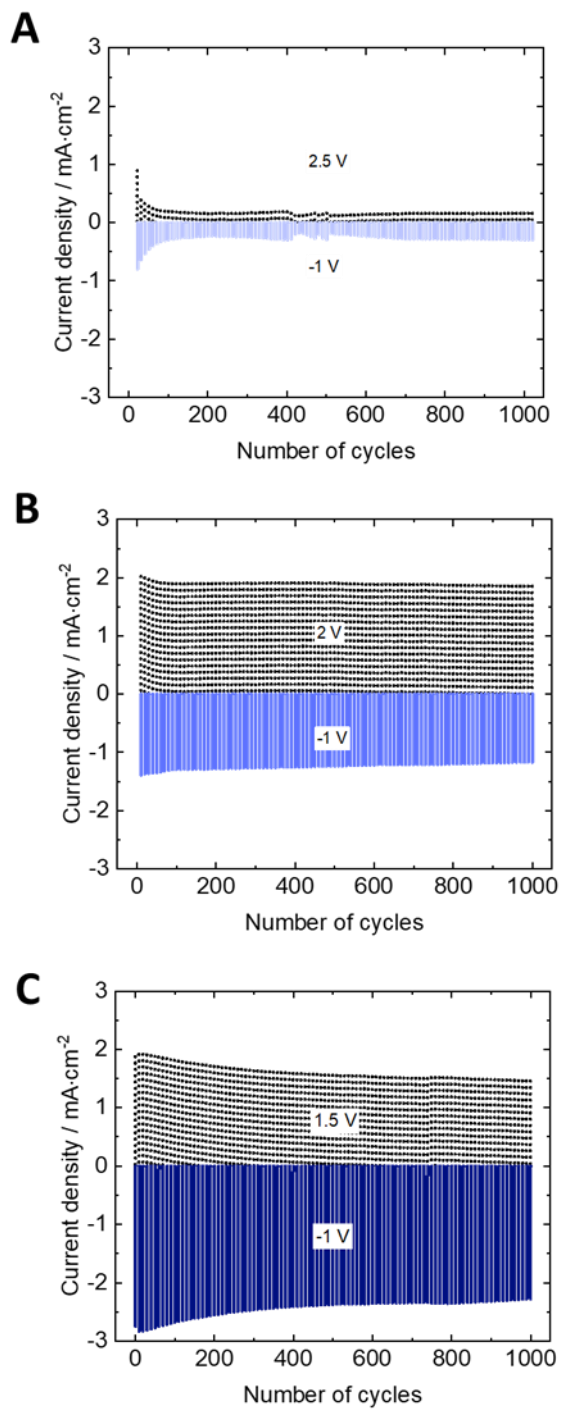


**Fig. S9:** Comparison of the CVs of the two-electrode and three-electrode full cells (A) **ECD1-1**, (C) **ECD1-2**, and (E) **ECD1-3** at a scan rate of 10 mV·s<sup>-1</sup> and the corresponding CVs of each EC electrode obtained from (B) **ECD1-1\_RE**, (D) **ECD1-2\_RE**, and (F) **ECD1-3\_RE**.

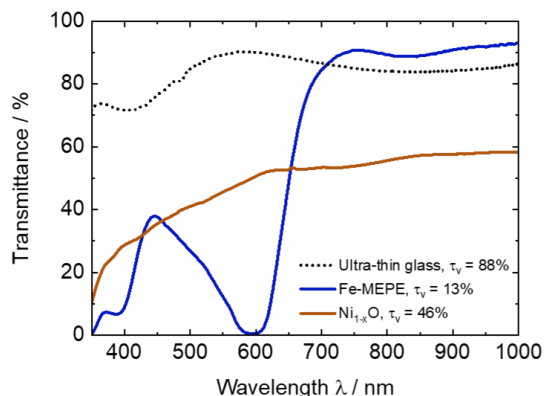


**Fig. S10:** (A) Galvanostatic charging/discharging measurements with a current density of 1 μA cm<sup>-2</sup> and (B) current-time profiles for **ECD1-1**, **ECD1-2**, and **ECD1-3**.





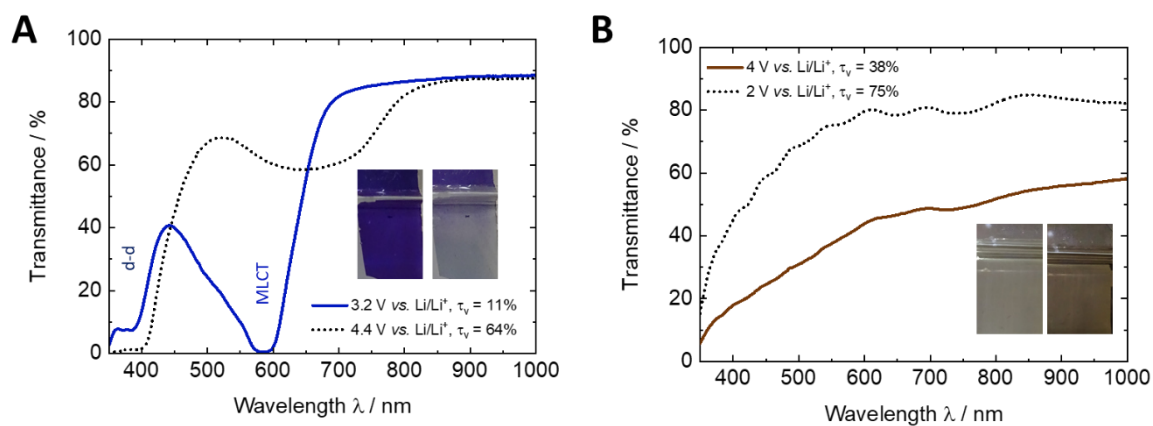
**Fig. S11:** Current-time profiles for (A) **ECD1-1\_RE**, (C) **ECD1-2\_RE**, and (E) **ECD1-3\_RE** over 1,000 potentiostatic switching cycles.



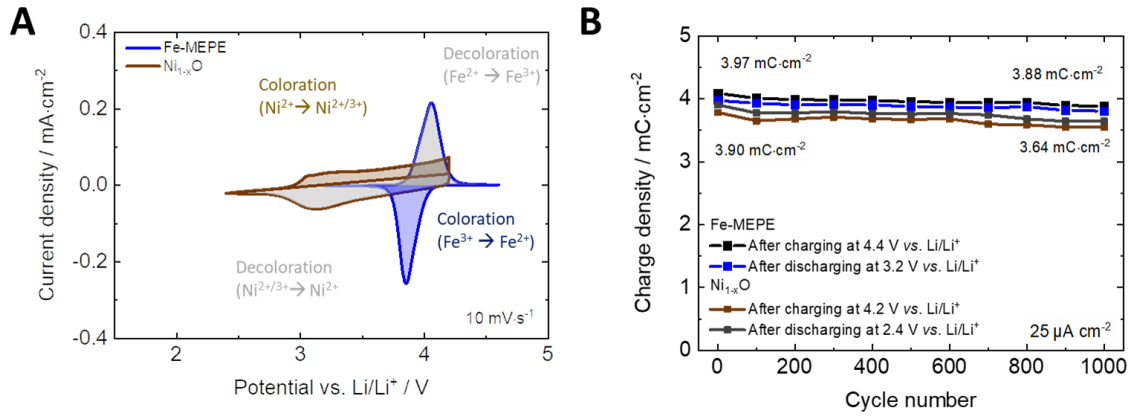
**Fig. S12:** Transmission spectra of the Fe-MEPE and Ni<sub>1-x</sub>O thin film electrodes on ultra-thin ITO glass.

**Tab. S2:** Color coordinates ( $L^*a^*b^*$ ), transmittance at 584 nm, visible light transmittance ( $\tau_v$ ) of the EC electrodes on ultra-thin ITO glass (Fe-MEPE and Ni<sub>1-x</sub>O).

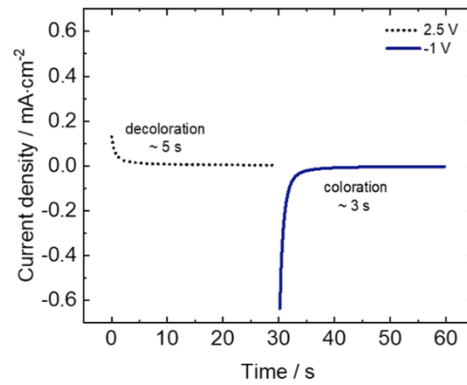
EC electrodes	$L^*$	$a^*$	$b^*$	T (at 584 nm) / %	$\tau_v$ / %	Haze / %
Fe-MEPE	45.5	-1.1	-32.6	0.8	13	1.0
Ni <sub>1-x</sub> O	74.1	1.8	12.8	49	46	0.8



**Fig. S13:** Spectroelectrochemical characterization of (A) Fe-MEPE and (B) Ni<sub>1-x</sub>O thin film electrodes on ultra-thin ITO glass with Li as CE and RE in 1 M LiClO<sub>4</sub>/PC as electrolyte.

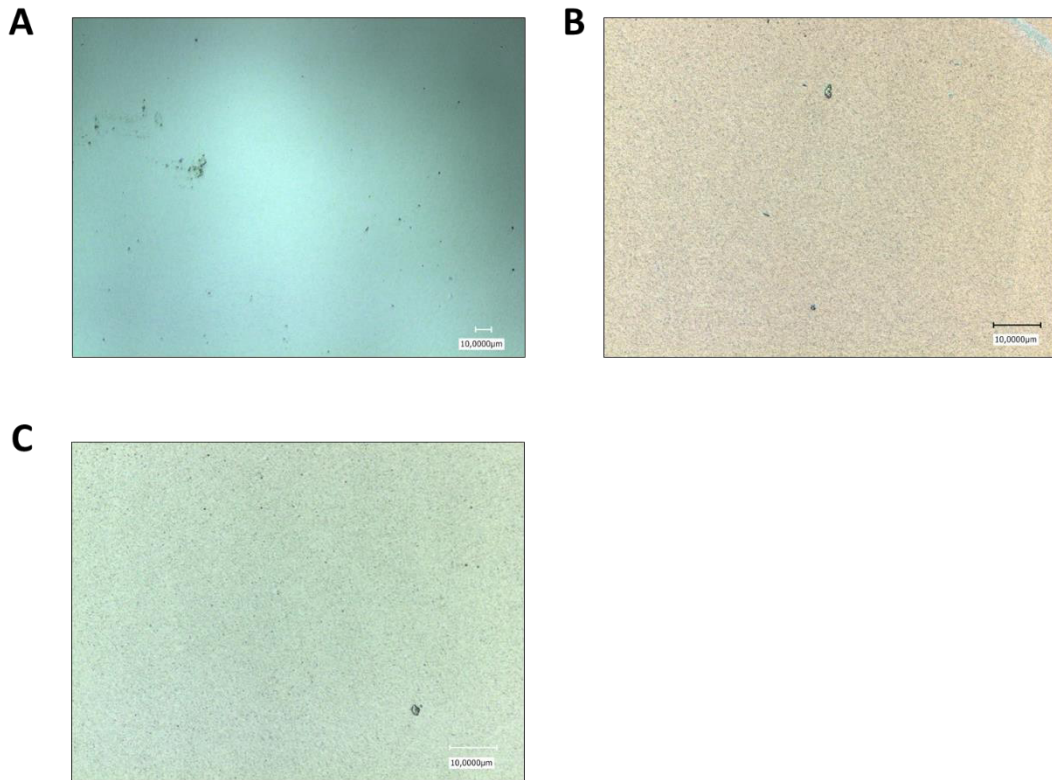


**Fig. S14:** (A) CVs (at  $10 \text{ mV} \cdot \text{s}^{-1}$ ) and (B) galvanostatic charging/discharging measurements with a current density of  $25 \mu\text{A} \cdot \text{cm}^{-2}$  over 1,000 switching cycles of Fe-MEPE and  $\text{Ni}_{1-x}\text{O}$  thin film electrodes on ultra-thin glass with Li as CE and RE in 1 M  $\text{LiClO}_4/\text{PC}$  as electrolyte.

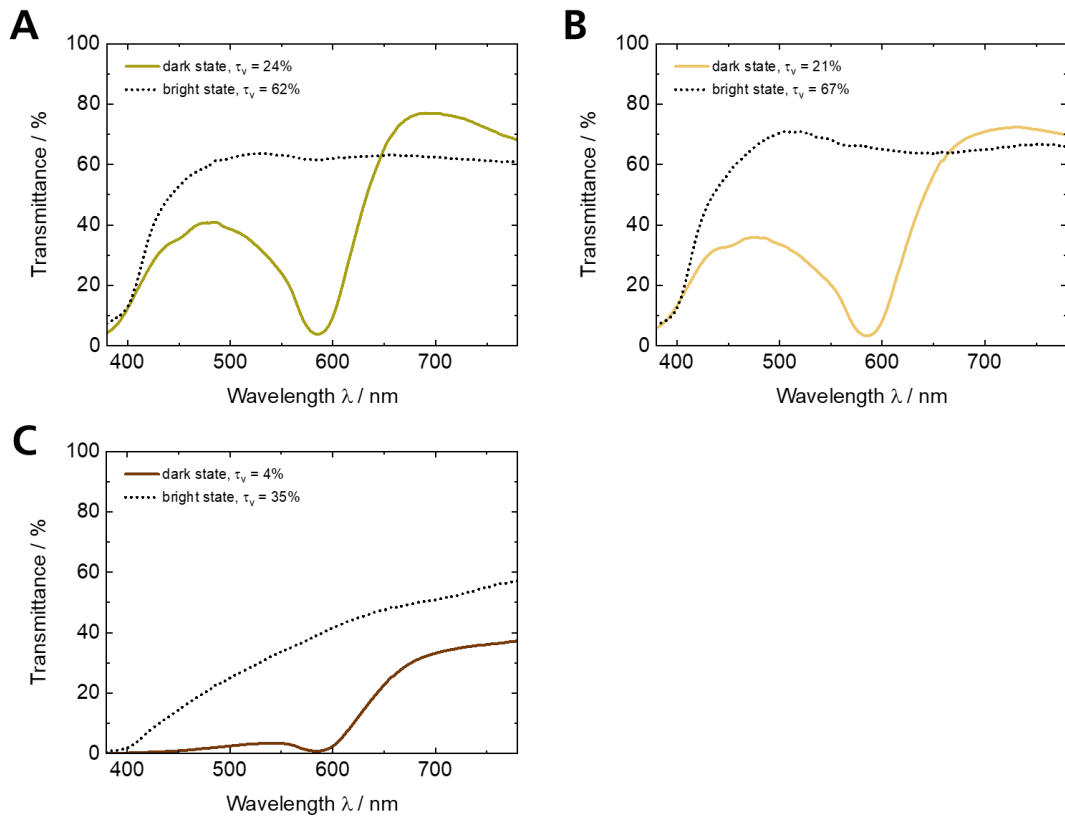


**Fig. S15:** Current density-time profile of the Fe-MEPE/ $\text{Ni}_{1-x}\text{O}$  ECDs on ultra-thin ITO glass.

## Part II: Optically-passive mixed metal oxides



**Fig. S16:** LSM images of the surface of (A)  $\text{TiVO}_x$ , (B) **TMO-1**, and (C) **TMO-2** thin films on FTO glass.

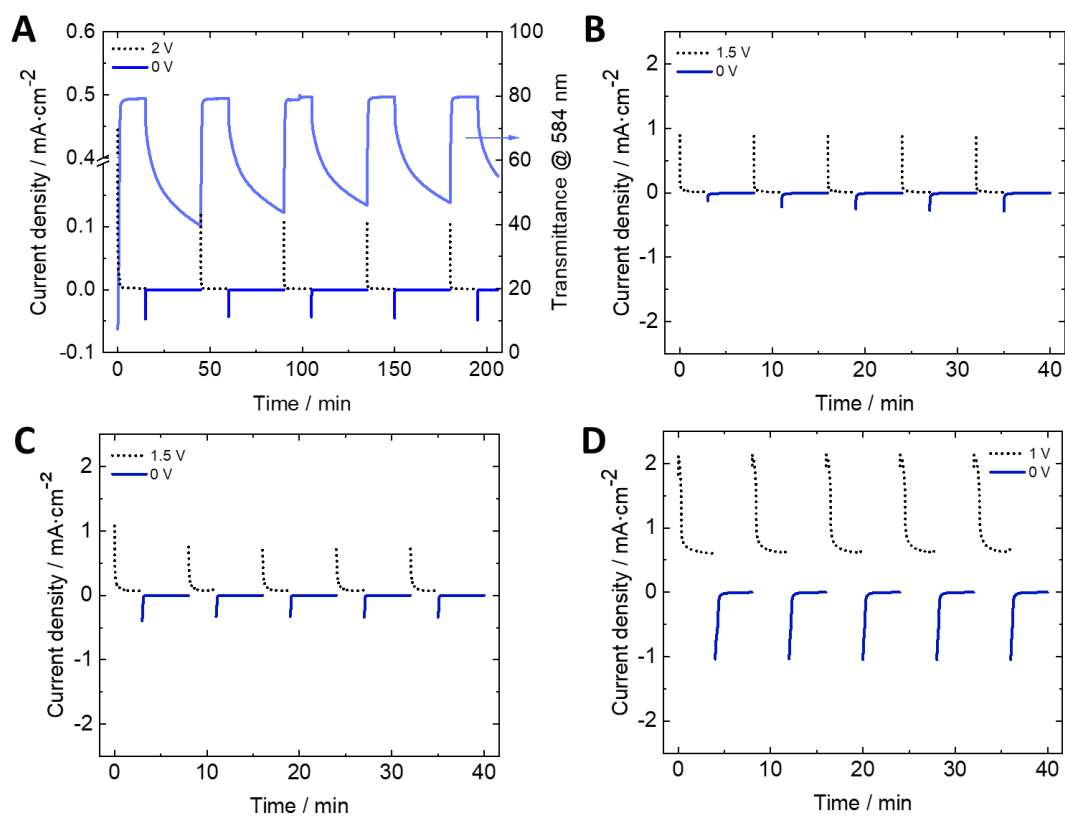


**Fig. S17:** Theoretical transmission spectra obtained from the combination of the transmission spectra of the single electrodes for (A) **ECD2-1** (Fe-MEPE/ $\text{TiVO}_x$ ), (B) **ECD2-2** (Fe-MEPE/**TMO-1**), and (C) **ECD2-3** (Fe-MEPE/**TMO-2**).

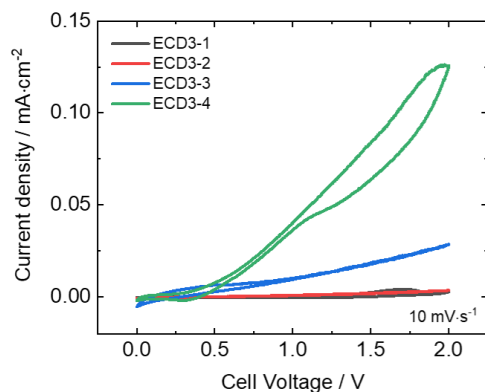
### Part III: Simplification of the cell architecture using redox mediators

**Tab. S3:** Redox potentials of the electrolyte redox mediator pairs and the EC electrodes.

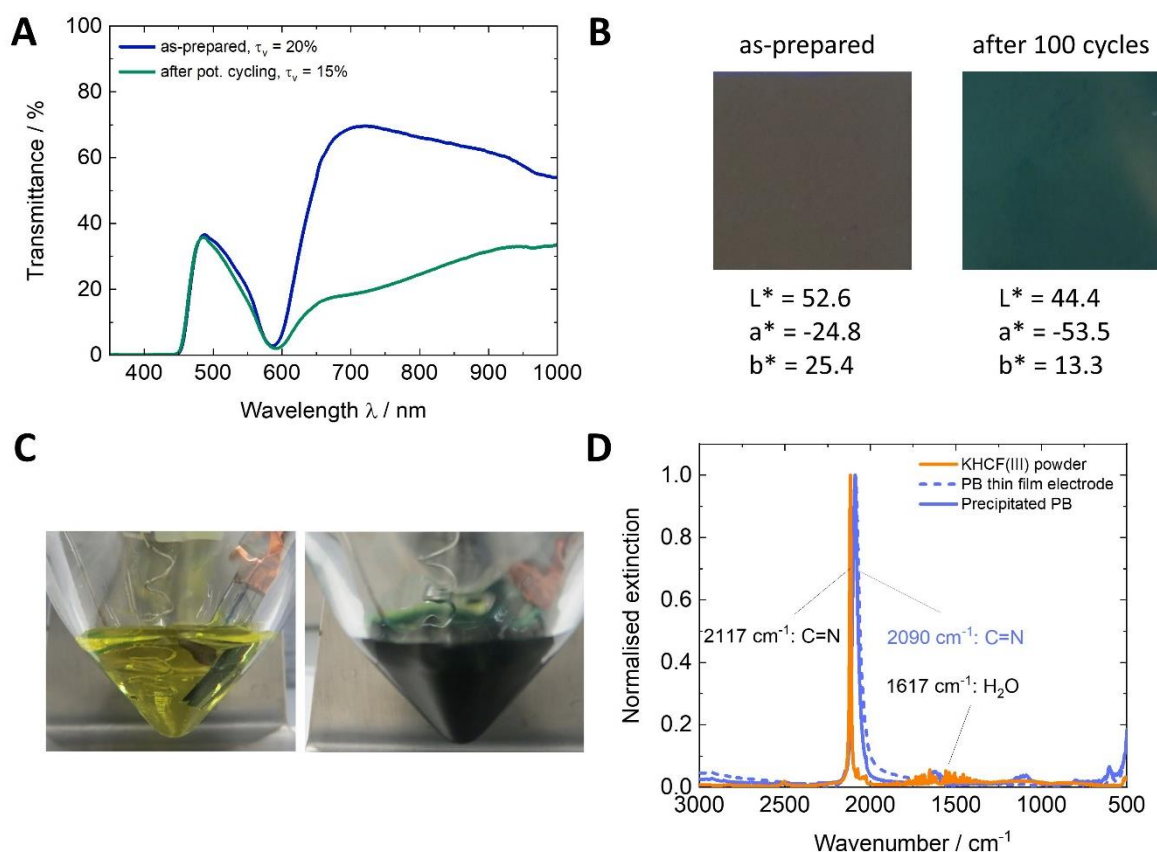
Redox pair	Redox potential vs. Ag/AgCl / V	Redox potential vs. Li/Li <sup>+</sup> / V
HCF(II)/(III)	0.25 <sup>[108]</sup>	3.07
Fc <sup>0/+</sup>	0.20 <sup>[260]</sup>	3.02
TMTU/TMFDS <sup>2+</sup>	0.45 <sup>[108]</sup>	3.27
Fe <sup>2+</sup> /Fe <sup>3+</sup> (Fe-MEPE)		3.95
Ni <sup>2+</sup> /Ni <sup>3+</sup> (Ni <sub>1-x</sub> O)		3.13



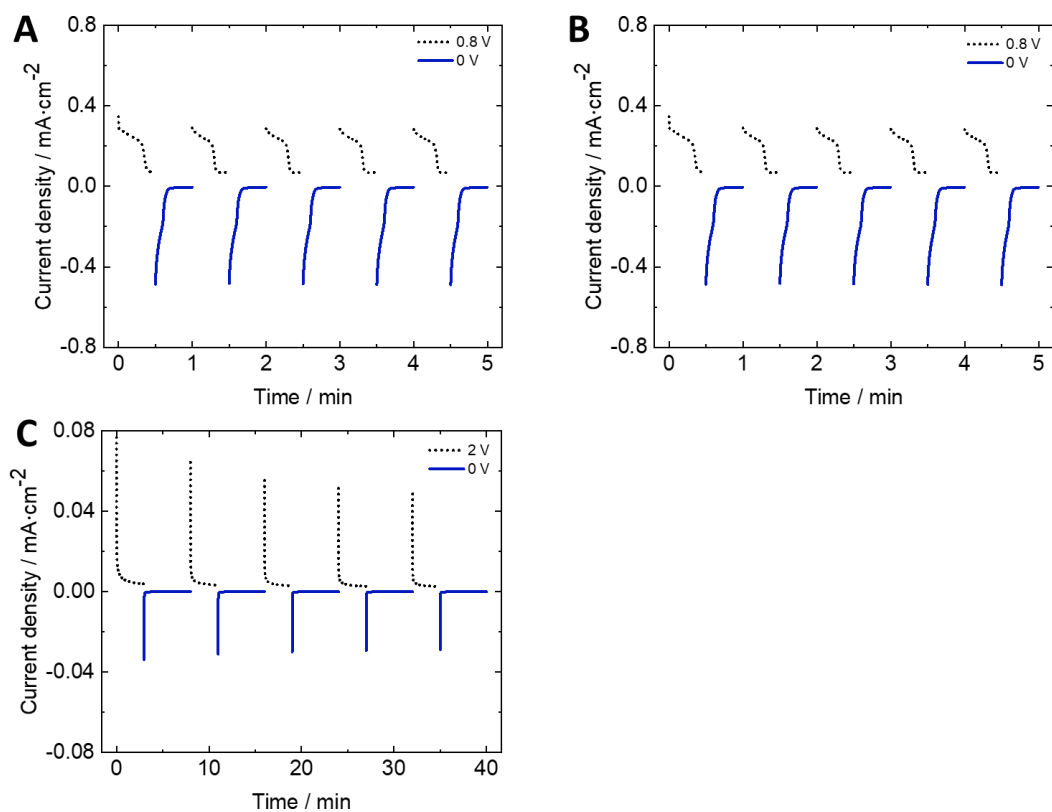
**Fig. S18:** Current density-time profiles of ECDs with increasing KHCF(III) concentration in 1 M LiClO<sub>4</sub>/H<sub>2</sub>O electrolyte: (A) **ECD3-1** (with transmittance @ 584 nm), (B) **ECD3-2**, (C) **ECD3-3**, and (D) **ECD3-4**.



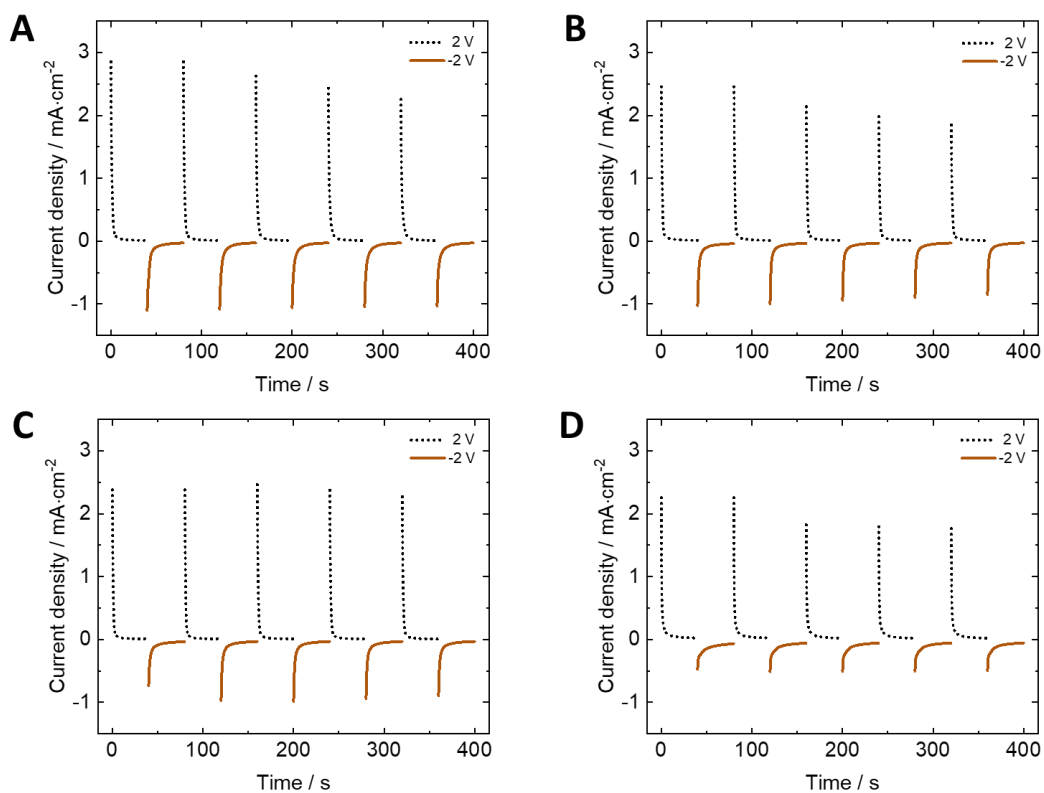
**Fig. S19:** CV measurements of ECDs with increasing KHCF(III) concentration in 1 M LiClO<sub>4</sub>/H<sub>2</sub>O electrolyte.



**Fig. S20:** (A) Transmission spectra of **ECD3-4** in the as-prepared (dark) state and after 100 cycles between 0 V and 1 V. (B) Photographs from of the ECDs in (A) and  $L^*a^*b^*$  color coordinates indicating a distinct color change due to the PB formation in the electrolyte. (C) Photographs of the electrolyte in the two-electrode set-up with Fe-MEPE (WE) and platinum (CE). (D) IR spectra of the KHCF(III) powder (orange line), a PB thin film electrode as reference (dotted blue line), and precipitated PB in the electrolyte (blue line).



**Fig. S21:** Current-time profiles of (A) **ECD3-5**, (B) **ECD3-6**, and (C) **ECD3-7** with 0.1 M Fc-PF<sub>6</sub>, 0.1 M Fc-BF<sub>4</sub>, and 0.1 M TMFDS<sup>2+</sup> in 1 M LiClO<sub>4</sub>/PC as electrolyte, respectively.



**Fig. S22:** Current-time profiles of (A) **ECD3-8**, (B) **ECD3-9**, (C) **ECD3-10**, and (D) **ECD3-11** with different molar ratios of 0.1 M TMTU/TMFDS<sup>2+</sup> (1:0, 1:0.1, and 1:1) in 1 M LiClO<sub>4</sub>/PC electrolyte, respectively.

## List of publications, posters, and conferences

This thesis is based on the following papers. The corresponding author is marked with \*. Reprints were made with permission from the respective publishers.

**Niklaus, L.**, Schott, M.\*, Mihelčič, M., Jerman, I., Posset, U., Sextl, G., Metallopolymers and non-stoichiometric nickel oxide: Towards neutral tint large-area electrochromic devices, *Sol. Energy Mater. Sol. Cells* 200 (2019), 9, 110002.

**Niklaus, L.**, Schott, M. \*, Posset, U., Giffin, G., Redox Electrolytes for Hybrid Type II Electrochromic Devices with Fe-MEPE or Ni<sub>1-x</sub>O as Electrode Materials, *ChemElectroChem* (2020), 7, 1-11.

**Niklaus, L.**, Schott, M. \*, Subel, J., Ulrich, S., Reichert, D., Posset, U., Giffin, G., Mixed metal oxides as optically-passive ion storage layers in electrochromic devices based on metallopolymers, *Sol. Energy Mater. Sol. Cells* 223 (2021), 110950.

**Niklaus, L.**, Schott, M. \*, Posset, U., Mihelčič, M., Jerman, I., Giffin, G., Charge balancing and optical contrast optimization in Fe-MEPE/Ni<sub>1-x</sub>O electrochromic devices containing a Li reference electrode, *Sol. Energy Mater. Sol. Cells* 227 (2021) 111080.

The results of the following papers are not included in this thesis:

Pai, S., Schott, M., **Niklaus, L.**, Posset, U., Kurth, D. G.\*, A study of the effect of pyridine linkers on the viscosity and electrochromic properties of metallo-supramolecular coordination polymers, *J. Mater. Chem. C* 6 (2018), 13, 3310-3321.

Schott, M. \*, **Niklaus, L.**, Clade, J., Posset, U., Electrochromic metallo-supramolecular polymers showing visible and near-infrared light transmittance modulation, *Sol. Energy Mater. Sol. Cells* 200 (2019), 110001, 8.

Schott, M. \*, **Niklaus, L.**, Bozkaya, B., Posset, U., Giffin, G. Flexible electrochromic devices prepared on ultra-thin ITO glass, *RSC Materials Advances* 2 (2021) 4659-4666.



## **Presentation**

**Niklaus, L.**, Zukunftstrend schaltbare Verglasung – Stand der Technik, Forschung und Entwicklung, (45. Rosenheimer Fenstertage, October **2017**)

## **Poster**

**Niklaus, L.**, Mihelčič, M., Jerman, I., Schott, M., Posset, U., SEXTL, G., Metallopolymers and non-stoichiometric nickel oxide: Towards neutral tint large-area electrochromic devices (ICCG 12, Würzburg, June **2018**)

**Niklaus, L.**, Mihelčič, M., Jerman, I., Schott, M., Posset, U., SEXTL, G., Metallo-supramolecular polyelectrolytes and non-stoichiometric nickel oxide: Towards neutral-tint flexible electrochromic devices (IME-13, Tokyo, Japan, August **2019**)

## Contribution to the publications

This cumulative dissertation is a shortened version of the obtained and published results. The individual contribution of each co-author for each publication is shown in the following forms.



### Erklärung zur Autorenschaft

Metallopolymers and non-stoichiometric nickel oxide: Towards neutral tint large-area electrochromic devices, Lukas Nikolaus, Marco Schott\*, Ivan Jerman, Uwe Posset, Gerhard Sextl, *Solar Energy Materials and Solar Cells* **2019**, 200, 110002.

Detaillierte Darstellung der Anteile an der Veröffentlichung (in %)  
Angabe Autoren/innen (ggf. Haupt- / Ko- / korrespondierende/r Autor/in) mit Vorname Nachname (Initialen)

Lukas Nikolaus (LN), Marco Schott* (MS), Mohor Mihelčić (MM), Ivan Jerman (IJ), Uwe Posset (UP), Gerhard Sextl (GS)								
Autor	LN	MS	MM	IJ	UP	GS	Σ in %	
Herstellung der EC Elektrode	2	3	4	4			13	
Charakterisierung EC Elektroden	7	2	2	2			13	
Auswertung XPS der Ni <sub>1-x</sub> O Elektroden	2		1				3	
Bau der 2-Elektroden-Vollzellen	7						7	
Charakterisierung der Vollzellen	15						15	
Verfassen der Veröffentlichung	7	6	1	1	4		19	
Korrektur der Veröffentlichung	3	3			1	3	10	
Koordination der Veröffentlichung	1	9			3	7	20	
<b>Summe</b>	<b>44</b>	<b>23</b>	<b>8</b>	<b>7</b>	<b>8</b>	<b>10</b>	<b>100</b>	

### Erklärung zur Autorenschaft

Redox electrolytes for hybrid type II electrochromic devices with Fe-MEPE or Ni<sub>1-x</sub>O as electrode materials, Lukas Niklaus, Marco Schott\*, Uwe Posset, Guinevere A. Giffin, *ChemElectroChem* **2020**, 7, 3274.

Detaillierte Darstellung der Anteile an der Veröffentlichung (in %)

Angabe Autoren/innen (ggf. Haupt- / Ko- / korrespondierende/r Autor/in) mit Vorname Nachname (Initialen)

**Lukas Niklaus (LN), Marco Schott\* (MS), Uwe Posset (UP), A4 Guinevere A. Giffin (GG)**

Autor	LN	MS	UP	GG	Σ in %
Herstellung EC Elektroden	5				5
Charakterisierung EC Elektroden und Redoxmediatoren	6	2	1		9
Bau der Vollzellen	13				13
Charakterisierung der Vollzellen	12	3	1		16
Analyse des Nebenproduktes	6	1		1	8
Verfassen der Veröffentlichung	8	3	3	4	18
Korrektur der Veröffentlichung	2	2	2	5	11
Koordination der Veröffentlichung	2	7	3	8	20
<b>Summe</b>	<b>54</b>	<b>18</b>	<b>10</b>	<b>18</b>	<b>100</b>

### Erklärung zur Autorenschaft

Mixed metal oxides as optically-passive ion storage layers in electrochromic devices based on metallopolymers, Lukas Niklaus, Marco Schott\*, Jonas Subel, Stephan Ulrich, Daniel Reichert, Uwe Posset, Guinevere A. Giffin, *Solar Energy Materials & Solar Cells* **2021**, 223, 110950.

Detaillierte Darstellung der Anteile an der Veröffentlichung (in %)  
Angabe Autoren/innen (ggf. Haupt- / Ko- / korrespondierende/r Autor/in) mit Vorname Nachname (Initialen)

<b>Autor</b>	<b>LN</b>	<b>MS</b>	<b>JS</b>	<b>SU</b>	<b>DR</b>	<b>UP</b>	<b>GG</b>	<b>Σ in %</b>
Herstellung EC Elektroden	3	1	3	2	3			12
Charakterisierung EC Elektroden	8	4	2	2	1			17
Bau der Vollzellen	7							7
Charakterisierung der Vollzellen	10	2						12
Verfassen der Veröffentlichung	6	4		2	1	2	4	19
Korrektur der Veröffentlichung	3	2		1		1	4	11
Koordination der Veröffentlichung	3	6				3	10	22
<b>Summe</b>	40	19	5	7	5	6	18	100

**Lukas Niklaus (LN), Marco Schott\* (MS), Jonas Subel (JS), Stephan Ulrich (SU), Daniel Reichert (DR), Uwe Posset (UP), Guinevere A. Giffin (GG)**

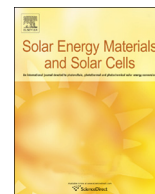
**Erklärung zur Autorenschaft**

Charge balancing and optical contrast optimization of Fe-MEPE/Ni<sub>1-x</sub>O electrochromic devices comprising a Li reference electrode, Lukas Niklaus, Marco Schott\*, Uwe Posset, Mohor Mihelčič, Ivan Jerman, Guinevere A. Giffin, *Solar Energy Materials and Solar Cells* **2021**, 227, 111080.

Detaillierte Darstellung der Anteile an der Veröffentlichung (in %)  
Angabe Autoren/innen (ggf. Haupt- / Ko- / korrespondierende/r Autor/in) mit Vorname Nachname (Initialen)

<b>Autor</b>	<b>LN</b>	<b>MS</b>	<b>UP</b>	<b>MM</b>	<b>IJ</b>	<b>GG</b>	<b>Σ in %</b>
Herstellung EC Elektroden	5			3	3		11
Charakterisierung aller Elektroden	7	1		1	1		10
Bau der 2-/3-Elektroden-Vollzellen	10						10
Charakterisierung der 2-/3-Elektroden-Vollzellen	15	2				2	19
Verfassen der Veröffentlichung	6	3	2	1	1	5	18
Korrektur der Veröffentlichung	3	4	2			3	12
Koordination der Veröffentlichung	4	8	1			7	20
<b>Summe</b>	<b>50</b>	<b>18</b>	<b>5</b>	<b>5</b>	<b>5</b>	<b>17</b>	<b>100</b>





# Metallopolymers and non-stoichiometric nickel oxide: Towards neutral tint large-area electrochromic devices

Lukas Niklaus<sup>a</sup>, Marco Schott<sup>a,\*</sup>, Mohor Mihelčič<sup>b</sup>, Ivan Jerman<sup>b</sup>, Uwe Posset<sup>a</sup>, Gerhard Sextl<sup>a</sup>

<sup>a</sup> Fraunhofer Institute for Silicate Research ISC, Fraunhofer R&D Center Electromobility, Neunerplatz 2, 97082, Würzburg, Germany

<sup>b</sup> National Institute of Chemistry NIC, Hajdrihova Ulica 19, 1000, Ljubljana, Slovenia

## ARTICLE INFO

### Keywords:

Metallo-supramolecular polyelectrolyte  
Non-stoichiometric nickel oxide  
Neutral tint  
Roll-to-roll process  
Electrochromic device

## ABSTRACT

Wet-chemical approaches were utilized to fabricate electrochromic (EC) thin films of different chemical nature, but compatible to each other in terms of coloration and electrochemical properties. A metallo-supramolecular polyelectrolyte (Fe-MEPE) thin film is shown to exhibit a large visible light transmittance change ( $\Delta\tau_v$ ) of 54% when switched from deep blue-violet ( $\text{Fe}^{2+}$ ) to colorless ( $\text{Fe}^{3+}$ ). On the other hand, a soft sol-gel peroxo-based approach was pursued to fabricate non-stoichiometric nickel oxide ( $\text{Ni}_{1-x}\text{O}$ ) thin films on transparent conductive glass at low process temperature.  $\text{Ni}_{1-x}\text{O}$ , due to the  $\text{Ni}^{2+}/\text{Ni}^{3+}$  redox couple, shows an EC response with a  $\Delta\tau_v$  of 44% when switched from a colorless state ( $\text{Ni}^{2+}$ ) to a grey-brown mixed-valence state ( $\text{Ni}^{2+}/\text{Ni}^{3+}$ ). Proof-of-concept is provided for a glass-based EC device combining Fe-MEPE and  $\text{Ni}_{1-x}\text{O}$  electrodes. The excellent EC performance is manifested in a  $\Delta\tau_v$  of 28% for the full cell and a low haze of < 2%. The EC films presented can be deposited on transparent conductive substrates *via* spin-coating, dip-coating, or slot-die deposition. The viability of this approach for later industrial production is demonstrated by the example of roll-to-roll (R2R) processing on transparent conductive films (TCF).

## 1. Introduction

Electrochromic (EC) materials exhibit optical transmittance modulation upon electrochemical oxidation and reduction [1,2]. In detail, charge carriers are injected in or extracted from the electrodes, thus producing redox states with different optical absorption characteristics. At the same time, cations or anions are inserted in or extracted from the electrolyte to provide charge compensation. Besides  $\text{WO}_3$ , with which the EC effect was studied first of all, a broad range of materials can be used for this purpose, such as metal oxides, viologens and conducting polymers [3]. A thoroughly investigated EC material class are the metallo-supramolecular polyelectrolytes (MEPEs) with a strong optical absorption in the visible range deriving from a metal-to-ligand charge-transfer (MLCT) transition [4–6]. Their optical properties can be modified by changing metal ions and/or ditopic ligands, which makes them a very versatile EC material [6–8]. The Fe-MEPE used in this study consists of  $\text{Fe}^{2+}$  ions, bis(terpyridine) ligands and acetate ( $\text{OAc}^-$ ) counter ions and it exhibits a reversible EC effect due to the oxidation from  $\text{Fe}^{2+}$  (blue-violet) to  $\text{Fe}^{3+}$  (colorless). In recent studies, it has been reported that MEPE display high contrast ratios, short response times, high cycle stability and high coloration efficiencies [4,5]. In addition, these materials can be deposited *via* different wet-chemical

techniques, *e.g.* dip-coating or layer-by-layer deposition [5]. Up to now, Fe-MEPE *vs.* metal oxide configurations are rarely studied in literature. Schott et al. recently reported a combination of Fe-MEPE and a metal oxide counter electrode ( $\text{V}_2\text{O}_5$ ) in flexible EC devices. *In operando* x-ray absorption fine structure (XAFS) measurements were performed to confirm that the octahedral coordination geometry in the Fe-MEPE material is not showing any structural change during the switching process [5]. The Fe-MEPE/ $\text{V}_2\text{O}_5$  EC device exhibits a  $\Delta\tau_v$  value of 36% – from 22% (colored) to 58% (bleached). However, the bleached state had a pronounced yellow tint due to the optical absorption of the reduced  $\text{V}_2\text{O}_5$ . Further flexible devices utilizing  $\text{Ni}_{1-x}\text{O}$  as anodically coloring electrode show a transmittance change  $\Delta T_{480\text{ nm}}$  of up to 34% when n-TiO<sub>2</sub> is used as cathodically coloring material. A  $\Delta T_{634\text{ nm}}$  of 25% was achieved with PEDOT or  $\text{WO}_3$  as working electrodes [9,10].

A well-known EC material anodically coloring from colorless to grey-brown is nickel oxide having high potential for attaining neutral tint coloration, which is highly demanded for smart windows [2,11,12]. The color and resistivity of nickel oxides is highly sensitive to the presence of higher valence states of nickel, even in traces [13]. Stoichiometric nickel oxide is an isolator, therefore, the resistance of nickel oxides can be reduced by suitable synthetic routes, in which  $\text{Ni}^{3+}$  and nickel vacancies are created or in which monovalent atoms, *e.g.*  $\text{H}^+$  or

\* Corresponding author.

E-mail address: [marco.schott@isc.fraunhofer.de](mailto:marco.schott@isc.fraunhofer.de) (M. Schott).

$\text{Li}^+$  are incorporated into the crystallites or onto the surface [14–16]. Sometimes this incorporation of atoms or post-treatments in liquid electrolyte leads to an enhanced durability and improved optical performance [17].

Consequently, a variety of methods have been used to prepare nickel oxide thin films. The commonly used physical vapor deposition (PVD) methods, e.g. sputtering or electron beam evaporation, involve high vacuum conditions and yield as-prepared films that may require pre-treatment before device assembly to obtain proper cell performance [18–20]. On the other hand, solution-processed EC materials are interesting due to the need of low cost/energy approaches. Such materials are relatively easy to deposit via wet-chemical processes, can be processed at low temperatures in many cases and enable low-cost mass production of flexible plastic-based EC devices. Both aspects were covered by the detailed studies of Mihelčič et al. [9,10,21]. There, the preparation and deposition of pre-prepared  $\text{Ni}_{1-x}\text{O}$  pigment particles led to porous EC thin films allowing facile ion insertion and de-insertion [21]. Moreover, in this study the deposition of  $\text{Ni}_{1-x}\text{O}$  on conductive films via wet-chemical deposition and subsequent heat-treatment at 150 °C was shown. The binder for preparing the pigment dispersion should be amorphous and exhibit EC properties as well. The as-prepared  $\text{Ni}_{1-x}\text{O}$  pigment coatings exhibited an immediate and strong EC effect when they were cycled in liquid electrolytes, e.g.,  $\text{LiClO}_4$  in propylene carbonate (PC). In addition, it was demonstrated that non-stoichiometric  $\text{Ni}_{1-x}\text{O}$  films exhibit reasonable stability in non-aqueous Li-containing electrolytes [2,22]. The method is simple and easy to adapt for large-scale wet-chemical deposition, such as dip-coating, spraying, printing and roll-to-roll (R2R) coating on appropriate substrates.

In this work, Fe-MEPE and wet-chemically prepared, non-stoichiometric  $\text{Ni}_{1-x}\text{O}$  electrodes are assembled in a glass-based EC device for the first time. It is an interesting combination because the Fe-MEPE electrodes show exceptional coloration efficiency, a vivid color and high cycle stability, while the  $\text{Ni}_{1-x}\text{O}$  electrodes exhibit a significant modulation of their broad Vis-NIR absorption in non-aqueous Li-based electrolytes. To the best of our knowledge, this is the first example of an EC device of this configuration made completely by solution-based processes.

## 2. Experimental

### 2.1. Materials and synthesis

All chemicals were purchased from Sigma-Aldrich and used without further purification.

### 2.2. Fe-MEPE synthesis and thin film preparation

4',4''-(1,4-phenylene)bis(2,2':6',2''-terpyridine) (tpy-ph-tpy) was synthesized according to the literature procedure given in Ref. [23]. The Fe-MEPE was synthesized with a metal ion-to-ligand molar ratio of 1:1 [4,5]. Fluorine-doped tin oxide (FTO) coated glass substrates ( Pilkington,  $14\ \Omega\cdot\text{sq}^{-1}$ .) were rinsed in ethanol and dried with compressed air prior to dip-coating. Homogeneous thin films were prepared by means of dip-coating from a 35 mmol Fe-MEPE solution at a withdrawing speed of  $35\ \text{mm}\cdot\text{min}^{-1}$ . A proprietary polyurethane–polysiloxane binder prepared by sol-gel processing was added to the coating solution to ensure good adhesion and film forming properties. The Fe-MEPE films (~330 nm) were annealed at 60 °C for 24 h. Fe-MEPE was deposited onto tin-doped indium oxide coated polyethylene terephthalate (PET-ITO) (coating width: 250 mm) by means of slot-die coating on a modular R2R coating line (from COATEMA Coating Machinery GmbH) running at a web speed of  $0.8\ \text{m}\cdot\text{min}^{-1}$ . The coatings were dried in-line at 120 °C for 2.5 min.

### 2.3. Preparation of $\text{Ni}_{1-x}\text{O}$ pigment dispersions and layers

The preparation of the  $\text{Ni}_{1-x}\text{O}$  pigment dispersion was carried out according to a literature-known procedure that yielded nickel oxide films with nickel vacancies and therefore higher  $\text{Ni}^{3+}$  content [9,21]. In brief, the  $\text{Ni}_{1-x}\text{O}$  pigment was synthesized via a sol-gel peroxoroute using a  $\text{H}_2\text{O}_2$ /urea mixture reacting with nickel (II) acetate powder. The obtained dried xerogel was thermally treated at 400 °C for 24 h to obtain the non-stoichiometric  $\text{Ni}_{1-x}\text{O}$  pigment ( $\text{Ni}^{2+}/\text{Ni}^{3+}$  ratio approx. 0.5) [21]. Secondly,  $\text{NiO}_x\text{H}_y$  dispersant and binder were prepared by precipitation of nickel (II) sulfate with sodium hypochlorite [9,24]. The precipitate was then rinsed in distilled water to remove sulfate anions and dried at 50 °C overnight. The pigment dispersion consisted of 10 wt % of  $\text{Ni}_{1-x}\text{O}$  pigment dispersed in distilled water in the presence of dispersant and was subsequently milled with zirconia beads [21]. The viscosity of the pigment dispersion was adjusted for a spin-coating process ( $1.9\ \text{mPa}\cdot\text{s}$  at a shear rate of  $500\ \text{s}^{-1}$ ). Thin  $\text{Ni}_{1-x}\text{O}$  films were deposited on FTO glass with a rotation speed of 500 rpm for 5 s, followed by 1000 rpm for 1 min. For an increase in film thickness the two-step spin-coating cycle was repeated several times. In this study, samples with four, five, and six layers were investigated and will be referred to as  $\text{Ni}_{1-x}\text{O}_4$ ,  $\text{Ni}_{1-x}\text{O}_5$ , and  $\text{Ni}_{1-x}\text{O}_6$ , respectively. The stoichiometry of the deposited films was measured with XPS – see Fig. S1. The binding energy of the peaks of the  $\text{Ni}^{2+}$  and  $\text{Ni}^{3+}$  states are in accordance with literature [21], where a more detailed XPS characterization is described. The deposition of thin  $\text{Ni}_{1-x}\text{O}$  films on flexible substrates was accomplished by means of R2R slot-die coating on a COATEMA Smart Coater with a web speed of  $0.1\ \text{m}\cdot\text{min}^{-1}$ . Several running meters of  $\text{Ni}_{1-x}\text{O}$  coated on PET-ITO (coating width: 100 mm) were obtained, while various deposition parameters were varied in order to control the  $\text{Ni}_{1-x}\text{O}$  coating thickness, e.g., concentration of the dispersion, coating speed, and amount of material deposited. The coatings were dried in-line at 150 °C for 6 min.

### 2.4. Preparation of glass-based EC devices

EC devices of the configuration glass/FTO/Fe-MEPE/electrolyte/ $\text{Ni}_{1-x}\text{O}$ /FTO/glass with an active area of  $2 \times 2\ \text{cm}^2$  were fabricated under argon atmosphere in a glove box by the following procedure: A proprietary  $\text{LiClO}_4$ -containing gel electrolyte was prepared under dry conditions and doctor blade coated onto the active area (wet film thickness:  $90\ \mu\text{m}$ ) of the Fe-MEPE electrode. The  $\text{Ni}_{1-x}\text{O}$  coated electrode was then aligned to match the electrolyte-coated Fe-MEPE electrode and laminated on top. Adhesive Cu tape was used as bus bars.

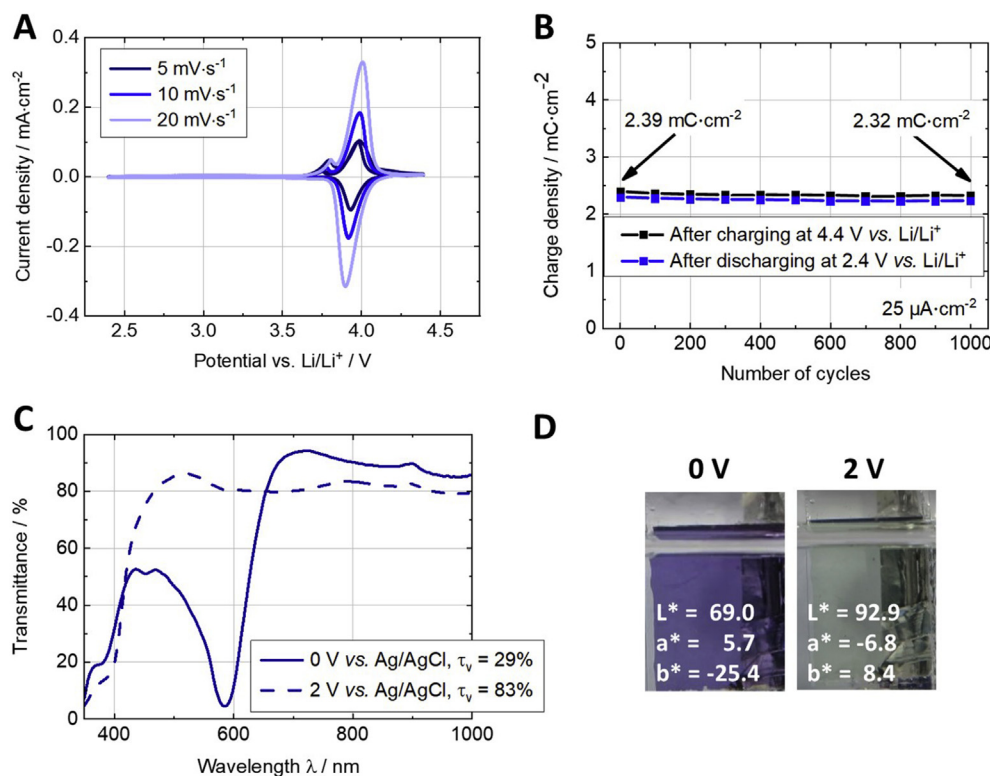
### 2.5. Methods and instruments

XPS spectra were recorded with a Surface Science Instruments S-Probe using monochromatic irradiation (Al K $\alpha$ ). The data was obtained and evaluated with ESCA Hawk 7 and Hawk Data Analysis 7, respectively.

The electrochemical properties of Fe-MEPE and  $\text{Ni}_{1-x}\text{O}$  thin films were determined in a conventional three-electrode set-up with Li as counter (CE) and reference electrodes (RE) by means of standard electrochemical techniques, such as cyclic voltammetry (CV) and charging/discharging measurements. 1 M  $\text{LiClO}_4$ /PC was used as electrolyte. Electrodes with an active area of  $1 \times 1\ \text{cm}^2$  were masked with tape and immersed in the electrolyte. Cu tape was attached to the FTO surface to maintain a good electrical contact.

Electrochemical characterization was performed by means of a Solartron Multistat 1470E potentiostat/galvanostat. UV-Vis spectra were recorded with an Avantes AvaSpec-2048 standard fiber optic spectrometer combined with a balanced deuterium–halogen light source. Spectro-electrochemical measurements were performed in a three-electrode set-up with platinum as CE, Ag/AgCl as RE and 1 M  $\text{LiClO}_4$ /PC as electrolyte.





**Fig. 1.** (A) Cyclic voltammograms at different scan rates and (B) charge density over 1000 charging/discharging cycles (current density:  $25 \mu\text{A}\cdot\text{cm}^{-2}$ ) of Fe-MEPE films on FTO glass in 1 M  $\text{LiClO}_4$  in PC with Li as CE and RE. (C) Transmission spectra of Fe-MEPE (MLCT band at 584 nm) in 1 M  $\text{LiClO}_4$  in PC with Pt as CE and Ag/AgCl as RE. (D) Corresponding photographs indicating the bleaching process.

Moreover, the change in visible light transmittance ( $\Delta\tau_v$ ) is calculated for the whole visible range according to the following equation:

$$\tau_v = \frac{\sum_{380 \text{ nm}}^{780 \text{ nm}} D_\lambda \cdot \tau(\lambda) \cdot V(\lambda) \cdot \Delta\lambda}{\sum_{380 \text{ nm}}^{780 \text{ nm}} D_\lambda \cdot V(\lambda) \cdot \Delta\lambda} \quad (1)$$

Where  $D_\lambda$  is the relative spectral distribution of illuminant D65,  $\tau(\lambda)$  the spectral transmittance, and  $V(\lambda)$  the spectral luminous efficiency.

### 3. Results and discussion

#### 3.1. Optical and (spectro-)electrochemical properties of Fe-MEPE electrodes

The Fe-MEPE-coated substrates were characterized via spectro-electrochemical measurements and electrochemical cycling. Fig. 1A shows the CV curves and transmission spectra obtained for Fe-MEPE on FTO glass. The CV curves in the potential range 2.4 V–4.4 V vs.  $\text{Li/Li}^+$  were obtained at different scan rates (from  $5 \text{ mV}\cdot\text{s}^{-1}$  to  $20 \text{ mV}\cdot\text{s}^{-1}$ ). The peak potential for the oxidation of  $\text{Fe}^{2+}$  to  $\text{Fe}^{3+}$  occurs at 4.01 V vs.  $\text{Li/Li}^+$ , whereas the reduction takes place at 3.90 V vs.  $\text{Li/Li}^+$  at a scan rate of  $20 \text{ mV}\cdot\text{s}^{-1}$ . The oxidation of the Fe-MEPE film is accompanied by a color change from blue-violet ( $L^* = 69.0$ ,  $a^* = 5.7$ ,  $b^* = -25.4$ ) to a virtually colorless state ( $L^* = 92.9$ ,  $a^* = -6.8$ ,  $b^* = 8.4$ ). This effect is illustrated by the transmission spectra in Fig. 1C, where the MLCT band at 584 nm completely disappears at an applied potential of 2 V vs. Ag/AgCl. The transmission changes from  $T_c = 5\%$  to  $T_b = 80\%$  at 584 nm, which corresponds to a visible light transmittance change ( $\Delta\tau_v$ ) of 54% ( $\Delta T_{584 \text{ nm}} = 75\%$ ) resulting in a contrast ratio ( $\text{CR} = \frac{T_b}{T_c}$ , where  $T_b$  and  $T_c$  are the transmittance values in the bleached and colored state, respectively) of 18 at 584 nm. Furthermore, the Fe-MEPE electrodes were electrochemically charged (bleached) and discharged (colored) with a current density of  $25 \mu\text{A}\cdot\text{cm}^{-2}$  in the same potential range – see Fig. 1B. The charge density of  $2.39 \text{ mC}\cdot\text{cm}^{-2}$  (Coulomb efficiency of 98%) decreases about 3% over 1000 continuous charging/discharging cycles, indicating very high cycle stability. The SEM images in Fig. 2 show that the FTO surface is well covered by the Fe-MEPE layer ( $\sim 330 \text{ nm}$ )

showing a unique needle-like entangled structure.

#### 3.2. Optical and (spectro-)electrochemical properties of $\text{Ni}_{1-x}\text{O}$ electrodes

In Fig. S2 transmission spectra of FTO glass coated with  $\text{Ni}_{1-x}\text{O}$  in different layer thicknesses are shown. The layers exhibit a broad absorption across the entire visible region of the spectrum. The thinner films have a higher visible transmittance  $\tau_v$ , also indicated by higher  $L^*$  values, as well as sharper absorption edges. Interestingly, films of higher thickness also exhibit lower haze. However, for all layer thicknesses the haze was below 1%, indicating a very good transparency.

All three  $\text{Ni}_{1-x}\text{O}$  coatings were characterized by spectro-electrochemical measurements – see Fig. S3. With increasing film thickness the  $\tau_v$  value is decreasing from 80% to 56% and from 48% to 18% for the bleached (2 V) and colored (0 V) states, respectively. Therefore, the  $\Delta\tau_v$  is 32%, 41%, and 38% for the  $\text{Ni}_{1-x}\text{O}$  electrodes with 4, 5, and 6 layers, respectively. As the maximum change in visible transmittance is observed in the coating with 5 repetitions of deposition in combination with just slight changes in the  $a^*$  and  $b^*$  values as compared to the one with 4 layers, all further experiments were carried out with the five-layer coating.

Fig. 3 shows the (spectro-)electrochemical data obtained for the non-stoichiometric  $\text{Ni}_{1-x}\text{O}$  electrodes. As expected, for all films no pre-cycling was needed and they could be immediately cycled in 1 M  $\text{LiClO}_4$  in PC. The CV curves in the potential range from 2.4 V to 4.2 V vs.  $\text{Li/Li}^+$  were measured at different scan rates (from  $1 \text{ mV}\cdot\text{s}^{-1}$  to  $20 \text{ mV}\cdot\text{s}^{-1}$ ) and are shown in Fig. 3A. The anodic peak centered around 3.1 V vs.  $\text{Li/Li}^+$  is assigned to the oxidation of  $\text{Ni}^{2+}$  to  $\text{Ni}^{3+}$  and concurrent de-insertion of  $\text{Li}^+$  ions. This process is accompanied by a reversible color change to a grey-brown tint ( $L^* = 58.6$ ,  $a^* = 5.2$ ,  $b^* = 17.1$ ). The cathodic peak centered around 3.2 V vs.  $\text{Li/Li}^+$  is due to the reduction of  $\text{Ni}^{3+}$  to  $\text{Ni}^{2+}$  and the simultaneous insertion of  $\text{Li}^+$  ions from the electrolyte onto the  $\text{Ni}_{1-x}\text{O}$  structure. The latter process is usually accompanied by adsorption of  $\text{Li}^+$  ions and desorption of perchlorate ions and eventually leading to a complete bleaching ( $L^* = 86.1$ ,  $a^* = 1.6$ ,  $b^* = 13.6$ ) of the grey-brown colored films. It is possible with a  $\text{Ni}_{1-x}\text{O}$

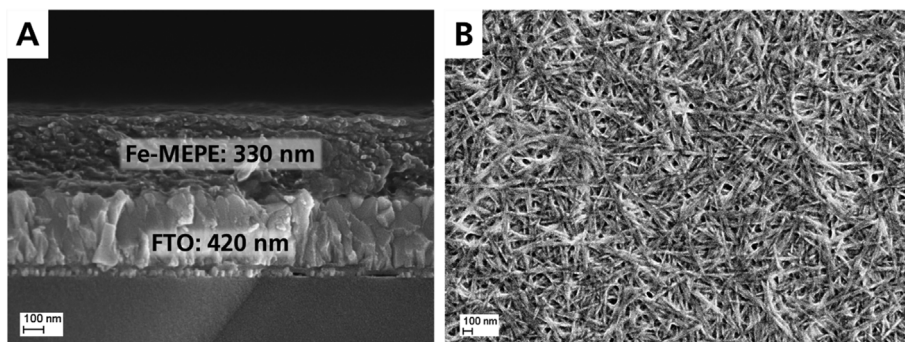
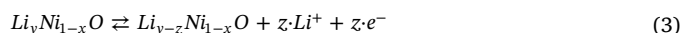
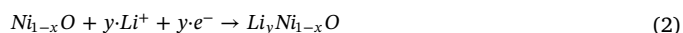


Fig. 2. SEM images depicting (A) the thickness and (B) the surface structure of the Fe-MEPE thin films on FTO glass.

film to obtain a  $\Delta\tau_v$  maximum of 50% and a CR of 3.3 ( $T_b = 75\%$ ,  $T_c = 23\%$ ) at 600 nm when switched between 0 V and 2 V vs. Ag/AgCl. Furthermore, the  $Ni_{1-x}O$  electrodes were electrochemically charged (colored) and discharged (bleached) at a current density of  $25 \mu A cm^{-2}$  in the same potential range – see Fig. 3B. The initial charge density of  $7.51 mC cm^{-2}$  (Coulomb efficiency of 95%) thereby decreased by about 7% over 1000 continuous charging/discharging cycles, indicating high cycle stability.

The different chemical processes occurring in the nickel oxide films are difficult to describe in only one simple redox reaction in contrast to the situation in aqueous electrolytes, where the redox reaction involves NiO and hydroxylated forms, such as  $Ni(OH)_2$  and  $NiOOH$  [2], and protons are reversibly inserted and de-inserted [25]. In the present study, a  $Li^+$ -containing non-aqueous electrolyte was used instead. The corresponding redox processes likely to take place for Li-doped nickel oxide films prepared by sputtering methods and cycled in a Li-based

electrolyte can be summarized by the following equations [2,14,26,27]:



Equation (2) describes the initial bleaching process while equation (3) represents the reversible EC reaction. Referring to the band structure, the color of the dark state is due to electron vacancies or holes around the nickel atoms, whereas the valence band is completely filled in the colorless state [26]. The mechanism of  $Li^+$  insertion into wet-chemically prepared nickel oxide is not as straightforward. Bonomo et al. [28] showed by XPS that in nickel oxide made through a wet-chemical approach, charge compensation is accomplished by  $ClO_4^-$  anions rather than by  $Li^+$  cations in  $LiClO_4$  as supporting electrolyte. In the case of hydroxylated  $Ni_{1-x}O$  films, it was found that protons were the species responsible for de-/insertion from aqueous alkaline solutions such as KOH [25]. In a non-aqueous  $Li^+$ -PC electrolyte, on the

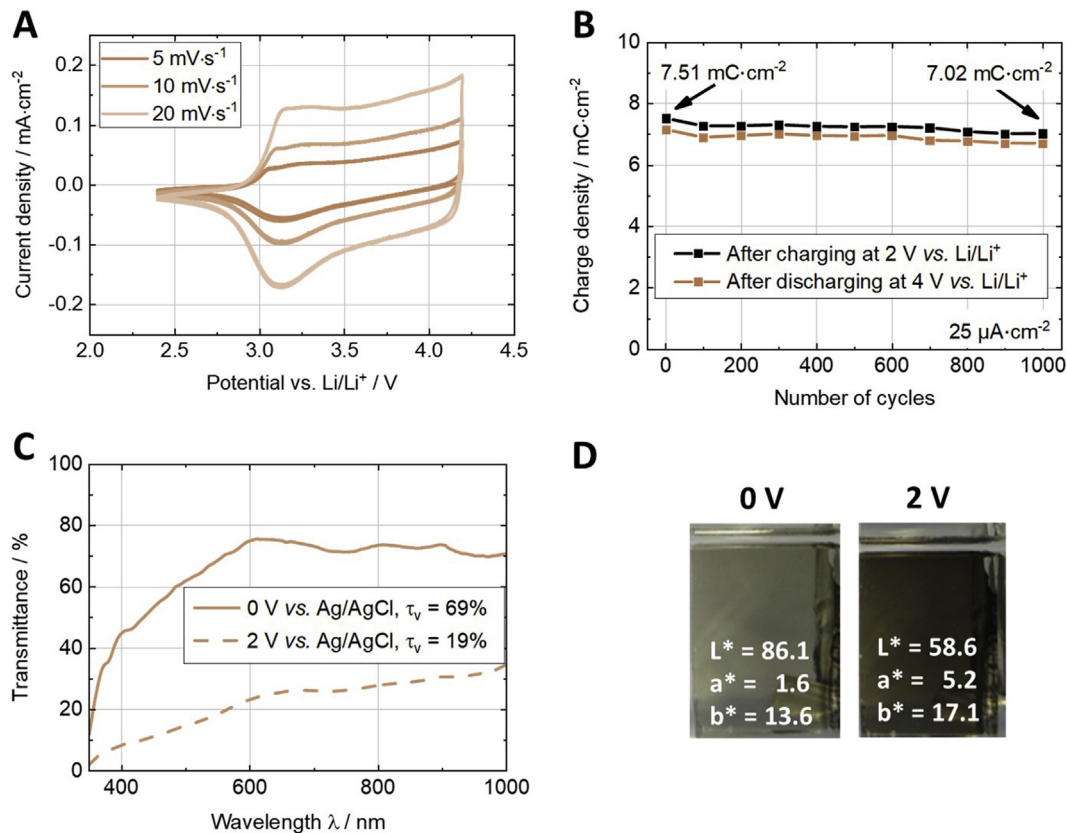


Fig. 3. (A) Cyclic voltammograms at different scan rates and (B) charge density over 1000 charging/discharging cycles (current density:  $25 \mu A cm^{-2}$ ) of the as-prepared  $Ni_{1-x}O$  films on FTO glass in 1 M  $LiClO_4$  in PC with Li as CE and RE. (C) Transmission spectra of the as-prepared  $Ni_{1-x}O$  in 1 M  $LiClO_4$  in PC with Pt as CE and Ag/AgCl as RE. (D) Corresponding photographs indicating the coloring process.

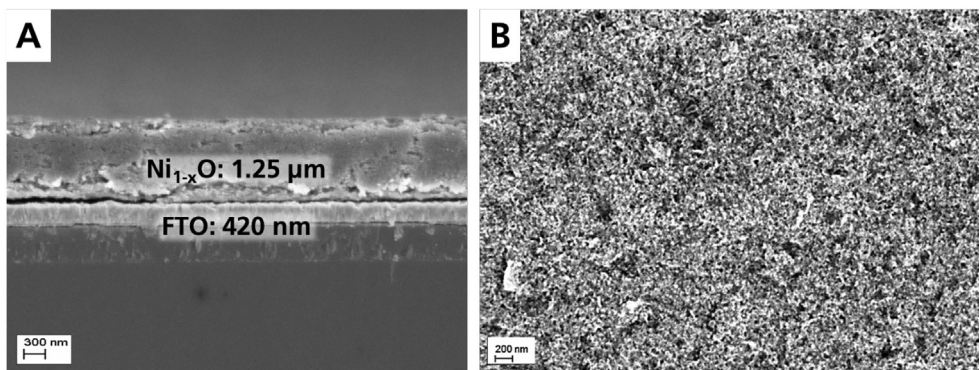


Fig. 4. SEM images depicting (A) the thickness and (B) the surface structure of the Ni<sub>1-x</sub>O thin films on FTO glass.

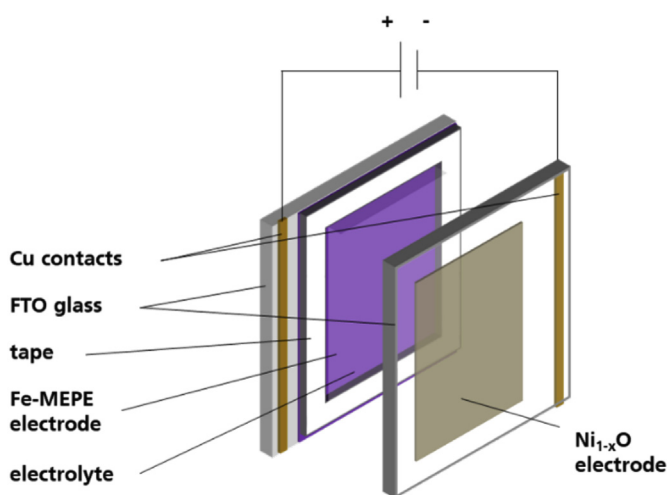


Fig. 5. Schematic set-up of the glass-based Fe-MEPE/Ni<sub>1-x</sub>O EC device.

other hand, no ions can be removed from the as-deposited film itself. The bleaching of the film is attained by insertion of Li<sup>+</sup> ions from the Li<sup>+</sup>-PC electrolyte into a defect Ni<sub>1-x</sub>O structure containing singly and doubly charged nickel vacancies [14]. Li<sup>+</sup> ions fill the cationic vacancies in the lattice of Ni<sub>1-x</sub>O. The SEM images in Fig. 4 show that the whole FTO surface is well covered by a porous nickel oxide deposit with a thickness of approx. 1.25 μm as derived from the cross-cut image.

### 3.3. EC properties of a glass-based Fe-MEPE/Ni<sub>1-x</sub>O device

EC devices with the configuration glass/FTO/Fe-MEPE/electrolyte/Ni<sub>1-x</sub>O/FTO/glass were fabricated to test the compatibility and efficiency of the Fe-MEPE electrodes in combination with Ni<sub>1-x</sub>O electrodes – see Fig. 5. From the detailed characterization of the single electrodes

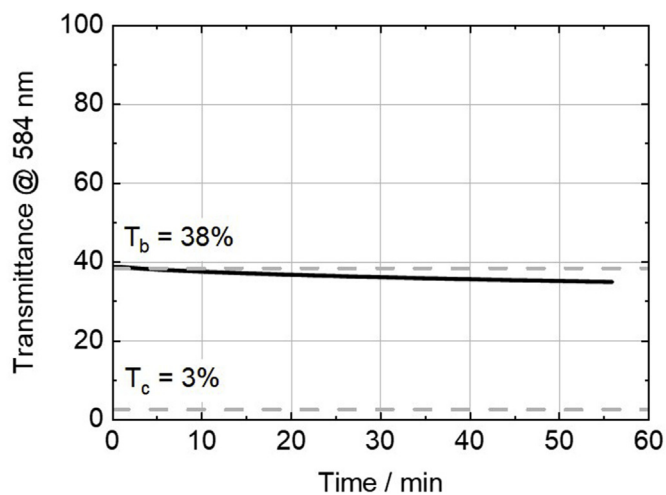


Fig. 7. Time-dependent transmittance change at 584 nm of the bleached EC device under open-circuit potential (OCP) conditions. The dotted grey lines indicate the transmittance levels of the completely bleached (T<sub>b</sub>) and colored states (T<sub>c</sub>) of the EC device.

and the mechanism discussed in literature, the redox processes going on in the presented EC device is schematically described in Fig. 6. The redox reaction can be summarized as follows (non-redox-active OAC<sup>-</sup> ions in Fe-MEPE polymer neglected):

WE:



blue-violet colorless.

CE:

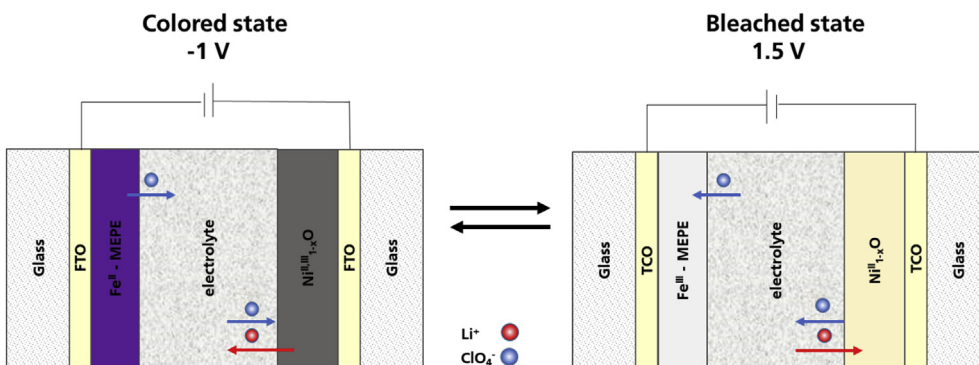
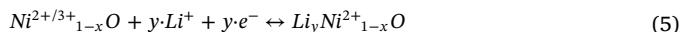
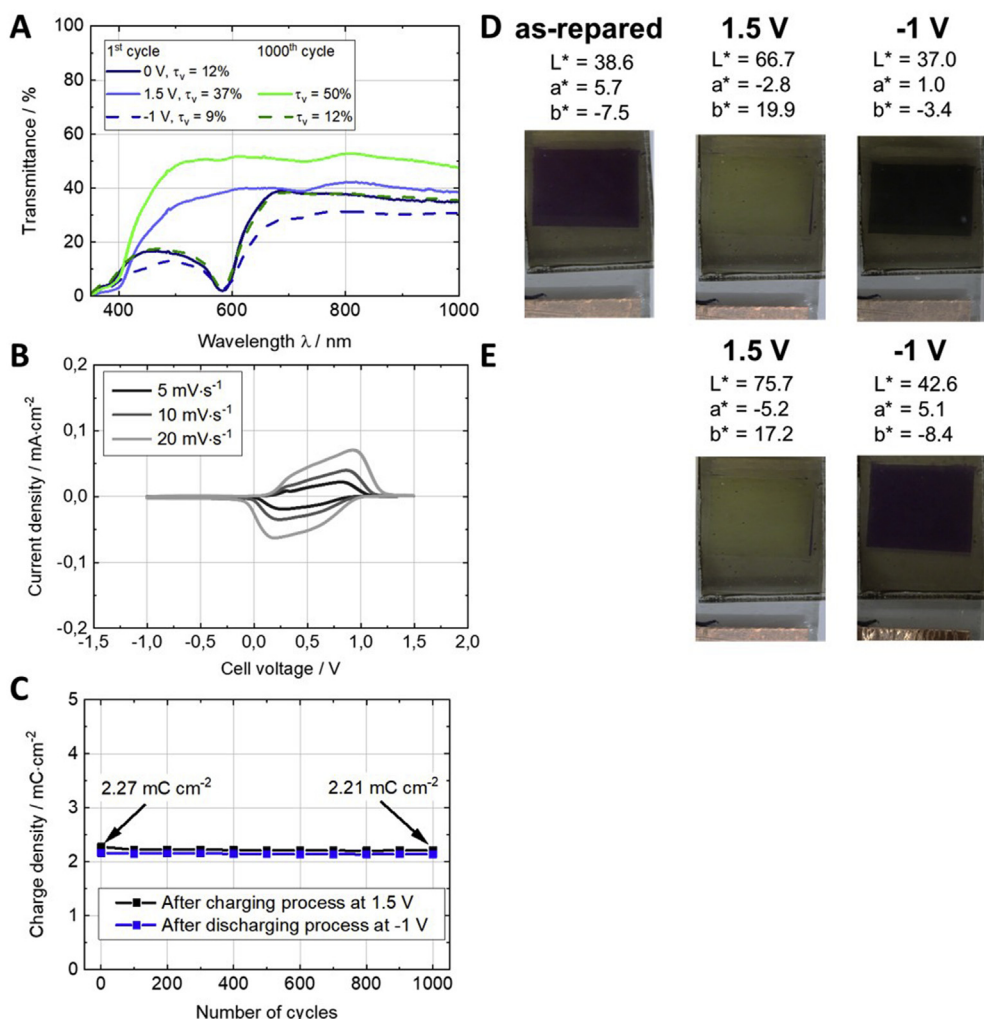


Fig. 6. Schematic principle of the redox processes occurring during bleaching and coloring.



**Fig. 8.** (A) Transmission spectra with (B) corresponding CV cycles (scan rates from 5 mV s<sup>-1</sup> to 20 mV s<sup>-1</sup>) and (C) cycle stability during charging and discharging cycles. Photographs with color coordinates (D) before and (E) after 1000 continuous charging/discharging cycles. (For interpretation of the references to color in this figure legend, the reader is referred to the Web version of this article.)

grey-brown colorless.

In order to achieve the maximum contrast, one electrode has to be pre-treated before device assembly. Therefore, the open-circuit memory, *i.e.*, the optical transmittance as a function of time under open-circuit (OCP) conditions, of electrochemically bleached Fe-MEPE and colored Ni<sub>1-x</sub>O electrodes were measured (Fig. S4). As the memory of the latter electrode immersed in the electrolyte surpasses that of the Fe-MEPE electrode by far, the Ni<sub>1-x</sub>O electrode was chosen for pre-treatment and a potential of 2 V vs. Ag/AgCl was applied for ~10 min before device fabrication. This treatment was sufficient to ensure that both electrodes were in their colored states prior to assembly and the assembled device showed a sufficient open-circuit memory - see Fig. 7.

Fig. 8 shows that the as-prepared EC device has a blue tint ( $L^* = 38.6$ ,  $a^* = 5.7$ ,  $b^* = -7.5$ ) as the MLCT band of Fe-MEPE is clearly apparent in the transmission spectrum. However, the device switches completely at an applied voltage of 1.5 V with a residual yellow hue ( $L^* = 66.7$ ,  $a^* = -2.8$ ,  $b^* = 19.9$ ). The transmission spectra as well as the corresponding photographic images of the bleached and colored states are depicted in Fig. 8D. When the voltage is set to -1 V, both the Fe-MEPE and the Ni<sub>1-x</sub>O are colored and an almost neutral tint with very low  $a^*$  and  $b^*$  values ( $< 5$ ) is reached ( $L^* = 37.0$ ,  $a^* = 1.0$ ,  $b^* = -3.4$ ). The visible light transmittance change from 9% (dark) to 37% (bleached) results in a  $\Delta\tau_v$  value of 28%.

A broadening of the peaks in comparison to the pure Fe-MEPE

electrodes can be observed in CV measurements carried out on the EC device (Fig. 8B). The CV curves between -1 V and 1.5 V were obtained at different scan rates (from 5 mV s<sup>-1</sup> to 20 mV s<sup>-1</sup>). The anodic peak for the oxidation of Fe<sup>2+</sup> to Fe<sup>3+</sup> occurs at 0.94 V, whereas the reduction takes place at 0.17 V at a scan rate of 20 mV s<sup>-1</sup>. The oxidation and reduction of the Fe-MEPE film is accompanied by a distinct color change from a blue-violet to a virtually colorless state and *vice versa*. This effect is illustrated by the transmittance spectra in Fig. 8A, wherein the MLCT band at 584 nm completely disappears at an applied voltage of around 1.5 V. In addition, the EC device was cycled *via* charging and discharging at a current density of 50  $\mu\text{A cm}^{-2}$ . The device exhibited excellent cycle stability over 1000 continuous switching cycles as the charge density decreased less than 3% from 2.27 mC cm<sup>-2</sup> to 2.21 mC cm<sup>-2</sup>, with a Coulomb efficiency over 95%. Moreover, spectro-electrochemical measurements performed after 1000 cycles (Fig. 8A) confirm that the device could reach a higher transmission in the bleached state as indicated by an obtainable  $\tau_v$  value of 50%, presumably indicating formation of the Ni<sub>1-x</sub>O electrode during cycling. Upon a closer look, a small change in the color coordinates is observable after 1000 cycles, *i.e.*, the completely bleached state ( $L^* = 66.7$ ,  $a^* = -5.2$ ,  $b^* = 17.2$ ) and the colored state ( $L^* = 42.6$ ,  $a^* = 5.1$ ,  $b^* = -8.4$ ) at applied voltages of 1.5 and -1 V, respectively (Fig. 8E). The change from  $\tau_v = 12\%$  (dark) to  $\tau_v = 50\%$  (bright) results in an improved  $\Delta\tau_v$  value of 38%.

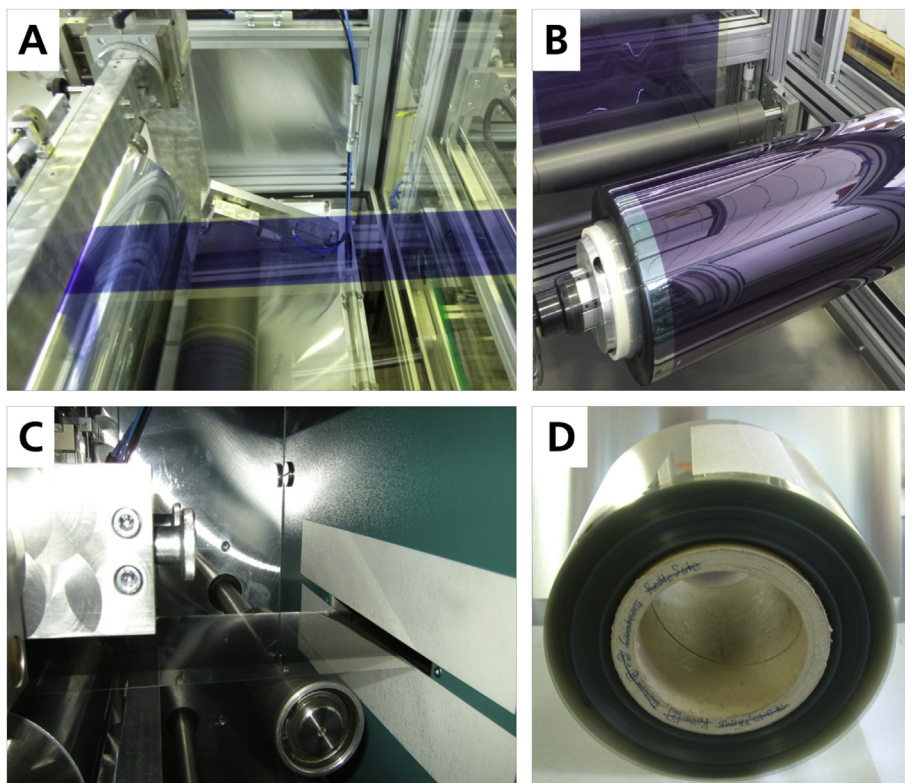


Fig. 9. R2R coating of Fe-MEPE (A,B) and Ni<sub>1-x</sub>O (C,D) electrodes on PET-ITO film.

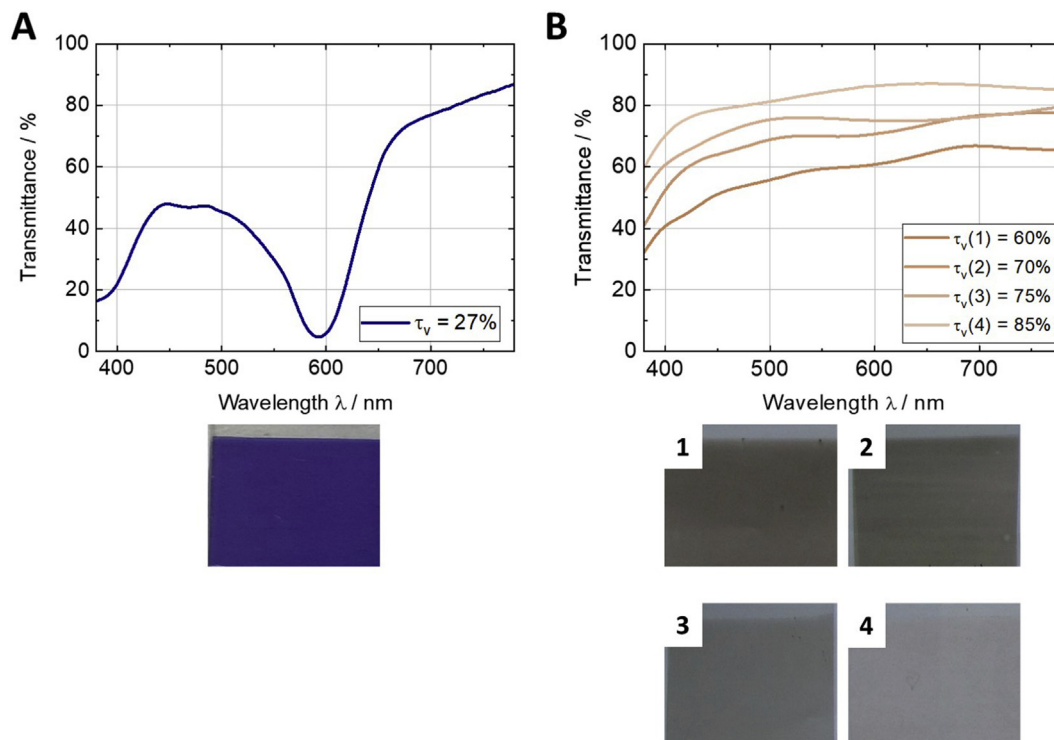


Fig. 10. Transmission spectra of (A) Fe-MEPE and (B) Ni<sub>1-x</sub>O electrodes prepared via R2R coating on PET-ITO with photographs below.

The results of this study provide proof-of-concept that Ni<sub>1-x</sub>O can be used as CE material in devices based on cathodically coloring Fe-MEPE electrodes. Devices of this configuration show two distinct, individually addressable states, *i.e.*, both electrodes simultaneously in their bright and colored states, with the individual colors supplementing each other

to close-to-neutral tints. With respect to future EC applications, *e.g.* in smart windows, it seems possible to still increase the optical contrast by an optimized charge balancing of both EC electrodes (2.4 mC cm<sup>-2</sup> for Fe-MEPE and 7.6 mC cm<sup>-2</sup> for Ni<sub>1-x</sub>O used in the current study). Hence, even more neutral tint should be attainable in charge-balanced devices

as a complete switching of the Ni<sub>1-x</sub>O electrode can be achieved.

### 3.4. Large-scale R2R coating of Fe-MEPE and Ni<sub>1-x</sub>O electrodes

The above-mentioned approach describes the preparation of glass-based devices with promising properties towards the achievement of neutral tint EC elements. In this section, the scale-up from laboratory to pilot fabrication level ("lab to fab") is described, enabling a future device production by continuous coating and lamination techniques [25]. Fig. 9 illustrates the result of the R2R slot-die coating process on PET-ITO rolls with Fe-MEPE and Ni<sub>1-x</sub>O, respectively. The aim was to demonstrate the feasibility of the large-area deposition of both electrode materials in a continuous process. The main challenge faced was to obtain homogeneous coatings with adjusted film thickness and charge density, eventually to obtain flexible, neutral tint EC devices.

Fig. 10 shows the spectroscopic characteristics of both electrodes. The transmission spectrum of the R2R-coated Fe-MEPE electrode exhibits the MLCT band at 584 nm with a  $\tau_v$  of 27%. The picture indicates that a homogeneous and transparent coating was achieved, which is emphasized by a  $\Delta E$  value and a haze value of < 1%. As-prepared Ni<sub>1-x</sub>O coatings obtained with different coating parameters exhibit  $\tau_v$  values ranging from 60% (highest) to 85% (lowest layer thickness), with the haze level increasing with increasing thickness. Thus, the MEPE vs. Ni<sub>1-x</sub>O system seems viable for future low-cost production of large-area EC film devices.

## 4. Summary and conclusion

In conclusion, it was demonstrated that the combination of Fe-MEPE and Ni<sub>1-x</sub>O electrodes on FTO-coated glass paves the way for a high-performance EC system. The dip-coated and cathodically coloring Fe-MEPE electrode exhibits color change from blue-violet ( $L^* = 69.0$ ,  $a^* = 5.7$ ,  $b^* = -25.4$ ) at low voltages (2 V vs. Ag/AgCl) to virtually colorless ( $L^* = 92.9$ ,  $a^* = -6.8$ ,  $b^* = 8.4$ ) with a very high visible light transmittance change  $\Delta\tau_v$  of 54% and a very good charge retention over 1000 charging/discharging cycles with a Coulomb efficiency of 98%. The combination of a pre-prepared nickel oxide pigment and a Ni-based dispersant results in porous grey-brown p-type Ni<sub>1-x</sub>O electrodes, showing immediate anodic switching between a colored (charged,  $L^* = 58.6$ ,  $a^* = 5.2$ ,  $b^* = 17.1$ ) and a bleached state (discharged,  $L^* = 86.1$ ,  $a^* = 1.6$ ,  $b^* = 13.6$ ) with a  $\Delta\tau_v$  of 50% and a Coulomb efficiency of 95% over 1000 charging/discharging cycles with a good charge retention. Finally, proof-of-concept is given for a glass-based EC device combining both electrode materials for the first time. The excellent EC performance of this device configuration did manifest in a  $\Delta\tau_v$  of 28% at the beginning, which increases to 38% due to the higher transmittance in the bleached state after 1000 charging/discharging cycles. The charge density slightly decreases from 2.27 mC cm<sup>-2</sup> by less than 3%, while maintaining a Coulomb efficiency of 95% during the cycling procedure.

The soft sol-gel peroxo-based approach with subsequent low temperature heat treatment for the fabrication of Ni<sub>1-x</sub>O thin coatings in association with the wet-chemical approach for the deposition of Fe-MEPE principally enables the technology to be transferred from a batch process on glass substrates to continuous high-throughput processes on TCFs, which has been demonstrated by R2R coating trials and the fabrication of film-based Fe-MEPE and Ni<sub>1-x</sub>O electrodes on pilot scale. Further investigations will concern the (pilot) fabrication of film-based EC cells by sheet-to-sheet and (later) R2R lamination, color optimization towards neutral tints, optical contrast enhancement, and durability validation for the Fe-MEPE/Ni<sub>1-x</sub>O system.

## Acknowledgment

The authors would like to acknowledge the financial support from the European Community's Seventh Framework program under Grant

Agreement no. 200431 (INNOSHADE) and the Bavarian Ministry of Economic Affairs and Media, Energy and Technology for funding the Fraunhofer R&D Center Electromobility. The contribution of Elena Fleder and Angelika Schmitt (Fraunhofer ISC) is gratefully acknowledged for SEM and XPS measurements, respectively.

## Appendix A. Supplementary data

Supplementary data to this article can be found online at <https://doi.org/10.1016/j.solmat.2019.110002>.

## Declaration of interest

The authors declare no potential conflict of interest.

## References

- [1] C.J. Cleveland, *Encyclopedia of Energy*, Elsevier, Amsterdam, 2004.
- [2] C.G. Granqvist, *Handbook of Inorganic Electrochromic Materials*, Elsevier Science, 1995.
- [3] C.G. Granqvist, M.A. Arvizu, İ. Bayrak Pehlivan, H.-Y. Qu, R.-T. Wen, G.A. Niklasson, Electrochromic materials and devices for energy efficiency and human comfort in buildings: a critical review, *Electrochim. Acta* 259 (2018) 1170–1182 <https://doi.org/10.1016/j.electacta.2017.11.169>.
- [4] M. Schott, H. Lorrmann, W. Szczerba, M. Beck, D.G. Kurth, State-of-the-art electrochromic materials based on metallo-supramolecular polymers, *Sol. Energy Mater. Sol. Cell.* 126 (2014) 68–73 <https://doi.org/10.1016/j.solmat.2014.03.032>.
- [5] M. Schott, W. Szczerba, U. Posset, A. Šurca Vuk, M. Beck, H. Riesemeier, A.F. Thünemann, D.G. Kurth, In operando XAFS experiments on flexible electrochromic devices based on Fe(II)-metallo-supramolecular polyelectrolytes and vanadium oxide, *Sol. Energy Mater. Sol. Cell.* 147 (2016) 61–67 <https://doi.org/10.1016/j.solmat.2015.10.015>.
- [6] S. Pai, M. Schott, L. Niklaus, U. Posset, D.G. Kurth, A study of the effect of pyridine linkers on the viscosity and electrochromic properties of metallo-supramolecular coordination polymers, *J. Mater. Chem. C* 6 (2018) 3310–3321 <https://doi.org/10.1039/C7TC04177B>.
- [7] F.S. Han, M. Higuchi, D.G. Kurth, Metallo-supramolecular polymers based on functionalized bis-terpyridines as novel electrochromic materials, *Adv. Mater.* 19 (2007) 3928–3931 <https://doi.org/10.1002/adma.200700931>.
- [8] F.S. Han, M. Higuchi, D.G. Kurth, Metallo-supramolecular polyelectrolytes self-assembled from various pyridine ring-substituted bisterpyridines and metal ions: photophysical, electrochemical, and electrochromic properties, *J. Am. Chem. Soc.* 130 (2008) 2073–2081 <https://doi.org/10.1021/ja710380a>.
- [9] M. Mihelčič, I. Jerman, B. Orel, Preparation of electrochromic Ni1-xO and TiO2 coatings from pigment dispersions and their application in electrochromic foil based devices, *Prog. Org. Coating* 76 (2013) 1752–1755 <https://doi.org/10.1016/j.porgcoat.2013.05.011>.
- [10] M. Mihelčič, A. Šurca Vuk, I. Jerman, B. Orel, F. Švegl, H. Moulki, C. Faure, G. Campet, A. Rougier, Comparison of electrochromic properties of Ni1-xO in lithium and lithium-free aprotic electrolytes: from Ni1-xO pigment coatings to flexible electrochromic devices, *Sol. Energy Mater. Sol. Cell.* 120 (2014) 116–130 <https://doi.org/10.1016/j.solmat.2013.08.025>.
- [11] M. Da Rocha, Y. He, X. Diao, A. Rougier, Influence of cycling temperature on the electrochromic properties of WO<sub>3</sub>/NiO devices built with various thicknesses, *Sol. Energy Mater. Sol. Cell.* 177 (2018) 57–65 <https://doi.org/10.1016/j.solmat.2017.05.070>.
- [12] H. Huang, J. Tian, W.K. Zhang, Y.P. Gan, X.Y. Tao, X.H. Xia, J.P. Tu, Electrochromic properties of porous NiO thin film as a counter electrode for NiO/WO<sub>3</sub> complementary electrochromic window, *Electrochim. Acta* 56 (2011) 4281–4286 <https://doi.org/10.1016/j.electacta.2011.01.078>.
- [13] D. Dini, Y. Halpin, J.G. Vos, E.A. Gibson, The influence of the preparation method of NiOx photocathodes on the efficiency of p-type dye-sensitized solar cells, *Coord. Chem. Rev.* 304–305 (2015) 179–201 <https://doi.org/10.1016/j.ccr.2015.03.020>.
- [14] W.-L. Jang, Y.-M. Lu, W.-S. Hwang, W.-C. Chen, Electrical properties of Li-doped NiO films, *J. Eur. Ceram. Soc.* 30 (2010) 503–508 <https://doi.org/10.1016/j.jeurceramsoc.2009.05.041>.
- [15] G.A. El-Shobaky, N.S. Petro, Effects of doping on the electrical properties and surface characteristics of NiO catalyst, *Surf. Technol.* 9 (1979) 415–426 [https://doi.org/10.1016/0376-4583\(79\)90090-6](https://doi.org/10.1016/0376-4583(79)90090-6).
- [16] N. Giordano, E. Cavaterra, D. Zema, Semiconductivity and catalytic behavior of doped nickel oxides in the low-temperature oxidation of ammonia, *J. Catal.* 5 (1966) 325–331 [https://doi.org/10.1016/S0021-9517\(66\)80015-5](https://doi.org/10.1016/S0021-9517(66)80015-5).
- [17] C.G. Granqvist, M.A. Arvizu, H.-Y. Qu, R.-T. Wen, G.A. Niklasson, Advances in electrochromic device technology: multiple roads towards superior durability, *Surf. Coating. Technol.* 357 (2019) 619–625 <https://doi.org/10.1016/j.surfcoat.2018.10.048>.
- [18] J. Liu, S.Y. Chiam, J. Pan, L.M. Wong, S.F.Y. Li, Y. Ren, Solution layer-by-layer uniform thin film dip coating of nickel hydroxide and metal incorporated nickel hydroxide and its improved electrochromic performance, *Sol. Energy Mater. Sol. Cell.* 185 (2018) 318–324 <https://doi.org/10.1016/j.solmat.2018.05.044>.

- [19] R.-T. Wen, C.G. Granqvist, G.A. Niklasson, Anodic electrochromism for energy-efficient windows: cation/anion-based surface processes and effects of crystal facets in nickel oxide thin films, *Adv. Funct. Mater.* 25 (2015) 3359–3370 <https://doi.org/10.1002/adfm.201500676>.
- [20] S. Green, J. Backholm, P. Georén, C.G. Granqvist, G.A. Niklasson, Electrochromism in nickel oxide and tungsten oxide thin films: ion intercalation from different electrolytes, *Sol. Energy Mater. Sol. Cell.* 93 (2009) 2050–2055 <https://doi.org/10.1016/j.solmat.2009.05.009>.
- [21] M. Mihelčič, I. Jerman, F. Švegl, A. Šurca Vuk, L. Slemenik Perše, J. Kovač, B. Orel, U. Posset, Electrochromic Ni<sub>1-x</sub>O/TiO<sub>2</sub> device with transmissive light modulation, *Sol. Energy Mater. Sol. Cell.* 107 (2012) 175–187 <https://doi.org/10.1016/j.solmat.2012.08.012>.
- [22] F. Michalak, K. von Rottkay, T. Richardson, J. Slack, M. Rubin, Electrochromic lithium nickel oxide thin films by RF-sputtering from a LiNiO<sub>2</sub> target, *Electrochim. Acta* 44 (1999) 3085–3092 [https://doi.org/10.1016/S0013-4686\(99\)00024-9](https://doi.org/10.1016/S0013-4686(99)00024-9).
- [23] E.C. Constable, A.M.W.C. Thompson, Multinucleating 2,2',6',2"-terpyridine ligands as building blocks for the assembly of co-ordination polymers and oligomers, *J. Chem. Soc., Dalton Trans.* 114 (1992) 3467–3475 <https://doi.org/10.1039/DT9920003467>.
- [24] C. Faure, C. Delmas, M. Fouassier, Characterization of a turbostratic  $\alpha$ -nickel hydroxide quantitatively obtained from an NiSO<sub>4</sub> solution, *J. Power Sources* 35 (1991) 279–290 [https://doi.org/10.1016/0378-7753\(91\)80112-B](https://doi.org/10.1016/0378-7753(91)80112-B).
- [25] E. Avendaño, A. Azens, G.A. Niklasson, C.G. Granqvist, Proton Diffusion and Electrochromism in Hydrated NiO<sub>[sub y]</sub> and Ni<sub>[sub 1-x]</sub>V<sub>[sub x]</sub>O<sub>[sub y]</sub> Thin Films, *J. Electrochem. Soc.* 152 (2005) F203 <https://doi.org/10.1149/1.2077308>.
- [26] Q. Liu, Q. Chen, Q. Zhang, Y. Xiao, X. Zhong, G. Dong, M.-P. Delplancke-Ogletree, H. Terryn, K. Baert, F. Reniers, X. Diao, In situ electrochromic efficiency of a nickel oxide thin film: origin of electrochemical process and electrochromic degradation, *J. Mater. Chem. C* 6 (2018) 646–653 <https://doi.org/10.1039/C7TC04696K>.
- [27] X. Hu, X. Chen, M.G. Hutchins, Study on the electrochromic mechanism of rf diode sputtered nickel oxide films, *Optical Materials Technology for Energy Efficiency and Solar Energy Conversion XI: Chromogenics for Smart Windows*, Toulouse-Labege, France, SPIE, 1992, p. 73.
- [28] M. Bonomo, A.G. Marrani, V. Novelli, M. Awais, D.P. Dowling, J.G. Vos, D. Dini, Surface properties of nanostructured NiO undergoing electrochemical oxidation in 3-methoxy-propionitrile, *Appl. Surf. Sci.* 403 (2017) 441–447 <https://doi.org/10.1016/j.apsusc.2017.01.202>.





# Redox Electrolytes for Hybrid Type II Electrochromic Devices with Fe–MEPE or Ni<sub>1-x</sub>O as Electrode Materials

Lukas Niklaus, Marco Schott,\* Uwe Posset, and Guinevere A. Giffin<sup>[a]</sup>

The use of redox electrolytes in electrochromic devices (ECDs) based on cathodically coloring metallopolymers (MEPEs) and various redox mediators, including potassium hexacyanoferrate (II)/(III) (KHCF(II)/(III)), ferrocene/ferrocenium (Fc<sup>0/+</sup>) and tetramethyl thiourea/tetramethylformaminium disulfide (TMTU/TMFDS<sup>2+</sup>), was investigated. By decreasing the concentration of KHCF(III) in the electrolyte, it was possible to significantly reduce the loss current. Although the unpleasant yellow tint could be diminished with lower concentrations, Prussian blue (PB, Fe<sub>4</sub>[Fe(CN)<sub>6</sub>]<sub>3</sub>) was formed during cycling. Fc<sup>0/+</sup> and TMTU/TMFDS<sup>2+</sup> were studied as the basis of alternative redox electrolytes and characterized in terms of their electrochemical and

optical properties. The maximum visible light transmittance changes ( $\Delta\tau_v$ ) of 50% and 48% were reached with the MEPE reference ECD and the MEPE-ECD with 0.001 M TMTU/TMFDS<sup>2+</sup>, respectively. Finally, an ECD combining an anodically coloring non-stoichiometric nickel oxide (Ni<sub>1-x</sub>O) electrode with a TMTU/TMFDS<sup>2+</sup> (molar ratio: 1/0.1) containing electrolyte exhibits a maximum  $\Delta\tau_v$  of 32%, with  $\tau_v$  ranging from 38% in the dark state to 70% in the bright state. These results imply that incorporating redox mediators into the electrolyte provides a straightforward and effective means of simplifying device structures and improving the performance of ECDs based on MEPEs and metal oxides.

## 1. Introduction

Electrochromic (EC) materials can reversibly change their optical properties (light absorption/transmission and/or reflection) upon electrochemical oxidation and reduction.<sup>[1,2]</sup> An ideal electrochromic device (ECD) is highly transmissive and neutral colored in the bright state but exhibits a significant optical modulation between the dark and the bright state. There are three common types of ECDs (Figure 1). Thin-film “battery-like” ECDs (type III) consist of two substrates coated with a transparent conductive oxide (TCO) or another transparent conductor, one EC layer and a second complementary switching EC or highly transparent, ideally colorless ion-storage layer. In principle, having an ion-storage layer with sufficient charge capacity assures that the redox reaction occurring in the active layer is fully compensated and able to complete its color change to yield an electrochemically stable cell. Both electrodes are separated by an ion-conducting electrolyte (gel or solid) and are therefore often considered as all-solid-state devices – see Figure 1C.<sup>[2,3]</sup> As ions are inserted/de-inserted into/from the EC electrodes, the accompanying transfer of electrons results in defined redox states having different optical absorption characteristics. This “battery-like” device structure has the advantage that it is usually bi-stable and the combination of complemen-

tary switching or coloring EC materials leads to an enhanced optical contrast. Solution-phase ECDs (type I) contain dissolved EC species in the electrolyte – see Figure 1A.<sup>[3,4]</sup> Thus, the main advantage of type I ECDs is the simple fabrication process because the electrolyte with the active EC species is sandwiched between two TCO substrates. To avoid leakage of the electrolyte these ECDs have to be properly sealed.

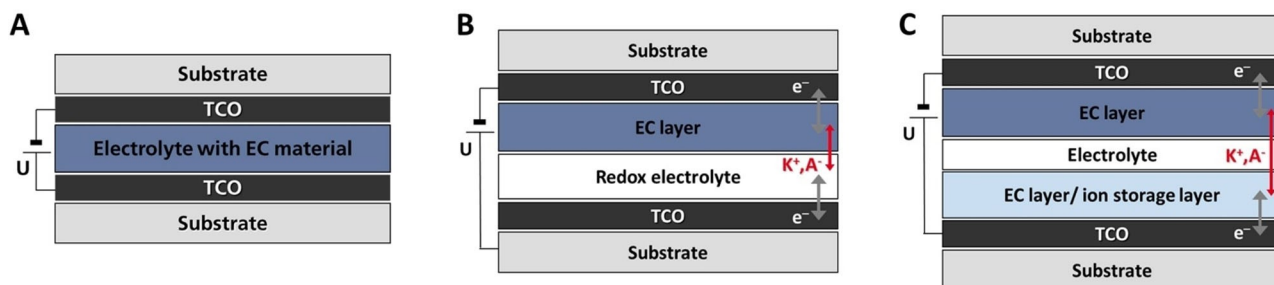
Hybrid ECDs (type II), like the ones studied in this work, combine the advantages of type I and III. Here, a redox mediator dissolved in the electrolyte counterbalances the redox reaction occurring during insertion/de-insertion of the cations (or anions) and electrons into/from the EC electrode, respectively – see Figure 1B.<sup>[3]</sup> The latter two types (type I and II) are simple to assemble, but require a constant current or voltage to maintain the redox states. This is a result of the direct contact of the redox electrolyte with the EC layer *via* diffusion. This electrical contact between the two electrodes leads to a so-called ‘loss current’ that has to be maintained to keep a constant voltage and a uniform coloration. With a low loss current, this process is slow and may take several hours,<sup>[5]</sup> but a high loss current causes high energy consumption to drive the ECD. According to Ref. [6], the loss current should be ideally below 10  $\mu\text{A}\cdot\text{cm}^{-2}$ . This can be realized by either electronic barrier layers<sup>[7,8]</sup> or a catalytic IrO<sub>x</sub> layer<sup>[9]</sup> between the redox electrolyte and the EC layer. EC materials and redox mediators with low redox potentials can be used in order to prevent degradation attributed to possible side reactions out of the stable electrochemical window of the electrolyte. Moreover, low potentials involve lower energy consumption for the switching to occur,<sup>[10]</sup> which leads to more competitive ECDs from the industrial point of view.<sup>[11]</sup>

An overview of the various redox mediators incorporated in type II ECDs has been published recently.<sup>[12]</sup> The most prominent candidate is iodide/triiodide (I<sup>-</sup>/I<sub>3</sub><sup>-</sup>), which is used in

[a] L. Niklaus, Dr. M. Schott, Dr. U. Posset, Dr. G. A. Giffin  
Fraunhofer Institute for Silicate Research ISC  
Fraunhofer R&D Center Electromobility  
Neunerplatz 2, 97082 Würzburg, Germany  
E-mail: marco.schott@isc.fraunhofer.de

Supporting information for this article is available on the WWW under <https://doi.org/10.1002/celec.202000583>

© 2020 The Authors. Published by Wiley-VCH Verlag GmbH & Co. KGaA. This is an open access article under the terms of the Creative Commons Attribution License, which permits use, distribution and reproduction in any medium, provided the original work is properly cited.

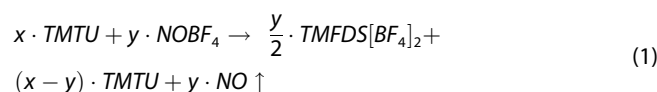


**Figure 1.** Schematic set-up of A) solution-phase (type I), B) hybrid (type II), and C) “battery-like” (type III) ECDs.  $K^+$ : e.g.  $Li^+$ ,  $H^+$ ;  $A^-$ : e.g.  $ClO_4^-$ ,  $Cl^-$ ,  $BF_4^-$ ,  $PF_6^-$ .

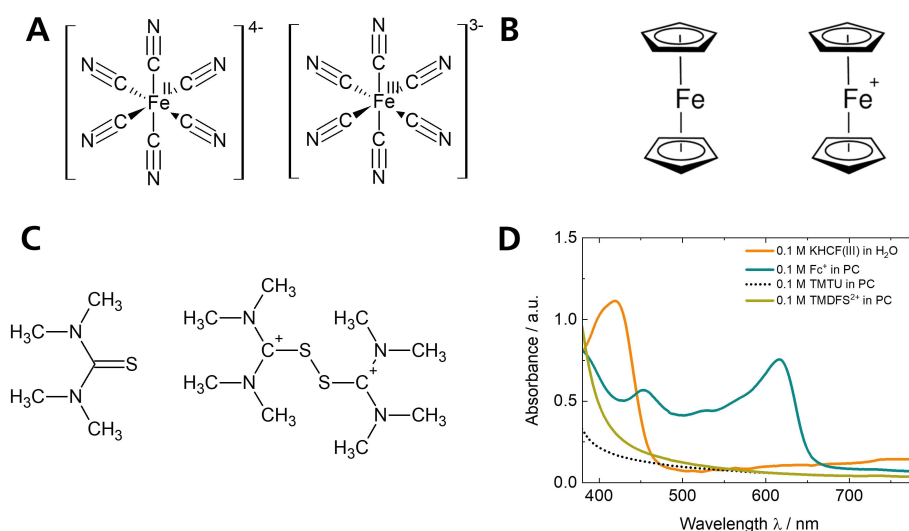
dye-sensitized solar cells (DSSCs). However, this redox mediator is not desirable for ECDs as its corrosiveness leads to poor stability and the absorption of visible light (brown-red colored) limits the use for EC applications.<sup>[13–15]</sup> This work focuses on redox mediators that have been investigated for DSSCs<sup>[12]</sup> and showed promising initial results with common inorganic EC materials, such as tungsten oxide ( $WO_3$ ) and Prussian blue (PB).<sup>[15]</sup> The selected redox mediators, potassium hexacyanoferrate(II)/(III) (KHCF(II)/(III)), ferrocene/ferrocenium ( $Fc^{0/+}$ ), and the organic tetramethylthiourea/tetramethylformaminium disulfide couple (TMTU/TMFDS<sup>2+</sup>) are non-corrosive, commercially available and non-toxic (Figure 2A–C). The redox potentials of KHCF(II)/(III),  $Fc^{0/+}$ , and TMTU/TMFDS<sup>2+</sup> are 252 mV,<sup>[6]</sup> 201 mV,<sup>[17]</sup> and 450 mV vs. Ag/AgCl,<sup>[6]</sup> respectively.

$Fc^{0/+}$  has been used in viologen-based ECDs<sup>[18,19]</sup> and in combination with Co–MEPE.<sup>[20,21]</sup> The Co–MEPE based ECD exhibits an optical change from a black colored (Co(II)–MEPE) to an almost neutral-colored bright state (Co(III)–MEPE) with good cycling stability. Recently, it was shown that KHCF(III) is not suitable for ECDs containing  $WO_3$  due to the very low charge transfer resistance, which results in high loss current and high power consumption.<sup>[6]</sup> TMTU/TMFDS<sup>2+</sup> is advantageous due to its non-corrosive nature, low cost, easy handling and high

transparency in both redox states.<sup>[13]</sup> The group of A. Georg demonstrated that a hybrid ECD consisting of TMTU/TMFDS<sup>2+</sup> and sol-gel-derived  $WO_3$  exhibits a visible light transmittance change ( $\Delta\tau_v$ ) of 57%, with  $\tau_v$  ranging from 14% (dark) to 71% (bright).<sup>[6]</sup> Moreover, the TMTU/TMFDS<sup>2+</sup> redox mediator can be used in a solid electrolyte based on an organopolysiloxane matrix<sup>[16]</sup> to reduce long term degradation.<sup>[6]</sup> A further advantage is that the ratio of TMTU:TMFDS<sup>2+</sup> can be simply adjusted using an oxidizing agent, such as nitrosonium tetrafluoroborate ( $NOBF_4$ )<sup>[6,13,22]</sup> as described in Equation (1):



In this study, the promising redox mediators are tested in type II ECDs with either cathodically coloring iron-based metallopolymer (Fe–MEPEs)<sup>[23,24]</sup> or anodically coloring non-stoichiometric nickel oxide ( $Ni_{1-x}O$ ).<sup>[25,26]</sup> Both electrode materials were selected due to their promising EC properties. MEPEs exhibit a strong optical absorption in the visible spectrum caused by a metal-to-ligand charge transfer (MLCT) transition. This transition enables high optical contrast, fast response times, high cycling



**Figure 2.** Chemical structures of the reduced (left) and oxidized (right) redox mediator species used in this work. A) Potassium hexacyanoferrate(II)/(III) (KHCF(II)/(III)), B) ferrocene/ferrocenium ( $Fc^{0/+}$ ), and C) tetramethylthiourea/tetramethylformaminium disulfide (TMTU/TMFDS<sup>2+</sup>) accompanied by D) the absorbance spectra of the redox electrolytes.

stability and high coloration efficiencies.<sup>[23,24,27–29]</sup> Moreover, as a matter of principle, the color of MEPEs can be varied by changing the metal ion and/or the ligand.<sup>[24,29]</sup> The Fe–MEPE used in this study consists of  $\text{Fe}^{2+}$  ions, a bis(terpyridine) ligand and acetate ( $\text{OAc}^-$ ) counter ions. This combination exhibits a reversible color change due to the oxidation from  $\text{Fe}^{2+}$  (blue-violet) to  $\text{Fe}^{3+}$  (colorless). Nickel oxide, as stoichiometric compound, is an insulator.<sup>[30]</sup> However, by utilizing a literature-known soft-peroxo approach, porous  $\text{Ni}_{1-x}\text{O}$  can be obtained that enables low-temperature deposition processes and facile ion insertion/de-insertion in the films formed.<sup>[26,31,32]</sup> Additionally,  $\text{Ni}_{1-x}\text{O}$  electrodes have a significant anodic EC effect between colorless and grey-brown states with acceptable stability in non-aqueous  $\text{Li}^+$ -containing electrolytes.<sup>[2,33]</sup> This study demonstrates the EC characteristics of devices based on Fe–MEPE or  $\text{Ni}_{1-x}\text{O}$  electrodes and gel electrolytes containing various redox mediators for the first time.

## 2. Results and Discussion

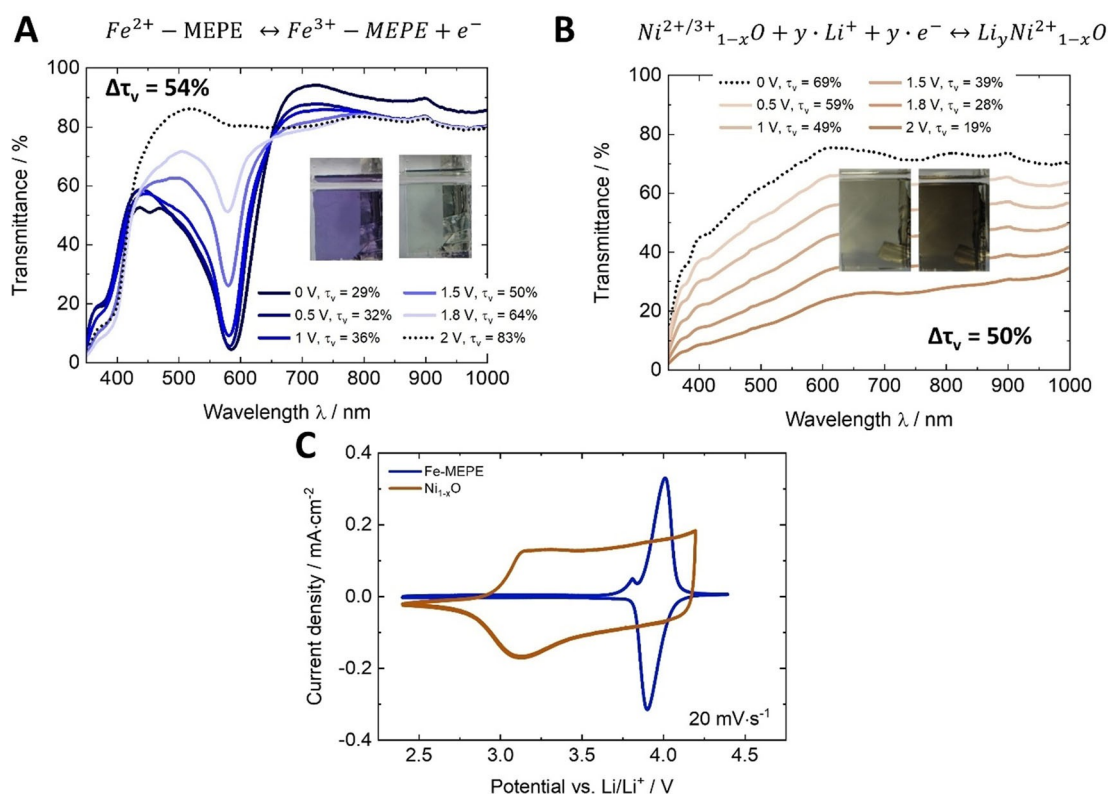
### 2.1. Optical Properties of the Redox Electrolytes

The optical properties of the redox mediators are summarized in Figure 2D.  $\text{KHCf(III)}$  dissolved in  $\text{H}_2\text{O}$  and ferrocenium in propylene carbonate (PC) show orange and blue tints with distinct maxima at 419 nm and 616 nm, respectively. In

contrast, TMTU does not exhibit any absorption in the visible region and the absorbance of  $\text{TMFDS}^{2+}$  extends slightly into the UV range. It should be noted that the colors appear to be very intensive due to the long optical path through the cuvette (1 cm). However, the electrolyte thickness is reduced in the ECD to around 100  $\mu\text{m}$ , hence the color impression is strongly diminished.

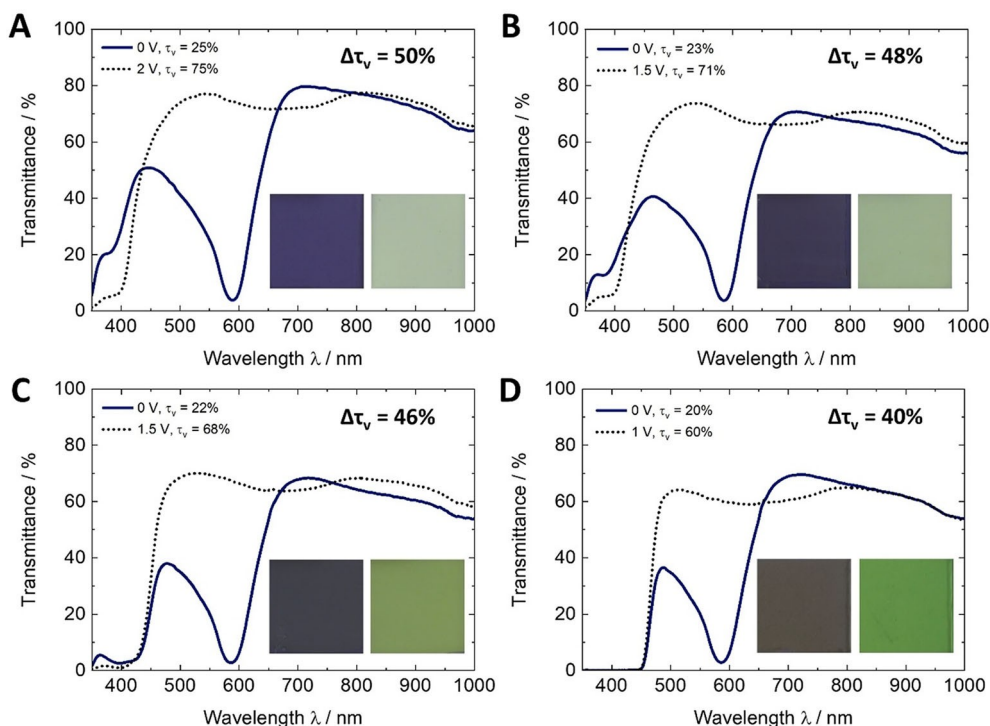
### 2.2. (Spectro-)Electrochemical Characterization of MEPE and $\text{Ni}_{1-x}\text{O}$ Electrodes

As both EC electrodes (Fe–MEPE and non-stoichiometric  $\text{Ni}_{1-x}\text{O}$ ) were investigated in detail in a recent publication,<sup>[25]</sup> only those aspects relevant for this study are presented here. Figure 3A shows the transmission spectra of Fe–MEPE in the dark (reduced,  $\text{Fe}^{2+}$ ) and bright (oxidized,  $\text{Fe}^{3+}$ ) state as well as the corresponding photographic images of the thin film electrodes. The oxidation of the Fe–MEPE film is accompanied by a color change from blue-violet ( $L^*=69.0$ ,  $a^*=5.7$ ,  $b^*=-25.4$ ) to a virtually colorless state ( $L^*=92.9$ ,  $a^*=-6.8$ ,  $b^*=8.4$ ) as illustrated by the transmission spectra showing that the MLCT band at 584 nm completely disappears at an applied potential of 2 V vs. Ag/AgCl. The transmittance values at 584 nm change from  $T_c=5\%$  (dark) to  $T_b=80\%$  (bright), which results in a total transmittance change  $\Delta T_{584\text{ nm}}$  of 75% (visible light transmittance change  $\Delta\tau_v=54\%$ ) and a contrast ratio ( $CR=T_b/T_c$ ) of



**Figure 3.** Spectroelectrochemical measurements at potentials of 0, 0.5, 1.0, 1.5, 1.8, and 2 V vs. Ag/AgCl of A) Fe–MEPE and B)  $\text{Ni}_{1-x}\text{O}$  with Pt as CE and Ag/AgCl as RE with the corresponding (simplified) redox equation. C) Cyclic voltammograms recorded with a scan rate of  $20\text{ mV}\cdot\text{s}^{-1}$  of Fe–MEPE and  $\text{Ni}_{1-x}\text{O}$  with Li as CE and RE. Electrolyte: 1 M  $\text{LiClO}_4/\text{PC}$ . Adapted from Ref. [25].

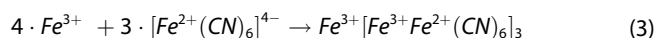




**Figure 4.** Spectroelectrochemical measurements of A) MEPE–ECD1, B) MEPE–ECD2\_HCF, C) MEPE–ECD3\_HCF, and D) MEPE–ECD4\_HCF and the corresponding photographs indicating the color changes. As shown in Table 1, the increasing number in the ECD name indicates increasing KHCF(III) concentration (0.001, 0.01, and 0.1 M) in the 1 M LiClO<sub>4</sub>/H<sub>2</sub>O electrolyte.

presence of the blue precipitate associated with the color change can be attributed to the formation of Prussian Blue (PB), an insoluble mixed-valence iron hexacyano complex, which is indicated by a broad peak appearing around 700 nm due to a metal-to-metal charge transfer (MMCT) between Fe<sup>2+</sup> and Fe<sup>3+</sup> ions in the PB crystal structure.<sup>[2,41]</sup> PB shows a broad absorption band extending into the NIR with a maximum at approx. 680 nm.<sup>[42]</sup>

In order to prove the formation of PB, 100 cycling steps between 0 V and 1 V were performed in a two-electrode set-up. Fe–MEPE was used as WE, platinum wire as CE, and 0.1 M KHCF(III) dissolved in 1 M LiClO<sub>4</sub>/H<sub>2</sub>O as redox electrolyte (Figure S3C). As with the aqueous system, a deep blue PB precipitate was formed. The precipitate was purified by filtration and the resultant blue powder was analyzed by FTIR spectroscopy. The FTIR spectrum is consistent with that of a PB thin film electrodeposited on FTO glass and slightly different from that of pristine KHCF(III) powder (Figure S3D). PB can be formed in the electrolyte during cycling between 0 V and 1 V according to the following redox reaction [Eq. (3)].<sup>[43]</sup>



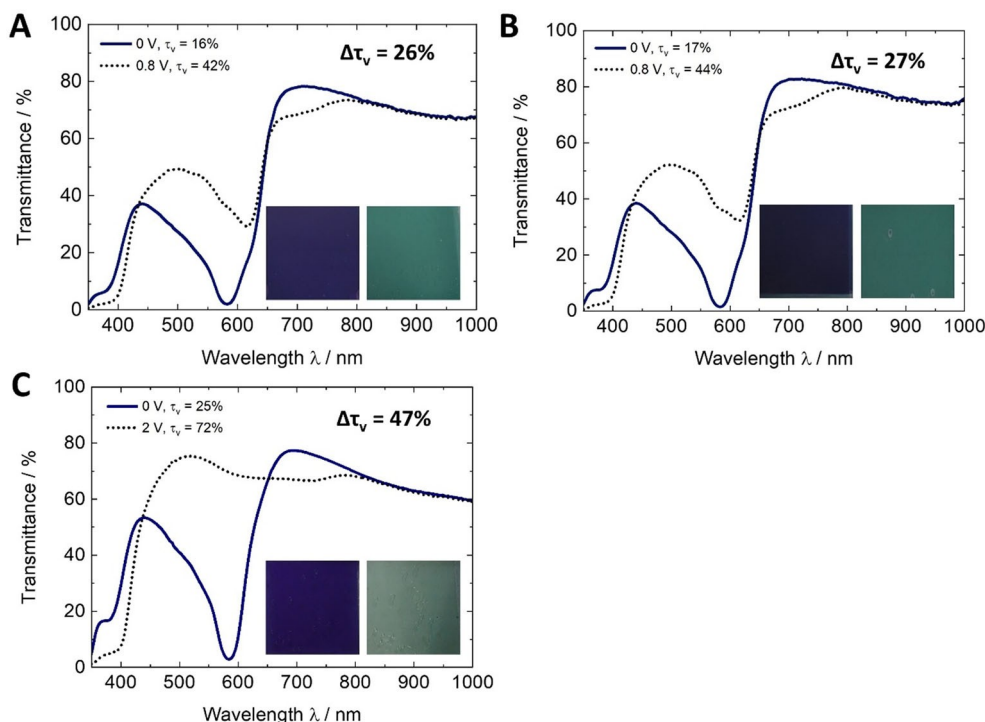
In summary, KHCF(III) facilitates the oxidation and reduction of Fe–MEPE as illustrated by a decrease in the cell voltage necessary for the bleaching process with increasing KHCF(III) concentration. Furthermore, the increased current densities associated with the bleaching and coloring processes show that the redox reactions take place in shorter time. However, the

yellow tint of the electrolyte in both dark and bright states intensifies with the increasing concentration of KHCF(III) resulting in a reduction of the optical contrast and higher loss currents. In addition, the cycling stability of KHCF(III) in combination with Fe–MEPE is poor as PB is formed in the electrolyte during cycling of the ECD. The precipitation of PB was not observed in recent literature as the studied WO<sub>3</sub> and Co–MEPE switch at slightly lower potentials.<sup>[6,20,21]</sup>

### 2.3.2. Electrolytes with Fc<sup>0/+</sup> and TMTU/TMFDS<sup>2+</sup> as Redox Mediators

Three further redox mediators (Fc–PF<sub>6</sub>, Fc–BF<sub>4</sub>, and TMTU) were tested in combination with Fe–MEPE and compared with the results obtained for MEPE–ECD4\_HCF (shown in Figure 4D). The redox species was added in its oxidized state, *i.e.*, either as Fc<sup>+</sup>-salt or NOBF<sub>4</sub>-oxidized TMTU. The transmission spectra for the ECDs, as well as the corresponding photographs of the dark and bright states, are depicted in Figure 5.

Using Fc–PF<sub>6</sub>, as in MEPE–ECD5\_Fc–PF<sub>6</sub>, a color change from dark blue ( $L^* = 48.6$ ,  $a^* = 6.5$ ,  $b^* = -28.6$ ) to faint green ( $L^* = 70.7$ ,  $a^* = -11.8$ ,  $b^* = 0.4$ ) was observed at an applied voltage of 0.8 V resulting in a visible light transmittance change of  $\Delta\tau_v$  of 26% (16% ↔ 42%). This behavior is similar to MEPE–ECD6\_Fc–BF<sub>4</sub>: The initial dark blue color ( $L^* = 49.4$ ,  $a^* = 9.0$ ,  $b^* = -28.3$ ) also changes to faint green ( $L^* = 72.6$ ,  $a^* = -11.6$ ,  $b^* = 1.6$ ) resulting in a  $\Delta\tau_v$  of 27% (17% ↔ 44%). In both cases, the Fe–MEPE electrode bleached completely as the MLCT



**Figure 5.** Spectroelectrochemical measurements of A) MEPE-ECD5\_Fc-PF<sub>6</sub>, B) MEPE-ECD6\_Fc-BF<sub>4</sub>, and C) MEPE-ECD7\_TMTU with 0.1 M of the respective redox mediator in 1 M LiClO<sub>4</sub>/PC electrolyte. The insets show the corresponding photographs of the dark and bright states.

band disappeared at an applied voltage of 0.8 V, whereby the blue-colored Fc<sup>+</sup> compound significantly influenced the bright state of the ECD as seen in Figure 5A,B. The peak visible at 616 nm in the bright state (0.8 V) can be attributed to the d-d transition of the 3d electrons of the central iron atom of the ferrocene complex.<sup>[44]</sup> This peak is also present in the spectrum of the dark state (0 V) as it is evident in the shoulder on the MEPE MLCT band.

By changing the electrolyte from an aqueous (Figure S1) to a non-aqueous system (Figure S4), the loss current is significantly lowered from 600 to 70  $\mu\text{A}\cdot\text{cm}^{-2}$ . This can be explained by the diminishing of the hydration shell in size around the Li<sup>+</sup> ion as described in the Ref. [45] and, therefore, a faster ion diffusion in the less polar solvent (PC). The change of the electrolyte solvent along with the slightly lower (~50 mV) redox potential of ferrocenium (201 mV vs. Ag/AgCl) as compared to KHCF(III) (252 mV vs. Ag/AgCl) enabled a decrease in the bleaching voltage.<sup>[5,16]</sup> In addition, a shift of the MLCT transition of the Fe-MEPE (at 584 nm) due to different ionic interactions between the Fe<sup>2+</sup> ions and the ferrocenium counter ions (PF<sub>6</sub><sup>-</sup> and BF<sub>4</sub><sup>-</sup>) was expected.<sup>[46]</sup> However, no wavelength shift of the MLCT band is observed and the EC behavior (response time,  $\Delta\tau_v$ , current density) is unaffected as shown in Figure 5A,B and Figure S3A,B. It can be assumed that the excess amount of LiClO<sub>4</sub> in the electrolytes diminishes the anion effects expected from Refs. [46,47].

The iron-based redox mediators (KHCF(III), Fc-PF<sub>6</sub>, and Fc-BF<sub>4</sub>) have a strong impact on the bright state color of the devices, as they are distinctively colored in both redox states. A decrease in the concentration of the redox mediator will likely

have similar positive effects concerning color and loss current as explained in section 2.3.1. for the KHCF(III)-containing ECDs.

The use of the redox mediator TMTU/TMFDS<sup>2+</sup> (0.1 M, molar ratio TMTU:TMFDS<sup>2+</sup> 1:10) in 1 M LiClO<sub>4</sub>/PC in combination with Fe-MEPE is a step towards a colorless bright state due to the high transparency ( $\tau_v=96\%$ ) and color neutrality ( $L^*=97.9$ ,  $a^*=0.2$ ,  $b^*=7.5$ ) of this electrolyte (Figure 2D). Figure 5C shows that MEPE-ECD7\_TMTU has a blue tint ( $L^*=59.2$ ,  $a^*=7.2$ ,  $b^*=-29.1$ ) in the dark state and switches completely at 2 V ( $L^*=87.7$ ,  $a^*=-9.2$ ,  $b^*=11.6$ ). The visible light transmittance changes from  $\tau_v=25\%$  (dark state) to 72% (bright state), which results in a  $\Delta\tau_v$  of 47%. The optical contrast, the color coordinates and the coloration efficiency ( $572\text{ cm}^2\cdot\text{C}^{-1}$  at 584 nm) are in good agreement with those of the pristine Fe-MEPE electrode (see Figure 3A). The expected increase of the bleaching voltage of 249 mV by the higher redox potential of TMTU/TMFDS<sup>2+</sup> (450 mV vs. Ag/AgCl)<sup>[6]</sup> as compared to Fc<sup>0/+</sup> (201 mV vs. Ag/AgCl)<sup>[17]</sup> cannot explain the actual increase. As both redox mediators have an uncharged reduced state, it is assumed that the further increase of the bleaching voltage for MEPE-ECD7\_TMTU may be attributed to the redox reaction in Equation (1).<sup>[7,20]</sup> Instead of the intramolecular one-electron redox reaction for Fc<sup>0/+</sup>, two TMTU molecules are combined to the bi-cation TMFDS<sup>2+</sup> as described in Ref. [6]. The higher charge transfer resistance of TMTU/TMFDS<sup>2+</sup> compared to I<sup>-</sup>/I<sub>3</sub><sup>-</sup> at the CE was given as a critical parameter for the response time of the corresponding ECDs. The difference in the 1-electron vs. 2-electron/2-molecules reaction may account for the decrease of the loss current from approx. 70  $\mu\text{A}\cdot\text{cm}^{-2}$  (for MEPE-ECD5\_Fc-PF<sub>6</sub> and MEPE-ECD6\_Fc-BF<sub>4</sub>) to 3  $\mu\text{A}\cdot\text{cm}^{-2}$



ECD is comparable to the bright state of the pristine  $\text{Ni}_{1-x}\text{O}$  electrode ( $L^* = 86.6$ ,  $a^* = -0.6$ ,  $b^* = 14.9$ ), while the dark state still has a higher transmittance. This indicates that the  $\text{Ni}_{1-x}\text{O}$  electrode is only partially oxidized, which is in accordance with the calculated charge density ( $q = 4.04 \text{ mC} \cdot \text{cm}^{-2}$ ) from the potentiostatic measurements in Figure S5 leading to a coloration efficiency of  $85 \text{ cm}^2 \cdot \text{C}^{-1}$  at 584 nm. Unfortunately, this leads to a decrease in the optical contrast (Figure 3B). The ECDs with the other two redox electrolytes have  $\Delta\tau_v$  values similar to that of the reference  $\text{Ni}_{1-x}\text{O}$ -ECD1 (between 21 to 24%) but are not as dark in both states as the pristine  $\text{Ni}_{1-x}\text{O}$  electrode. Therefore, it seems that for the tested TMTU/TMDS<sup>2+</sup> ratios, 1:0.1 best fits the  $\text{Ni}^{2+}/\text{Ni}^{3+}$  ratio in the as-prepared  $\text{Ni}_{1-x}\text{O}$  electrode. Nonetheless, further improvement of the  $\Delta\tau_v$  values may be possible through optimization of the TMTU/TMDS<sup>2+</sup> ratio. The necessary switching voltages with TMTU/TMFDS<sup>2+</sup> as the redox mediator are higher than expected from the redox potential of  $\text{Ni}_{1-x}\text{O}$  and TMTU/TMFDS<sup>2+</sup> (see Table S1). In addition, the response time is in the range of minutes, a possible explanation for which is given in section 2.3.2.<sup>[7,20]</sup> However, the loss current is very low (approx.  $10 \mu\text{A} \cdot \text{cm}^{-2}$ ) and all four Ni-oxide-based ECDs have comparable current densities during the first switching cycle, with only  $\text{Ni}_{1-x}\text{O}$ -ECD3\_TMTU exhibiting no decrease during the first five cycles (Figure S5).

### 3. Conclusions

This work illustrates that different redox mediators (KHCF(III), Fc-PF<sub>6</sub>, Fc-BF<sub>4</sub> and TMTU) can be utilized in functional hybrid type II ECDs made up of cathodically (Fe-MEPE) or anodically coloring (non-stoichiometric  $\text{Ni}_{1-x}\text{O}$ ) electrochromic thin film electrodes. The combination of KHCF(III) with Fe-MEPE electrodes (MEPE-ECD2\_HCF) exhibits a maximum  $\Delta\tau_v$  of 48%, when cycled between 0 V and 1.5 V. However, the cycling stability of this ECD configuration is poor at redox mediator concentrations  $> 0.01 \text{ M}$  due to the formation of PB. This undesirable side reaction can be avoided by using ferrocenium- or TMTU-based redox mediators. The ferrocenium-based ECDs (MEPE-ECD5\_Fc-PF<sub>6</sub> and MEPE-ECD5\_Fc-BF<sub>4</sub>) are distinctively colored in both their dark and the bright states (dark blue vs. light green) resulting in  $\Delta\tau_v$  values of only 26% and 27%, respectively. In contrast, a relatively high  $\Delta\tau_v$  value of 47% was obtained for MEPE-ECD7\_TMTU showing a bright state transmittance of 72% ( $L^* = 87.7$ ,  $a^* = -9.2$ ,  $b^* = 11.6$ ) at an applied voltage of 2 V. Low concentrations of KHCF(III) and TMTU influence the electrochemical response positively, but do not have a significant impact on the optical properties of the ECDs. TMTU/TMFDS<sup>2+</sup> was successfully employed as a redox mediator in combination with  $\text{Ni}_{1-x}\text{O}$  electrodes. The ECD with a TMTU/TMFDS<sup>2+</sup> molar ratio of 1:0.1 in 1 M LiClO<sub>4</sub>/PC as electrolyte ( $\text{Ni}_{1-x}\text{O}$ -ECD3\_TMTU) showed the best results in terms of visible light transmittance change ( $\Delta\tau_v = 32\%$ ) between the dark state ( $\tau_v = 38\%$  at 2 V) and the bright state ( $\tau_v = 70\%$  at -2 V) among the  $\text{Ni}_{1-x}\text{O}$ -based cells investigated. As compared to the ECDs without a redox mediator, the operating voltages with KHCF(III)- and ferrocenium-containing electrolytes were distinctly

reduced from 2 V to 1 V. This result implies that incorporating redox mediators into the electrolyte provides a straightforward and effective means of simplifying device structures and of improving the performance of ECDs based on Fe-MEPE and  $\text{Ni}_{1-x}\text{O}$ . Additionally, the colorless TMTU/TMFDS<sup>2+</sup> redox mediator is a potential substitute for commonly used redox electrolytes with the goal of achieving the highly sought-after neutral tint ECDs. Future studies will focus on a detailed understanding of the unexpectedly high cell voltage for the bleaching process involving the TMTU/TMFDS<sup>2+</sup> redox mediator. Along with the scale-up of the layer deposition and device assembly, this could pave the way for cost-efficient ECDs with promising optical properties.

## Experimental Section

### Materials and synthesis

All chemicals were purchased from Sigma-Aldrich and used without further purification.

### Fe-MEPE synthesis and thin film preparation

The terpyridine ligand, 4',4''''-(1,4-phenylene)bis(2,2':6',2''-terpyridine) (tpy-ph-tpy), was synthesized as previously described.<sup>[34]</sup> Fe-MEPE was prepared with a metal ion-to-ligand molar ratio of 1:1.<sup>[23,27]</sup> Fe(OAc)<sub>2</sub> was obtained by refluxing Fe in glacial acetic acid, which was then added to a solution of tpy-ph-tpy. After refluxing for 2 h the solvent was removed *in vacuo*. The formation of coordination complexes and successful synthesis of MEPEs can be easily observed by increasing viscosity and rapid color change of the solution during the self-assembly process. Fluorine-doped tin oxide (FTO) coated glass substrates (Pilkington,  $14 \Omega \cdot \text{sq}^{-1}$ ) were used and rinsed in ethanol before coating. Homogeneous thin films were prepared by means of dip coating (withdrawal speed:  $35 \text{ mm} \cdot \text{min}^{-1}$ ) from a Fe-MEPE solution (35 mM in methanol/ethanol/2-butoxyethanol) containing a proprietary polyurethane-polyisiloxane binder to improve the film-forming properties. Finally, the Fe-MEPE thin films (thickness:  $\sim 330 \text{ nm}$ ) were annealed at 60 °C for 24 h to ensure good adhesion on the TCO layer.

### Preparation of $\text{Ni}_{1-x}\text{O}$ pigment dispersions and thin film electrodes

The preparation of the  $\text{Ni}_{1-x}\text{O}$  pigment dispersion was carried out according to a published procedure that yielded nickel oxide films with nickel vacancies, *i.e.* higher  $\text{Ni}^{3+}$  content.<sup>[26,31]</sup> In brief, the  $\text{Ni}_{1-x}\text{O}$  pigment was synthesized via a sol-gel peroxoroute using a H<sub>2</sub>O<sub>2</sub>/urea mixture reacting with nickel(II) acetate powder. The obtained dried xerogel was thermally treated at 400 °C for 24 h to obtain the non-stoichiometric  $\text{Ni}_{1-x}\text{O}$  pigment ( $\text{Ni}^{2+}/\text{Ni}^{3+}$  ratio approx. 0.5).<sup>[31]</sup> Secondly, NiO<sub>x</sub>H<sub>y</sub> dispersant and binder were prepared by precipitation of nickel(II) sulfate with sodium hypochlorite.<sup>[26]</sup> The precipitate was then rinsed in distilled water to remove sulfate anions and dried at 50 °C overnight. The dispersion consisted of 10 wt% of  $\text{Ni}_{1-x}\text{O}$  pigment dispersed in deionized water<sup>[31]</sup> and the viscosity of the pigment dispersion was adjusted for spin coating ( $1.9 \text{ mPa} \cdot \text{s}$  at a shear rate of  $500 \text{ s}^{-1}$ ). The  $\text{Ni}_{1-x}\text{O}$  thin films were deposited on FTO glass with a rotation speed of 500 rpm for 5 s, followed by 1000 rpm for 1 min. To increase the film thickness, five layers of  $\text{Ni}_{1-x}\text{O}$  were deposited consecutively,



resulting in an overall thickness of around 1.25  $\mu\text{m}$ . Subsequently, the  $\text{Ni}_{1-x}\text{O}$  electrodes were annealed at 150  $^{\circ}\text{C}$  for 30 min.

### Preparation of glass-based ECDs

ECDs with the cell configuration [glass/FTO/Fe-MEPE/redox electrolyte/FTO/glass] were fabricated with an active (switchable) area of  $4 \times 3.5 \text{ cm}^2$ , while the [glass/FTO/electrolyte/ $\text{Ni}_{1-x}\text{O}$ /FTO/glass] ECDs had an active area of  $2 \times 2 \text{ cm}^2$ . The redox electrolytes used are summarized in Table 1. As  $\text{KHCF(III)}$  was only soluble in an aqueous  $\text{Li}^+$ -containing electrolyte, the corresponding ECDs were fabricated under lab conditions. The Fe-MEPE-based ECDs with 0 M, 0.001 M, 0.01 M, and 0.1 M  $\text{KHCF(III)}$  in 1 M  $\text{LiClO}_4/\text{H}_2\text{O}$  as the redox electrolyte are referred to as MEPE-ECD1, MEPE-ECD2\_HCF, MEPE-ECD3\_HCF, and MEPE-ECD4\_HCF, respectively.

The devices containing Fe-MEPE and ferrocenium hexafluorophosphate ( $\text{Fc-PF}_6$ ), ferrocenium tetrafluoroborate ( $\text{Fc-BF}_4$ ) or tetramethylthiourea (TMTU) dissolved in 1 M  $\text{LiClO}_4/\text{PC}$  were prepared under argon atmosphere in a glove box ( $\text{H}_2\text{O} < 5 \text{ ppm}$ ) and are referred to as MEPE-ECD5\_Fc-PF<sub>6</sub>, MEPE-ECD6\_Fc-BF<sub>4</sub>, and MEPE-ECD7\_TMTU, respectively.

The combinations of  $\text{Ni}_{1-x}\text{O}$  electrodes with different molar ratios of TMTU and  $\text{TMFDS}^{2+}$  were also fabricated in a glove box. The ECD not containing any redox mediator ( $\text{Ni}_{1-x}\text{O\_ECD1}$ ) was used as a reference. The ECDs with TMTU/ $\text{TMFDS}^{2+}$  (molar ratios of 1:0, 1:0.1, 1:1) are referred to as  $\text{Ni}_{1-x}\text{O-ECD2\_TMTU}$ ,  $\text{Ni}_{1-x}\text{O-ECD3\_TMTU}$ , and  $\text{Ni}_{1-x}\text{O-ECD4\_TMTU}$ . The ECDs were assembled according to the procedure previously described in Ref. [25].

### Methods and instruments

Cyclic voltammetry (CV) measurements on the Fe-MEPE and  $\text{Ni}_{1-x}\text{O}$  thin film electrodes were performed with a Solartron Multistat 1470E potentiostat/galvanostat in a conventional three-electrode set-up with Li as counter (CE) and reference electrode (RE) in a liquid electrolyte (1 M  $\text{LiClO}_4/\text{PC}$ ).<sup>[24]</sup> Spectroelectrochemical properties were determined in a three-electrode set-up with platinum as CE, Ag/AgCl as RE and 1 M  $\text{LiClO}_4/\text{PC}$  as electrolyte. The Prussian Blue (PB) precipitation reference experiment was carried out in a two-electrode set-up with 0.1 M  $\text{K}_3[\text{Fe}(\text{CN})_6]$  in 1 M  $\text{LiClO}_4/\text{H}_2\text{O}$ , Fe-MEPE as working electrode (WE) and platinum as CE.

The ECDs were characterized by means of potentiostatic measurements and UV-Vis spectra were recorded with an Avantes AvaSpec-2048 standard fiber optic spectrometer combined with a balanced deuterium-halogen light source.

**Table 1.** Redox electrolytes with 1 M  $\text{LiClO}_4$  in  $\text{H}_2\text{O}$  or PC and gelling agent used in this study.

ECD	Redox mediator	c (redox mediator) [mol·l <sup>-1</sup> ]	Solvent
MEPE-ECD1	–	–	$\text{H}_2\text{O}$
MEPE-ECD2_HCF	$\text{K}_3[\text{Fe}(\text{CN})_6]$	0.001	$\text{H}_2\text{O}$
MEPE-ECD3_HCF	$\text{K}_3[\text{Fe}(\text{CN})_6]$	0.01	$\text{H}_2\text{O}$
MEPE-ECD4_HCF	$\text{K}_3[\text{Fe}(\text{CN})_6]$	0.1	$\text{H}_2\text{O}$
MEPE-ECD5_Fc-PF <sub>6</sub>	$\text{Fc-PF}_6$	0.1	PC
MEPE-ECD6_Fc-BF <sub>4</sub>	$\text{Fc-BF}_4$	0.1	PC
MEPE-ECD7_TMTU	TMTU/ $\text{TMFDS}^{2+}$	0.1	PC
$\text{Ni}_{1-x}\text{O-ECD1}$	–	–	PC
$\text{Ni}_{1-x}\text{O-ECD2\_TMTU}$	TMTU/ $\text{TMFDS}^{2+}$	1:0	PC
$\text{Ni}_{1-x}\text{O-ECD3\_TMTU}$	TMTU/ $\text{TMFDS}^{2+}$	1:0.1	PC
$\text{Ni}_{1-x}\text{O-ECD4\_TMTU}$	TMTU/ $\text{TMFDS}^{2+}$	1:1	PC

The switching voltages of the ECDs were determined by applying a stepwise increase of the cell voltage. The bleaching voltage is defined as the threshold voltage where the device was fully bleached and no further changes in the transmittance observed at higher voltages. The visible light transmittance ( $\tau_v$ ) was calculated according to DIN EN 410. Fourier-transform infrared (FTIR) spectroscopy was performed on an IR-spectrometer Nicolet iS5 from ThermoScientific.

### Acknowledgements

The authors acknowledge the financial support from the Bavarian Ministry of Economic Affairs and Media, Energy and Technology for funding the Fraunhofer R&D Center for Electromobility Bavaria. We would like to thank Dr. Mohor Mihelčič and Dr. Ivo Jerman from the National Institute of Chemistry (NIC), Ljubljana, Slovenia for the preparation of the  $\text{Ni}_{1-x}\text{O}$  thin film electrodes. The contribution of Christine Müller (Fraunhofer ISC) for assisting in the cell preparation is gratefully acknowledged. Open access funding enabled and organized by Projekt DEAL.

### Conflict of Interest

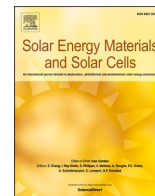
The authors declare no conflict of interest.

**Keywords:** electrochemistry · electrochromic device · metallopolymer · non-stoichiometric nickel oxide · redox electrolytes · UV-Vis spectroscopy

- [1] C. J. Cleveland, R. U. Ayres, *Encyclopedia of energy*, Elsevier, Amsterdam, Boston **2004**. ISBN: 978-0-12-176480-7.
- [2] C. G. Granqvist, *Handbook of Inorganic Electrochromic Materials*, Elsevier, Amsterdam **1995**, <https://doi.org/10.1016/B978-0-444-89930-9.X5000-4>.
- [3] R. D. Rauh, *Electrochim. Acta* **1999**, *44*, 3165–3176, [https://doi.org/10.1016/S0013-4686\(99\)00034-1](https://doi.org/10.1016/S0013-4686(99)00034-1).
- [4] R. J. Mortimer, D. R. Rosseinsky, P. M. S. Monk, *Electrochromic Materials and Devices*, Wiley-VCH **2015**. ISBN: 978-3-527-33610-4.
- [5] A. Hauch, A. Georg, U. O. Krašovec, B. Orel, *J. Electrochem. Soc.* **2002**, *149*, H159, <https://doi.org/10.1149/1.1496487>.
- [6] S. Bogati, A. Georg, C. Jerg, W. Graf, *Sol. Energy Mater. Sol. Cells* **2016**, *175*, 454–461, <https://doi.org/10.1016/j.solmat.2016.07.023>.
- [7] S. Bogati, A. Georg, W. Graf, *Sol. Energy Mater. Sol. Cells* **2017**, *159*, 395–404, <https://doi.org/10.1016/j.solmat.2016.08.023>.
- [8] P. M. Allemand, R. F. Grimes, A. R. Ingle, J. P. Cronin, S. R. Kennedy, A. Agrawal, J. M. Boulton, (Donnelly Corporation) *US 6178034 B1* **1997**.
- [9] S. Bogati, R. Basnet, A. Georg, *Sol. Energy Mater. Sol. Cells* **2019**, *189*, 206–213, <https://doi.org/10.1016/j.solmat.2018.09.026>.
- [10] Q. Tang, H. Li, Y. Yue, Q. Zhang, H. Wang, Y. Li, P. Chen, *Mater. Des.* **2017**, *118*, 279–285, <https://doi.org/10.1016/j.matdes.2017.01.033>.
- [11] H. Oh, D. G. Seo, T. Y. Yun, C. Y. Kim, H. C. Moon, *ACS Appl. Mater. Interfaces* **2017**, *9*, 7658–7665, <https://doi.org/10.1021/acsami.7b00624>.
- [12] Y. Saygili, M. Stojanovic, N. Flores-Díaz, S. M. Zakeeruddin, N. Vlachopoulos, M. Grätzel, A. Hagfeldt, *Inorganics*, **2019**, *7*, 30, <https://doi.org/10.3390/inorganics7030030>.
- [13] D. Li, H. Li, Y. Luo, K. Li, Q. Meng, M. Armand, L. Chen, *Adv. Funct. Mater.* **2010**, *20*, 3358–3365, <https://doi.org/10.1002/adfm.201000150>.
- [14] M. Grätzel, *Inorg. Chem.* **2005**, *44*, 6841–6851, <https://doi.org/10.1021/ic0508371>.
- [15] A. Georg, A. Georg, *Sol. Energy Mater. Sol. Cells*, **2009**, *93*, 1329–1337, <https://doi.org/10.1016/j.solmat.2009.02.009>.
- [16] M. Hočvar, U. Opara Krašovec, *Sol. Energy Mater. Sol. Cells* **2019**, *196*, 9–15, <https://doi.org/10.1016/j.solmat.2019.03.027>.

- [17] R. R. Gagne, C. A. Koval, G. C. Lisensky, *Inorg. Chem.* **1980**, *19*, 2854–2855, <https://doi.org/10.1021/ic50211a080>.
- [18] H. Tahara, K. Uranaka, M. Hirano, T. Ikeda, T. Sagara, H. Murakami, *ACS Appl. Mater. Interfaces* **2019**, *11*, 1–6, <https://doi.org/10.1021/acsaami.8b16410>.
- [19] J. R. Lompfrey, T. F. Guarr, (Gentex Corporation), *WO 2001063350 A1* **2001**.
- [20] M. Higuchi, S.-Y. Kao, K.-C. Ho, (National Institute for Material Science, National Taiwan University) *WO 2017034036 A1* **2017**.
- [21] C.-Y. Hsu, J. Zhang, T. Sato, S. Moriyama, M. Higuchi, *ACS Appl. Mater. Interfaces* **2015**, *7*, 18266–18272, <https://doi.org/10.1021/acsaami.5b02990>.
- [22] Z. Zhang, P. Chen, T. N. Murakami, S. M. Zakeeruddin, M. Grätzel, *Adv. Funct. Mater.* **2008**, *18*, 341–346, <https://doi.org/10.1002/adfm.200701041>.
- [23] M. Schott, H. Lorrmann, W. Szczerba, M. Beck, D. G. Kurth, *Sol. Energy Mater. Sol. Cells* **2014**, *126*, 68–73, <https://doi.org/10.1016/j.solmat.2014.03.032>.
- [24] F. S. Han, M. Higuchi, D. G. Kurth, *J. Am. Chem. Soc.* **2008**, *130*, 2073–2081, <https://doi.org/10.1021/ja710380a>.
- [25] L. Niklaus, M. Schott, M. Mihelčič, I. Jerman, U. Posset, G. Sextl, *Sol. Energy Mater. Sol. Cells* **2019**, *200*, 110002, <https://doi.org/10.1016/j.solmat.2019.110002>.
- [26] M. Mihelčič, I. Jerman, F. Švegl, A. Šurca Vuk, L. Slemenik Perše, J. Kovač, B. Orel, U. Posset, *Sol. Energy Mater. Sol. Cells* **2012**, *107*, 175–187, <https://doi.org/10.1016/j.solmat.2012.08.012>.
- [27] M. Schott, W. Szczerba, U. Posset, A. Šurca Vuk, M. Beck, H. Riesemeier, A. F. Thünemann, D. G. Kurth, *Sol. Energy Mater. Sol. Cells* **2016**, *147*, 61–67, <https://doi.org/10.1016/j.solmat.2015.10.015>.
- [28] S. Pai, M. Schott, L. Niklaus, U. Posset, D. G. Kurth, *J. Mater. Chem. C* **2018**, *6*, 3310–3321, <https://doi.org/10.1039/C7TC04177B>.
- [29] F. S. Han, M. Higuchi, D. G. Kurth, *Adv. Mater.* **2007**, *19*, 3928–3931, <https://doi.org/10.1002/adma.200700931>.
- [30] B. H. Brandow, *Adv. Phys.* **1977**, *26*, 651–808, <https://doi.org/10.1080/00018737700101443>.
- [31] M. Mihelčič, I. Jerman, B. Orel, *Prog. Org. Coat.* **2013**, *76*, 1752–1755, <https://doi.org/10.1016/j.porgcoat.2013.05.011>.
- [32] M. Mihelčič, A. Šurca Vuk, I. Jerman, B. Orel, F. Švegl, H. Moulki, C. Faure, G. Campet, A. Rougier, *Sol. Energy Mater. Sol. Cells* **2014**, *120*, 116–130, <https://doi.org/10.1016/j.solmat.2013.08.025>.
- [33] F. Michalak, K. von Rottkay, T. Richardson, J. Slack, M. Rubin, *Electrochim. Acta* **1999**, *44*, 3085–3092, [https://doi.org/10.1016/S0013-4686\(99\)00024-9](https://doi.org/10.1016/S0013-4686(99)00024-9).
- [34] E. C. Constable, A. M. W. C. Thompson, *J. Chem. Soc. Dalton Trans.* **1992**, *144*, 3467–3475, <https://doi.org/10.1039/DT9920003467>.
- [35] M. Bonomo, A. G. Marrani, V. Novelli, M. Awais, D. P. Dowling, J. G. Vos, D. Dini, *Appl. Surf. Sci.* **2017**, *403*, 441–447, <https://doi.org/10.1016/j.apsusc.2017.01.202>.
- [36] F. Švegl, A. Šurca Vuk, M. Hajzeri, L. Slemenik Perše, B. Orel, *Sol. Energy Mater. Sol. Cells* **2012**, *99*, 14–25, <https://doi.org/10.1016/j.solmat.2011.11.043>.
- [37] D. Wang, L. Wei, P. Shi, Y. Chen, S. Yan, Y. Tian, J. Jiao, *J. Alloys Compd.* **2019**, *771*, 100–105, <https://doi.org/10.1016/j.jallcom.2018.08.268>.
- [38] Y. Alesanco, J. Palenzuela, A. Viñuales, G. Cabañero, H. J. Grande, I. Odriozola, *ChemElectroChem* **2015**, *2*, 218–223, <https://doi.org/10.1002/celec.201402265>.
- [39] D. Rochefort, *Curr. Opin. Electrochem.* **2019**, *15*, 125–132, <https://doi.org/10.1016/j.coelec.2019.04.028>.
- [40] H.-C. Lu, S.-Y. Kao, H.-F. Yu, T.-H. Chang, C.-W. Kung, K.-C. Ho, *ACS Appl. Mater. Interfaces* **2016**, *8*, 30351–30361, <https://doi.org/10.1021/acsaami.6b10152>.
- [41] S. Duluard, A. Celik-Cochet, I. Saadeddin, A. Labouret, G. Campet, G. Schottner, U. Posset, M.-H. Delville, *New J. Chem.* **2011**, *35*, 2314, <https://doi.org/10.1039/c1nj20231f>.
- [42] D. M. D'Alessandro, F. R. Keene, *Chem. Rev.* **2006**, *106*, 2270–2298, <https://doi.org/10.1021/cr050010o>.
- [43] A. F. Holleman, E. Wiberg, N. Wiberg, M. Eagleson, W. Brewer, B. J. Aylett, *Inorganic chemistry*, 1st ed., Acad. Press, San Diego, Calif. **2001**, ISBN: 0123526515.
- [44] R. E. Bozak, *Photochemistry in the Metallocenes*, G. S. Hammond, W. A. Noyes, J. N. Pitts (Eds.), *Adv. Photochem.*, Wiley-Interscience, New York **1971**, 227–244, <https://doi.org/10.1002/9780470133385.ch5>.
- [45] K. Ueno, J. Murai, K. Ikeda, S. Tsuzuki, M. Tsuchiya, R. Tatara, T. Mandai, Y. Umebayashi, K. Dokko, M. Watanabe, *J. Phys. Chem. C* **2016**, *120*, 15792–15802, <https://doi.org/10.1021/acs.jpcc.5b11642>.
- [46] J. Zhang, C.-Y. Hsu, M. Higuchi, *J. Photopolym. Sci. Technol.* **2014**, *27*, 297–300, <https://doi.org/10.2494/photopolymer.27.297>.
- [47] G. Schwarz, I. Haßlauer, D. G. Kurth, *Adv. Colloid Interface Sci.* **2014**, *207*, 107–120, <https://doi.org/10.1016/j.cis.2013.12.010>.

Manuscript received: April 23, 2020  
Revised manuscript received: May 25, 2020  
Accepted manuscript online: June 2, 2020



# Mixed metal oxides as optically-passive ion storage layers in electrochromic devices based on metallopolymers

Lukas Niklaus<sup>a</sup>, Marco Schott<sup>a,\*</sup>, Jonas Subel<sup>b</sup>, Stephan Ulrich<sup>b</sup>, Daniel Reichert<sup>c</sup>, Uwe Posset<sup>a</sup>, Guinevere A. Giffin<sup>a</sup>

<sup>a</sup> Fraunhofer Institute for Silicate Research ISC, Neunerplatz 2, 97082, Würzburg, Germany

<sup>b</sup> Fraunhofer Institute for Surface Engineering and Thin Films IST, Bienroder Weg 54 E, 38108, Braunschweig, Germany

<sup>c</sup> EControl-Glas GmbH & Co. KG, Otto-Erbert-Str. 8, 08527, Plauen, Germany

## ARTICLE INFO

### Keywords:

Electrochromic devices  
Metallopolymers  
Ion storage layer  
Vanadium-titanium oxide  
Titanium-manganese oxide

## ABSTRACT

Electrochromic devices (ECDs) based on iron metallopolymers (Fe-MEPE) and different oxide-based ion storage electrodes on fluorine-doped tin oxide (FTO)-coated glass as transparent, conductive substrates are investigated in detail. Titanium-manganese oxide (TMO) thin film electrodes deposited by reactive magnetron co-sputtering on FTO glass were compared to commercially available titanium-vanadium oxide (TiVO<sub>x</sub>) for use as optically-passive ion storage layers. The ECDs with Fe-MEPE combined with TiVO<sub>x</sub> (coloration efficiency  $\eta = 2 \text{ cm}^2 \text{ C}^{-1}$  at 584 nm) and Ti-rich TMO ( $\eta = -4 \text{ cm}^2 \text{ C}^{-1}$ ) are blue-purple in the dark state at 0 V and become highly transmissive when 1.5 V is applied with a visible light transmittance ( $\tau_v$ ) change from 28% to 69% and 21% to 57% in 3 s and 13 s, respectively. The ECDs show fast responses and high reversibility over more than 100 cycles. The combination of Fe-MEPE and Mn-rich TMO ( $\eta = -24 \text{ cm}^2 \text{ C}^{-1}$ ) leads to a dark brown ECD, which can be brightened at 2.5 V ( $\tau_v$ : 4%  $\leftrightarrow$  17%, 9 s for decoloring).

## 1. Introduction

Electrochromic devices (ECDs) are able to change their optical properties (absorption, reflection) by applying a low potential supplied by an external power source [1,2]. In comparison to gasochromic [3], photochromic [4], or thermochromic [5] devices, ECDs exhibit better user-controlled and color-tuning ability. Thus, this technology is attractive for applications such as anti-glare rear-view mirrors [6], smart windows [7–10] or electrochromic displays [11]. Electrochromic (EC) glazing can increase the energy efficiency in buildings as well as enhance the indoor comfort by avoiding glare. A recent study showed that EC smart windows for architectural glazing should be capable to change their visible light transmittance ( $\tau_v$ ) from less than 10% in the colored (dark) state to 50–70% in the bright state [12,13]. State-of-the-art EC products, e.g. from View, Saint-Gobain (SageGlass®), Kinestral (Halio™), ChromoGenics (ConverLight®), and EControl-Glas (ec smart glass 2), fulfill most of these optical requirements [13]. However, the main drawbacks of commercial EC products are their high price and relatively long response time, in particular, for large-area devices based on inorganic materials. Roll-to-roll production,

high-rate thin film deposition techniques and continuous lamination processes could lead to inexpensive manufacturing of ECDs [14]. Metallopolymers (MEPE) have thoroughly been investigated as cathodically-coloring (coloration upon reduction and Li<sup>+</sup> insertion) EC materials in recent studies [15–18]. A strong metal-to-ligand charge-transfer (MLCT) transition in the visible spectrum is responsible for the intense color of the metallopolymers. They are synthesized by metal ion coordination of suitable metal ions, such as Fe, Co, Cu, Ru, Ni, Zn and a ditopic ligand such as 1,4-bis(2,2':6',2''-terpyridine-4'-yl)benzene [19, 20]. Fe-MEPEs consisting of Fe<sup>2+</sup> ions, bis(terpyridine) ligands and acetate (OAc<sup>-</sup>) counter ions show outstanding EC properties and exhibit a reversible color change upon oxidation from blue (Fe<sup>2+</sup>) to colorless (Fe<sup>3+</sup>) [21]. MEPEs show high contrast ratios (demonstrated by T<sub>MLCT</sub> values from < 5% (dark) to > 80% (bright), short response times (depending on the active area), high cycle stability (charge retention) over thousands of switching cycles, and high coloration efficiencies ( $\eta > 500 \text{ cm}^2 \text{ C}^{-1}$ ) [22–25]. By employing wet-chemical processes for fabricating MEPE thin films, e.g. dip-coating [26] or roll-to-roll processing [27], there is a high potential for cost reduction in comparison to inorganic EC materials such as tungsten oxide (WO<sub>3</sub>) [9,28–30] or nickel

\* Corresponding author.

E-mail address: [marco.schott@isc.fraunhofer.de](mailto:marco.schott@isc.fraunhofer.de) (M. Schott).

<https://doi.org/10.1016/j.solmat.2020.110950>

Received 24 August 2020; Received in revised form 22 December 2020; Accepted 25 December 2020

Available online 18 January 2021

0927-0248/© 2021 Elsevier B.V. All rights reserved.

oxide (NiO) [31–33] prepared by sputtering techniques.

It has been shown that for a given pair of EC materials, the maximum contrast realized by one material may be higher than for any combination involving those two materials [34]. Therefore, a second coloring EC material may not be needed and a transparent counter electrode may be the best solution to achieve the maximum possible contrast [35]. The use of transparent, optically-passive counter electrodes has been explored in the past [35,36]. S. Hassab et al. used a cathodically-coloring thiophene derivative ( $2.2 \text{ mC cm}^{-2}$ ,  $\eta = 379 \text{ cm}^2 \text{ C}^{-1}$ ) as the working electrode and  $\text{WO}_3$  ( $24 \text{ mC cm}^{-2}$ ,  $\eta = 19 \text{ cm}^2 \text{ C}^{-1}$ ) as an optically-passive transparent counter electrode. The difference in coloration efficiencies between these materials in combination with the high transparency of  $\text{WO}_3$  films, enabled a high optical contrast (57% at 566 nm), fast response times (3 s), and low operating voltages (+0.8/−0.7 V) of this strongly unbalanced configuration. The group of S. Ulrich prepared several mixed Ti-Nb oxide films for optically-passive electrodes with high transmittance values (> 75%) in both, the dark and bright, states.

In this study, the ion storage layer has to have a higher charge density to balance the complete switching of the Fe-MEPE electrode with a negligible optical contribution of its own. Recently, it has been shown that Fe-MEPEs and metal oxide materials like vanadium oxide can be combined in an ECD switching from blue-purple ( $L^* = 55.2$ ,  $a^* = -4.4$ ,  $b^* = -3.8$ ,  $\tau_v = 22\%$ ) to light yellow ( $L^* = 80.2$ ,  $a^* = -12.3$ ,  $b^* = 17.6$ ,  $\tau_v = 58\%$ ) when voltages of 0 V and 1.6 V are applied, respectively [37]. In order to increase the optical contrast, new EC cell configurations based on Fe-MEPE and mixed metal oxide electrodes (titanium-vanadium oxide,  $\text{TiVO}_x$ , and titanium-manganese oxide, TMO) are investigated here. Ti-V oxides are particularly useful as ion storage materials in combination with Fe-MEPE due to their high charge density and low coloration efficiency [37]. By incorporating Ti into the V oxide, the electrical conductivity, electrochemical stability and reversibility is enhanced, the crystallization during cycling is prevented and the transmittance change during cycling is decreased [38,39]. Mn oxides as EC materials have been thoroughly investigated in literature [14,40,41]. However, addition of Ti offers interesting new Ti-Mn oxides, which are presented for the first time in combination with Fe-MEPE in an ECD in this paper.

## 2. Experimental

All chemicals were purchased from Sigma-Aldrich and used without further purification.

### 2.1. Deposition of Fe-MEPE, $\text{TiVO}_x$ , and TMO electrodes on FTO glass

The bis(terpyridine) ligand 1,4-bis(2,2':6',2''-terpyridin-4'-yl)benzene (tpy-ph-tpy) and Fe-MEPE were synthesized according to the procedure given in the literature [21,42]. The deposition of Fe-MEPE thin films (thickness of approx. 330 nm) on fluorine-doped tin oxide (FTO)-coated glass substrates (Pilkington, approx.  $14 \Omega \text{ sq.}^{-1}$  sheet resistance) was performed via a dip-coating process as previously explained in detail in the literature [21].

The sputter-deposited  $\text{TiVO}_x$  electrodes were provided by EControl-Glas GmbH & Co. KG. TMO depositions on unheated substrates were carried out within a Systec ZVL 1000 *in-line* coater using a co-sputtering setup and reactive DC sputtering processes – Fig. 1.

Two of the three cathodes were equipped with Ti and Mn targets. Thin films with a thickness of 172 nm (Ti-rich) and 223 nm (Mn-rich) were prepared on rotating FTO glass substrates (sample size:  $10 \times 10 \text{ cm}^2$ ) and Si-wafers and EagleXG glasses. The Ti- and Mn-rich compositions were obtained by varying the power ratios of the Ti and Mn cathodes – Table 1. For enhanced porosity, which promotes Li-intercalation, a high pressure of 2.8 Pa was applied. The Ti-rich and Mn-rich TMO electrodes are further referred to as TMO-1 and TMO-2, respectively. The TMO layer thicknesses were obtained from modelling of transmittance and reflectance spectra using an in house

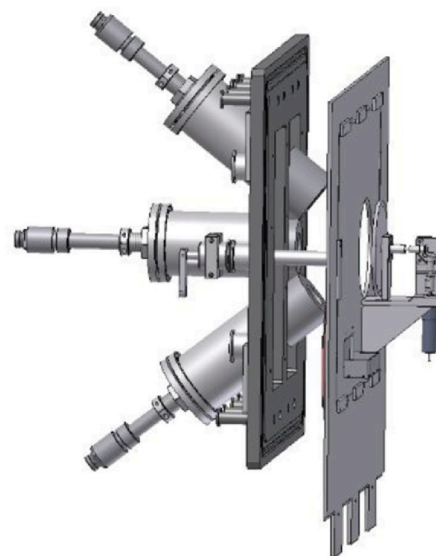


Fig. 1. Co-sputtering setup for the deposition of TMO thin films.

developed software RIG-VM and a Tauc-Lorentz model dielectric function [43]. Optical spectra were measured with an Agilent Cary 5000 UV-Vis-NIR photometer. The TMO films on silicon wafers were investigated by electron probe micro analysis (EPMA) using a CAMECA SX100 instrument ( $U_{\text{Beam}} = 10 \text{ keV}$ ,  $I_{\text{Beam}} = 100 \text{ nA}$ , 5 measurements for each sample, reference samples for stoichiometry calibration:  $\text{TiMnO}_3$  and 10 wt% Ar implanted in Si). The evaluation was conducted with STRATAGEM software from SAMx using the thin film analysis scheme by Pouchou and Pichoir [44,45]. The resulting chemical composition is given in Table 1.

### 2.2. Preparation of glass-based ECDs

ECDs with the configuration glass/FTO/Fe-MEPE/electrolyte/ $\text{TiVO}_x$ /FTO/glass (referred to as ECD-1) and glass/FTO/Fe-MEPE/electrolyte/TMO/FTO/glass (referred to as ECD-2 and ECD-3 for TMO-1 and TMO-2 as ion storage layers, respectively) with an active (switchable) area of  $2 \times 2 \text{ cm}^2$  were fabricated under argon atmosphere in a glove box by the following procedure: A proprietary  $\text{LiClO}_4$ -containing gel electrolyte was prepared under dry conditions and coated on the MEPE electrode with a wet film thickness of approx.  $90 \mu\text{m}$  by using a doctor-blade device. In a second step, the  $\text{TiVO}_x$  or TMO electrode was laminated on top and Cu tape was attached as bus bars.

### 2.3. Optical and electrochemical measurements

Laser scanning microscope (LSM) images were obtained with a Keyence VK-X200 microscope. The lateral and vertical resolution (beam width) is 219 nm and 3 nm, respectively. A magnification of 150 was used with a numerical aperture (NA) of 0.95 and a wavelength of 408 nm.

The optical and colorimetric (according to CIELAB color space) measurements were performed with an Avantes AvaSpec-2048 standard fibre optic spectrometer combined with a balanced deuterium-halogen light source under lab conditions, while the spectroelectrochemical measurements were performed in a glove box under argon atmosphere. The  $\tau_v$  value is calculated according to DIN EN410. The electrochemical characterization (cyclic voltammetry (CV), charging/discharging behavior over 1000 switching cycles) of the electrode materials was performed in a three-electrode setup with Li as counter/reference electrode (CE/RE) and 1 M  $\text{LiClO}_4/\text{PC}$  as electrolyte. Cu tape was attached to the FTO glass to contact the electrodes. The *in-situ*

**Table 1**

Sputtering conditions and sample composition: gas flow  $q$ , pressure  $p$ , cathode power  $P$ , thickness  $t$  and deposition rate  $r_d$ . Target-substrate distance: 170 mm, target-size:  $2''\varnothing$ .

	Sputtering conditions								Sample composition		
	$q(\text{Ar})$ / sccm	$q(\text{O}_2)$ / sccm	$p$ / Pa	$p\text{-O}_2$ / mPa	$P(\text{Ti})$ / W	$P(\text{Mn})$ / W	$t$ / nm	$r_d$ / $\text{nm}\cdot\text{min}^{-1}$	Mn / at. %	Ti / at. %	O / at. %
TMO-1	400	15	2.76	53.2	168	36	182	1.40	8.2	25.1	66.5
TMO-2	400	15	2.75	54.4	75	91	223	1.35	33.7	2.9	63.0

spectroelectrochemical measurements were carried out in a three-electrode setup with platinum as CE, Ag/AgCl as RE and 1 M LiClO<sub>4</sub>/PC as electrolyte. The ECDs were characterized by means of potentiostatic measurements and the UV-Vis spectra and colorimetric values were recorded with an Avantes AvaSpec-2048 standard fiber optic spectrometer combined with a balanced deuterium-halogen light source. The optimal operating voltages of the ECDs were determined by a stepwise increase of the cell voltage. The decoloring voltage is defined as the threshold voltage where the device was in the clear state and no further changes in the transmittance were observed at higher voltages. The electrochemical characterization (potentiostatic steps) of the ECDs was performed with a Solartron Multistat 1470E potentiostat/galvanostat. The charge density of the ECDs was calculated from the potentiostatic cycling measurements (Fig. 5). All measurements were carried out under inert atmosphere (glove box) at room temperature.

### 3. Results and discussion

#### 3.1. Optical characterization of Fe-MEPE, TiVO<sub>x</sub>, and TMO electrodes on FTO glass

The optical properties of the electrodes used for the ECDs were investigated in detail and the results are summarized in Table 2. The Fe-MEPE, TiVO<sub>x</sub>, and TMO thin films on FTO glass are highly transparent (haze < 1%) and show a homogeneous and defect-free surface as is evident from the LSM images in Fig. S1.

Fe-MEPE shows a strong absorption at around 594 nm resulting in a very low transmittance of only 4% ( $\tau_v = 27\%$ ) as seen in Fig. 2A. This is attributed to a MLCT transition from a d orbital of the Fe<sup>2+</sup> ion to a  $\pi^*$  orbital of the bis(terpyridine) ligand [15]. In the near-infrared range of the electromagnetic spectrum (> 780 nm) Fe-MEPE is highly transmissive. In contrast, the metal oxide electrodes do not feature distinct transmittance peaks but have broad d-d intervalence charge transfer (IVCT) transitions in the visible and near-infrared region [2]. The TiVO<sub>x</sub> layer has a light-yellow hue and is highly transmissive ( $\tau_v = 77\%$ ) – Fig. 2B. The TMO-1 and TMO-2 layers exhibit a yellowish ( $L^* = 85.7$ ,  $a^* = -2.3$ ,  $b^* = 14.9$ ) and brown tint ( $L^* = 32.3$ ,  $a^* = 22.1$ ,  $b^* = 47.6$ ) with  $\tau_v$  values of 67% and 9%, respectively. As can be seen in Table 2, the

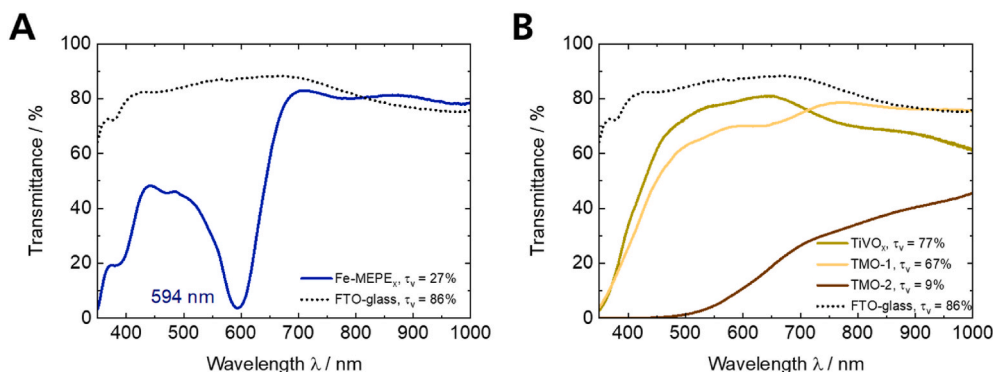
TiVO<sub>x</sub> and TMO-1 have similar color coordinates, with very high  $L^*$  values of over 85,  $|a^*| < 5$  and  $|b^*|$  values around 10, which potentially allows these materials to be implemented as virtually colorless counter electrodes. In contrast, TMO-2 has a very low  $\tau_v$  of 9% and an unpleasant brown tint in the as-deposited film, which is attributed to the higher amount of Mn in the crystal structure.

#### 3.2. (Spectro-)electrochemical characterization of Fe-MEPE, TiVO<sub>x</sub>, and TMO

The EC properties of the electrodes were investigated by *in-situ* spectroelectrochemical measurements and the results are summarized in Table 3. Despite the fact that the Fe-MEPE electrode was already characterized in previous publications, the results are included and summarized for the sake of completeness and clarity [46,47]. The spectroelectrochemical characterization of Fe-MEPE can be seen in Fig. S2A, showing a high visible light transmittance change between the colored state ( $\tau_v = 29\%$ ) at 0 V vs. Ag/AgCl and the bright state ( $\tau_v = 83\%$ ) at 2 V vs. Ag/AgCl. The CV measurements of the Fe-MEPE thin film electrode in Fig. S2B shows an oxidation peak (Fe<sup>2+</sup> → Fe<sup>3+</sup>) at 4.03 V vs. Li/Li<sup>+</sup> and reduction peak (Fe<sup>3+</sup> → Fe<sup>2+</sup>) at 3.89 V vs. Li/Li<sup>+</sup> for decoloring/coloring. The Fe-MEPE electrode shows a high charge retention of around 98% after 1000 switching cycles (2.43 mC cm<sup>-2</sup> → 2.30 mC cm<sup>-2</sup>), determined at a current density of 50  $\mu\text{A cm}^{-2}$  – Fig. S2C.

The spectroelectrochemical properties of the mixed metal oxide electrodes (TiVO<sub>x</sub>, TMO-1 and TMO-2) were investigated to explore their potential use as an ion storage layer with high charge density and low optical contrast – Fig. 3A–C and Table 3. The TiVO<sub>x</sub> electrode shows a weak color change upon reduction from light yellow to light grey, indicating a cathodically-coloring behavior (coloration upon reduction and Li<sup>+</sup> insertion) with a  $\tau_v$  change between 85% (at 0 V vs. Ag/AgCl) and 75% (at -2 V vs. Ag/AgCl). In contrast, TMO-1 is anodically-coloring (coloration upon oxidation and Li<sup>+</sup> de-insertion) from light yellow to light grey with a small  $\tau_v$  change between 72% (at 0 V vs. Ag/AgCl) and 81% (at -2.5 V vs. Ag/AgCl). Moreover, TMO-2 shows an anodic behavior with a color change from deep brown ( $\tau_v = 14\%$ ) at 0 V vs. Ag/AgCl to light brown ( $\tau_v = 42\%$ ) at -2.5 V vs. Ag/AgCl.

The electrochemical properties of the mixed metal oxide electrodes



**Fig. 2.** Transmittance spectra of (A) Fe-MEPE ( $T = 4\%$  at 594 nm) and (B) TiVO<sub>x</sub>, TMO thin films on FTO glass. The dotted line shows the spectrum of uncoated FTO glass as a reference.

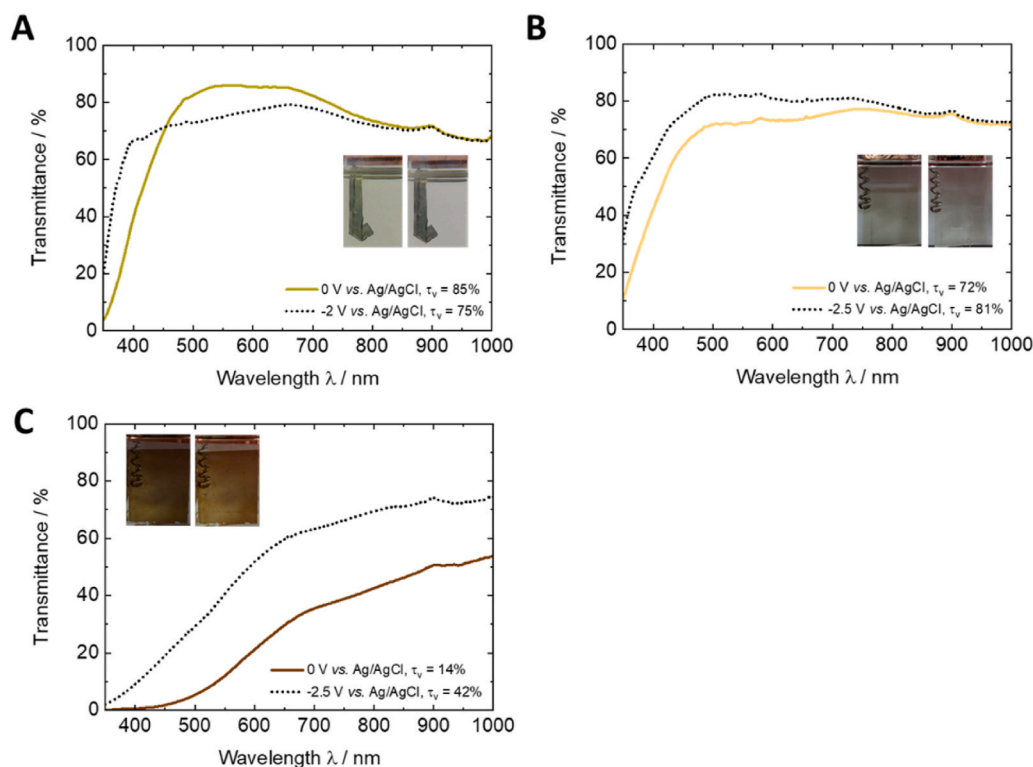


Fig. 3. Spectroelectrochemical measurements of (A)  $\text{TiVO}_x$ , (B) TMO-1, and (C) TMO-2 with Pt as CE and Ag/AgCl as RE in 1 M  $\text{LiClO}_4/\text{PC}$  as electrolyte.

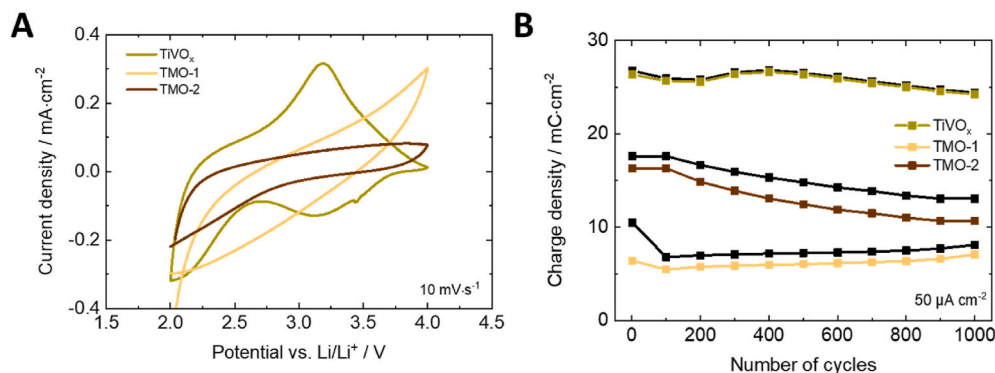
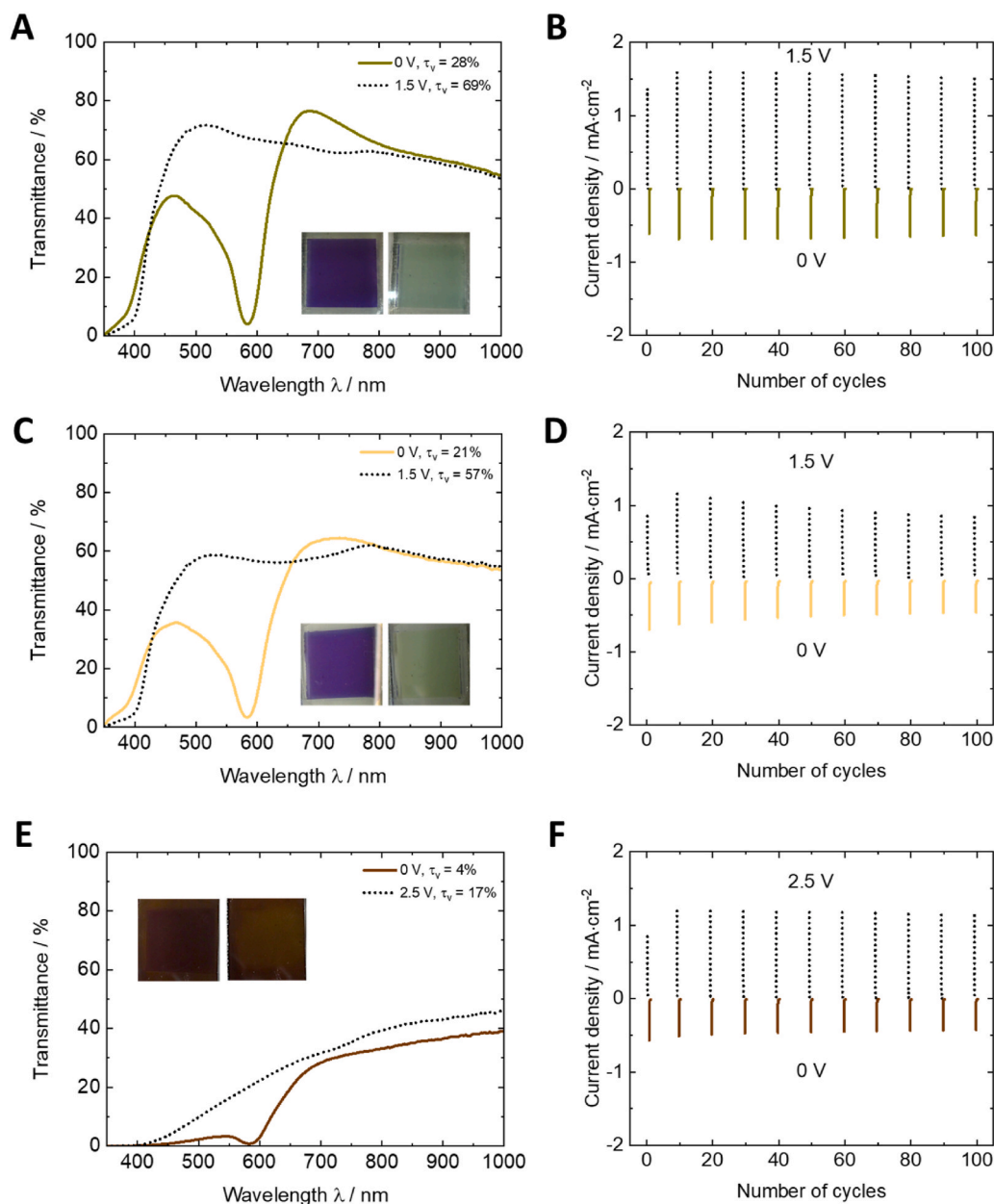


Fig. 4. (A) Cyclic voltammograms of  $\text{TiVO}_x$ , TMO-1, and TMO-2 at a scan rate of  $10 \text{ mV s}^{-1}$  and (B) charging (black lines)/discharging (colored lines) behavior over 1000 switching cycles between 2 V and 4 V vs.  $\text{Li/Li}^+$  (current density:  $50 \mu\text{A cm}^{-2}$ ). Li as CE/RE and 1 M  $\text{LiClO}_4/\text{PC}$  as electrolyte.

are investigated by CV measurements at  $10 \text{ mV s}^{-1}$  in a potential range from 2 V to 4 V vs.  $\text{Li/Li}^+$  – Fig. 4A. Broad redox peaks indicate that as the voltage is increased, the  $\text{V}^{5+}$  is reduced to  $\text{V}^{4+}$  for  $\text{TiVO}_x$ , while  $\text{Mn}^{4+}$  is reduced to  $\text{Mn}^{3+}$  for the TMO electrodes. The broader peaks of the metal oxides, as compared to the Fe-MEPE, can be explained by slower processes, e.g., redox reaction, ion de/insertion and ad/desorption processes leading to longer response times. For Fe-MEPE, the  $\text{ClO}_4^-$  anion can easily adsorb onto and migrate into the polymeric structure, while for metal oxides the intercalation process is slower due to the higher thickness and the compactness of the film.

As a high long-term cycling stability is required for most commercial ECD applications like smart windows, the cycle stability of the electrode materials is measured over 1000 charging/discharging cycles at a current density of  $50 \mu\text{A cm}^{-2}$  – Fig. 4B. The charge density reaches approx.  $27 \text{ mC cm}^{-2}$ ,  $10 \text{ mC cm}^{-2}$ , and  $18 \text{ mC cm}^{-2}$  with a high charge retention of 91%, 77%, and 75% for the  $\text{TiVO}_x$ , TMO-1, and TMO-2 electrodes, respectively. Additionally,  $\text{TiVO}_x$  films are more stable than pure vanadium oxide films, which show a decrease of charge density after a few

hundred cycles [39]. As the results obtained for the chosen ion storage materials indicate that only a small fraction of the charge density is necessary to completely oxidize the Fe-MEPE (see charge density ratio shown on Table 4), it can be assumed that the contribution of these layers to the overall change in the transmittance of the ECDs will be even smaller. Moreover, the Coulombic efficiency (= ratio of discharge density over charge density of the electrode) is as high as 98%, 87%, and 92%, respectively. A further important parameter for EC materials to be characterized as optically passive is a low coloration efficiency ( $\eta$ ), which can be calculated by the following equation:  $\eta = \log(T_b/T_c)/q$ , where  $T_b$  and  $T_c$  are the transmittance values of the bright and colored (dark) state, respectively, and  $q$  is the charge density. Cathodically- and anodically-coloring materials are denoted with a positive and negative value, respectively. While Fe-MEPE has a coloration efficiency of  $496 \text{ cm}^2 \text{ C}^{-1}$  at 584 nm, the  $\eta$  values for  $\text{TiVO}_x$ , TMO-1, and TMO-2 are  $2 \text{ cm}^2 \text{ C}^{-1}$ ,  $-4 \text{ cm}^2 \text{ C}^{-1}$ , and  $-24 \text{ cm}^2 \text{ C}^{-1}$  at 584 nm, respectively. Thus, Ti-containing vanadium and manganese oxides could be particularly useful as ion storage materials operating in conjunction with Fe-MEPE



**Fig. 5.** Spectroelectrochemical characterization of (A) ECD-1 (Fe-MEPE/TiVO<sub>x</sub>), (C) ECD-2 (Fe-MEPE/TMO-1), and (E) ECD-3 (Fe-MEPE/TMO-2). Photographic images of the ECDs in the dark (left) and bright (right) state before cycling are shown as insets. Cycling stability over 100 switching cycles of (B) ECD-1, (D) ECD-2, and (F) ECD-3.

**Table 2**

Color ( $L^*a^*b^*$ ) coordinates, visible light transmittance ( $\tau_v$ ) and haze values of the bare Fe-MEPE and mixed metal oxide thin film electrodes.

	$L^*$	$a^*$	$b^*$	$\tau_v / \%$	Haze / %
Fe-MEPE	60.3	-13.1	-22.4	27	1.0
TiVO <sub>x</sub>	90.0	-2.6	13.9	77	1.0
TMO-1	85.7	-2.3	14.9	67	0.3
TMO-2	32.3	22.1	47.6	9	0.8

electrodes in ECDs due to their good ion storage capability.

### 3.3. (Spectro-)electrochemical characterization of glass-based ECDs

The redox processes of the ECDs consisting of the Fe-MEPE and mixed metal oxide electrodes occur as follows. During the decoloring

process (at 1.5 V for ECD-1 and ECD-2, and 2.5 V for ECD-3), the Fe-MEPE electrode is oxidized and the mixed metal oxide (counter) electrode is reduced. The charge balance is maintained by the insertion of ClO<sub>4</sub><sup>-</sup> and Li<sup>+</sup> ions in the MEPE and ion storage layer, respectively. The coloring process (at 0 V) occurs via the reduction of the Fe-MEPE and oxidation of the mixed metal oxide electrodes and is accompanied by deinsertion of ClO<sub>4</sub><sup>-</sup> and Li<sup>+</sup> ions. In the following section, the EC properties of ECD-1, ECD-2, and ECD-3 are described in detail. The relevant optical and electrochemical data are summarized in Table 4.

The switching behavior of the three ECDs was investigated by means of *in-situ* spectroelectrochemical measurements as shown in Fig. 5. Fig. 5A illustrates the EC properties of ECD-1 (Fe-MEPE/TiVO<sub>x</sub>), which is blue-purple colored in the initial state. By applying a voltage of 1.5 V, the color of ECD-1 changes from blue-purple ( $\tau_v = 28\%$ ) to nearly colorless with a high bright state transmittance of  $\tau_v = 69\%$  in 3 s. By using TiVO<sub>x</sub> instead of undoped V<sub>2</sub>O<sub>5</sub> [37], the bright state

**Table 3**

Color ( $L^*a^*b^*$ ) coordinates, transmittance (T) and visible light transmittance ( $\tau_v$ ) values and charge densities (q) between the redox states, as well as Coulombic efficiency and coloration efficiency ( $\eta$ ) of the thin film electrodes.

	Potential / V vs. Ag/AgCl	$L^*$	$a^*$	$b^*$	T (at 584 nm) / %	$\tau_v$ / %	Charge density q / $\text{mC cm}^{-2}$	Coulombic efficiency / %	$\eta$ (at 584 nm) / $\text{cm}^2 \text{C}^{-1}$
Fe-MEPE	0	61.3	-5.2	-22.7	5	29	2.43	97	496
	2	88.6	-6.0	11.1	80	83			
TiVO <sub>x</sub>	0	93.5	-4.5	12.6	86	85	26.76	98	2
	-2	88.9	0.7	3.1	77	75			
TMO-1	0	88.1	-2.3	10.0	74	72	10.49	87	-4
	-2.5	92.3	-2.8	4.8	82	81			
TMO-2	0	45.7	8.3	38.2	18	14	17.61	92	-24
	-2.5	68.6	5.9	30.4	48	42			

**Table 4**

Color ( $L^*a^*b^*$ ) coordinates, transmittance (T) and visible light transmittance ( $\tau_v$ ) values, response times, charge densities (q) at 0 V (dark state) and 1.5 V or 2.5 V (bright state), respectively, as well as coloration efficiency ( $\eta$ ) of the ECDs.

	Charge density ratio / MEPE:ion storage layer	Cell voltage / V	$L^*$	$a^*$	$b^*$	T (at 584 nm) / %	$\tau_v$ / %	Response time / s	Charge density q / $\text{mC cm}^{-2}$	$\eta$ (at 584 nm) / $\text{cm}^2 \text{C}^{-1}$
<b>ECD-1</b>	0.09	0	61.0	0.8	-18.4	4	28	15	2.57	476
Fe-MEPE/TiVO <sub>x</sub>		1.5	86.3	-8.9	13.3	67	69	3	2.61	
<b>ECD-2</b>	0.23	0	54.2	2.1	-16.9	3	21	25	2.39	535
Fe-MEPE/TMO-1		1.5	80.3	-7.9	15.9	57	57	13	2.56	
<b>ECD-3</b>	0.14	0	21.8	17.2	23.0	1	4	11	2.39	544
Fe-MEPE/TMO-2		2.5	47.4	8.0	39.8	20	17	9	2.44	

transmittance can be significantly increased from 58% to 69%. In Fig. 5C, the transmittance spectra in the dark and bright states of ECD-2 (Fe-MEPE/TMO-1) are depicted. The color changes from blue-purple ( $\tau_v = 21\%$ ) to light yellow upon applying a voltage of 1.5 V in 13 s. By applying 2.5 V, ECD-3 (Fe-MEPE/TMO-2) switches from dark brown to brown in 9 s – Fig. 5E. Unfortunately, the transmittance of ECD-3 changes from 4% to only 17% due to the deeply-colored TMO-2 electrode – Fig. 3C. Therefore, ECD-3 containing TMO-2 is not suitable for ‘smart window’ application as it does not meet the requirements mentioned above.

While discussing the characterization of the metal oxide films (see section 3.2) it was already mentioned that only a small fraction of the charge density is necessary to completely oxidize (decolor) the Fe-MEPE. This is demonstrated in Fig. S3, where the theoretical transmittance spectra of the dark and bright state of the ECDs are calculated by taking both states of the single electrodes into consideration. Especially for ECD-3, the optical effect of TMO-2 is much smaller than can be expected from the spectroelectrochemical characterization – Fig. 3. This is explained as the theoretical and experimental dark state match ( $\tau_v = 4\%$ ), but the theoretical bright state ( $\tau_v = 34\%$ ) is not achieved, which means that the TMO-2 electrode is not fully reduced due to its high charge density of around  $17.6 \text{ mC cm}^{-2}$ . Similar, but less significant effects occur for ECD-1 and ECD-2.

Finally, the cycling stability of the ECDs was measured over 100 switching cycles under inert conditions and the results are illustrated in Fig. 5B, D, and F. ECD-1 shows a reversible color change from blue-purple to nearly colorless switching over 100 cycles between 0 V and 1.5 V without any signs of degradation. There is only a marginal decrease in the charge density for the decoloring process from  $2.61 \text{ mC cm}^{-2}$  to  $2.56 \text{ mC cm}^{-2}$  (charge retention: approx. 98%) – Table 4. In contrast, the ECDs based on Fe-MEPE and TMO electrodes (ECD-2 and ECD-3) show a decrease in charge density for the decoloring process from  $2.56 \text{ mC cm}^{-2}$  to  $1.53 \text{ mC cm}^{-2}$  (60% charge retention) and  $2.44 \text{ mC cm}^{-2}$  to  $1.84 \text{ mC cm}^{-2}$  (75% charge retention), respectively. As the optical contrast is solely due to the Fe-MEPE electrode, the necessary charge density to completely brighten these ECDs matches that of the pristine Fe-MEPE electrode and hence, the  $\eta$  value at 584 nm, i.e.,  $476 \text{ cm}^2 \text{C}^{-1}$ ,  $535 \text{ cm}^2 \text{C}^{-1}$ , and  $544 \text{ cm}^2 \text{C}^{-1}$  for ECD-1, EC-2, and ECD-3,

respectively match that of Fe-MEPE as well. This was expected as the ion storage electrodes were chosen with higher charge density and no significant color change. In addition, the charge retention of the ECDs matches that obtained for the pristine EC electrodes, i.e., 91%, 77%, and 75% for TiVO<sub>x</sub>, TMO-1, and TMO-2, respectively – Fig. 4B. The results of this study demonstrate the potential of binary mixed metal oxide materials, such as TiVO<sub>x</sub> and TMO, for the use as an ion storage layer in MEPE-based ECDs. These ECDs show two distinct, individually addressable color states, with the color change pre-dominantly stemming from the Fe-MEPE, while the counter electrodes are largely optically passive. With respect to future EC applications, e.g. for architectural glazing, the aim is to increase the optical contrast and ensure the long-term stability of the ECDs to meet the requirements stated above. Both issues can be solved by optimizing the charge balance of both electrodes in the device. First, a Fe-MEPE electrode with a higher charge density combined with a TiVO<sub>x</sub> or TMO-1 electrode can lead to a decrease of the dark state transmittance, while maintaining a high bright state transmittance. Second, low threshold voltages for the ECDs are achieved by low charge density ratios of working to counter electrode, which will also result in a higher cycle stability as no degradation and side reactions occur in the ECD.

#### 4. Summary and conclusion

In this study, ECDs based on TiVO<sub>x</sub>, TMO-1 (Ti-rich: 8.2 at.% Mn, 25.1 at.% Ti, 66.5 at.% O) and TMO-2 (Mn-rich: 33.7 at.% Mn, 2.9 at.% Ti, 63.0 at.% O) thin films deposited on FTO glass as optically-passive ion storage layers and an iron metallopolymer (Fe-MEPE) as the active EC layer was demonstrated. The cathodically-coloring Fe-MEPE ( $2.4 \text{ mC cm}^{-2}$ ) switches between blue ( $\tau_v = 29\%$ ) and colorless with a high bright state transmittance  $\tau_v$  of 83%. TiVO<sub>x</sub> ( $26.8 \text{ mC cm}^{-2}$ ) exhibits a color change from yellow to pale grey at 2 V vs. Ag/AgCl, while the anodically-coloring TMO-1 ( $10.5 \text{ mC cm}^{-2}$ ) switches from light yellow to colorless at -2.5 V vs. Ag/AgCl. These materials only exhibit a small visible light transmittance change from 85% to 75% and from 72% to 81%, respectively, fulfilling the requirements for highly transparent optically-passive ion storage layers. TMO-2 ( $17.6 \text{ mC cm}^{-2}$ ) shows a color change from dark brown ( $\tau_v = 14\%$ ) to light brown ( $\tau_v = 42\%$ ) at -2.5 V



vs. Ag/AgCl.

The glass-based ECDs with Fe-MEPE and mixed metal oxides TiVO<sub>x</sub> or TMO-1 as ion storage material exhibit good EC properties in terms of visible light transmittance change ( $\tau_v = 28\% \leftrightarrow 69\%$  for ECD-1 and  $\tau_v = 21\% \leftrightarrow 57\%$  for ECD-2), charge density (2.61 mC cm<sup>-2</sup> and 2.56 mC cm<sup>-2</sup>) and cycling stability. ECD-1, with a very high bright state transmittance of close to 70%, meets the state-of-the-art EC products and therefore, these device configurations are promising candidates for next generation smart window applications. In contrast, the combination of Fe-MEPE and TMO-2 (ECD-3) has undesirable optical properties (residual brown tint in the bright state combined with a low transmittance change from  $\tau_v = 4\%$  to 17%), making TMO-2 with such a high charge density largely not applicable for see-through EC applications (e.g. in smart windows), where high optical contrasts and high bright state transmittances are required. An advantage of the combination of optically-passive counter electrodes, such as TiVO<sub>x</sub> and TMO-1, is that they are highly transmissive even with high charge density and therefore the optical contrast can be completely controlled by the cathodically-coloring material (in this study, Fe-MEPE has a very high coloration efficiency > 500 cm<sup>2</sup> C<sup>-1</sup>). Thus, a high transmittance change can be obtained even with low charge densities (layer thicknesses), minimizing the amount of EC material and more important the power consumption for operating the device. Future work will focus on color optimization towards neutral tints, optical contrast enhancement, and durability validation for the EC systems based on Fe-MEPE and mixed metal oxide electrodes.

#### CRedit authorship contribution statement

**Lukas Niklaus:** Investigation, Validation, Visualization, Writing - original draft. **Marco Schott:** Conceptualization, Supervision, Writing - review & editing, Project administration. **Jonas Subel:** Investigation. **Stephan Ulrich:** Resources, Writing - review & editing, Project administration. **Daniel Reichert:** Resources, Project administration. **Uwe Posset:** Writing - review & editing, Funding acquisition. **Guinevere A. Giffin:** Supervision, Writing - review & editing.

#### Declaration of competing interest

The authors declare that they have no known competing financial interests or personal relationships that could have appeared to influence the work reported in this paper.

#### Acknowledgement

This work was supported by the Federal Ministry of Education and Research under VDI grant No. 13N13375 (ECWin2.0). The contribution of Annalena Götz and Christine Müller (Fraunhofer ISC) is gratefully acknowledged for LSM measurements and assembly of the electrochromic devices, respectively.

#### Appendix A. Supplementary data

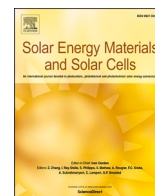
Supplementary data to this article can be found online at <https://doi.org/10.1016/j.solmat.2020.110950>.

#### References

- [1] R.J. Mortimer, D.R. Rosseinsky, P.M.S. Monk (Eds.), *Electrochromic Materials and Devices*, Wiley-VCH Verlag GmbH & Co. KGaA, Weinheim Germany, 2015.
- [2] C.G. Granqvist, *Handbook of Inorganic Electrochromic Materials*, 1995.
- [3] W. Feng, L. Zou, G. Gao, G. Wu, J. Shen, W. Li, Gasochromic smart window: optical and thermal properties, energy simulation and feasibility analysis, *Sol. Energy Mater. Sol. Cell.* 144 (2016) 316–323, <https://doi.org/10.1016/j.solmat.2015.09.029>.
- [4] H. Dürr, H. Bouas-Laurent (Eds.), *Photochromism: Molecules and Systems*, Elsevier, Amsterdam, 2006.

- [5] M. Kamalifarvestani, R. Saidur, S. Mekhilef, F.S. Javadi, Performance, materials and coating technologies of thermochromic thin films on smart windows, *Renew. Sustain. Energy Rev.* 26 (2013) 353–364, <https://doi.org/10.1016/j.rser.2013.05.038>.
- [6] F.G.K. Baucke, Electrochromic applications, *Mater. Sci. Eng., B* 10 (1991) 285–292, [https://doi.org/10.1016/0921-5107\(91\)90104-4](https://doi.org/10.1016/0921-5107(91)90104-4).
- [7] R. Baetens, B.P. Jelle, A. Gustavsen, Properties, requirements and possibilities of smart windows for dynamic daylight and solar energy control in buildings: a state-of-the-art review, *Sol. Energy Mater. Sol. Cell.* 94 (2010) 87–105, <https://doi.org/10.1016/j.solmat.2009.08.021>.
- [8] D.T. Gillaspie, R.C. Tenent, A.C. Dillon, Metal-oxide films for electrochromic applications: present technology and future directions, *J. Mater. Chem.* 20 (2010) 9585, <https://doi.org/10.1039/c0jm00604a>.
- [9] G.A. Niklasson, C.G. Granqvist, Electrochromics for smart windows: thin films of tungsten oxide and nickel oxide, and devices based on these, *J. Mater. Chem.* 17 (2007) 127–156, <https://doi.org/10.1039/B612174H>.
- [10] A. Azens, C. Granqvist, Electrochromic smart windows: energy efficiency and device aspects, *J. Solid State Electrochem.* 7 (2003) 64–68, <https://doi.org/10.1007/s10008-002-0313-4>.
- [11] R.J. Mortimer, Electrochromic materials, *Annu. Rev. Mater. Res.* 41 (2011) 241–268, <https://doi.org/10.1146/annurev-matsci-062910-100344>.
- [12] R. Baetens, B.P. Jelle, A. Gustavsen, Properties, requirements and possibilities of smart windows for dynamic daylight and solar energy control in buildings: a state-of-the-art review, *Sol. Energy Mater. Sol. Cell.* 94 (2010) 87–105, <https://doi.org/10.1016/j.solmat.2009.08.021>.
- [13] A. Cannavale, U. Ayr, F. Fiorito, F. Martellotta, Smart electrochromic windows to enhance building energy efficiency and visual comfort, *Energies* 13 (2020) 1449, <https://doi.org/10.3390/en13061449>.
- [14] C.G. Granqvist, Electrochromics for smart windows: oxide-based thin films and devices, *Thin Solid Films* 564 (2014) 1–38, <https://doi.org/10.1016/j.tsf.2014.02.002>.
- [15] M. Higuchi, Stimuli-responsive metallo-supramolecular polymer films: design, synthesis and device fabrication, *J. Mater. Chem. C* 2 (2014) 9331–9341, <https://doi.org/10.1039/C4TC00689E>.
- [16] C.-W. Hu, T. Sato, J. Zhang, S. Moriyama, M. Higuchi, Three-dimensional Fe(II)-based metallo-supramolecular polymers with electrochromic properties of quick switching, large contrast, and high coloration efficiency, *ACS Appl. Mater. Interfaces* 6 (2014) 9118–9125, <https://doi.org/10.1021/am5010859>.
- [17] M.D. Hossain, T. Sato, M. Higuchi, A green copper-based metallo-supramolecular polymer: synthesis, structure, and electrochromic properties, *Chem. Asian J* 8 (2013) 76–79, <https://doi.org/10.1002/asia.201200668>.
- [18] C.-W. Hu, T. Sato, J. Zhang, S. Moriyama, M. Higuchi, Multi-colour electrochromic properties of Fe/Ru-based bimetallo-supramolecular polymers, *J. Mater. Chem. C* 1 (2013) 3408, <https://doi.org/10.1039/c3tc30440j>.
- [19] F.S. Han, M. Higuchi, D.G. Kurth, Metallo-supramolecular polyelectrolytes self-assembled from various pyridine ring-substituted bisterpyridines and metal ions: photophysical, electrochemical, and electrochromic properties, *J. Am. Chem. Soc.* 130 (2008) 2073–2081, <https://doi.org/10.1021/ja710380a>.
- [20] F.S. Han, M. Higuchi, D.G. Kurth, Metallo-Supramolecular polymers based on functionalized bis-terpyridines as novel electrochromic materials, *Adv. Mater.* 19 (2007) 3928–3931, <https://doi.org/10.1002/adma.200700931>.
- [21] M. Schott, H. Lorrmann, W. Szczerba, M. Beck, D.G. Kurth, State-of-the-art electrochromic materials based on metallo-supramolecular polymers, *Sol. Energy Mater. Sol. Cell.* 126 (2014) 68–73, <https://doi.org/10.1016/j.solmat.2014.03.032>.
- [22] L.-Y. Hsiao, T.-H. Chang, H.-C. Lu, Y.-C. Wang, Y.-A. Lu, K.-C. Ho, M. Higuchi, A panchromatic electrochromic device composed of Ru(II)/Fe(II)-based heterometallo-supramolecular polymer, *J. Mater. Chem. C* 7 (2019) 7554–7562, <https://doi.org/10.1039/C9TC01452G>.
- [23] S. Roy, C. Chakraborty, Sub-second electrochromic switching and ultra-high coloration efficiency in halloysite nanoclay incorporated metallo-supramolecular polymer nano-hybrid based electrochromic device, *Sol. Energy Mater. Sol. Cell.* 208 (2020), 110392, <https://doi.org/10.1016/j.solmat.2019.110392>.
- [24] M. Schott, L. Niklaus, J. Clade, U. Posset, Electrochromic metallo-supramolecular polymers showing visible and near-infrared light transmittance modulation, *Sol. Energy Mater. Sol. Cell.* 200 (2019), 110001, <https://doi.org/10.1016/j.solmat.2019.110001>.
- [25] Sandesh Pai, Marco Schott, Lukas Niklaus, Uwe Posset, D.G. Kurth, A study of the effect of pyridine linkers on the viscosity and electrochromic properties of metallo-supramolecular coordination polymers, *J. Mater. Chem. C* 6 (2018) 3310–3321, <https://doi.org/10.1039/C7TC04177B>.
- [26] M. Schott, W. Szczerba, D.G. Kurth, Detailed study of layer-by-layer self-assembled and dip-coated electrochromic thin films based on metallo-supramolecular polymers, *Langmuir* 30 (2014) 10721–10727, <https://doi.org/10.1021/la501590a>.
- [27] J. Jensen, F.C. Krebs, From the bottom up—flexible solid state electrochromic devices, *Adv. Mater.* 26 (2014) 7231–7234, <https://doi.org/10.1002/adma.201402771>.
- [28] C.G. Granqvist, Oxide electrochromics: an introduction to devices and materials, *Sol. Energy Mater. Sol. Cell.* 99 (2012) 1–13, <https://doi.org/10.1016/j.solmat.2011.08.021>.
- [29] C.G. Granqvist, Electrochromic tungsten oxide films: review of progress 1993–1998, *Sol. Energy Mater. Sol. Cell.* 60 (2000) 201–262, [https://doi.org/10.1016/S0927-0248\(99\)00088-4](https://doi.org/10.1016/S0927-0248(99)00088-4).

- [30] D. Vernardou, K. Psifis, D. Louloudakis, G. Papadimitropoulos, D. Davazoglou, N. Katsarakis, E. Koudoumas, Low pressure CVD of electrochromic WO<sub>3</sub> at 400°C, *J. Electrochem. Soc.* 162 (2015) H579, <https://doi.org/10.1149/2.0281509jes>.
- [31] R.S. Conell, D.A. Corrigan, B.R. Powell, The electrochromic properties of sputtered nickel oxide films, *Sol. Energy Mater. Sol. Cell.* 25 (1992) 301–313, [https://doi.org/10.1016/0927-0248\(92\)90075-Z](https://doi.org/10.1016/0927-0248(92)90075-Z).
- [32] K. Yoshimura, T. Miki, S. Tanemura, Nickel oxide electrochromic thin films prepared by reactive DC magnetron sputtering, *Jpn. J. Appl. Phys.* 34 (1995) 2440, <https://doi.org/10.1143/JJAP.34.2440>.
- [33] X. Song, G. Dong, F. Gao, Y. Xiao, Q. Liu, X. Diao, Properties of NiOx and its influence upon all-thin-film ITO/NiOx/LiTaO<sub>3</sub>/WO<sub>3</sub>/ITO electrochromic devices prepared by magnetron sputtering, *Vacuum* 111 (2015) 48–54, <https://doi.org/10.1016/j.vacuum.2014.09.007>.
- [34] J. Padilla, T.F. Otero, Contrast limitations of dual electrochromic systems, *Electrochem. Commun.* 10 (2008) 1–6, <https://doi.org/10.1016/j.elecom.2007.10.004>.
- [35] S. Hassab, J. Padilla, Using WO<sub>3</sub> as a transparent, optically-passive counter electrode in an unbalanced electrochromic configuration, *Electrochem. Commun.* 72 (2016) 87–90, <https://doi.org/10.1016/j.elecom.2016.09.001>.
- [36] S. Ulrich, C. Szyszko, S. Jung, M. Vergöhl, Electrochromic properties of mixed oxides based on titanium and niobium for smart window applications, *Surf. Coating. Technol.* 314 (2017) 41–44, <https://doi.org/10.1016/j.surfcoat.2016.11.078>.
- [37] M. Schott, W. Szczerba, U. Posset, A. Šurca Vuk, M. Beck, H. Riesemeier, A. F. Thünemann, D.G. Kurth, In operando XAFS experiments on flexible electrochromic devices based on Fe(II)-metallo-supramolecular polyelectrolytes and vanadium oxide, *Sol. Energy Mater. Sol. Cell.* 147 (2016) 61–67, <https://doi.org/10.1016/j.solmat.2015.10.015>.
- [38] J.W. Lim, S.J. Yoo, S.H. Park, S.U. Yun, Y.-E. Sung, High electrochromic performance of co-sputtered vanadium–titanium oxide as a counter electrode, *Sol. Energy Mater. Sol. Cell.* 93 (2009) 2069–2074, <https://doi.org/10.1016/j.solmat.2009.03.008>.
- [39] M.B. Sahana, C. Sudakar, C. Thapa, V.M. Naik, G.W. Auner, R. Naik, K. R. Padmanabhan, The effect of titanium on the lithium intercalation capacity of V<sub>2</sub>O<sub>5</sub> thin films, *Thin Solid Films* 517 (2009) 6642–6651, <https://doi.org/10.1016/j.tsf.2009.04.063>.
- [40] N. Sakai, Y. Ebina, K. Takada, T. Sasaki, Electrochromic films composed of MnO<sub>2</sub> nanosheets with controlled optical density and high coloration efficiency, *J. Electrochem. Soc.* 152 (2005) E384, <https://doi.org/10.1149/1.2104227>.
- [41] M. Röder, A.B. Beleke, U. Guntow, J. Buensow, A. Guerfi, U. Posset, H. Lorrmann, K. Zaghbi, G. Sextl, Li<sub>4</sub>Ti<sub>5</sub>O<sub>12</sub> and LiMn<sub>2</sub>O<sub>4</sub> thin-film electrodes on transparent conducting oxides for all-solid-state and electrochromic applications, *J. Power Sources* 301 (2016) 35–40, <https://doi.org/10.1016/j.jpowsour.2015.09.063>.
- [42] E.C. Constable, A.M.W.C. Thompson, Multinucleating 2,2',6',2''-terpyridine ligands as building blocks for the assembly of co-ordination polymers and oligomers, *J. Chem. Soc., Dalton Trans.* 114 (1992) 3467–3475, <https://doi.org/10.1039/DT9920003467>.
- [43] G.E. Jellison Jr., F.A. Modine, Parameterization of the optical functions of amorphous materials in the interband region, *Appl. Phys. Lett.* 69 (1996) 371–373, <https://doi.org/10.1063/1.118064>.
- [44] K.I. Schiffmann, C. Steinberg, EPMA-Analyse dünner PVD- und CVD-Schichten, *Vakuum Forsch. Praxis* 31 (2019) 26–36, <https://doi.org/10.1002/vipr.201900714>.
- [45] J.L. Pouchou, F. Pichoir, Determination by X-ray microprobe of thickness and composition of thin surface layers, *J. Microsc. Spectrosc. Electron.* 10 (1985) 279–290.
- [46] L. Niklaus, M. Schott, M. Mihelčič, I. Jerman, U. Posset, G. Sextl, Metallopolymers and non-stoichiometric nickel oxide: towards neutral tint large-area electrochromic devices, *Sol. Energy Mater. Sol. Cell.* 200 (2019), 110002, <https://doi.org/10.1016/j.solmat.2019.110002>.
- [47] L. Niklaus, M. Schott, U. Posset, G.A. Giffin, Redox electrolytes for hybrid type II electrochromic devices with Fe-MEPE or Ni<sub>1-x</sub>O as electrode materials, *ChemElectroChem* (2020), <https://doi.org/10.1002/celec.202000583>.



# Charge balancing and optical contrast optimization in Fe-MEPE/Ni<sub>1-x</sub>O electrochromic devices containing a Li reference electrode

Lukas Niklaus<sup>a</sup>, Marco Schott<sup>a,\*</sup>, Uwe Posset<sup>a</sup>, Mohor Mihelčič<sup>b</sup>, Ivan Jerman<sup>c</sup>, Guinevere A. Giffin<sup>a</sup>

<sup>a</sup> Fraunhofer Institute for Silicate Research ISC, Neunerplatz 2, 97082, Würzburg, Germany

<sup>b</sup> University of Ljubljana, Faculty for Mechanical Engineering, Laboratory of Experimental Mechanics, Askerčeva ulica 6, 1000, Ljubljana, Slovenia

<sup>c</sup> National Institute of Chemistry NIC, Hajdrihova ulica 19, 1000, Ljubljana, Slovenia

## ARTICLE INFO

### Keywords:

Electrochromic devices  
Metallopolymers  
Non-stoichiometric nickel oxide  
Reference electrode

## ABSTRACT

A three-electrode cell setup enables to evaluate the redox behavior of both electrodes, *i.e.*, iron-based metallopolymers (Fe-MEPE) and a complementary switching non-stoichiometric nickel oxide (Ni<sub>1-x</sub>O, multilayer structure), in detail during full cell operation. In this work, electrochromic devices (ECDs) with a Li reference electrode and different charge density ratios between the electrode materials have been studied (spectro-)electrochemically. The charge density ratio between the electrodes affects the cell voltage, optical contrast, response time, and cycling stability. Here, a neutral-colored bright state was obtained for the unbalanced configuration (ECD-1, charge density ratio Fe-MEPE:Ni<sub>1-x</sub>O<sub>2</sub> = 2:1, underbalanced) and the balanced configuration (ECD-2, charge density ratio Fe-MEPE:Ni<sub>1-x</sub>O<sub>3</sub> = 1:1, balanced). The operating voltage range of the ECDs can be narrowed by using a balanced or overbalanced Ni<sub>1-x</sub>O electrode, *e.g.*, 1.5 V ↔ -1 V for ECD-3 (charge density ratio Fe-MEPE:Ni<sub>1-x</sub>O<sub>5</sub> = 1:3, overbalanced). Moreover, the cycling stability is enhanced from just a few cycles (ECD-1) to over 1000 potentiostatic switching cycles (ECD-2 and ECD-3).

## 1. Introduction

Electrochromic (EC) materials, which are commonly deposited as thin films on transparent conductive substrates, undergo changes in their optical properties (absorbance, transmittance, and reflectance) upon electrochemical oxidation or reduction [1]. They are characterized by their optical contrast, color change, response time, and charge density in a defined potential window. In addition to the EC layer, a conventional all-solid-state electrochromic device (ECD) also incorporates a second complementary switching EC layer or an ion storage layer and an ion-conductive electrolyte that is sandwiched between the two electrodes [2]. In principle, having a counter electrode (CE) of sufficient charge density assures that the redox reaction in the EC active layer is fully compensated. Thus, it facilitates an electrochemically stable cell configuration enabling the complete coloration and decoloration of the EC materials, respectively. Ion storage layers can be employed as optically-passive CEs [3]. Several organic [4] and inorganic [5–7] materials have been designed for this purpose, *e.g.*, poly(2,2,6,6-tetramethylpiperidinyloxy-4-yl methacrylate) (PTMA), poly(thieno[3,

4-b]thiophene) (PT34bT), cerium oxide, and doped vanadium oxides. A balanced EC cell configuration (charge density of the first EC layer equal to the charge density of the second EC or ion-storage layer) may lead to an optimal EC performance with a maximum transmittance modulation or color change [3]. However, this is only the case when both layers are complementary coloring and exhibit no residual coloration in their bright state. Unbalanced cell configurations, in which one of the electrodes has a higher charge density and acts as an optically-passive CE, can exhibit almost the same optical contrast as the high transparency of the ion storage layer is maintained during switching [5,6]. In a publication by Hassab and Padilla, combinations of cathodically-coloring EC materials with significantly different charge densities and coloration efficiencies, *i.e.*, PProDOT-Me<sub>2</sub> (2.2 mC cm<sup>-2</sup>, 379 cm<sup>2</sup> C<sup>-1</sup>) and WO<sub>3</sub> (24 mC cm<sup>-2</sup>, 19 cm<sup>2</sup> C<sup>-1</sup>), were used in an unbalanced configuration to fully switch the polymer with a minimal corresponding color change of the WO<sub>3</sub> film, leading to a narrow operating voltage of 1.5 V [8]. A further work by Hassab et al. investigated the influence of the charge density ratio of a black-to-transmissive EC polymer, 3,4-propylenedioxythiophene/benzothiadiazole (ProDOT-BTD, ECP-Black), with an optically-passive ion

\* Corresponding author.

E-mail address: [marco.schott@isc.fraunhofer.de](mailto:marco.schott@isc.fraunhofer.de) (M. Schott).

<https://doi.org/10.1016/j.solmat.2021.111080>

Received 22 December 2020; Received in revised form 4 March 2021; Accepted 23 March 2021

Available online 11 April 2021

0927-0248/© 2021 Elsevier B.V. All rights reserved.

storage layer, poly(3,4-propylenedioxyppyrrrole), in a three-electrode setup with 0.1 M LiClO<sub>4</sub>/PC as the electrolyte [9]. That work showed that the performance loss in ECDs during cycling tests under lab conditions is not necessarily due to an irreversible electrochemical or structural degradation of the active EC materials. Instead, it is resulting from a shift of the state of charge of both EC layers. Therefore, it can be assumed that the loss of charge is reversible and could be mitigated through proper electrochemical control of the cells. A previous study by the current authors was carried out with a three-electrode ECD (sidechain-modified poly(3,4-ethylene dioxythiophene) (PEDOT) and Prussian blue (PB) as working electrode (WE) and CE, respectively) to investigate, in particular, the stability of the conductive indium tin oxide (ITO) layer under ambient and humid conditions during potentiostatic cycling [10]. It was shown that the degradation of ITO could be prevented by applying an appropriate cell potential.

It was recently demonstrated that an unbalanced ECD containing an iron-based metallo-supramolecular polymer (Fe-MEPE, 2.4 mC cm<sup>-2</sup>) and a non-stoichiometric nickel oxide (Ni<sub>1-x</sub>O, 7.5 mC cm<sup>-2</sup>) as EC materials, both obtained by wet-chemical deposition methods, switches reversibly. It changes between the dark blue colored state at -1 V and the bright state at 1.5 V with a visible light transmittance ( $\tau_v$ ) change from 9% to 37% [11]. For this cell configuration, high optical contrast is desirable for Fe-MEPE, while a high degree of transmissivity in both states is desirable for Ni<sub>1-x</sub>O. Here, the nickel oxide allows modulation of the broad absorption band, which extends across the electromagnetic spectrum (starting around 350 nm–1000 nm). A pre-treatment of the Ni<sub>1-x</sub>O electrode was necessary to obtain a configuration where initially both EC electrodes are present in their colored states (Fe-MEPE: reduced, Ni<sub>1-x</sub>O: oxidized). This pre-treatment led to improved cycling stability, as was also shown for WO<sub>3</sub> thin films [12]. Although high charge retention during potentiostatic cycling (1000 switching cycles) was obtained for the Fe-MEPE/Ni<sub>1-x</sub>O devices, a continuous brightening ( $\tau_v$  in the colored/bright state changes from 9%/37% to 12%/50%) was observed for the transmittance of the ECD in both the colored and bright state. This drift can be attributed to Li trapping in the crystal structure of the Ni<sub>1-x</sub>O electrode [12–14]. An even more neutral coloration should be attainable in MEPE/Ni<sub>1-x</sub>O-based devices if a complete decoloration (oxidation) of the Ni<sub>1-x</sub>O electrode is made possible.

In this study, the EC properties of Fe-MEPE/Ni<sub>1-x</sub>O devices (*i.e.*, optical contrast, color values, response time, electrode/cell potentials, and cycling stability) with unbalanced and balanced cell configurations are studied in order to work out how their EC performance can be optimized. The glass-based ECDs with different charge density ratios of Fe-MEPE and Ni<sub>1-x</sub>O were investigated in detail to verify the influence of the charge density ratio of both electrodes on the overall cell voltage. With this approach of optimizing the charge balancing, it will be possible to increase the change in visible light transmittance for future EC applications, *e.g.*, ‘Smart Windows’, visors, and camouflage use.

## 2. Experimental

All chemicals were purchased from Sigma-Aldrich and used without further purification.

### 2.1. Synthesis of the EC materials and thin film electrodes

As the synthetic approach is published in recent literature [11,15,16], only a brief overview is given here. The synthesis of the ligand 4',4''''-(1,4-phenylene)bis(2,2':6',2''-terpyridine), was carried out according to Ref. [17]. Fe-MEPE was prepared with a metal ion-to-ligand molar ratio of 1:1 [18,19]. Homogeneous thin films with a thickness of around 330 nm were deposited on fluorine-doped tin oxide (FTO)-coated glass substrates (Pilkington K Glass™ N, approx. 14 Ω·sq<sup>-1</sup>). The electrode was dip-coated (withdrawal speed: 35 mm min<sup>-1</sup>) from a Fe-MEPE solution (35 mM in methanol/ethanol/2-butoxyethanol) containing a proprietary polyurethane-polysiloxane binder. The Fe-MEPE thin films were annealed at 60 °C for 24 h.

The Ni<sub>1-x</sub>O layers were prepared according to a published procedure that yielded nickel oxide films with nickel vacancies, *i.e.*, higher Ni<sup>3+</sup> content [20,21]. In brief, the Ni<sub>1-x</sub>O pigment was synthesized via a sol-gel peroxy route to yield xerogels with a Ni<sup>2+</sup>/Ni<sup>3+</sup> ratio of approx. 0.5 [21]. A freshly-prepared NiO<sub>x</sub>H<sub>y</sub> dispersant [20] was added to an aqueous dispersion consisting of 10 wt% of the Ni<sub>1-x</sub>O pigment to adjust the viscosity for deposition (1.9 mPa s at a shear rate of 500 s<sup>-1</sup>) [21]. The resulting Ni<sub>1-x</sub>O dispersion was spin-coated on FTO glass with 500 rpm for 5 s and 1000 rpm for 1 min, and the samples subsequently annealed at 150 °C for 30 min. To increase the film thickness, and thereby the charge density, two, three, and five layers of Ni<sub>1-x</sub>O were deposited consecutively, resulting in an overall thickness of around 330 nm, 490 nm, and 1.25 μm for Ni<sub>1-x</sub>O<sub>2</sub>, Ni<sub>1-x</sub>O<sub>3</sub>, and Ni<sub>1-x</sub>O<sub>5</sub>, respectively (Fig. S1).

### 2.2. Preparation of glass-based ECDs

ECDs with the cell configuration glass/FTO/Fe-MEPE/electrolyte/Ni<sub>1-x</sub>O/FTO/glass were prepared under argon atmosphere in a glove box (H<sub>2</sub>O, O<sub>2</sub> < 5 ppm) according to the following procedure. A dry LiClO<sub>4</sub>-containing gel electrolyte was coated using a doctor blade method onto the Fe-MEPE electrodes with a wet film thickness of approx. 90 μm. Before cell assembly, the Ni<sub>1-x</sub>O electrode was potentiostatically oxidized (colored) at 4.5 V vs. Li/Li<sup>+</sup> for 120 s and then laminated on top of the MEPE electrode. Adhesive Cu tape was used as bus bars for both electrodes. The standard two-electrode ECDs (switchable area: 2 × 2 cm<sup>2</sup>) with Ni<sub>1-x</sub>O<sub>2</sub>, Ni<sub>1-x</sub>O<sub>3</sub>, and Ni<sub>1-x</sub>O<sub>5</sub> as CEs with charge density ratios (Fe-MEPE:Ni<sub>1-x</sub>O) of 2:1, 1:1, and 1:3 are referred to as ECD-1, ECD-2, and ECD-3, respectively. The three-electrode ECDs (3.5 × 3.5 cm<sup>2</sup>) with a Li reference electrode (RE) are referred to as ECD-1\_RE, ECD-2\_RE, and ECD-3\_RE following the nomenclature of the standard two-electrode configurations (Fig. 1). The Li RE was used to measure the individual electrode potentials during device operation.

### 2.3. Methods and instruments

Electrochemical measurements in the range of 2.4 V–4.2 V vs. Li/Li<sup>+</sup> (cyclic voltammetry at a scan rate of 10 mV s<sup>-1</sup>, galvanostatic charge/discharge over 1000 cycles at 25 μA cm<sup>-2</sup>) on Fe-MEPE and Ni<sub>1-x</sub>O thin film electrodes were performed in a three-electrode setup with Li as CE and RE in a liquid electrolyte (1 M LiClO<sub>4</sub>/PC) using a Solartron Multistat 1470E potentiostat/galvanostat [11,16]. The spectroelectrochemical data were determined by means of an Avantes AvaSpec-2048 standard fiber optic spectrometer combined with a balanced deuterium-halogen light source in a three-electrode setup with platinum as CE, Ag/AgCl as RE, and 1 M LiClO<sub>4</sub>/PC as the electrolyte.

The spectroelectrochemical measurements of the thin film electrodes (potential range: 0 V–2 V vs. Ag/AgCl, ambient conditions) and ECDs (voltage range: -1 V up to 2.5 V, inert conditions), *incl.* UV-Vis and L\*a\*b\* color coordinates according to CIELAB color space of the dark and bright state were performed *in-situ* during operation. The visible light transmittance ( $\tau_v$ ) was calculated according to DIN EN410. The optimal operating voltages of the ECDs were determined by stepwise increasing the cell voltage. The decoloration voltage was defined as the threshold voltage where the device was in the bright state and no further transmittance changes were observed at higher voltages. The electrochemical characterization (potentiostatic cycling) of the ECDs was performed with a Solartron Multistat 1470E potentiostat/galvanostat.

All measurements were carried out under inert atmosphere (glove box) at room temperature.

## 3. Results and discussion

### 3.1. Characterization of MEPE and Ni<sub>1-x</sub>O thin film electrodes

The Fe-MEPE thin film on FTO glass (haze = 1%) was previously characterized in detail and the results are summarized in Table 1 [11,15,

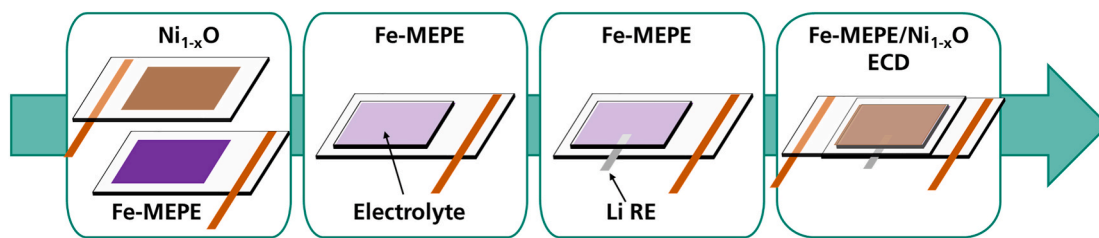


Fig. 1. Schematic illustration of the assembly of the three-electrode Fe-MEPE/Ni<sub>1-x</sub>O ECDs. RE: Li.

16]. Fe-MEPE shows a strong absorption band at around 584 nm ( $\tau_v = 29\%$ ) attributed to a metal-to-ligand charge transfer (MLCT) transition from a d orbital of the Fe<sup>2+</sup> ion to a  $\pi^*$  orbital of the bis(terpyridine) ligand [22]. When applying 2 V vs. Ag/AgCl to the Fe-MEPE electrode the MLCT band completely vanishes. Moreover, the Fe-MEPE electrode exhibits a high coloration efficiency of 525.8 cm<sup>2</sup> C<sup>-1</sup> at 584 nm and high charge retention after 1000 switching cycles (2.39 mC cm<sup>-2</sup> to 2.32 mC cm<sup>-2</sup>, 98% at 50  $\mu$ A cm<sup>-2</sup>) when cycled between 2.4 V and 4.4 V vs. Li/Li<sup>+</sup> in 1 M LiClO<sub>4</sub>/PC.

The Ni<sub>1-x</sub>O thin films on FTO glass (haze < 1%) with three different layer thicknesses were characterized by spectroelectrochemical and electrochemical methods (cyclic voltammetry and galvanostatic charging/discharging over 1000 cycles) (Fig. 2 and Table 1). With increasing film thickness, the change in visible light transmittance ( $\tau_v$ , colored at 2 V/ $\tau_{v,bright}$  at 0 V [in %]) decreases from 66/89 to 57/83 to 28/69 for Ni<sub>1-x</sub>O<sub>2</sub>, Ni<sub>1-x</sub>O<sub>3</sub>, and Ni<sub>1-x</sub>O<sub>5</sub>, respectively. The tints of the Ni<sub>1-x</sub>O<sub>2</sub> and Ni<sub>1-x</sub>O<sub>3</sub> electrodes are considered neutral in both states as their  $|a^*, b^*|$  values are below 5. Due to the increased thickness for Ni<sub>1-x</sub>O<sub>5</sub>, the electrode is darker in the colored state, and the yellow hue in the bright state is intensified.

The CV curves in Fig. 2B were measured in the potential range from 2.4 V to 4.2 V vs. Li/Li<sup>+</sup> at a scan rate of 10 mV s<sup>-1</sup>. For all three Ni<sub>1-x</sub>O electrodes, the anodic peak centered at a potential of around 3.1 V vs. Li/Li<sup>+</sup> is assigned to the oxidation of Ni<sup>2+</sup> to Ni<sup>3+</sup> and the concurrent extraction of Li<sup>+</sup> ions. A reversible color change from virtually colorless ( $L^* = 92.9$ ,  $a^* = 0.1$ ,  $b^* = 4.4$  for Ni<sub>1-x</sub>O<sub>2</sub> and  $L^* = 89.3$ ,  $a^* = -0.8$ ,  $b^* = 4.2$  for Ni<sub>1-x</sub>O<sub>3</sub>) or light yellow ( $L^* = 86.1$ ,  $a^* = 1.6$ ,  $b^* = 13.6$  for Ni<sub>1-x</sub>O<sub>5</sub>) to grey-brown with varying intensities, depending on the film thickness, accompanies this process. The cathodic peak around 3.2 V vs. Li/Li<sup>+</sup> is due to the reduction of Ni<sup>3+</sup> to Ni<sup>2+</sup> and the simultaneous insertion of Li<sup>+</sup> ions from the electrolyte into the cationic vacancies of the Ni<sub>1-x</sub>O structure, which leads to a complete brightening [23,24].

The Ni<sub>1-x</sub>O electrodes were galvanostatically charged (colored) and discharged (decolored) at a current density of 25  $\mu$ A cm<sup>-2</sup> in the same potential range. The initial charge density of 1.27, 2.68, and 7.51 mC cm<sup>-2</sup> changed by about 17%, 5%, and 7% over 1000 galvanostatic charging/discharging cycles for Ni<sub>1-x</sub>O<sub>2</sub>, Ni<sub>1-x</sub>O<sub>3</sub>, and Ni<sub>1-x</sub>O<sub>5</sub>, respectively. The charge retention combined with Coulombic efficiencies (ratio of discharge density over charge density of the electrode)

of 96.1%, 91.8%, and 95.1%, respectively, indicate high cycle stability. A further important parameter for EC materials is the coloration efficiency ( $\eta$ ), which can be calculated by the following equation:  $\eta = \log(T_b/T_c)/q$ , where  $T_b$  and  $T_c$  are the transmittance values of the bright and colored (dark) states, respectively, and  $q$  is the charge density. This value decreases from 95.8 to 60.0 and 49.5 cm<sup>2</sup> C<sup>-1</sup> with increasing film thickness (Fig. S1), which can be explained by the effect that different surface structures and topologies have on the EC properties of nickel oxide. I. Sorar et al. found that surface effects dominate the electrochromism of Ni-oxide-based films (sputtered and reactive gas deposition) in Li<sup>+</sup> ion-conducting electrolytes and that the transmittance modulation increases with increasing film thickness [25].

### 3.2. Comparison of the (spectro-)electrochemical characterization of the two- and three-electrode MEPE/Ni<sub>1-x</sub>O ECD configurations

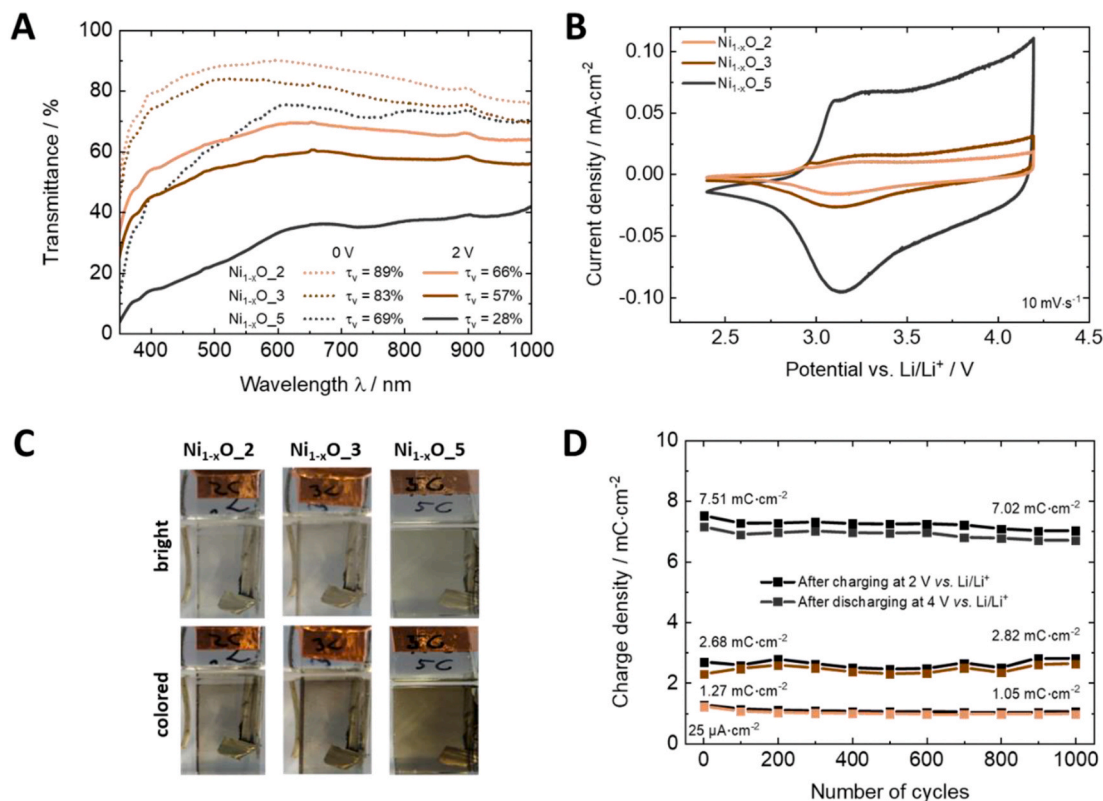
A series of three ECDs of the configuration glass/FTO/Fe-MEPE/electrolyte/Ni<sub>1-x</sub>O/FTO/glass was investigated, whereby the charge density of the Fe-MEPE electrodes was 2.39 mC cm<sup>-2</sup> and the charge density of Ni<sub>1-x</sub>O was varied (1.27 for Ni<sub>1-x</sub>O<sub>2</sub>, 2.68 for Ni<sub>1-x</sub>O<sub>3</sub>, and 7.51 mC cm<sup>-2</sup> for Ni<sub>1-x</sub>O<sub>5</sub>). The redox reaction occurring in the Fe-MEPE/Ni<sub>1-x</sub>O ECDs is summarized from the mechanism previously discussed in the literature [24,26,27]. During decoloration, the Fe-MEPE electrode is oxidized and the Ni<sub>1-x</sub>O electrode is reduced. The charge is compensated by the insertion of ClO<sub>4</sub> into the Fe-MEPE and the insertion of Li<sup>+</sup> ions into the Ni<sub>1-x</sub>O layer. Consequently, the coloration occurs via the reduction of the Fe-MEPE and oxidation of the nickel oxide electrode. The corresponding redox reaction is accompanied by extraction of ClO<sub>4</sub> from the Fe-MEPE and extraction of Li<sup>+</sup> ions from Ni<sub>1-x</sub>O. The EC properties of ECD-1, ECD-2, and ECD-3 are described in detail in the following section. The relevant optical and electrochemical data are summarized in Table 2.

The switching behavior of the three ECDs was investigated using *in-situ* spectroelectrochemical measurements as shown in Figs. 3A–C. The complete decoloration of Fe-MEPE defines the endpoint of switching for the ECDs. In this case, the charge consumed at each electrode is equal to that of the Fe-MEPE electrode, which switches completely between its fully colored (reduced) and colorless (oxidized) state. A reduced cell voltage may minimize film degradation resulting from over-oxidation and thus could enhance the cyclability of the ECDs. According to

Table 1

Applied potential (V), color coordinates ( $L^*a^*b^*$ ), transmittance (T) at 584 nm, visible light transmittance ( $\tau_v$ ), charge densities (q) after charging (2 V) and discharging (0 V), coulombic efficiency, and coloration efficiency ( $\eta$ ) of the EC thin film electrodes.

EC electrode	Potential vs. Ag/AgCl / V	L*	a*	b*	Transmittance T (at 584 nm) / %	Visible light transmittance $\tau_v$ / %	Potential vs. Li/Li <sup>+</sup> / V	Charge density q / mC cm <sup>-2</sup>	Coulombic efficiency / %	Coloration efficiency $\eta$ / cm <sup>2</sup> C <sup>-1</sup>
Fe-MEPE	0	69.0	5.7	-25.4	5	29	2.4	2.29	95.8	525.8
	2	92.9	-6.8	8.4	80	83	4.4	2.39		
Ni <sub>1-x</sub> O <sub>2</sub>	0	92.9	0.1	4.4	90	89	2	1.27	96.1	95.8
	2	84.6	0.8	6.4	68	66	4	1.22		
Ni <sub>1-x</sub> O <sub>3</sub>	0	89.3	-0.8	4.2	84	83	2	2.68	91.8	60.0
	2	79.6	0.3	6.7	58	57	4	2.46		
Ni <sub>1-x</sub> O <sub>5</sub>	0	86.1	1.6	13.6	73	69	2	7.51	95.1	49.5
	2	58.6	5.2	17.1	31	28	4	7.14		



**Fig. 2.** (A) Spectroelectrochemical measurements of  $\text{Ni}_{1-x}\text{O}$  with Pt as CE and Ag/AgCl as RE in 1 M  $\text{LiClO}_4/\text{PC}$ . (B) Cyclic voltammograms at a scan rate of  $10 \text{ mV s}^{-1}$  with Li as CE/RE and (C) photographic images of the bright (reduced) and colored (oxidized) state. (D) Charge retention over 1000 charging/discharging cycles (current density:  $25 \mu\text{A cm}^{-2}$ ) with Li as CE/RE and 1 M  $\text{LiClO}_4/\text{PC}$  as electrolyte.

**Table 2**

Cell voltage (V), color coordinates ( $L^*a^*b^*$ ), transmittance (T) at 584 nm, visible light transmittance ( $\tau_v$ ), charge densities (q) after charging (1.5, 2, or 2.5 V, bright) and discharging (-1 V, dark), coloration efficiency ( $\eta$ ), and response time of the ECDs.

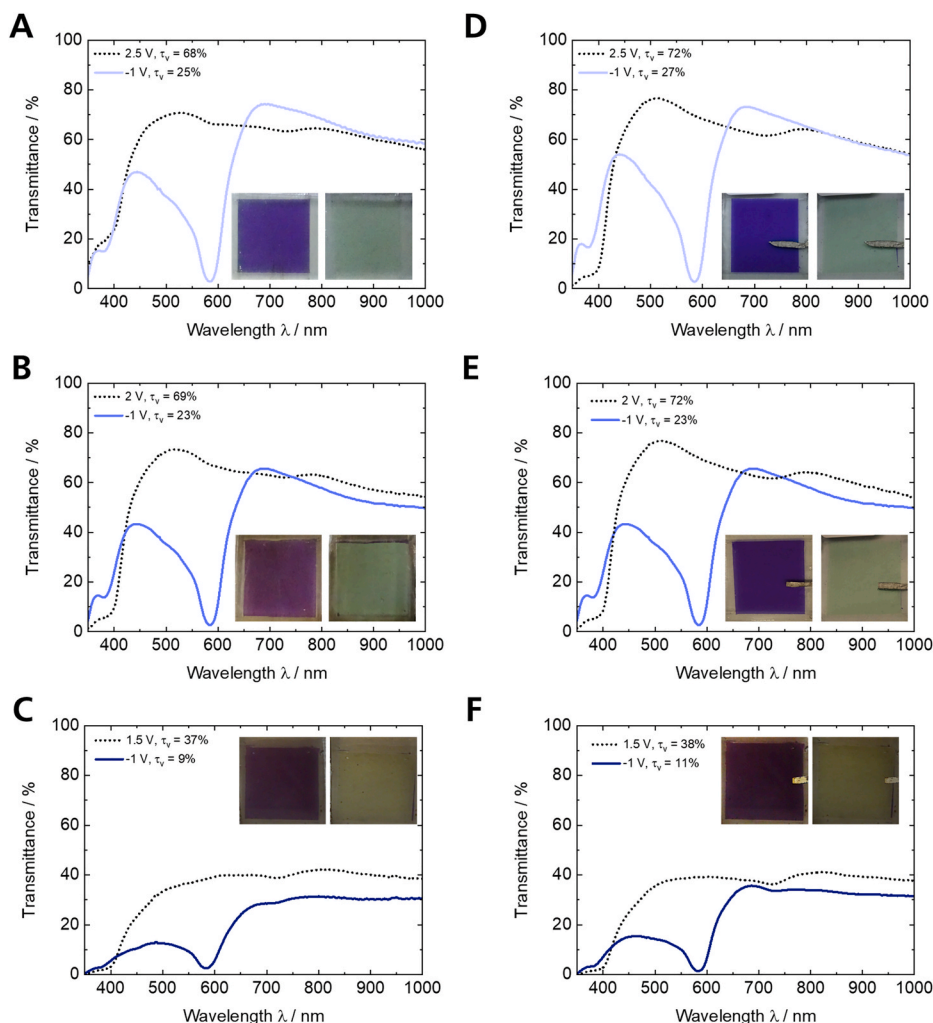
	Cell voltage / V	$L^*$	$a^*$	$b^*$	Transmittance T (at 584 nm) / %	Visible light transmittance $\tau_v$ / %	Charge density q / $\text{mC cm}^{-2}$	Coloration efficiency $\eta$ / $\text{cm}^2 \text{ C}^{-1}$	Response time / s
ECD-1	-1	54.8	7.5	-23.5	3	25	2.30	583.6	0.4
	2.5	86.2	-6.7	8.8	66	68	2.36		
ECD-2	-1	56.7	6.2	-23.4	3	23	2.36	571.7	0.8
	2	87.1	-9.0	10.1	67	69	2.45		
ECD-3	-1	37.0	1.0	-3.4	3	9	2.42	455.6	1.0
	1.5	66.7	-2.8	19.9	38	37	2.32		
ECD-1_RE	-1	58.1	8.2	-24.5	3	27	2.36	579.6	0.4
	2.5	86.1	-6.4	8.4	70	72	2.39		
ECD-2_RE	-1	60.3	6.6	-28.0	3	72	2.69	508.5	0.8
	2.0	88.0	-9.9	9.7	70	23	2.29		
ECD-3_RE	-1	39.7	7.9	-9.0	2	11	2.44	528.7	1.0
	1.5	67.6	-5.1	18.9	39	38	2.42		

literature [9], the lowest device voltage to fully oxidize the WE is achieved when a high charge density CE is used. The minimum cell voltage to completely decolor the Fe-MEPE is decreased from 2.5 V to 2 V and 1.5 V going from the underbalanced (ECD-1), to the balanced (ECD-2) and the overbalanced cell configuration (ECD-3), respectively.

All ECDs are blue-purple colored in their dark state due to the MLCT band of Fe-MEPE, which is apparent in the transmission spectrum of the reduced material (at -1 V). ECD-1 and ECD-2 switch reversibly between a dark-blue colored state and a virtually colorless state ( $L^* = 86.2$ ,  $a^* = -6.7$ ,  $b^* = 8.8$  and  $L^* = 87.1$ ,  $a^* = -9.0$ ,  $b^* = 10.1$ , respectively), while the thicker nickel oxide layer in ECD-3 leads to a distinct yellow hue ( $b^* \sim 20$ ) in the bright state. In comparison to ECD-1 ( $\tau_v$ : 25%  $\rightarrow$  68%) and ECD-2 ( $\tau_v$ : 23%  $\rightarrow$  69%), ECD-3 shows a smaller change in  $\tau_v$  from 9% to only 37%. This can be explained with the lower transmittance of

the  $\text{Ni}_{1-x}\text{O}_5$  film compared to the one of  $\text{Ni}_{1-x}\text{O}_2$  and  $\text{Ni}_{1-x}\text{O}_3$  films due to the larger layer thickness (charge density) as is expected from the half-cell characterization. All ECDs exhibit high coloration efficiency at the absorption maximum of 584 nm with approx.  $500 \text{ cm}^2 \text{ C}^{-1}$ , thus closely matching the  $\eta$  values obtained for the Fe-MEPE electrodes (Table 1). Based on this result, it can be assumed that the  $\text{Ni}_{1-x}\text{O}$  electrode barely changes its transmittance. The thinner  $\text{Ni}_{1-x}\text{O}$  electrodes ( $\text{Ni}_{1-x}\text{O}_2$  and  $\text{Ni}_{1-x}\text{O}_3$ ) show only a slight change in transmittance (Fig. 2A). As the charge density of  $\text{Ni}_{1-x}\text{O}_5$  is higher as the one of Fe-MEPE, it is only partially reduced/oxidized (not completely brightened) during the decoloration/coloration process of ECD-3 due to its high charge density.

A further figure of merit is the response time of the cells that is defined as the time until a value of 10% of the initial current density is



**Fig. 3.** Comparison of the spectroelectrochemical measurements of the two-electrode ECDs: (A) ECD-1 (Fe-MEPE/ $\text{Ni}_{1-x}\text{O}_2$ ), (B) ECD-2 (Fe-MEPE/ $\text{Ni}_{1-x}\text{O}_3$ ), (C) ECD-3 (Fe-MEPE/ $\text{Ni}_{1-x}\text{O}_5$ ) and the three-electrode ECDs: (D) ECD-1\_RE, (E) ECD-2\_RE, and (F) ECD-3\_RE. The insets show the photographic images of the colored and bright state.

reached [28]. In order to be able to compare the response times of the three ECDs, the following prerequisites have to be met. The charge density of the Fe-MEPE film is held constant ( $2.4 \text{ mC cm}^{-2}$ , Table 1) and Fe-MEPE is completely oxidized (decolored) in all cell configurations (Fig. 3). Thus, the charge consumed by all three ECDs is ideally the same when no side reactions or current losses occur. Therefore, the experimentally determined charge density is 2.30, 2.36, and  $2.42 \text{ mC cm}^{-2}$  for ECD-1, ECD-2, and ECD-3, respectively (Fig. S2A and Table 2). The decoloration process is slightly faster (1.8 s vs. 2.0 s response time) and the coloration process is slower (1.0 s vs. 0.4 s response time) with increasing charge density of the CE (Fig. S2B). The incorporation of the  $\text{Ni}_{1-x}\text{O}$  CE increases the response time for coloration (at -1 V), likely due to the inherently slower switching kinetics and higher boundary layer resistance at the electrolyte/electrode interface of  $\text{Ni}_{1-x}\text{O}$  compared to Fe-MEPE [9].

The results of the spectroelectrochemical measurements performed on the three-electrode ECDs in Fig. 3D–F and the summarized data in Table 2 are consistent with the results obtained for the two-electrode ECDs. The introduction of the Li RE does not influence the optical and electrochemical properties of the three-electrode ECDs, making it a useful tool to evaluate the redox behavior of the single electrodes. The cyclic voltammetry results, performed in the cell voltage range from -1 V to 1.5 V, are shown in Figs. S3A,C,E. The CV data obtained from the two- and three-electrode ECDs are also comparable in terms of form and peak

position, further indicating that the three-electrode setup provides reliable results for the electrode potentials. In general, a broadening of the CV peaks is observable for the underbalanced and balanced configurations as compared to the overbalanced one. This can be explained by looking at the electrode potentials depicted in Figs. S3B,D,F. The current density  $j$  of the Fe-MEPE oxidation peak at around 0.9 V and the  $\text{Ni}_{1-x}\text{O}$  reduction peak around 0.3 V in Figs. S3A,C,E become more pronounced with increasing charge density of the  $\text{Ni}_{1-x}\text{O}$  electrode ( $j_{\text{ECD-1\_RE}} < j_{\text{ECD-2\_RE}} < j_{\text{ECD-3\_RE}}$ ). The peaks corresponding to the Fe-MEPE redox process (at around 4 V vs.  $\text{Li/Li}^+$  in Figs. S3B,D,F) are more pronounced for the overbalanced ECD (Fig. S3F) than those of the pristine Fe-MEPE electrodes, as was previously described in literature [11]. Hence, this demonstrates that the upper cut-off cell voltage of 1.5 V is suitable for brightening the overbalanced ECD (ECD-3\_RE), but is insufficient to decolor the other two ECDs (ECD-1\_RE and ECD-2\_RE). These results are consistent with the detailed (spectro-)electrochemical characterization of the two-electrode cells above (Fig. 3), and are further corroborated by the electrode potentials obtained with the three-electrode ECDs in Figs. S3B,D,F. Both films can be reversibly switched (complete decoloration of Fe-MEPE) for the overbalanced (ECD-3\_RE) and balanced (ECD-2\_RE) configuration in this cell voltage window, while neither oxidation nor reduction peaks for the Fe-MEPE and  $\text{Ni}_{1-x}\text{O}_2$  electrode, respectively, can be detected (both electrode potentials remain below 4.1 V vs.  $\text{Li/Li}^+$ ) with the underbalanced ECD (ECD-1\_RE).

### 3.3. Cycling stability of the three-electrode Fe-MEPE/ $\text{Ni}_{1-x}\text{O}$ ECDs

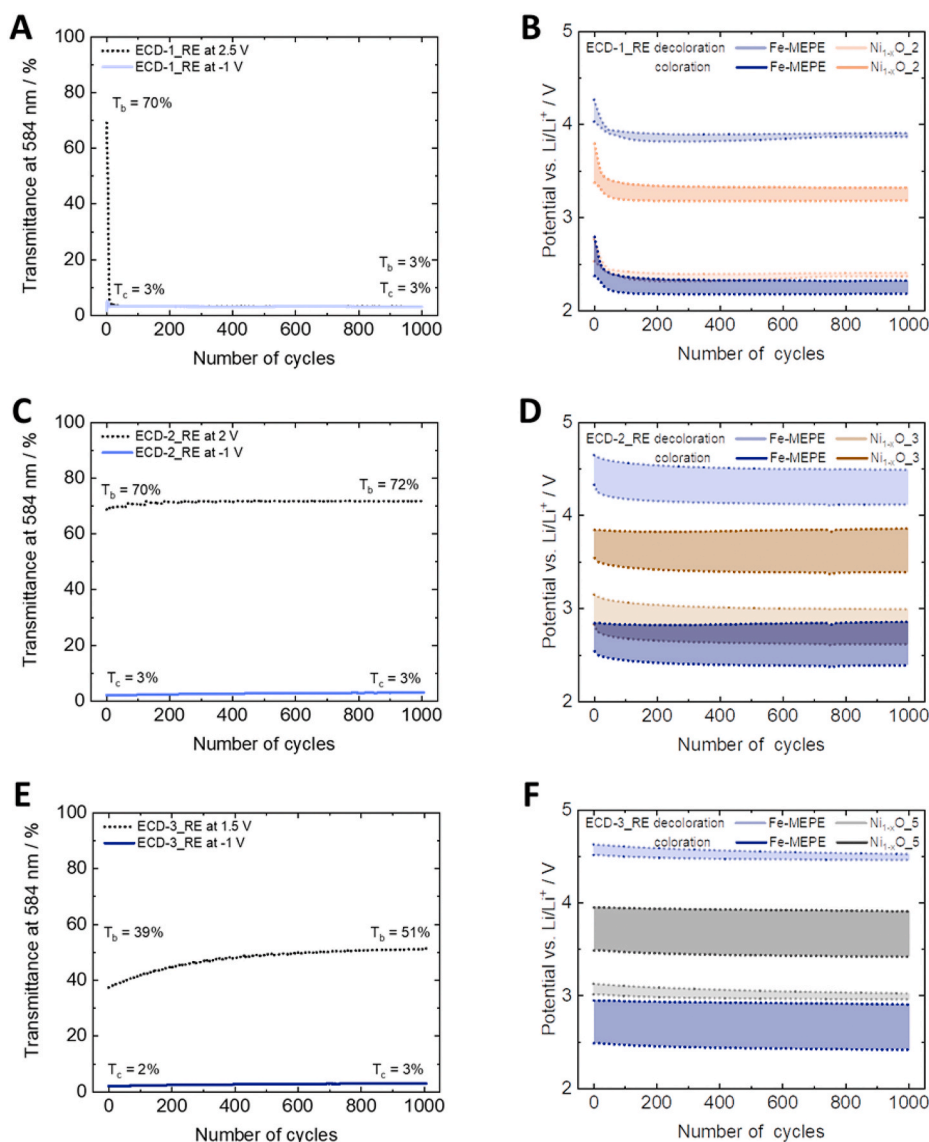
Long-term cycling stability is required for most commercial EC applications. Therefore, the cyclability of the three-electrode Fe-MEPE/ $\text{Ni}_{1-x}\text{O}$  ECDs was measured over 1000 cycles with lower and upper cut-off voltages of  $-1\text{ V} \leftrightarrow 2.5\text{ V}$ ,  $-1\text{ V} \leftrightarrow 2\text{ V}$ , and  $-1\text{ V} \leftrightarrow 1.5\text{ V}$  for ECD-1, ECD-2, and ECD-3, respectively. The potential at each electrode was measured to monitor the decoloration of the Fe-MEPE film electrochemically in addition to the spectroelectrochemical characterization in Figs. 3D,E,F.

ECD-1\_RE (Fig. 4A) shows a significant decrease of the bright state transmittance after only a few cycles ( $<20$ ,  $T_c$  at  $2.5\text{ V}/T_b$  at  $-1\text{ V}$  [in %] from 70/3 to 3/3). Additionally, the MLCT band of Fe-MEPE is maintained even at applied voltages of  $2.5\text{ V}$ , i.e., no oxidation of the Fe-MEPE electrode occurs. During the first cycles, the Fe-MEPE electrode was completely oxidized in ECD-1, which can be explained by the additional charge density provided by the FTO layer (Fig. S4). The CV curve shows that above  $1.5\text{ V vs. Li/Li}^+$  no side reactions or degradation occur, although double layer capacitance can be detected. It should be noted that the current density ( $<0.1\text{ }\mu\text{A cm}^{-2}$ ) is significantly lower than that observed for the CEs (around  $0.1\text{ mA cm}^{-2}$ ) as shown in Fig. 2B. The

irreversibility of the decoloration/coloration process for ECD-1 means that after a few cycles the FTO can no longer supply the additional charge density ( $\text{Ni}_{1-x}\text{O}_2 = 1.27\text{ mC cm}^{-2}$ ) necessary to decolor the Fe-MEPE electrode [29].

The evolution of the electrode potentials can explain this fast deterioration of the switching behavior. During the decoloration process at  $2.5\text{ V}$ , the potential range of the cathodically-coloring Fe-MEPE electrode is above  $4.2\text{ V vs. Li/Li}^+$  in the first cycles and drops below  $4\text{ V vs. Li/Li}^+$  as the ECD is switched to the bright state (Fig. 4B). As a consequence of this shift to lower potentials, the potential of the Fe-MEPE electrode no longer reaches its oxidation potential at around  $4.0\text{ V vs. Li/Li}^+$  and remains in its reduced (colored) state. This is accompanied by a substantial decrease in current density (Fig. S5A) [11]. This phenomenon has already been observed in previous studies [8,30]. Moreover, degradation of the electrodes does not occur during the potentiostatic cycling of ECD-1 as the potentials of the Fe-MEPE electrode (during coloration of ECD-1\_RE at  $-1\text{ V}$ ) and the  $\text{Ni}_{1-x}\text{O}_2$  electrode (during decoloration of ECD-1 at  $2.5\text{ V}$ ) are close to but above  $2\text{ V vs. Li/Li}^+$ . Below  $2\text{ V vs. Li/Li}^+$  side reactions occur at the FTO substrate (Fig. S4) [10].

During the brightening of ECD-3\_RE (Fig. 4F), the Fe-MEPE electrode potential is around  $4.5\text{ V vs. Li/Li}^+$ , which is above its oxidation



**Fig. 4.** Cycle stability over 1000 potentiostatic switching cycles monitored by transmittance change at 584 nm and the measured electrode potentials of the Fe-MEPE and  $\text{Ni}_{1-x}\text{O}$  electrodes in (A,B) ECD-1\_RE, (C,D) ECD-2\_RE, and (E,F) ECD-3\_RE, respectively.



potential, and the potential of the anodically-coloring  $\text{Ni}_{1-x}\text{O}_5$  is between 2.9 V and 3.1 V vs.  $\text{Li}/\text{Li}^+$ . This leads to a complete decoloration of the Fe-MEPE electrode and, hence, the ECD reaches its bright state. The potentials of the Fe-MEPE and  $\text{Ni}_{1-x}\text{O}_5$  electrodes during coloration of the cell are approximately 2.5 V–3.0 V vs.  $\text{Li}/\text{Li}^+$  and 3.5 V and 4.0 V vs.  $\text{Li}/\text{Li}^+$ , respectively. Despite the constant electrode potential during 1000 switching cycles, a continuous brightening of the device ( $T_c$  at 1.5 V/ $T_b$  at -1 V [in %] from 39/2 to 51/3) is observed in Fig. 4E. This brightening is due to increasing amounts of  $\text{Li}^+$  ions irreversibly intercalated into the  $\text{Ni}_{1-x}\text{O}$  layer to balance the charge during the redox reactions. Such irreversible  $\text{Li}^+$ -ion trapping in the nickel oxide crystal structure has already been described in literature [12–14]. In Fig. 4D, a similar result was obtained for the balanced ECD-2\_RE, where the electrode potentials remain almost constant during the potentiostatic cycling (Fe-MEPE: between 4.6 V and 4.2 V vs.  $\text{Li}/\text{Li}^+$  and 2.8 V–2.4 V vs.  $\text{Li}/\text{Li}^+$ ;  $\text{Ni}_{1-x}\text{O}_3$ : between 3.1 V and 2.6 V vs.  $\text{Li}/\text{Li}^+$  and 3.9 V–3.4 V vs.  $\text{Li}/\text{Li}^+$ , for decoloration and coloration, respectively). Finally, the high cycle stability of ECD-2\_RE was further confirmed by the measurement in Fig. 4C that shows a continuous switching behavior for more than 1000 cycles between the fully colored (at 1 V) and the decolored state (at 2 V) with a constant transmittance change from 3% to 70/72%, respectively. The stable behavior of the electrode potentials for ECD-2\_RE and ECD-3\_RE is also demonstrated in the corresponding current-time profiles depicted in Figs. S5B and C.

#### 4. Summary and conclusion

The required cell voltage to obtain the maximum change in transmittance in Fe-MEPE/ $\text{Ni}_{1-x}\text{O}$  ECDs, *i.e.*, a complete switching of the Fe-MEPE WE, is decreased with a higher charge density of the  $\text{Ni}_{1-x}\text{O}$  CE ( $V_{\text{ECD-3}} (1.5 \text{ V}) < V_{\text{ECD-2}} (2 \text{ V}) < V_{\text{ECD-1}} (2.5 \text{ V})$ ). The underbalanced (ECD-1, Fe-MEPE: $\text{Ni}_{1-x}\text{O} \sim 2:1$ ) and the balanced configuration (ECD-2, Fe-MEPE: $\text{Ni}_{1-x}\text{O} \sim 1:1$ ) both yield a slightly yellowish tint with a high bright state transmittance of nearly 70%. The balanced as well as the overbalanced ECD (ECD-3, Fe-MEPE: $\text{Ni}_{1-x}\text{O} \sim 1:3$ ) configurations are characterized by a high cycle stability over 1000 potentiostatic cycles. In general, the overbalanced configuration offers the advantage of a smaller voltage window, *i.e.*, avoidance of degradation. However, in terms of EC performance, the transmittance values at 584 nm of the overbalanced cell configuration (ECD-3,  $T_b/T_c = 39/2\%$ ) are lower than those for ECD-2 ( $T_b/T_c = 70/3\%$ ) due to the thicker  $\text{Ni}_{1-x}\text{O}_5$  electrode (higher charge density). The results highlight the importance of using balanced or (slightly) overbalanced configurations with complimentary-coloring EC electrodes for fast switching and stable ECDs operating at low cell voltage. By integrating a Li RE into the ECDs, the individual redox potentials of both EC electrodes (Fe-MEPE and  $\text{Ni}_{1-x}\text{O}$ ) could be measured *in-operando* during device operation. Incomplete switching of the Fe-MEPE electrode was observed for ECD-1\_RE but degradation processes, as well as side reactions at both electrodes, could be excluded. A detailed investigation of the three-electrode ECDs showed that a shift to lower potentials of both electrodes occurred during potentiostatic cycling, especially for ECD-1\_RE, with the result that the applied cell voltage of 2.5 V is not sufficient anymore to switch the cell. In terms of electrochemical performance and cycle stability, Fe-MEPE: $\text{Ni}_{1-x}\text{O}$  charge density ratios equal to 1 or lower are feasible, and maximum optical contrasts can be reached while keeping the operating cell voltages between -1 V and 2 V. Thus, this three-electrode cell configuration offers an excellent method for *in-situ* electrochemical characterization of the individual EC electrodes to better understand the redox processes during device operation and to further improve the optical contrast and durability of ECDs in the future.

#### CRedit authorship contribution statement

**Lukas Niklaus:** Investigation, Validation, Visualization, Writing – original draft. **Marco Schott:** Conceptualization, Supervision, Writing –

review & editing, Project administration. **Uwe Posset:** Writing – review & editing, Funding acquisition. **Mohor Mihelčić:** Investigation, Writing – review & editing. **Ivan Jerman:** Resources. **Guinevere A. Giffin:** Writing – review & editing, Supervision.

#### Declaration of competing interest

The authors declare that they have no known competing financial interests or personal relationships that could have appeared to influence the work reported in this paper.

#### Acknowledgment

The authors acknowledge the financial support from the Bavarian Ministry of Economic Affairs and Media, Energy, and Technology for funding the Fraunhofer R&D Center for Electromobility Bavaria (grant no. 43-6629/86). The contribution of Christine Müller (Fraunhofer ISC) for assisting in the full cell preparation and of Werner Strack (Fraunhofer ISC) for the SEM measurements is gratefully acknowledged.

#### Appendix A. Supplementary data

Supplementary data to this article can be found online at <https://doi.org/10.1016/j.solmat.2021.111080>.

#### References

- [1] R.J. Mortimer, D.R. Rosseinsky, P.M.S. Monk (Eds.), *Electrochromic Materials and Devices*, Wiley-VCH Verlag GmbH & Co. KGaA, Weinheim, 2015.
- [2] C.G. Granqvist, M.A. Arvizu, I. Bayrak Pehlivan, H.-Y. Qu, R.-T. Wen, G. A. Niklasson, Electrochromic materials and devices for energy efficiency and human comfort in buildings: a critical review, *Electrochim. Acta* 259 (2018) 1170–1182, <https://doi.org/10.1016/j.electacta.2017.11.169>.
- [3] S.V. Vasilyeva, E. Unur, R.M. Walczak, E.P. Donoghue, A.G. Rinzier, J.R. Reynolds, Color purity in polymer electrochromic window devices on indium-tin oxide and single-walled carbon nanotube electrodes, *ACS Appl. Mater. Interfaces* 1 (2009) 2288–2297, <https://doi.org/10.1021/am900435j>.
- [4] M.A. Invernale, V. Seshadri, D.M.D. Mamangun, Y. Ding, J. Filloramo, G. A. Sotzing, Polythieno[3,4- b ]thiophene as an optically transparent ion-storage layer, *Chem. Mater.* 21 (2009) 3332–3336, <https://doi.org/10.1021/cm900843b>.
- [5] C.O. Avellaneda, M.A.C. Berton, L.O.S. Bulhões, Optical and electrochemical properties of CeO<sub>2</sub> thin film prepared by an alkoxide route, *Sol. Energy Mater. Sol. Cell.* 92 (2008) 240–244, <https://doi.org/10.1016/j.solmat.2007.03.035>.
- [6] A. Azens, L. Kullman, D.D. Ragan, C.G. Granqvist, Optically passive counter electrodes for electrochromic devices: transition metal–cerium oxide thin films, *Sol. Energy Mater. Sol. Cell.* 54 (1998) 85–91, [https://doi.org/10.1016/S0927-0248\(97\)00267-5](https://doi.org/10.1016/S0927-0248(97)00267-5).
- [7] L. Niklaus, M. Schott, J. Subel, S. Ulrich, D. Reichert, U. Posset, G.A. Giffin, Mixed Metal Oxides as Optically-Passive Ion Storage Layers in Electrochromic Devices Based on Metallopolymers (Submitted), *Solar Energy Materials and Solar Cells*.
- [8] S. Hassab, J. Padilla, Using WO<sub>3</sub> as a transparent, optically-passive counter electrode in an unbalanced electrochromic configuration, *Electrochem. Commun.* 72 (2016) 87–90, <https://doi.org/10.1016/j.elecom.2016.09.001>.
- [9] S. Hassab, D.E. Shen, A.M. Österholm, J.R. Reynolds, J. Padilla, Exploring unbalanced electrode configurations for electrochromic devices, *J. Mater. Chem. C* 6 (2018) 393–400, <https://doi.org/10.1039/C7TC04730D>.
- [10] S. Macher, M. Rumpel, M. Schott, U. Posset, G.A. Giffin, P. Löbmann, Avoiding voltage-induced degradation in PET-ITO-based flexible electrochromic devices, *ACS Appl. Mater. Interfaces* (2020), <https://doi.org/10.1021/acsami.0c07860>.
- [11] L. Niklaus, M. Schott, M. Mihelčić, I. Jerman, U. Posset, G. Sextl, Metallopolymers and non-stoichiometric nickel oxide: towards neutral tint large-area electrochromic devices, *Sol. Energy Mater. Sol. Cell.* 200 (2019) 110002, <https://doi.org/10.1016/j.solmat.2019.110002>.
- [12] M.A. Arvizu, H.-Y. Qu, G.A. Niklasson, C.G. Granqvist, Electrochromic pretreatment of electrochromic WO<sub>3</sub> films gives greatly improved cycling durability, *Thin Solid Films* 653 (2018) 1–3, <https://doi.org/10.1016/j.tsf.2018.02.032>.
- [13] H.-Y. Qu, D. Primetzhofner, M.A. Arvizu, Z. Qiu, U. Cindemir, C.G. Granqvist, G. A. Niklasson, Electrochemical rejuvenation of anodically coloring electrochromic nickel oxide thin films, *ACS Appl. Mater. Interfaces* 9 (2017) 42420–42424, <https://doi.org/10.1021/acsami.7b13815>.
- [14] R.-T. Wen, C.G. Granqvist, G.A. Niklasson, Eliminating degradation and uncovering ion-trapping dynamics in electrochromic WO<sub>3</sub> thin films, *Nat. Mater.* 14 (2015) 996–1001, <https://doi.org/10.1038/nmat4368>.
- [15] M. Schott, L. Niklaus, J. Clade, U. Posset, Electrochromic metallo-supramolecular polymers showing visible and near-infrared light transmittance modulation, *Sol. Energy Mater. Sol. Cell.* 200 (2019) 110001, <https://doi.org/10.1016/j.solmat.2019.110001>.

- [16] L. Niklaus, M. Schott, U. Posset, G.A. Giffin, Redox electrolytes for hybrid type II electrochromic devices with Fe-MEPE or Ni1-xO as electrode materials, *ChemElectroChem*. <https://doi.org/10.1002/celec.202000583>.
- [17] E.C. Constable, A.M.W.C. Thompson, Multinucleating 2,2',6',2''-terpyridine ligands as building blocks for the assembly of co-ordination polymers and oligomers, *J. Chem. Soc., Dalton Trans.* (1992) 3467–3475, <https://doi.org/10.1039/DT9920003467>.
- [18] M. Schott, H. Lorrmann, W. Szczerba, M. Beck, D.G. Kurth, State-of-the-art electrochromic materials based on metallo-supramolecular polymers, *Sol. Energy Mater. Sol. Cell.* 126 (2014) 68–73, <https://doi.org/10.1016/j.solmat.2014.03.032>.
- [19] M. Schott, W. Szczerba, U. Posset, A. Šurca Vuk, M. Beck, H. Riesemeier, A. F. Thünemann, D.G. Kurth, In operando XAFS experiments on flexible electrochromic devices based on Fe(II)-metallo-supramolecular polyelectrolytes and vanadium oxide, *Sol. Energy Mater. Sol. Cell.* 147 (2016) 61–67, <https://doi.org/10.1016/j.solmat.2015.10.015>.
- [20] M. Mihelčić, I. Jerman, F. Švegl, A. Šurca Vuk, L. Slemenik Perše, J. Kovač, B. Orel, U. Posset, Electrochromic Ni1-xO pigment coatings and plastic film-based Ni1-xO/TiO2 device with transmissive light modulation, *Sol. Energy Mater. Sol. Cell.* 107 (2012) 175–187, <https://doi.org/10.1016/j.solmat.2012.08.012>.
- [21] M. Mihelčić, I. Jerman, B. Orel, Preparation of electrochromic Ni1-xO and TiO2 coatings from pigment dispersions and their application in electrochromic foil based devices, *Prog. Org. Coating* 76 (2013) 1752–1755, <https://doi.org/10.1016/j.porgcoat.2013.05.011>.
- [22] M. Higuchi, Stimuli-responsive metallo-supramolecular polymer films: design, synthesis and device fabrication, *J. Mater. Chem. C* 2 (2014) 9331–9341, <https://doi.org/10.1039/C4TC00689E>.
- [23] M. Bonomo, A.G. Marrani, V. Novelli, M. Awais, D.P. Dowling, J.G. Vos, D. Dini, Surface properties of nanostructured NiO undergoing electrochemical oxidation in 3-methoxy-propionitrile, *Appl. Surf. Sci.* 403 (2017) 441–447, <https://doi.org/10.1016/j.apsusc.2017.01.202>.
- [24] W.-L. Jang, Y.-M. Lu, W.-S. Hwang, W.-C. Chen, Electrical properties of Li-doped NiO films, *J. Eur. Ceram. Soc.* 30 (2010) 503–508, <https://doi.org/10.1016/j.jeurceramsoc.2009.05.041>.
- [25] Idris Sorar, Tesfalem G. Welearegay, Daniel Primetzhofer, Lars Österlund, Claes G. Granqvist, Gunnar A. Niklasson, Electrochromism in Ni oxide thin films made by advanced gas deposition and sputtering: a comparative study demonstrating the significance of surface effects, *J. Electrochem. Soc.* 167 (2020) 116519, <https://doi.org/10.1149/1945-7111/aba5d9>.
- [26] C.G. Granqvist, *Handbook of Inorganic Electrochromic Materials*, Elsevier, Amsterdam, 1995.
- [27] Q. Liu, Q. Chen, Q. Zhang, Y. Xiao, X. Zhong, G. Dong, M.-P. Delplancke-Ogletree, H. Terry, K. Baert, F. Reniers, X. Diao, In situ electrochromic efficiency of a nickel oxide thin film: origin of electrochemical process and electrochromic degradation, *J. Mater. Chem. C* 6 (2018) 646–653, <https://doi.org/10.1039/C7TC04696K>.
- [28] M. Panagopoulou, D. Vernardou, E. Koudoumas, N. Katsarkis, D. Tsoukalas, Y. S. Raptis, Tunable properties of Mg-doped V2O5 thin films for energy applications: Li-Ion batteries and electrochromics, *J. Phys. Chem. C* 121 (2017) 70–79, <https://doi.org/10.1021/acs.jpcc.6b09018>.
- [29] D. Wang, L. Wei, P. Shi, Y. Chen, S. Yan, Y. Tian, J. Jiao, Electrochromic behavior of fluorine-doped tin oxide film via guided motion of Li ions, *J. Alloys Compd.* 771 (2019) 100–105, <https://doi.org/10.1016/j.jallcom.2018.08.268>.
- [30] J. Remmele, D.E. Shen, T. Mustonen, N. Fruehauf, High performance and long-term stability in ambiently fabricated segmented solid-state polymer electrochromic displays, *ACS Appl. Mater. Interfaces* 7 (2015) 12001–12008, <https://doi.org/10.1021/acsami.5b02090>.



